Imperial College London

Mechanical Engineering PhD Thesis

IMPERIAL COLLEGE LONDON

DEPARTMENT OF MECHANICAL ENGINEERING

Impact Testing of Pristine and Repaired Carbon Fibre Reinforced Polymer Composite Materials for Aircraft Structures

Name:

Zoe Hall

Supervisor:

Prof. John P. Dear

March 2023

Abstract

Aircraft technologies and materials have been developing and improving drastically over the last hundred years. Over the last three decades, an interest in the use of composites for the external structures has become prominent. For this to be possible, thorough research on the performance of composite materials, specifically the impact performance, is required. Previous research of impact testing for pristine carbon-reinforced epoxy composites describes matrix cracks, fibre fracture and delamination as the failure modes that require monitoring. An area of concern with the use of composites for aerostructures is their ability to be repaired and retain a suitable level of performance. Currently, since there are limitations in non-destructive testing (NDT) methods for adhesive bonding, adhesively joined or repaired composite materials are restricted to being used for secondary structures within the aircraft, unless another joining method – such as mechanical fasteners – are also implemented. Rigorous research and testing are required in this area because the current technique for metals, of bolting an undamaged piece of material over the damaged area, is not effective for composites as it introduces detrimental damage.

There are two main repair techniques for composite materials: scarf and patch repair. Investigating the potential of the latter to restore the impact properties of carbon fibre reinforced polymer (CFRP) composite panels contributes to a large section of the research in this thesis. Two different types of lay-up (quasi-isotropic and cross-ply) were tested, with repair variables such as the patch diameter, patch thickness, inclusion of a plug and distance of the impact site from the centre of the patch being adjusted to see how each affects the overall performance of the repair. It was seen that the patch diameter has little to no effect on the repair performance, with both 55 and 65 mm patches giving similar load traces. The patch thickness and inclusion of a plug had a more significant effect on the impact properties of the repairs, with the two best performing repair configurations being a thick patch and a thin patch reinforced with a plug. The location of the impact site also greatly affected the performance of the panel, with impacting on the patch but not centrally giving the largest damage area of all the configurations tested.

Two primary types of impact will be considered in this thesis: hard and soft. Hard impacts are defined as having limited deformation of the impactor upon impact, examples of which include metal debris hitting the aircraft. Soft impacts have a significant amount of deformation of the impactor and include hail stones or bird

strikes. Considering the transition from a hard to a soft impact and the effect this has on the failure modes seen in the CFRP is investigated as part of the research in this thesis. To consider this, a rounded stainless-steel impactor, flat ended stainless-steel impactor and a flat ended stainless-steel impactor with different thicknesses of neoprene adhered to the end were used to impact pristine quasi-isotropic material. The results suggested that, although a lower damage initiation value was observed for the samples impacted with the round-nosed impactor in comparison, the samples impacted with the flat-ended impactor had a larger damage area once damage did initiate. The addition of rubber reduced the peak load and increased the displacement of the samples. It was also seen that the damage area reduced slightly as the thickness of rubber increased.

Another area of interest is accurately predicting the impact performance of pristine panels under both hard and soft impact loading conditions through the use of numerical modelling. This allows for various scenarios and the transition between the two types of impact to be considered without the cost and time of experimental work. In this thesis, a model has been developed and compared with the experimental results for the hard and soft impact research to investigate the potential for it to be used to determine suitable scenarios to test experimentally. The numerical analysis results reflected the overall trends observed experimentally when increasing impact energy for round-nosed impacts and also when increasing the softness of the impact, with excellent agreement between the simulation and experimental testing for the damage area produced by a 7.5 J round-nosed impact. This demonstrates the potential to use a model similar to the one in this thesis to predict the performance of CFRP panels under impact loading conditions, but also highlights some drawbacks and a need for further development and refinement to improve the accuracy.

Declaration of Originality

I declare that the work presented in this thesis is entirely my own and all testing, results and analysis was performed during my PhD studies at Imperial College London. Any work from others has been highlighted as such by being referenced appropriately in the text and the bibliography. Lastly, this work has not been submitted elsewhere for another qualification.

Copyright Declaration

Acknowledgements

I would firstly like to thank my primary supervisor, Professor John P. Dear. His help, guidance and support throughout this project allowed me to learn not only about the research area I was investigating but also professionalism and invaluable skills that I will take forward throughout the rest of my career. Additionally, I would like to thank my co-supervisors, Professor Anthony J. Kinloch, Professor Bamber R.K. Blackman and Dr Haibao Liu. Their knowledge and input helped me to refine my project. Without all my supervisors I would not have been able to achieve the work presented in this thesis and I am extremely grateful that I was able to learn from such knowledgeable and talented individuals.

Furthermore, I would like to thank my colleagues, the technicians, support staff, my fellow PhD students and everyone within the Mechanics of Materials Division at Imperial College London, particularly my research group. A special thanks to Dr Jun Liu, Mr Richard Brooks and Mr Yuzhe Ding for their help throughout my PhD but especially with experimental work. I would also like to thank Dr Lee Harper and Dr Adam Joesbury from Nottingham University for their help manufacturing the composite panels used for the work in this thesis. The work in this thesis was undertaken at the AVIC Centre for Structural Design and Manufacture at Imperial College London and the University of Nottingham.

I gratefully acknowledge the financial support from the Aviation Industry Corporation of China (AVIC) the Aircraft Strength Research Institute (ASRI), without whom this project would not have been possible. Their support and backing allowed the research in this thesis to be performed and the project to evolve over the course of my PhD.

I would like to thank Polar Manufacturing Ltd, who repaired the composite panels, for their assistance and guidance in designing the repairs. Their expertise in the repair of composite materials was extremely helpful.

Lastly, I would like to thank my friends and family for their love and support during this PhD. I would especially like to thank my parents for their encouragement to pursue my interests from a young age and their constant support.

Table of Contents

List of Figures

List of Tables

Nomenclature

c_{10} Neo Hookean material constant 1

d General damage parameter

d_f Fibre failure damage variable

d_f^c Compressive fibre failure damage parameter

d_f^t Tensile fibre failure damage parameter

d_m Matrix failure damage variable

d_m^c Compressive matrix failure damage parameter

d_m^t Tensile matrix failure damage parameter

d_s Shear failure damage variable

d_1 Neo Hookean material constant 2

E_{ii} Elastic modulus in longitudinal and transverse directions $(i = 1,2)$

F_f^c Compressive fibre failure damage criterion

F_f^t Tensile fibre failure damage criterion

F_m^c Compressive matrix failure damage criterion

F_m^t Tensile matrix failure damage criterion

G_c Interlaminar fracture energy

G_i Shear modulus in the longitudinal-transverse, longitudinal-normal and transverse-normal directions $(i = 12,13,23)$

G_I Mode I energy release rate

G_{Ic} Mode I interlaminar fracture energy

$G_{Ic|fc}$ Compressive intralaminar fracture energy in the longitudinal direction

$G_{Ic|ft}$ Tensile intralaminar fracture energy in the longitudinal direction

$G_{Ic|mc}$ Compressive intralaminar fracture energy in the transverse direction

$G_{Ic|mt}$ Tensile intralaminar fracture energy in the transverse direction

G_{II} Mode II energy release rate

G_{IIc} Mode II interlaminar fracture energy

$G_{IIc|ms}$ Shear intralaminar fracture energy

$\bar{I}_1$ First deviatoric strain invariant

J Total volume ratio

J^{el} Elastic volume ratio

k Cohesive law stiffness

S_{1t} Longitudinal tensile strength

S_{1c} Longitudinal compressive strength

S_{2t} Transverse tensile strength

S_{2c} Transverse compressive strength

S_{12} Longitudinal shear strength

S_{13} Transverse shear strength

t_i^0 Initial cohesive law strengths ($i = 33{,}31{,}32$)

U Strain energy potential per unit volume

ε Strain

ε^0 Initial failure strain

ε^f Final failure strain

ε_{ii} Longitudinal or transverse strain ($i = 1{,}2$)

ε_{ii}^0 Longitudinal or transverse initial failure strain ($i = 1{,}2$)

ε_{ii}^f Longitudinal or transverse final failure strain ($i = 1{,}2$)

η Benzeggagh-Kenane exponent

λ_i Principle stretches

$\bar{\lambda}_i$ Deviatoric stretches

υ_{12} Poisson's ratio

$\hat{\sigma}_{ii}$ Effective stress in the longitudinal and transverse directions ($i = 1{,}2$)

$\hat{\tau}_{12}$ Effective shear stress tensor in the longitudinal-transverse direction

Abbreviations

2D	Two dimensional
3D	Three dimensional
ASRI	Aircraft Strength Research Institute
ASTM	American Society for Testing and Materials
AVIC	Aviation Industry Corporation of China
B-K	Benzaggagh-Kenane
CFRP	Carbon Fibre Reinforced Polymer
CPU	Central Processing Unit
DA	Damage Area
FE	Finite Element
FEA	Finite Element Analysis
GFRP	Glass Fibre Reinforced Polymer
HDPE	High Density Polyethylene
NDT	Non-Destructive Testing
PEEK	Polyether Ether Ketone
PLA	Polylactic Acid
QIT	Quasi-Isotropic
SEM	Scanning Electron Microscopy
SPH	Smoothed Particle Hydrodynamics
URS	Ultrasonic Resonance Spectroscopy

1 Introduction

1.1 Background

An area of interest when considering the performance of composite materials for aircraft is the impact performance of repaired composites. The performance of the materials after repair are of great interest because the life of an aircraft is significantly longer than some of its components, meaning repair is critical. It is especially critical for composite materials because the residual strength of the material is significantly reduced after damage. To mitigate this drawback, repair can be used to increase the residual strength of the damaged composite laminates. However, a restriction of repair is the limited number of NDT methods to monitor the performance of the adhesive bonding within it. Currently, repaired composite materials are limited by this and, as such, are primarily used for secondary structures in aircraft. If they are to be used in primary aerostructures, an additional joining method must be used in conjuncture with the composite repair. The most commonly used of these is titanium fasteners, which are expensive, add weight and must be earthed due to the risk of lightning strikes. This is because they are easily monitored using NDT methods. Impact performance is of particular interest because there are a number of types of impact that an aircraft will be subjected to regularly. For example, bird strike and hail stones are both soft impacts whilst runway debris flying up and hitting the aircraft is a hard impact. Further examples include ground equipment driving up to the side of the plane and hard landings. Clark et al. found that damaged panels loaded under compression-based fatigue experienced an increase in the damage area, with the rate of expansion depending on the size of the initial damage from the low velocity impact [1]. This implies that impact damage is likely to lead to failure from fatigue if it does not fail immediately, meaning considering how to repair or replace composite panels is of interest. For this reason, damage monitoring and composite repair is vital to ensure any damage is found and repaired before it causes failure. Barely visible damage is of high concern to aircraft designers and so composite components are generally over-designed to ensure the risks are mitigated. Another area of interest is to consider the transition from hard to soft impacts and how this affects the damage mechanisms and failure modes that occur in the composite materials. An impact is classified as hard if the impactor does not significantly deform upon initial impact. This type of interaction results in permanent indentation on the impacted surface of the composite laminates, whereas soft impacts do not leave any marks on the impacted surface. This is because the impactor deforms

while impacting the sample, which causes a reduction in the stress concentration from the impact. Varying the hardness of the impactor will change the damage in the sample but there is limited research on how the failure modes differ between hard and soft impacts and even less on transitioning between the two and at what point the classification changes. Investigating this area will allow for the damage in composites to be categorised more easily and for suitable repair techniques to implemented when necessary. In this thesis, research will be discussed where different features of patch repairs are varied to investigate the effect each has on the overall impact performance and how patch repairs might be used to restore the impact properties of carbon fibre reinforced polymer (CFRP) composite materials. Additionally, testing with both hard and soft impactors was performed to gain more of an understanding of how the damage mechanisms change between the two. Lastly, numerical modelling of pristine and patch repaired composite panels will be explored.

1.2 Aims and Objectives

- To review the literature available and consider research that has been performed up to the time of this thesis on the impact performance of repaired carbon fibre reinforced polymer composite materials.
- To review the literature available and consider research that has been performed up to the time of this thesis on the damage characteristics of hard and soft impacts and the transition between the two.
- To consider how the properties of a patch repair affect the impact performance of a carbon fibre reinforced polymer composite sample compared to a pristine and a damaged sample of the same lay-up.
- To consider the transition between hard and soft impacts on carbon fibre reinforced polymer composite materials and how this affects the type of damage observed.
- To verify a numerical model that is made up of composite damage models and finite element analysis with experimental results and use this to further consider the impact response of carbon fibre reinforced composite panels.

1.3 Structure of the Thesis

The chapters in this thesis are outlined as follows.

Chapter 1 introduces the topic of research for this thesis by discussing the background, aims and objectives and overall structure.

Chapter 2 summarises the impact performance of pristine and repaired composite panels, how changing variables of the repair can influence the impact properties, some of the differences between hard and soft impacts and the damage mechanisms observed, and the use of numerical models to predict the impact event of pristine and repaired composite panels through a review of the literature available.

Chapter 3 details the specific CFRP composite used in testing, how both pristine and repaired panels were prepared, and the equipment used to impact the panels and inspect them after impact. The four different lay-ups of the unidirectional carbon fibre reinforced epoxy prepreg utilised in this work are discussed in this section. Descriptions of the drop-weight tower and c-scanning equipment used for testing and inspecting the panels are given.

Chapter 4 discusses the low-velocity impact testing of pristine and patch repaired quasi-isotropic CFRP panels, considering the effect on the repair performance when the patch diameter, patch thickness and inclusion of a plug were varied. The samples were impacted, giving load-time and load-displacement traces, and the damage area examined to allow for comparison between the different repair scenarios.

Chapter 5 discusses the low-velocity impact testing of pristine and patch repaired cross-ply CFRP panels, considering the effect on the repair performance when the impact site was offset from the centre of the repair. The samples were impacted, giving load-time and load-displacement traces, and the damage area examined to allow for comparison between the different impact locations.

Chapter 6 discusses the low-velocity impact testing of pristine quasi-isotropic CFRP panels using round-nosed and flat-ended stainless-steel impactors, adhering different thicknesses of neoprene to the flat-ended impactor for some impacts to allow the differences between hard and soft impacts to be considered. The samples were impacted, giving load-time and load-displacement traces, and the damage area examined to allow for comparison between the different impactors and types of impact.

Chapter 7 explores the use of a numerical model implementing composite damage models and finite element analysis to predict the damage produced during both hard and soft impacts of pristine CFRP panels. The model was verified using the testing results from Chapter 6.

Chapter 8 summarises the conclusions drawn from the results of all the testing in this thesis.

Chapter 9 suggests further work that could be performed to continue the research in this thesis.

2 Literature Review

2.1 Introduction

There are various ways to repair a composite sample, shown by Rider et al. in Figure 2-1 [2], with the two main techniques being patch and scarf repairs. Firstly, patch repairs are when the damaged area is covered by a patch of material that is usually only one or two plies thick, shown in Figure 2-1 (a). This repair can be single or double, with a single only patching on one side and double patching on both sides of the material. Secondly, scarf repairs are performed by removing the damage area with a circular cut and inserting a frustum. This frustum should have the same lay-up as the parent material to optimise the stresses through the adhesive [3]. The scarf joints used for repair are shown in Figure 2-1 (b) and (c), with the former demonstrating that steps can be used on the scarf surface to alter the performance of the repaired composite, with the latter having preferable stress distributions but, in practice, there is minimal difference between the two types of scarf repair [4]. It is also possible to combine scarf and patch repairs, as can be seen in Figure 2-1 (d), to further improve the repair performance.

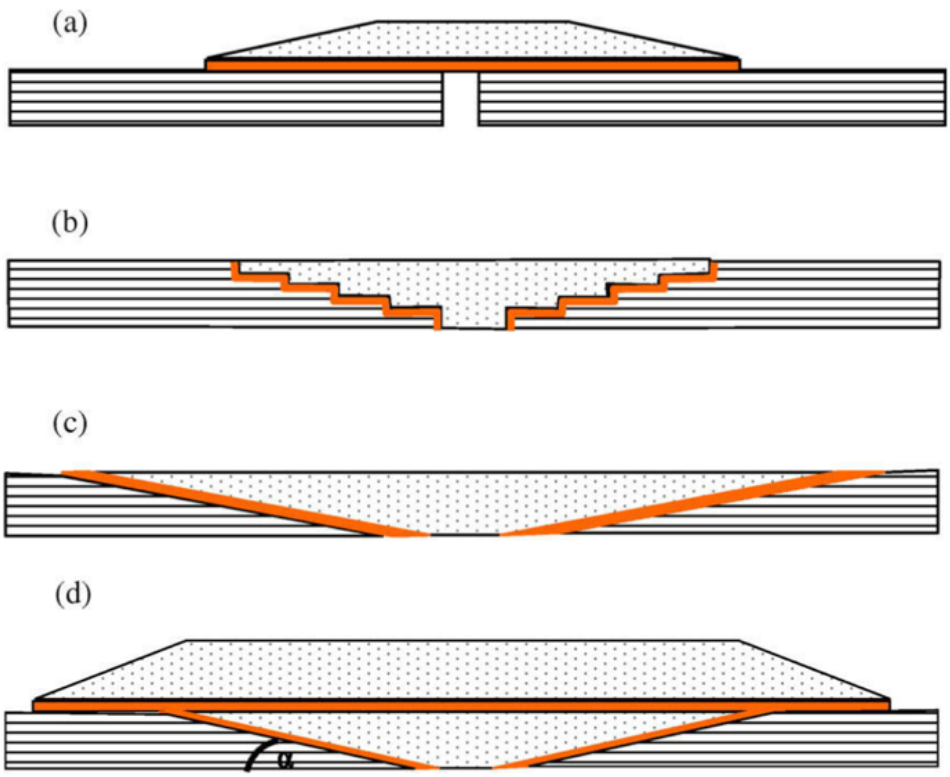

Figure 2-1. Repair configurations discussed by Rider et al. (a) patch repair, (b) stepped scarf repair, (c) scarf repair and (d) scarf and patch repair [2].

Comparing scarf and patch repairs, there are a number of advantages and disadvantages for each. The reasoning for choosing scarfed repairs over patch repairs was discussed by Pinto et al., with one of the primary reasons being that the former of the two does not result in significant bending when in use. This means that the peel stresses experienced by the material are reduced. In continuation, the shape of the scarf repair causes a more uniform distribution of shear stress, which adds to the benefits of utilising this repair technique [5]. Furthermore, the aerodynamics of the component remain more or less unchanged when this method is utilised [5,6]. Alternatively, the patch repair technique is preferable due to the lack of material removal, meaning the parent material is subjected to minimal damage [7,8]. Katnam et al. discuss this as being a significant drawback for scarf repair, since large amounts of undamaged parent material must be removed, especially with a small scarf angle. Material removal in itself is a challenge for composite materials, with traditional machining techniques generating too much heat and causing damage [6]. In continuation, research from Baker et al. implies that single patch repairs effectively transfer loads from the patch itself to the undamaged parent material, allowing the repair to be successful [7]. Furthermore, the join between the patch and parent material is lightweight and so does not cause significant stress concentrations, unlike the cut-outs required for scarf repairs [8]. Both types of repair require an adhesive and, as a result, both experience the challenges that come with this, such as surface preparation and voids. Effective surface preparation is required to ensure the adhesive is efficient and free of defects [6,7]. However, factors that compromise the strength of the adhesive are not limited to surface preparation, with under-curing increasing the risk of voids [6]. Preau et al. investigated the latter phenomenon for scarf repair and their results showed a reduction in strength recovery of 4.5% for every 1% of void content in the adhesive. The void content was also said to influence the failure mode, with the more porous adhesive joints failing from cohesive failure in comparison to tensile failure for the void-free joints [9]. In general, it is commented that automating various processes in this repair technique offers opportunities to improve the performance and repeatability of the joints, by removing the factor of human error [6].

When considering impacts of composite materials, there is often a focus on those that would be categorised as hard rather than soft. This is due to the fact that the damage produced from this type of impact is much easier to detect and so is primarily used when testing the impact properties of new materials or repair configurations. There is limited testing of soft impacts and very little research considering the transition between hard and soft impacts and how the damage mechanisms vary between the two. Abrate considered soft impacts

on aerostructures to show that the response is different from hard impacts. It is often assumed in literature that numerical models for predicting the damage produced by hard impacts can be applied to soft impact cases, with Abrate's research showing that soft impacts, specifically rain drops, bird strikes and hailstones, require the fluidity of the projectile and dissipation on kinetic energy to be considered when simulating the impact, demonstrating that these types of impact differ from hard impacts [10]. Furthermore, although there are a large number of definitions for how to categorise an impact and determine if it is hard or soft in nature, Koechlin et al. found that a lot of these were not precise enough to distinguish between the two types of impact [11]. This implies that the first hurdle when considering soft impacts is understanding how they differ from hard impacts and understanding the transition between the two might allow for this comparison to be made more clearly.

2.2 Composite Impact Failure Modes

2.2.1 Intralaminar failure

Intralaminar failure is when damage occurs within the composite plies and there are two main types: matrix cracking and fibre breakage. Matrix cracking is the first failure mode to be observed within the composite and, although it may affect the strength, stiffness and moisture absorption, among other properties, it is the more harmful damage mechanisms that it leads to that result in the composite ultimately losing its load carrying capacity [12]. Matrix failure can occur from tensile, compressive or shear forces and occurs when the matrix element of the composite is the primary load-bearing element of the material leading to cracking through the thickness of the material [13] and Figure 2-2 shows a schematic of matrix cracks under these different loading conditions.

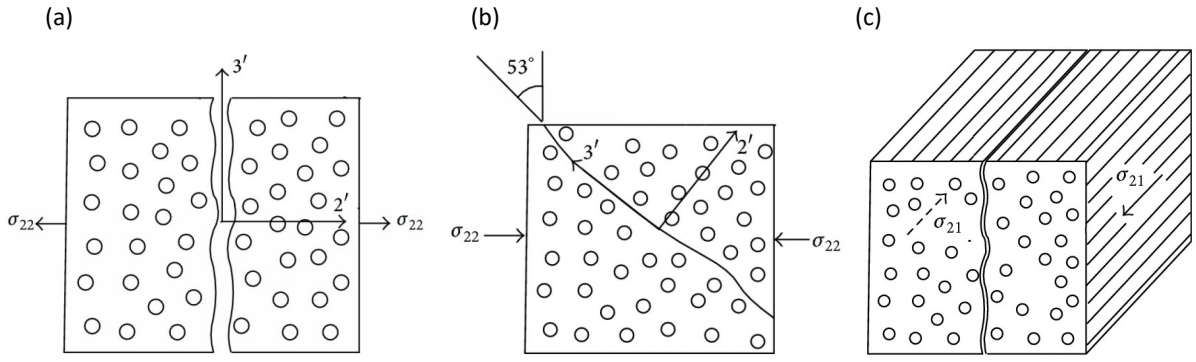

Figure 2-2. Matrix cracking in composite laminates under (a) tension, (b) compression, and (c) shear loading [14].

For matrix cracking to initiate, there must first be de-bonding of the fibre from the matrix as these join together to form a macroscopic crack [15,16]. At the maximum stress value the material can withstand under tension and just before this value under compression, fibre and matrix de-bonding initiates, which causes the stress to drop and leads to a matrix crack between two cases of de-bonding that are close together [16], as shown in Figure 2-3.

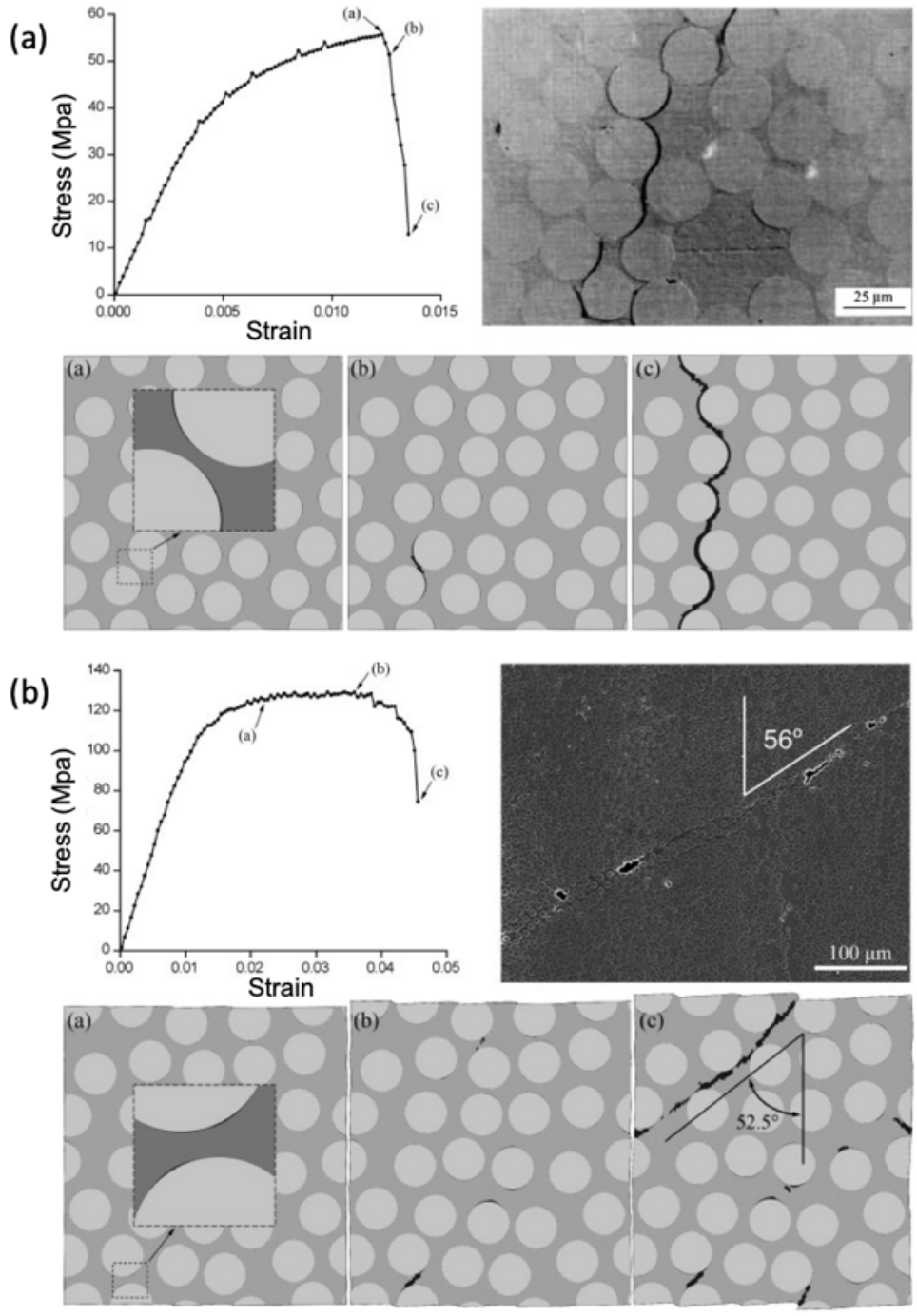

Figure 2-3. Fibre and matrix de-bonding leading to matrix cracking in a fibre reinforced composite loaded under (a) tension, and (b) compression [16].

The second type of intralaminar damage is fibre failure and it has been observed that unidirectional fibre-reinforced composite materials have a lower compressive strength along the fibre direction value compared to their tensile strength value due to micro-buckling of the fibres along the 0° direction [17-20]. This failure in compression occurs due to a phenomenon known as kink bands, where the fibre breaks in multiple places causing a bend and offset in the fibres [17,21-27], shown in Figure 2-4.

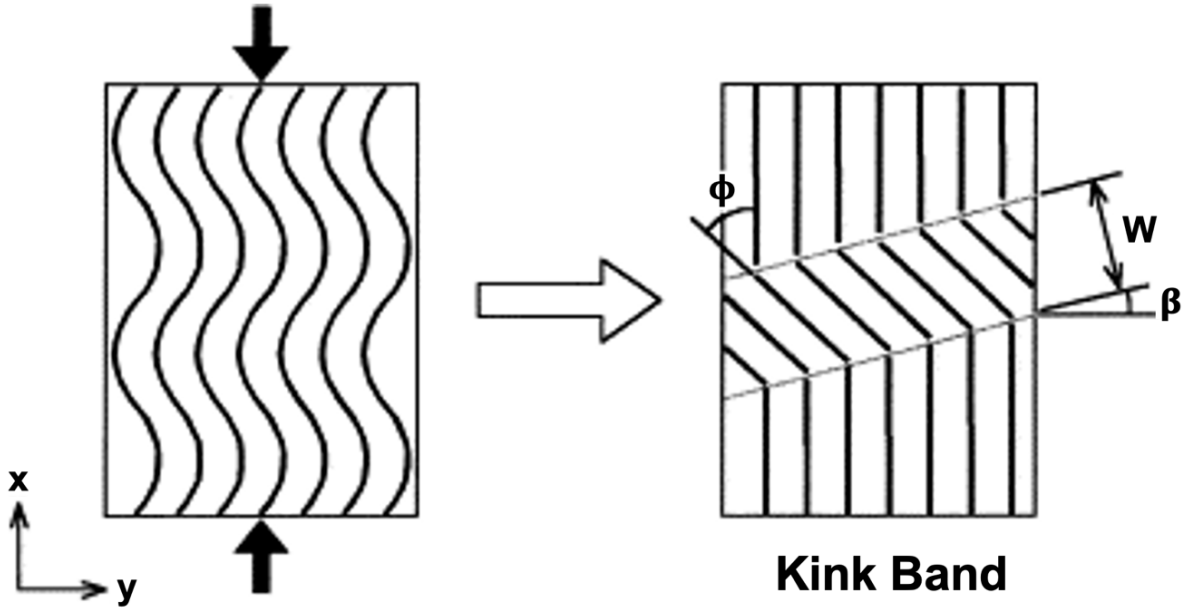

Figure 2-4. Diagram of a kink band [17].

In contrast, the compressive strength is higher than the tensile strength of unidirectional fibre-reinforced composite materials when the force is not applied along the fibre direction and, when subjected to tensile loads, the fibre failure that occurs is primarily fibre pull-out [28]. Fibre pull-out and other features of fibre failure under tension are shown in Figure 2-5.

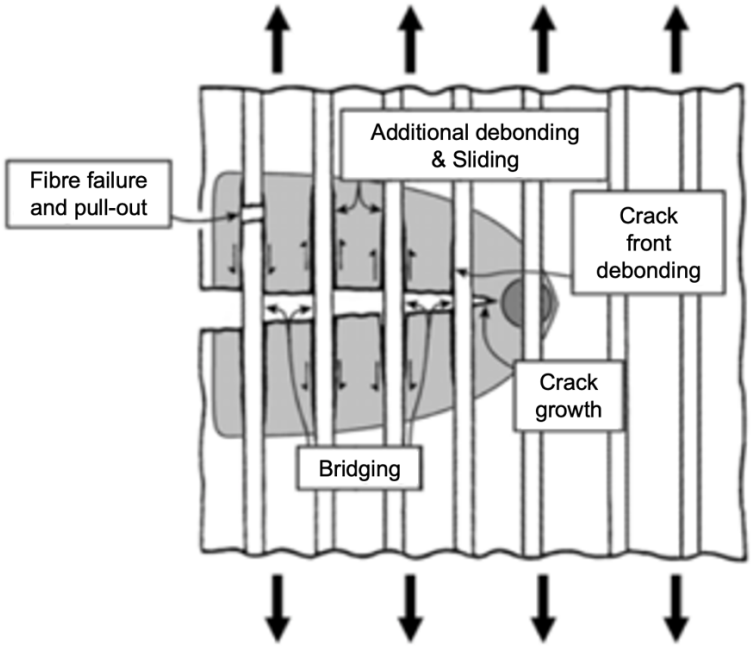

Figure 2-5. Fibre failure mechanisms under tension [29].

2.2.2 Interlaminar failure

Interlaminar failure, often referred to as delamination, is when damage occurs between the plies of composite within a panel, causing a gap as the two layers de-bond from each other. The matrix cracking through a ply leads to interlaminar failure when the crack propagates to a ply interface and continues to grow along this boundary, which can then lead to fibre breakage in the load bearing ply [12], as shown in Figure 2-6 below.

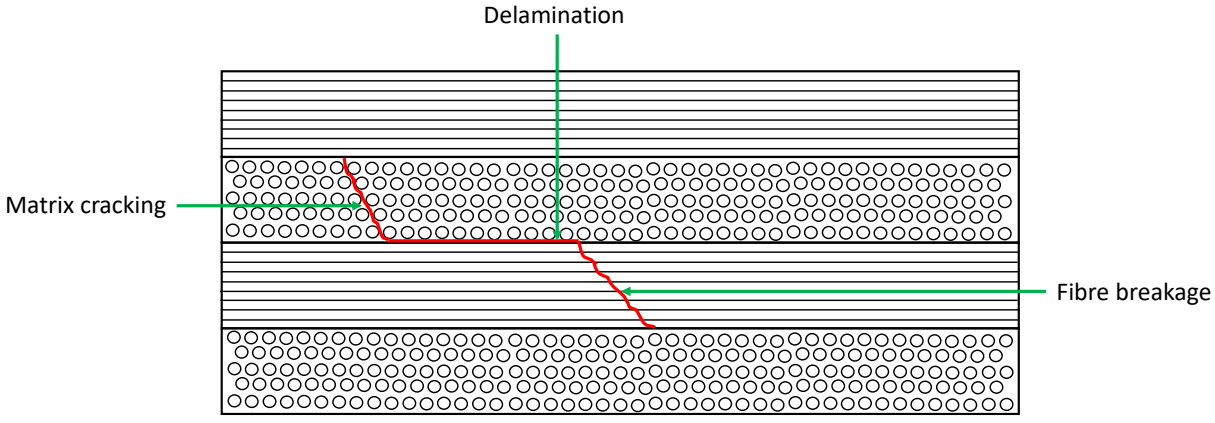

Figure 2-6. Diagram of the damage path in a cross-ply composite panel

Delamination leads to fibre breakage since, when de-bonding occurs, the once joined laminate becomes multiple sub-laminates that experience out-of-plane buckling and thus cause a reduction in the compressive strength of the laminate as a whole [30-33]. The buckling of sub plies around the delamination

applies unsymmetric loading to the rest of the material resulting in greater stresses than would be experienced by a laminate with no delaminations [30]. How much the compressive strength is affected depends on the location and size of the delamination within the composite and two different modes of buckling: local and global [30,32,34,35], shown in Figure 2-7.

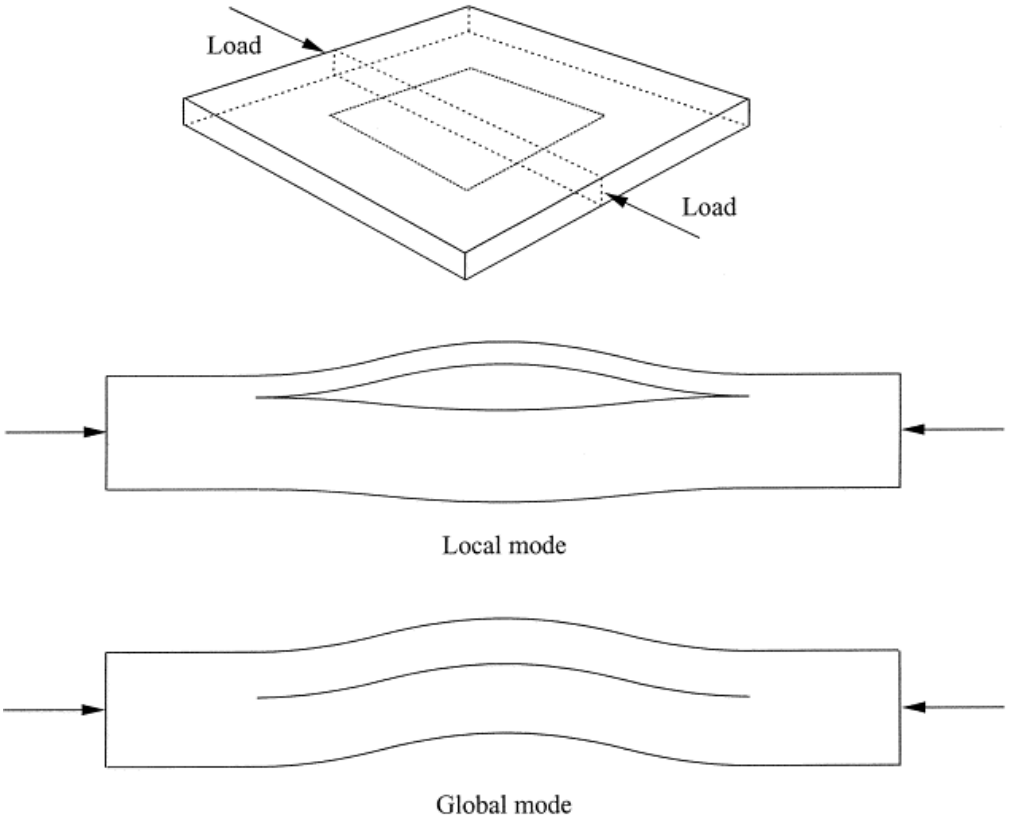

Figure 2-7. Modes of buckling caused by delaminations: (a) local mode when the delamination is large and near the surface of the laminate, and (b) global mode when the delamination is smaller and further down in the laminate [30].

Hashemi et al. [36] state that since a delamination can be regarded as a crack that propagates between plies, the toughness of the matrix, and thus the resistance against this failure mode, can be characterised through the energy per unit crack area, G_C. Depending on the loading conditions, there are three main modes of crack propagation i.e., delamination growth: mode I, mode II and a combination of these modes, which are denoted by G_{IC}, G_{IIC} and $G_{IC/IIC}$, respectively [36,37]. There is also a mode III loading type, denoted by G_{IIIC}, with loading conditions for modes I, II and III shown in Figure 2-8.

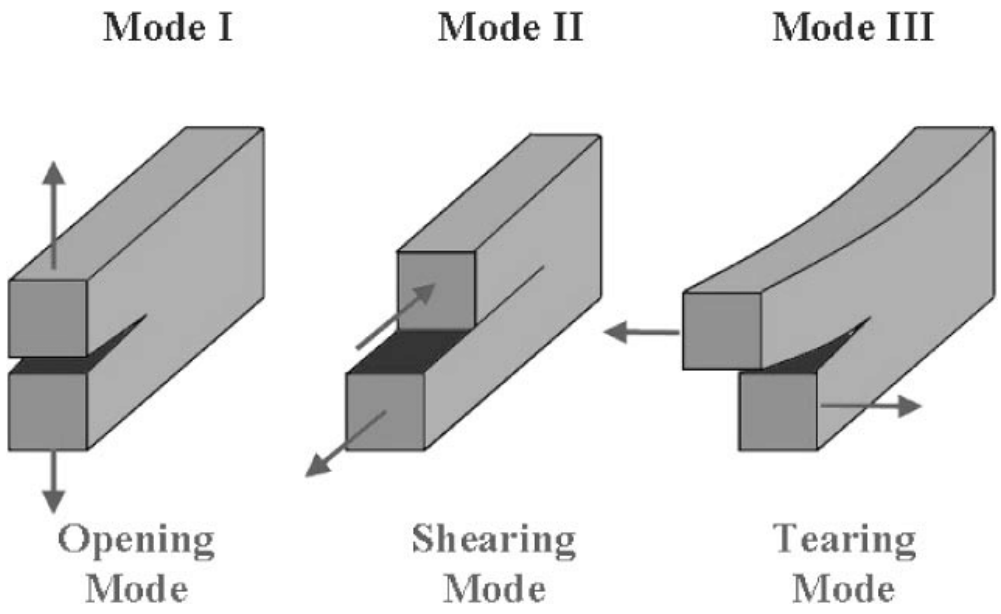

Figure 2-8. Loading conditions that can cause delaminations to grow: (a) Mode I - opening mode, (b) Mode II - sliding mode, and (c) Mode III - Tearing mode [38].

2.3 Impact Experimental Testing

The most common impact testing carried out on repaired composites is low velocity, hard impacts, with minimal consideration for soft impacts of these materials. Hard impacts have clearer failure modes that are easier to detect, whereas soft impacts generally just cause the material to bend slightly, with minimal to no delamination. This makes it hard to detect the damage.

2.3.1 Effect of Repair Type

2.3.1.1 Scarf Repair

Liu et al. used a drop test machine to investigate how scarf repaired composite material samples would respond to impact. For the sample testing, a critical impact energy of 23 J was found, above which adhesive damage occurred and below which delamination and matrix cracking were the only failure modes. This suggests that, below a specific impact energy, the repaired joint behaves like a pristine sample in terms of the failure modes that are present. The damage above this critical value was seen to primarily initiate at the edge of the scarf repair on the rear face, highlighting this as a weak point [39].

Low velocity impacts were performed on scarf repaired CFRP composites by Liu et al. using a drop weight machine. Impact energies of 3, 4, 5, 6, 8 and 10 J were used, with an energy above 4 J causing damage

along the adhesive line. The adhesive damage occurred within steps one to five, which were subjected to tensile forces in addition to the shear forces throughout the material. In contrast, steps six to ten had little to no adhesive damage due to experiencing compressive forces that do not aid in the progression of the adhesive failure. Figure 2-9 below demonstrates where the adhesive damage occurred after undergoing a 10 J impact [40].

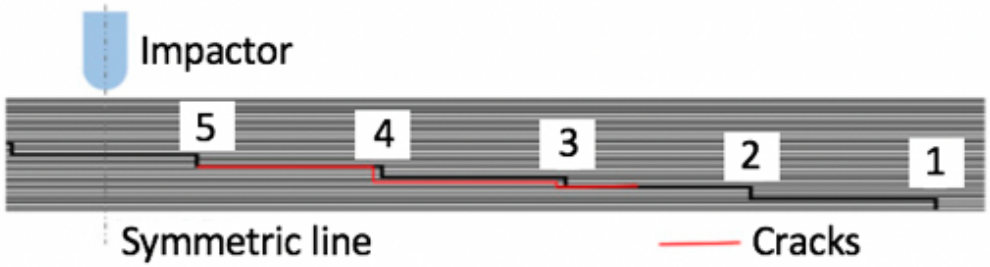

Figure 2-9. Location of cracks from 10 J impact done by Liu et al. [40]

Two observations from the experimentation are that the adhesive failure from the impacts reduces the residual strength of the material, since the ability to withstand tensile forces is greatly reduced. Additionally, delamination of the composite itself initiates before the adhesive cracking and progresses at a slow rate through the material [40].

Atas et al. also conducted some low velocity impact testing to compare two techniques of performing this type of repair: vacuum assisted resin infusion process and hand lay-up technique. Undamaged samples were tested alongside both repair types to allow a comparison, not only between the two repairs, but to the pristine composite. The samples repaired using the hand lay-up process were seen to have a lower bending stiffness than those repaired with the infusion technique, but this relationship was only observed at low impact energies, with higher impact energies resulting in similar performance from both techniques. When comparing the pristine and repaired samples, it was seen that the former experienced damage formation in the fibre direction while the latter primarily failed along the repair line and the perforation energy for the pristine sample was around 30 J higher than that of both repair types [41].

Considering how pristine and scarf joined composites perform under impact when subjected to a tensile preload, Li et al. impacted pre-strained CFRP composites. The pristine samples were deemed to be unaffected by the pre-strain, with the impact damage area remaining more or less unchanged for all values of

pre-strain [42]. However, the repaired samples were seen to be sensitive to the pre-strain and unpredictable, with two specimens loaded at 3000 με and impacted with projectile momentum values of 2.62 kg m/s and 2.80 kg m/s, the former failing catastrophically and the latter suffering minor damage [42,43]. In general, it was found that the impact tolerance of the scarf joint was lower than that of the pristine material [42,43]. Herszberg et al. theorised that there are two failure events, with a weak connection between them, that occur during the catastrophic failure: crushing and delamination, from the strains through the material thickness, and vibration throughout the sample. Within the range of pre-strain values tested, it is the vibration mode that could cause failure of the repaired sample, with this value being dependent on the impact momentum rather than the impact energy [43].

2.3.1.2 Patch Repair

Tie et al. tested the performance of single side patch repairs on CFRP composites, looking at different patch shapes and sizes. The testing had three stages: cutting out 3 mm radius holes from the parent material to represent damage; adhering either a circular or hexagonal patch, with the radius of the circular patch being double the side length of the hexagonal patch, which had a value of 3.30 mm; and using a drop weight machine to impact the sample. This impact was located in line with, but not directly above, the damage area since the repair was located 20 mm from the centre of the sample. It was found that the circular patch had a smaller delamination surface area, with a value of 558 mm^2 in comparison to 572 mm^2 for the hexagonal patch repair. This implies that a circular patch is more effective at reducing the damage due to impact [44].

How the properties of the external patch affect the performance of the repair was also considered by Andrew et al., with glass fibre reinforced epoxy composite samples and looking at how the lay-up influenced the results. Three different woven patches were used in a total of five configurations, which can be seen in Figure 2-10 below [45].

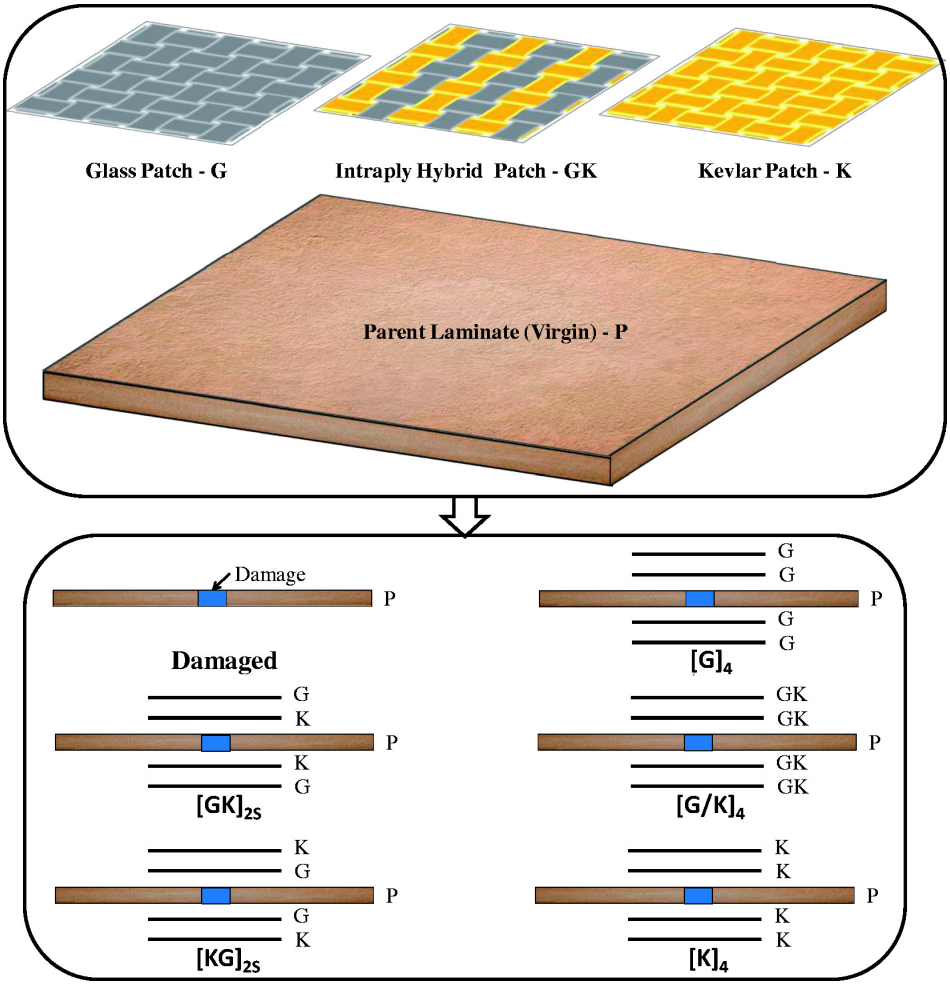

Figure 2-10. Woven glass, kevlar and hybrid patch configurations used by Andrew et al. [45]

There were multiple findings from this testing. Firstly, as the impact energy levels increased, the energy absorbed by the sample became increasingly dependent on the patch composition and lay-up. It was also seen that the $[G/K]_4$ patch performed the best, restricting interlaminar delamination more than both $[KG]_{2S}$ and $[G]_4$ and reducing fibre breakage on the rear face more than the pristine samples as well as both $[G]_4$ and $[GK]_{2S}$ patches. Lastly, although both the $[GK]_{2S}$ and $[KG]_{2S}$ patches contained glass and Kevlar in the same quantities, their performance was rather different. The former demonstrated rear face fibre breakage prematurely, where the latter did not. This result implies that the response of the repair depends on both the mechanical properties of the patch material and the lay-up used. Kevlar is more ductile than glass and so can displace more upon impact to limit fibre breakage but can be combined with glass in an optimal patch configuration to overcome other failure modes at the same time, as demonstrated by the superior performance of the $[G/K]_4$ patches [45].

Coelho et al. performed impact tests on single and double patch repaired composites to allow a comparison to be made between the two configurations. The composite used was a glass fibre reinforced epoxy

and 20 mm diameter holes were cut from the 100 x 100 x 3 mm^3 samples to emulate damage. The hole was filled with an epoxy resin that was enhanced with nanoclays and the patches, of 40 x 40mm^2, were then adhered to the surface. It was observed that the double patch can withstand higher loads, with a load value of 97.1% higher than the single patch at an impact energy of 6 J. Furthermore, the double patch had an elastic energy that was higher by 51.2% at that same impact energy and also had a maximum displacement value of ca. 50% less than that of the single patch. These results imply that the double patch is not only superior but significantly so, due to its higher stiffness and therefore its higher impact fatigue life [46].

2.3.1.3 Combination of Scarf and Patch Repair

Harman et al. considered specimens repaired using the scarf repair method and then with a single patch to raise the strength of the scarf repair [47]. The repair technique tested is shown in Figure 2-1 (d) in Section 2.1. This repair technique could be used when only one side of the component can be accessed [2], which is likely to be the case when repairing aircraft because the internal face is ordinarily covered with other materials that form the interior lining of the plane. Patch repairs are theorised to experience increased stress concentrations when subjected to non-linear bending, where using a scarf repair reduces these effects [2], hence implementing a scarf repair in conjunction with a patch. When impact testing was performed, the impact locations were chosen to be on the edge of the patch and over the scarf repair. It was seen that the size of the delamination area was greater when impacting on only the patch than the combination repair since the increased thickness of the latter aids in the dissipation of energy, thus implying that using scarf and patch repair together has superior impact performance than patch repair alone and, where possible, a combination should be implemented [47].

2.3.2 Effect of Impact Location after Repair

Liu et al. performed low velocity impact testing of scarf repaired CFRP composites, considering the impact energy and location. It was observed that a larger damage area was produced when the impact was applied to the connection point between the parent and repair piece and also when a larger impact energy was used. This implies that the weakest part of the repaired composite is the join itself and that this is the area with the lowest residual strength [48].

The effect of the impact location was also considered by Hou et al., who tested the low velocity impact performance of patch repaired CFRP composites. Holes with a radius of 3 mm were cut in the 100 x 150 x 3.6 mm^3 samples to represent damage, with the centre of the hole being either 20 or 30 mm from the centre of the sample. The holes were filled with an adhesive film and then a circular patch, with a radius twice that of the hole, was adhered on one side of the damage. It was seen that the peak impact force and delamination area for the 20 mm distance impact were 6124.2 N and 558 mm^2 respectively. These can then be compared to values of 6288.3 N and 536 mm^2 for the 30 mm distance impact. This shows that, even though more force was subjected to the specimens with the impact further from the damage, there was still a smaller area of delamination. However, both distances have relatively similar values and so no clear conclusions can be drawn from only two distances having been tested [49].

Glass fibre reinforced epoxy was repaired with the scarf technique and a patch was adhered to the top surface by Balaganesan et al. who then performed high velocity impact testing. Various different impact sites were tested for the repaired samples: on the patch centre and then 5, 10, 15 and 20 mm offset from the centre. In comparison to a pristine sample, it was observed that the energy absorbed during the impact decreased as the impact site moved away from the patch centre up to 15 mm offset. At the 20 mm offset, this value began to increase again. This suggests that this offset is far enough away from the repair for the performance to be similar to that of the undamaged composite. Furthermore, the delamination area on the rear face was highest for the pristine sample at 1600 mm^2 and the values for 0, 5, 10, 15 and 20 mm offsets were 0, 0, 192, 857 and 947 mm^2 respectively. This shows that the delamination area is greatly affected by repair and location of impact, with the area for the pristine sample having a value of around 1.7 times the largest delamination area of a repaired composite [50].

2.3.3 Effect of Impact Hardness

All of the sources discussed up to this point are impacts performed using a hard impactor. This is because the damage from this type of impact is more easily identified and so the suitability of a material can be assessed more effectively.

2.3.3.1 Soft Impact

There is limited research on the soft impact of composite materials in comparison to hard impacts, meaning that the papers considered in this literature review are not limited to low velocity impact of CFRP panels. Firstly, Dau et al. subjected woven carbon fibre/epoxy panels to low velocity impact tests using a rubber impactor that deformed upon impact. One of the main findings was that there is a critical threshold energy above which perforation occurs, with this value being found to be between 272 and 307 J and the development of this damage being shown in Figure 2-11. It was, however, also found that there was a disparity between tests, which was concluded to be largely due to a number of factors including the dispersion of fibres in the woven material varied largely between samples and the unpredictability of the rubber performance [51]. These results highlight the difference between hard and soft impacts in the extreme energy values required for perforation in this testing.

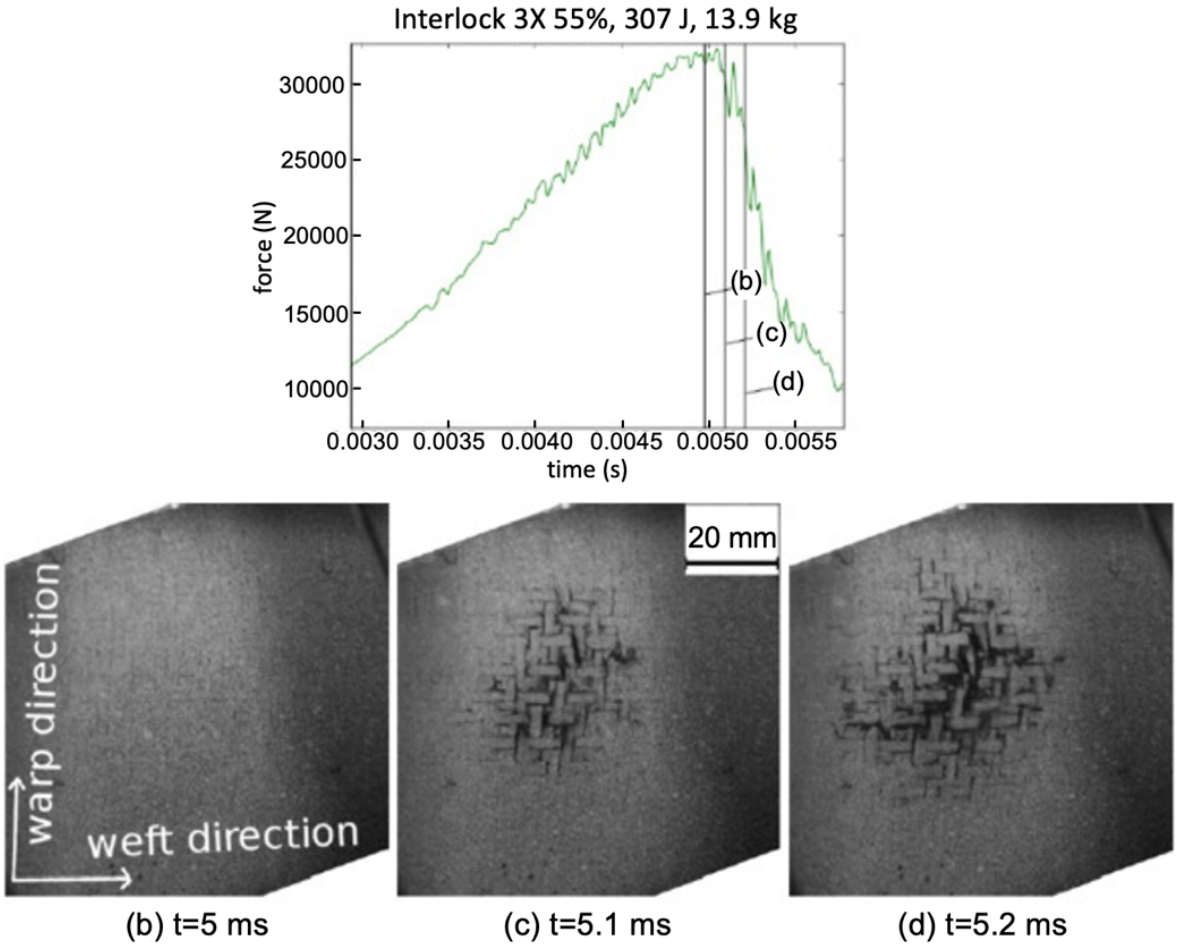

Figure 2-11. Damage progression in a CFRP woven panel with an epoxy matrix at an impact energy of 307 J by Dau et al. [51]

Secondly, assessing some papers on high velocity soft impacts of woven CFRP panels, Liu et al. considered the behaviour of woven carbon fibre/epoxy and woven carbon fibre/PEEK samples under high velocity soft impact using a gelatine projectile. It was found that the former experiences more damage under soft impact as the damage initiation energy fell between 64 and 72 J for the carbon fibre/PEEK samples and below 38 J for the carbon fibre/epoxy samples, with the damage observed in the samples being cracking in the matrix with no fibre breakage [52]. Previous testing in this area by the same research group found the largest damage area in a carbon fibre/epoxy sample was within the depth region of 0.4-1.5 mm, with the damage area spanning ca. 20 mm, which was significantly larger than the damage area observed in carbon fibre/PEEK samples [53]. Heimbs et al. also tested CFRP panels under high velocity soft impact conditions but subjected them to tensile and compressive loads before impacting them, with this affecting the damage observed in the samples. Overall, the soft impacts were seen to cause the contact of the projectile with the panel to be distributed causing an elastic response and, like Liu et al., matrix cracking rather than fibre breakage. Additionally, tensile preloading led to less bending upon impact while compressive preloading led to more, meaning that the former had more intralaminar damage and less interlaminar damage [54].

2.3.3.2 Transition

Liu et al. impacted carbon fibre/epoxy samples at high velocities with both hard and soft projectiles, investigating the difference between the two. It was seen that damage, in the form of fibre breakage, was only observed at a velocity of 100 $m.s^{-1}$ and lower velocities resulted in no visible damage apart from some slight damage to the paint in some cases. In contrast, damage was observed with a hard projectile from speeds of ca. 30 $m.s^{-1}$ and the sample was perforated and a large hole produced when impacted at ca. 70 $m.s^{-1}$, the highest velocity for this projectile [55]. It is difficult to compare the two types of impact beyond this in this case since a damage area is not present at 70 $m.s^{-1}$ for the soft gelatine projectile but an impact of 100 $m.s^{-1}$ would likely all but destroy the sample with an aluminium projectile. Additionally, the out-of-plane displacement maps produced for the soft projectile cannot be produced with the hard projectile as the perforation compromises the images.

Liu et al. specifically considered the difference between hard and soft impacts, using HDPE and gelatine projectiles respectively. Impacting at a velocity of ca. 60 $m.s^{-1}$ for both types of impact showed that, when impacted with a hard projectile, more out-of-plane displacement was seen in the sample. This was concluded to likely be due to the higher contact pressures that are produced by a harder impactor. When considering the

theory of soft versus hard impacts, Liu et al. produced Figure 2-12 to show how the contact pressure is reduced by the softness of the gelatine projectile. This is because the projectile deforms and the pressure is spread out over a larger area, thus reducing the pressure at each point [56].

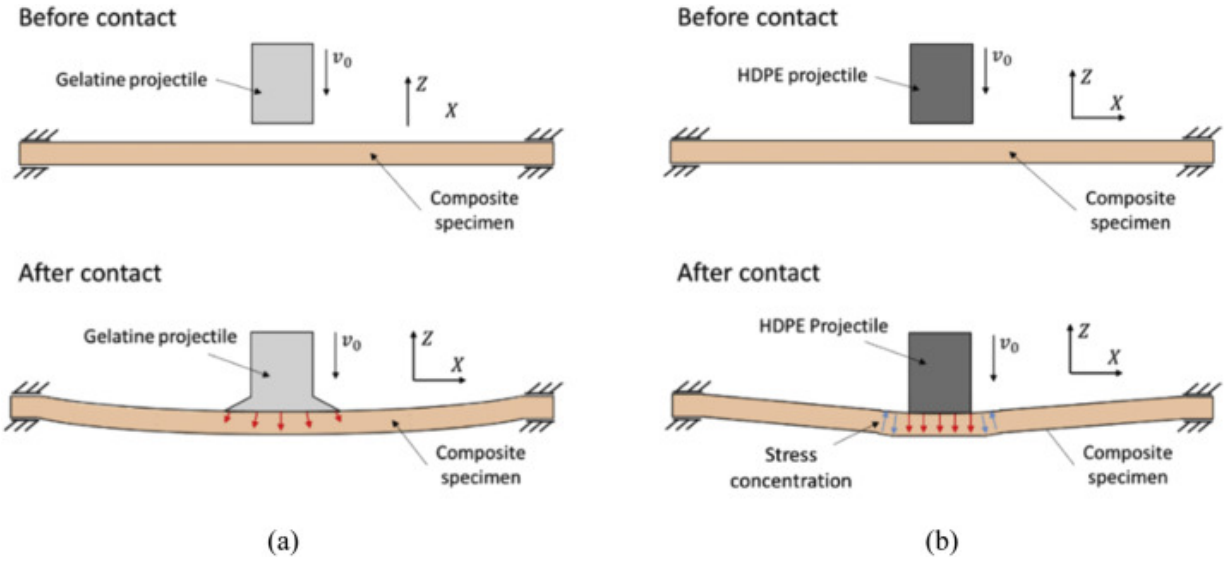

Figure 2-12. Diagrams of the interaction of soft and hard projectiles by Liu et al. [56]

2.3.4 Effect of Impactor Geometry

Mitrevski et al. impacted carbon-fibre reinforced epoxy composite panels with a hemispherical, ogival and conical impactor under low velocity conditions at impact energies of 4 and 6 J to compare the damage caused by each. It was found that damage initiated at the lowest for the conical and highest for the hemispherical impactor, which suggests that the sharper the impactor the less force it takes for damage to be introduced into the panel. Furthermore, comparing the sharpest (conical) and bluntest (hemispherical) impactors, the panel impacted with the former absorbed the most energy and had the deepest indentation whereas the latter resulted in the highest peak force value and least time that the impactor was in contact with the panel [57]. Mitrevski et al. continued their research by also including a flat-ended impactor that was now the bluntest of the four used, which solidified their findings as the flat impactor resulted in the highest peak load [58].

Impactor shape was also investigated by Kazemianfar et al. who impacted glass-fibre reinforced polymer composite panels at an impact energy of 21 J with conical, hemispherical and flat-ended impactors. The main conclusions of this research were that damage initiated at a lower force value when sharper impactors

were used, but the time at which this occurred was not affected by the impactor, and panels impacted with the blunter impactors were seen to have less intense damage [59].

2.4 Impact Damage Assessment Techniques

2.4.1 Non-Destructive Testing (NDT) Techniques

A critical part of repairing composite materials that are used for aerostructures is monitoring and detecting the damage, without which the repair can't be implemented successfully. There are a number of techniques that are currently being investigated for their suitability for this use. A technique that is successful, non-intrusive and can be performed without removing the composite panels is required. There is currently no technique available that can successfully detect all composite damage mechanisms, with the use of multiple methods being required to do so [6]. The majority of which entail the removal of the damaged component to allow non-destructive testing to occur [60]. Four damage monitoring techniques will be discussed as well as assessing the challenges presented by kissing bonds and the research around this.

2.4.1.1 Visual inspection and the tap test

The first category of damage monitoring techniques is quick and low-cost, such as visual inspection and the tap test. These methods are beneficial due to being relatively inexpensive and easy to implement, however each has its own drawbacks [6]. Visual inspection allows surface damage to be identified but is limited as such and cannot be used to detect damage below the surface, which is undesirable since composite materials often exhibit minimal damage on their external faces, especially if the defect was caused by a soft impact [6, 60]. Having said this, coatings, and such, can be utilised to improve the detection success rate of this technique [60]. Furthermore, an improvement on the use of visual inspection, called D-sight, was developed and patented by Diffracto Ltd., which can provide a higher resolution but requires preparation of the surface to ensure it is reflective [61]. Alternatively, the tap test can be used to find through thickness damage due to the higher frequency and clearer sound that is given off from damage free areas, in comparison to those with damage, when tapped [6]. However, this technique struggles to detect smaller defects and is limited to thinner materials, with ultrasound, thermography and shearography being alternatives that show potential [6].

2.4.1.2 Ultrasonic techniques

Ultrasonic techniques are the second category of damage monitoring techniques, where ultrasonic waves are transmitted through the material and the reflections can be used to detect subsurface damage [6]. There must be a compromise between the sensitivity and the distance through the material the waves can move, due to the frequency [6]. The main disadvantage with this technique is that the component must be submerged in a water bath to ensure accurate readings of the waveforms, meaning that it is not often possible to perform in situ inspection using this technique [6,60]. Alternatively, laser ultrasounds techniques do not require submersion in a liquid couplant and the probe doesn't have to be normal to the component, making it a viable alternative but it is more expensive and sensitivity can be an issue [6,60].

One of the main causes of failure within composites, especially repaired composites, and a potential application for ultrasonic NDT techniques is when the adhesive and substrate are in contact but there is no true adhesion, and therefore no joint strength. This is known as kissing bonds and development is required to, not only allow composite repair techniques to be used for primary aerostructures, but adhesive bonding in general. One of the most challenging elements of finding a suitable technique to detect kissing bonds is creating this type of failure artificially. The criteria that a bond must meet to be classified as a kissing bond vary slightly from paper to paper, but a conservative and concise definition was given by Marty et al. by stating three criteria: '1. Their strength in a lap shear test must be below 20% of the nominal strength. 2. The mode of failure must be adhesive, that is purely at the interface between the adherent and adhesive. 3. They must be undetectable from normal bonds with classical amplitude c-scans.' [62]. A variety of contaminants within the joint have been tested, including oil, frekote, baking powder, sand and wax, with sand demonstrating the most potential to help emulate kissing bonds as it was not visible from c-scans and allowed the epoxy through minute gaps to achieve partial bonding [63]. Having said this, more testing is required to verify the first two criteria since this technique currently only meets the final of the three. To detect kissing bonds, the primary techniques that are considered involve the use of ultrasound. For example, ultrasonic resonance spectroscopy (URS) equipment is traditionally unable to successfully identify kissing bonds, but a broad band version shows promise as it can detect variances in the shear wave resonances when the bond is weak in comparison to a good bond [62]. Furthermore, an ultrasonic wave of large magnitude can be used to introduce nonlinearities in the adhesively bonded samples, with a higher value of the nonlinear parameter occurring for kissing bond samples than for those with a good

bond, showing that there is potential for this to aid in detecting this type of adhesive failure [64]. In continuation, vibrothermography is an ultrasonic technique that combines the use of ultrasound with the thermography methods discussed above, with this combination detecting a simulated kissing bond and, therefore, showing potential [65]. Overall, the emulating of kissing bonds and developing of techniques to detect them still requires more research and fine-tuning to improve the results enough to be used on aircraft components, with the current techniques proving to be promising.

2.4.1.3 Thermography

Thirdly, thermography uses infrared radiation to detect damage by measuring the temperature gradients and thermal impendence from defects within the material, with both passive and active versions being possible, and can be performed when there is only access to one side of a component [6]. The active version requires heating the component through the use of an external heat source, which can cause thermal damage if the temperature is increased beyond that which the material can withstand [60]. Another disadvantage of this technique is that the equipment is relatively expensive, with highly sensitive thermal cameras and external sources being utilised [6]. Grammatikos et al. used an infrared thermography technique to identify debonding of a patch repair on a composite material by using it to find the stress concentrations that cause this failure mode to occur, showing that this method can work in practice [66].

2.4.1.4 Shearography

The fourth and final damage monitoring technique to be discussed in this paper is shearography, which consists of shining light on the component, taking images when the object is in a stressed and unstressed state and then using these to find stress concentrations [60]. This technique is suitable for composites, including repaired composite samples, because it can be set up in such a way that allows failure mechanisms such as delamination to automatically be detected and it could be used for the non-destructive testing of repairs to analyse their performance and ensure their success [6]. The primary disadvantage is that the results can be largely affected by the size and location of the defect, meaning the success might be limited [6].

2.4.2 Destructive Testing Techniques

Damage monitoring techniques are non-destructive methods for detecting and locating damage within composite panels, however there are also advantages to techniques that are not non-destructive and so require cutting the panel to assess the damage. This option allows for a more thorough inspection and thus a better understanding as to how the damage initiates and propagates through the material. Damage monitoring techniques are useful for assessing damage when materials are in use and damage detecting techniques are useful for analysing and learning about damage when testing and characterising materials.

2.4.2.1 Optical Microscopy

One of the most common destructive testing techniques implemented to investigate damage initiation and propagation in composite materials is optical microscopy. Samples are prepared for inspection by cutting through the damage, grinding and then polishing the surface to be viewed [67-69]. Optical microscopy allows for the intralaminar damage to be viewed as well as the interlaminar damage, where techniques such as ultrasonic c-scanning only show the delaminations and not the fibre breakage or matrix cracking within a panel. However, a major drawback to this method is that it only gives a two-dimensional view of a single section on the damage area [67], meaning that the damage through the material is not viewable, even if multiple sections are taken. Additionally, it can be difficult to identify areas of damage, depending on the material, but this can be overcome by using fluorescent dye that highlights the cracks in the matrix [67]. This technique is most beneficial when used in conjunction with another technique, as the damage area cannot be found through analysing the cross-section, but it does give an insight into how the damage filtrates through the plies.

2.4.2.2 Scanning Electron Microscopy

Scanning Electron Microscopy (SEM) is another technique for viewing the damage cross-section of a composite panel. However, unlike optical microscopy, the resolution power of SEM is not limited to visible light, meaning that greater magnification is possible [70]. When scanning a sample, it must be cut, ground and polished and then coated with a metal, such as gold, to avoid overheating by conducting the electrons away from the examination area [67]. Many failure mechanisms can be identified through this technique, including observing the fracture path and surface to determine the direction of crack propagation from the crack initiation site [67,71,72]. A diagram of the set-up of a scanning electron microscope is shown in Figure 2-13 below.

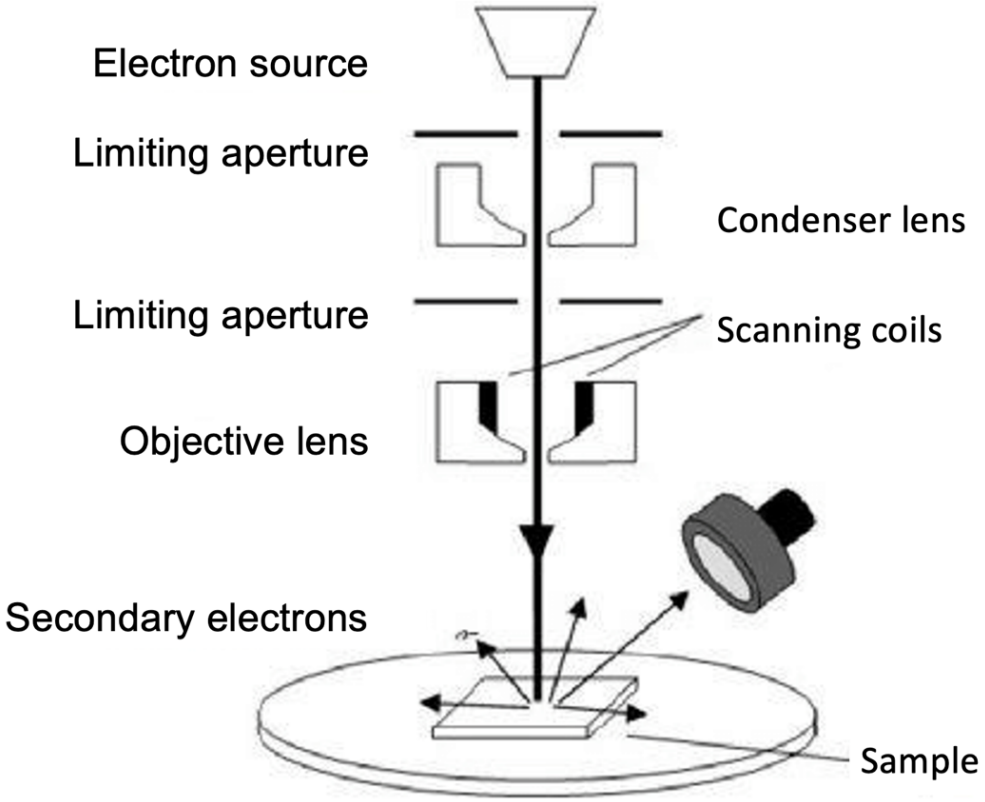

Figure 2-13. Diagram of the set-up of a scanning electron microscope [73].

2.5 Modelling of Impact Events

Simulating impacts, with the use of minimal testing to verify the model, allows optimum variables to be calculated prior to investing in complex experimentation. This can save both time and money since the viability of research opportunities can be evaluated – and the research halted if necessary – before manufacturing materials for testing.

2.5.1 Pristine Composites

Xin et al. proposed a progressive damage model to predict the performance of fibre reinforced polymer composites under impact. The model is described as having three elements: quadratic stress-based failure criteria to predict the onset of failure; a combination of a linear form damage evolution law and the fracture energy approach to model the post-damage softening process; and the strain rate dependency of strength and modulus are taken into consideration. A number of failure modes are accounted for in this model, including matrix fracture, fibre breakage and delamination. This model considered both in-plane and out of plane stresses, where other continuum damage mechanics models, at the time this model was developed, only catered for the

effect the in-plane stresses had on the matrix and fibre failure modes, ignoring out of plane stresses and their effect on the results. The model was said to be in good agreement with the experimental data and it is commented that the fracture energy approach can be seen to reduce the mesh dependency [74].

Fibre reinforced composite laminates were also considered by Ansari et al. who performed a numerical investigation into the penetration and perforation behaviour of the composites under impact. There were four main conclusions from the modelling. Firstly, the damage in the composite plate and the ease of penetration of the projectile are both reduced with the employment of a fully restrained boundary condition. Secondly, for high velocity impacts, the damage is primarily located near the impact site and thinner samples had a smaller damage area. Thirdly, the length of the composite plate was seen to have an inversely proportional relationship with the ballistic limit velocity. Lastly, there was good agreement with the experimental data from literature [75].

Pham et al. considered the low-velocity impact response of fibre reinforced composite materials, as well as the compression after impact failure, using an enhanced continuum damage model that incorporated a 3D maximum stress criterion and then a fracture-energy-based smeared crack model. The interaction between delaminations and matrix cracking was investigated, and the model was used to see how these failure modes would affect the compressive strength after impact, once it was verified to be in good agreement with experimental data from static open-hole tensile testing. The results of this research were that the compressive strength is affected by the delaminations caused from impact and the model is successful at giving information about impact and post-impact performance of the composite materials, as well as the damage that results from the impact event, quickly and efficiently [76].

2.5.2 Scarf Repaired Composites

Simulating a low velocity impact of a scarf repair with a cohesive zone model based on Dugdale-Barenblatt model, Liu et al. obtained results that implied that the finite element model used can simulate the damage propagation for composites with scarf repairs that are impacted. Experimental data, discussed in Section 2.4.1, was used to validate the model. From the model, it was seen that, when the impact energy increased to 10 J, composite intralaminar damage grew but adhesive shear fracture no longer did, which is a significant finding

because the adhesive shear fracture was seen to be a major failure mode for the other impact energies simulated [40].

Herszberg et al. modelled the catastrophic failure, discussed in Section 2.4.1, using finite element analysis to test the hypothesis of what caused the catastrophic failure. The model used was simplified to only allow damage to occur in the adhesive and both simple tensile testing and impacting pre-strained samples were modelled. The former was to validate the adhesive damage models, with a conservative cohesive model being chosen to be used for the impact studies. This model was worse at predicting the response of the scarf joints when compared with an elastic-plastic model and experimental data but had superior numerical stability making it more suitable. The results from the impact modelling at different pre-strain values are shown in Figure 2-14 below [43].

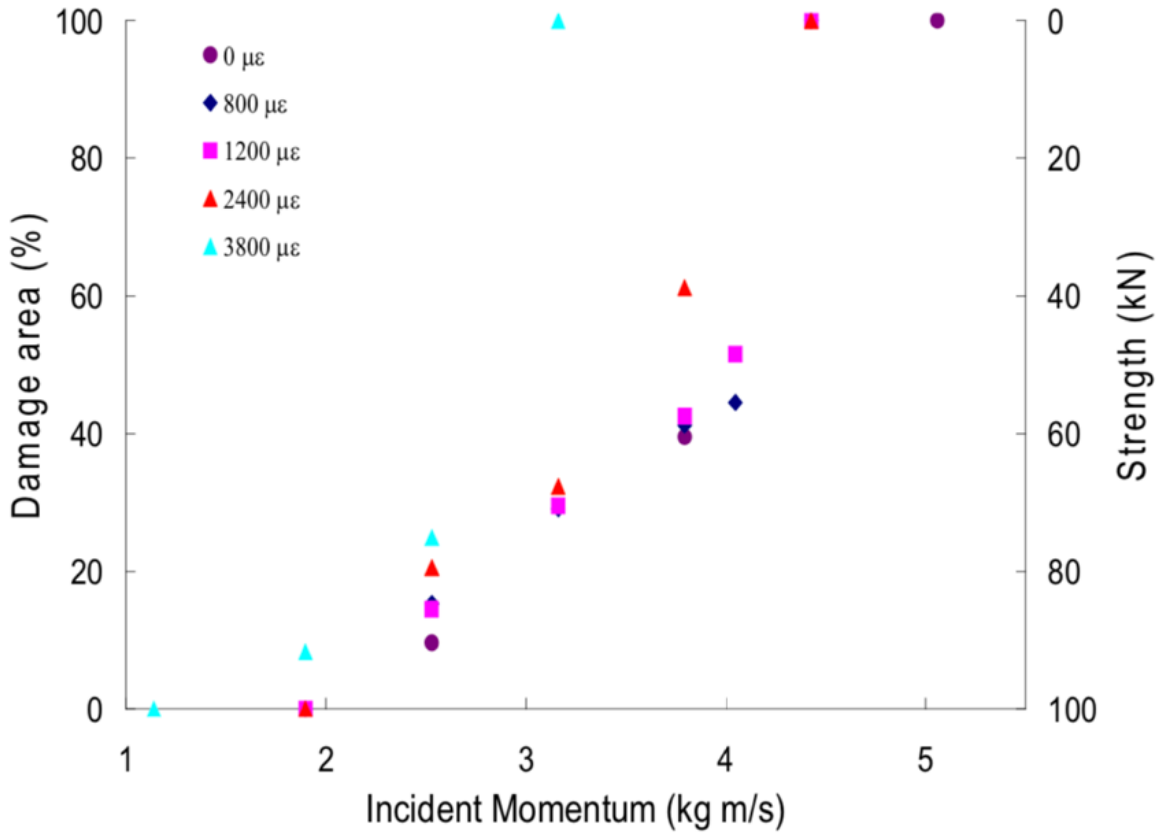

Figure 2-14. Relationship between damage area, strength and incident momentum of scarf repaired composites by Herszberg et al. [43]

From the data above, it was concluded that, for a given pre-strain value, increasing the incident momentum increases the damage area. It can also be seen that, as the residual strength increases, the damage

area decreases, from Figure 2-14 above. Finally, the method allowed the critical impact velocity for each pre-strain to be calculated by seeing at what value the modelled samples failed.

Cheng et al. considered the effect that the stacking sequence and rotation angle of the scarf repair have on the impact performance. Fibre breakage and matrix cracking were modelled using 3D Hashin criteria, whilst in- and out-of-plane shear damage was found using maximum strain criteria. The final composite damage considered in this model was interface delamination, which was achieved through the use of cohesive elements. This finite element analysis model was found to have good agreement with experimental results, with a relative error of 8.2% between their average delamination areas. Three different scarf lay-ups were considered, along with a sequence of the same order as the parent material: the original lay-up was $[45/0_2/\text{-}45/90/45/0_2/\text{-}45/0]_S$; sequence 1 was $[0/\text{-}45/0_2/45/90/\text{-}45/0_2/45]_S$; sequence 2 was $[0_5/90/\text{-}45/45/\text{-}45/45]_S$; and sequence 3 was $[45/\text{-}45/45/\text{-}45/90/0_5]_S$. It was found that sequence 2 had the smallest delamination and adhesive damage areas, whilst sequence 3 had the largest adhesive damage area. Furthermore, sequence 1 was the most similar lay-up to the original lay-up of the parent material, but there was a difference between the sum damage of the original patch and the one made with sequence 1, demonstrating that a small change in the stacking sequence causes a change in the impact performance of the scarf repair. Ten rotation angles – ±3°, ±5°, ±7°, ±9° and ±11° – were simulated. From the results, it was noted that the patch rotation has an effect on the delamination damage, with a positive rotation angle having a bigger effect than the negative angles. Finally, it is said that adjusting the rotation angle affects the overall performance of the scarf repair more so than changes in the stacking sequence [77].

A similar model was utilised by Cheng et al. to consider the effect that scarf angle, adhesive thickness and patch off-axis angle have on the overall repair performance. Additionally, the adhesive was modelled using a plastic model based on experimentation of the specific adhesive. Comparing the model results to experimental data, it was decided that the impact behaviour was predicted to a suitable accuracy. Firstly, the scarf angle was considered, with four angles from 5° to 8° being simulated. Both 7° and 8° had minimal delamination in the parent material, but 5° and 6° gave better tensile and compressive strength. Of these two angles, 6° gives the least adherend delamination, however 7° and 8° scarf angles are still recommended. Secondly, five adhesive thickness values were modelled between 0.1 and 0.25 mm, with results implying that thickness values within

the range of 0.15 to 0.25 mm gave both better tensile and compressive strengths as well as better impact performance. Finally, eight angles between 0° and 180° were simulated for the patch off-axis angle. The maximum ultimate impact force was seen at a value of 0° and the minimum occurred at 10°, suggesting that the patch off-axis angle has a notable effect on the impact performance. To reduce the damage to both the adhesive and adherend, an angle between 135° and 160° is recommended [78].

2.5.3 Patch Repaired Composites

Tie et al. used a continuum damage mechanics model, based on 3D Hashin failure criteria, and a cohesive zone model to investigate the effect of patch size and shape on the effectiveness of the repair. Five patch shapes were modelled: circle, square, rhombus, hexagon and octagon, and it was seen that the initiation of damage happens at almost the same time for each sample. Additionally, the circular patch had the minimum impact force variation, meaning less impact energy was absorbed and it is therefore the patch shape with the best performance, and the rhombus was seen to have the largest variation and therefore the worst performance. To consider the effect of patch size on the repair performance, circular patches with radii of 1.5, 2, 2.25, 2.5, 2.75, 3 and 3.5 times that of the hole radius were modelled. The smallest patch was found to have the worst performance, absorbing the most impact energy and having the largest damage area of all the modelled samples. All the other patch sizes were difficult to separate from the history curves alone, due to having such similar values. However, looking at the specific values of delamination area and energy absorption, it was seen that a circular patch with a radius of 2.5 that of the hole had the lowest values for both. This implies that the best repair performance is achieved with a circular patch that has a radius 2.5 times the size of the hole radius [44].

A similar model was used by Hou et al., who also used 3D Hashin damage criteria and a cohesive zone model to create a continuum damage mechanics model. The model had 65239 and 3331 elements for the parent material and patch respectively, which was to ensure the damage behaviours from the impact would be captured to a suitable resolution. It was found that the delamination areas from the numerical simulation for both experimental cases, impacting 20 and 30 mm from the damage site, had differences of 3.8% and 2.7% from the experimental values respectively, demonstrating that the model is suitably accurate. For this reason, the model was used to consider a larger range of distances: 0, 10, 20, 30 and 40 mm from the damage. It was seen

that the sample impacted directly on the repair absorbed the most energy and the sample impacted 30 mm away from the repair absorbed the least, after which, the impact energy absorbed starts to increase again. The delamination area has less of a clear pattern, with a decrease between 0 and 10 mm and then a large increase when the distance is increased to 20 mm before then stabilising around 30 mm. Both of these results can be seen in Figure 2-15 below and imply more detail is needed through testing of a larger range of distances to understand the patterns [49].

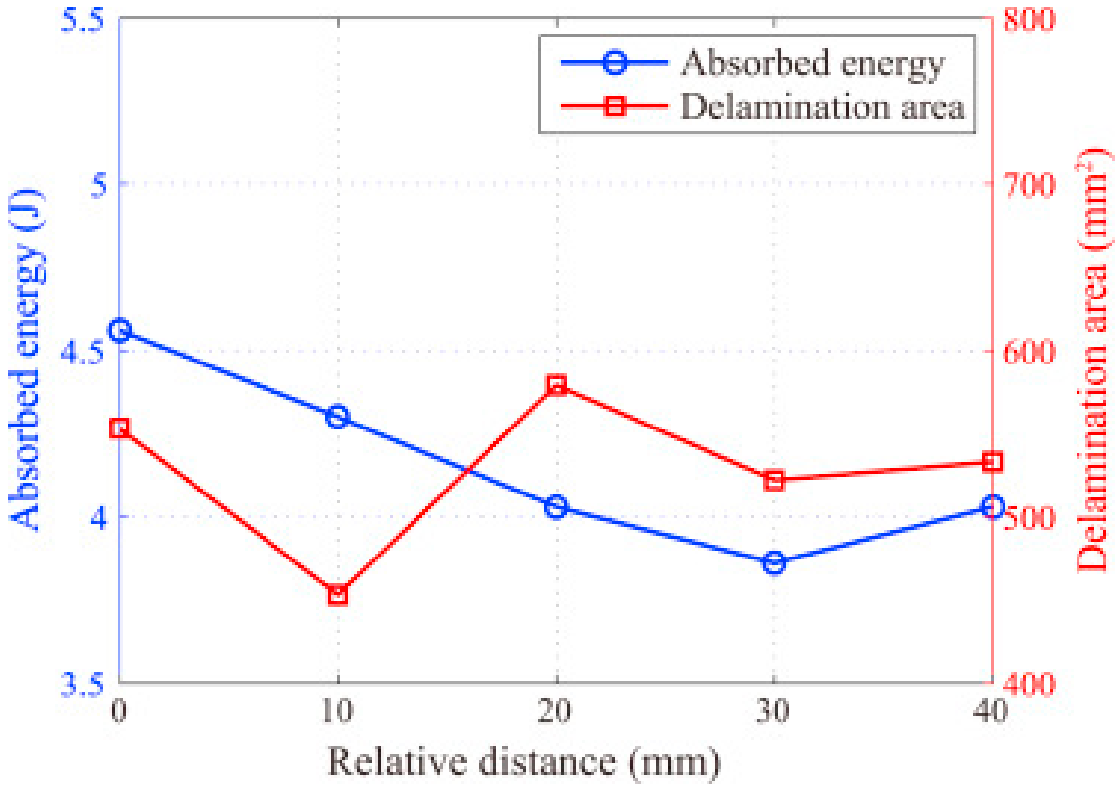

Figure 2-15. Absorbed energy and delamination area of impacts at different distances from the repair by Hou et al. [49]

2.5.4 Soft Impact

Firstly, considering the modelling of soft impacts, Liu et al. used experimental work, prior to performing numerical modelling, to determine the characteristics of a soft projectile during high velocity impact and found that it behaves as a viscoelastic-plastic fluid. From this finding, there was more understanding of how the projectile interacts with the composite panel leading to the use of the Smoothed Particle Hydrodynamics (SPH) modelling technique, allowing the deformation of the soft projectile to be modelled successfully. To model the damage initiation in the panel, tensile and compressive fibre and matrix failure were all considered using Hashin's approach. Comparing the modelling results to those seen in the experimental work, good agreement

was found [79]. This same model was used in further simulations by Liu et al. and good agreement was seen, but the model predicted values slightly lower than that seen experimentally, which is commented to be likely due to the composite panel being woven and the curvature effects that come with this [53].

Johnson et al. also modelled soft projectiles with the SPH modelling technique, considering both hailstones and bird strikes. The former can be modelled with solid finite elements as there is minimal element distortion, but the latter requires a different technique to allow for deformation of the gelatine projectile. This realisation led to the use of the SPH modelling technique as it consists of interacting discrete particles rather than solid elements. It was decided to utilise this technique for both types of impactor, with reasonably good agreement for both. It was concluded that there are elements of the ice projectile that are not covered in the model, such as the effect of temperature on the elastic/plastic response [80]. In previous work, Johnson et al. found that this modelling technique accurately simulated the impact with a gelatine projectile and showed potential to be adapted for predicting damage from other impactor types [81].

The SPH modelling technique is a mesh-free Langrangian model, with the removal of the mesh allowing for the deformation of the soft projectile to be more accurately predicted. The need for this is shown by Heimbs et al. who compared Langrangian and Eulerian models, both of which include meshing, and saw an over-prediction of the contact force upon impact of 11% and 5% respectively. Having said this, relatively good agreement was still seen using both of these methods [54].

Lastly, Liu at al. modelled both hard and soft high velocity impacts to consider the effect of the projectile hardness on the impact response of the composite. Since the two types of projectile behave differently upon impact, it was required to create two simulations. As in the papers above, the SPH modelling technique was used for the soft projectile. Contrastingly, the hard projectile was much simpler to model, with elastic material elements being employed. The good agreement achieved from both simulations can be seen in Figure 2-16 [82].

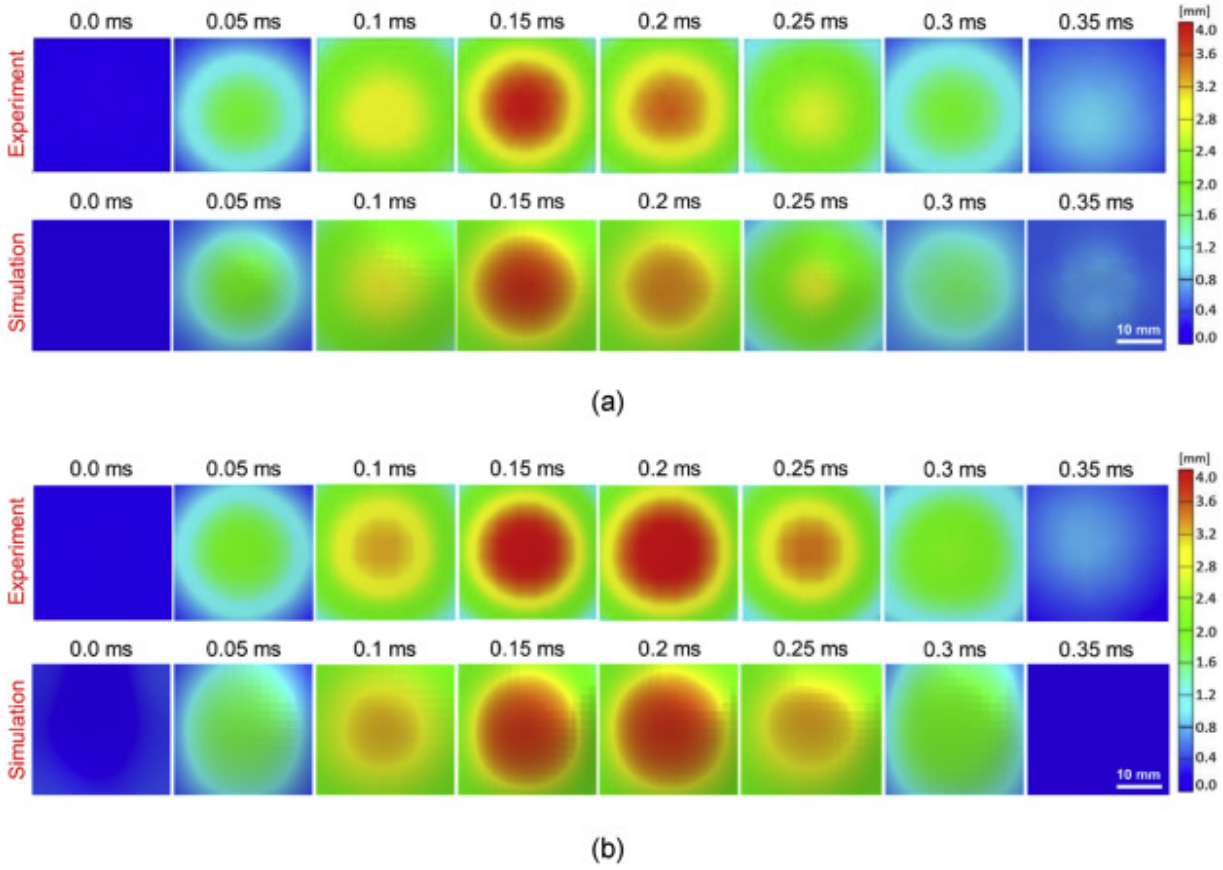

Figure 2-16. The out-of-plane displacement traces of high velocity impacts on woven carbon fibre/PEEK samples from experimental and numerical work for (a) a gelatine projectile, and (b) a HDPE projectile by Liu et al. [82]

2.6 Summary

It was found, by multiple sources, that there is a critical energy value for a repaired composite impacted at a low velocity, below which the material behaves similarly to a pristine sample and above which the repair is where the failure occurs [39, 40]. This implies that repairs are successful to a certain extent. When lower energy impacts occur, the repairs mean that the material behaves as though it had not been previously damaged. However, this critical value was seen to be relatively low, with values of 23 J [39] and 4 J [40] being concluded to be this turning point in the failure mode by the respective sources, and so further improvements to the repairs are required. Differences in the critical energies are likely due to variables in each experiment, but further research could be carried out to consider how the critical energy value is affected by the properties of the material and the repair technique.

Atas et al. compared two different methods of performing scarf repairs with pristine samples, finding that the damage propagated along the repair line for the repaired samples rather than in the fibre direction as

was seen for the pristine material and that the perforation energy for the repaired samples was significantly lower than that of the pristine samples, being 30 J lower, suggesting that pristine materials perform better than repaired materials [41]. This is furthered by the research of Li et al. who performed impact testing on pre-strained samples, comparing pristine and scarf repaired materials. It was seen that the pristine materials were generally unaffected by the pre-strain, but the repaired samples were seen to have a larger damage area when a more significant pre-strain was applied [42]. These results show that repaired samples do not perform as well as pristine samples when under tension during impact.

Various research has been carried out considering the effect of patch shape and configuration on the performance of the repair. Tie et al. considered the patch shape and size using both experimental and modelling means, finding circular patches with a radius of 2.5 times that of the damage hole give the best repair performance [44]. Andrew et al. considered the lay-up of the repair patch, varying the order of Kevlar and glass fibre reinforced epoxy in woven patches, and found that the mechanical properties and the configuration of the patch both change the performance, with a combination of the two materials giving the best performance as the ductility and brittleness were balanced [45]. Furthermore, Coelho et al. compared single and double patches, finding that the double patch repair could withstand a higher load than that of the single patch repair [46]. Finally, Harman et al. performed testing of a combination of a scarf repair with a single patch, impacting both on the patch alone and on the patch over the scarf joint, with the latter demonstrating superior impact performance [47]. Although there is not much research on how these properties of the patch repair affect the performance of the materials when subjected to high velocity impacts, the fact that they have such an influence on the results at a low velocity implies that they would have similar effects at a higher velocity. For this reason, testing of patch configurations with high velocity impacts would be beneficial to see if there is more or less reliance on patch properties than for low velocity impacts.

Both Liu et al. and Hou et al. considered how the impact location affected the performance of a repaired composite at low velocity. Liu et al. tested scarf repaired composites and found that the weakest part of the material was the join itself as it was the part with the lowest residual strength [48]. Hou et al. tested single patch repairs, impacting 20 mm and 30 mm from the damage site, and the results demonstrated that impacting further from the damage results in a smaller delamination area [49]. Balaganesan et al. also researched the impact distance from the damage site, but at high velocity and on a sample that was both scarf and patch repaired,

which resulted in a larger delamination area the further away it was from the damage site. This is the opposite of what was seen in low velocity impacts, with the pristine sample having a delamination area 1.7 times larger than any repaired sample [50]. This implies that the repair works to significantly reduce the delamination from high velocity impacts and performs better at a higher velocity than at low velocities.

When comparing hard and soft impacts, the energy required to cause damage and perforation in samples is much greater for the latter. This can be seen from the fact damage only occurs at 100 $m.s^{-1}$ for a soft projectile but perforation occurs at 70 $m.s^{-1}$ for a hard projectile under the same conditions [55] and, when looking at the out-of-plane displacement, a greater amount is seen with a hard projectile for the same impact velocity [56]. The large energies required is shown by the critical energy for perforation seen by Dau et al. that falls between 272 and 307 J [51] and the damage initiation value between 64 and 72 J seen by Liu et al. [52]. This is most likely due to the deformation that a soft projectile undergoes when interacting with the sample, which results in the contact pressure being applied over a larger area, thus reducing the force on each point [56]. Therefore, more energy is required to achieve the same damage as for a projectile that does not deform.

Research investigating the difference between the damage observed and force-time traces for different shapes of impactor under low velocity loading conditions suggests that the sharpness of the impactor has a significant effect on the performance of the composite panel. This was shown by Mitrevski et al. who found that blunter impactors had higher peak loads while sharper impactors absorbed more energy [57,58]. Additionally, at a higher energy value, the bluntest impactor also resulted in the highest load value for damage initiation [59]. This is likely due to the fact that the blunt impactors spread the force over a larger area and so the panel can withstand more force before damage occurs, whereas the sharper impactor allows the panel to bend more around it and thus more energy can be absorbed upon impact.

With regards to modelling, some simulations of impact events on pristine composites have been discussed in this paper. Firstly, Xin et al. developed a model that considered a large number of failure modes, catering for both in-plane and out of plane stresses and their effects of the results, finding that the fracture energy approach utilised aided in reducing the mesh dependency [74]. Secondly, Ansari et al. used their model to find that fully restrained boundary conditions reduce the damage of the composite and the ease of penetration of the projectile, as well as the fact that thinner plates had smaller damage areas when impacted at

a high velocity [75]. Pham et al. also modelled the impact response of pristine composite materials, but considered the compressive strength after the impact itself, with the results implying that the delaminations from the impact led to a reduction in the compressive strength [76]. The conclusions found from pristine modelling, and the models themselves, could be used to improve repaired composite models.

Herszberg et al. used a cohesive model for low velocity scarf repair impact simulations, which was shown to have worse performance when predicting the response of the repaired materials than the elastic-plastic model it was chosen over, but the superior numerical stability of this model meant it was more suitable for use in the simulations. This implies that there is a compromise between stability and accuracy within this model and that the results it gives could be inaccurate when compared to experimental data [43]. Furthermore, Cheng et al. [77] and Cheng et al. [78] both also considered low velocity scarf repairs with similar models, both implementing the 3D Hashin failure criteria but looking at different outputs. For this reason, each implemented slightly different failure criteria and models within their simulations. To check the reliability of the models, the results were compared to the small amount of experimental data that had been collected by each respectively, with both claiming to have good agreement. Cheng et al. used their model to compare the scarf rotation angle with the lay-up and found that the former had a greater effect on the overall performance of the repair [77]. However, it would be beneficial to also test this theory experimentally by using the model as a guide for testing.

To model a hard projectile, simple elastic material elements can be used but, for a soft projectile, a different method is required to ensure the deformation is accurately captured [82]. The most commonly used is the SPH modelling technique, which is a meshless Langrangian model, that does not have solid elements but instead uses discrete particles that interact with each other [52, 79-82]. Heimbs et al. used a standard Langrangian method and found that this gave an over-prediction of the initial contact force of 11% [54], showing why the SPH modelling technique is preferable as it removes this issue. Overall, modelling a soft projectile is more complex than a hard projectile due to the deformation upon impact and the fact that the model has to be adjusted for different types of soft projectiles (such as gelatine for bird strike, ice for hailstones etc.). This is shown by Johnson et al. who used a model, which was successfully able to predict the impact of samples with a gelatine projectile, to simulate an impact with an ice projectile but the results were not as accurate due to the need to include the effect of temperature on the projectile behaviour [80].

In conclusion, composite repair techniques have the potential to ensure aerostructure components can continue to be used without being fully replaced or failing due to fatigue during use of the aircraft. Of the two types of repair discussed, scarf repair has the better performance but requires more complex machinery and significant material removal and, depending on the scarf angle, a large amount of good parent material can be wasted. All of these factors mean that sometimes a patch repair is more suitable. Having said this, a combination of the two can be seen to be the most effective repair. There is a large amount of testing of repaired composite performance under low velocity impacts, with the overall result suggesting that the repaired samples are not as effective at withstanding the impact as pristine samples. There is also testing to suggest that the join itself is the weakest area of the repair and there are a large number of variables in the success of the adhesive, including the number of voids present and the adhesive thickness. The most common testing that has been carried out is low velocity, hard impacts due to the ease with which they can be performed as well as the fact that the damage modes are clearer to identify. There is also limited research into the transition from hard to soft impacts, especially at a low velocity, for the same reason. Considering soft impact of pristine materials, it can be seen that the results vary significantly from the same tests with a hard projectile. Higher energies are required for damage and perforation to occur, which suggests the response to hard impacts is more critical, however the damage from a soft impact is harder to detect due to no obvious defects on the surface. This leads to another difficulty with composite repair is the damage monitoring techniques available. There are no methods currently that allow all damage types to be identified simultaneously, but there are a few that show potential to identify defects that are difficult to detect, such as kissing bonds. Further research is required, especially in ensuring kissing bonds can be effectively replicated, as this is critical in being able to test the viability of detection techniques. Research suggests that the impactor shape significantly affects the performance of composite panels under impact conditions. More blunt impactors spreading the force out over a larger area to give higher peak force values and sharper impactors allowing for the panel to bend more and thus absorb more energy. Finally, modelling is commonly used alongside minimal experimental testing for verification. This allows complex variables to be optimised before experimentation begins, thus saving money and time. It can be seen that using modelling allows for events to be simulated and data collected that would ordinarily be much more difficult in practice. For example, recording the initial and residual velocity throughout the entire impact event and testing a large number of patch and scarf repair configurations. It is also possible to model different types of projectiles, with the SPH modelling technique allowing for the deformation of a soft projectile to be captured with good

agreement to experimental work. Further development of models is required for specific applications, such as different repair configurations and hailstone soft projectiles, but those that have been developed thus far demonstrate the potential for models to effectively predict the damage that will occur after impact.

3 Materials and Experimental Procedures

Parts of this chapter come from the following paper: 'The effectiveness of patch repairs to restore the impact properties of carbon-fibre reinforced-plastic composites' [83].

3.1 Introduction

The research summarised by this thesis focused on the testing of carbon fibre reinforced polymer composite materials, specifically with an epoxy matrix. Detail is given in this chapter on the mechanical properties of the unidirectional prepreg and film adhesive used, the manufacturing processes to make pristine and repaired samples, and the methods used for testing and inspecting the samples.

3.2 Materials

3.2.1 Unidirectional fibre reinforced composites

The CFRP panels used for the research in this thesis were manufactured from unidirectional prepreg (MTC510-UD300-HS-33%RW) supplied by SHD Composite Materials Ltd, UK. This prepreg contains an epoxy matrix (MTC510) and T700 carbon fibres at a fibre volume fraction of 60%. Flat panels were prepared using an autoclave and cut using a cut-off saw according to ASTM D7136 [84].

Table 3-1 gives the measured and theoretical properties of the MTC510 unidirectional prepreg material. This information was supplied by the material supplier, SHD Composites Ltd, UK.

Table 3-1. Material properties for MTC510 unidirectional prepreg

Test	**Results**			**Standard**
Fibre volume fracture (VF)	Measured	60.20	%	N/A
	Theoretical	57.71	%	
Cured ply thickness (CPT)	Measured	0.286	mm	N/A
	Theoretical	0.289	mm	
Tension 0°	Tensile strength	2282	MPa	BS EN ISO 527-5
	Tensile modulus	119.3	GPa	
	Poisson's Ratio	0.34		
Tension 90°	Tensile strength	54	MPa	BS EN ISO 527-5
	Tensile modulus	8.2	GPa	
	Poisson's Ratio	0.01		

Compression 0°	Compressive strength	1067	MPa	EN 2850 Type B
	Compressive modulus	113.6	GPa	
Compression 90°	Compressive strength	200	MPa	EN 2850 Type B
	Compressive modulus	9.3	GPa	
In-plane shear ±45°	In-plane shear strength	99	MPa	ASTM D3518
	In-plane shear modulus	3.60	GPa	
Interlaminar shear strength	Interlaminar shear strength	84.8	MPa	BS EN ISO 14130
DMA	Tg Onset	123	°C	Modified ASTM D7028 (Single Cantilever)
	Peak tan delta	133	°C	

3.2.2 Film adhesive

When repairing samples, MTFA-500 film adhesive was used to attach a patch over the removed damage area, supplied by SHD Composite Materials Ltd, UK. This particular film adhesive was chosen because it was recommended for the purpose by the company who repaired the samples, Polar Manufacturing Ltd, UK. The volatile content and voidage after autoclave curing of the adhesive are both given as less than 1% by the supplier. Some further properties are given in Table 3-2 below.

Table 3-2. Material properties for MTFA-500 film adhesive

Test	**Results**			**Standard**
Climbing drum peel	Peel strength (T)	437	N	ASTM D3165
	Peel strength (L)	538	N	ASTM D1781
DMA	Tg – storage modulus onset	141	°C	AITM 1-0003 Issue 3
	Tg – Tan δ peak	150	°C	

3.3 Manufacturing Processes

3.3.1 Pristine sample preparation

The prepreg was cured in an autoclave under a constant pressure of 6 bar with a 120-minute dwell-time at 110°C, using a 2°C per minute temperature ramp, and the glass transition temperature of the cured composite was 133°C. Figure 3-1 shows a diagram of the curing process and the autoclave used.

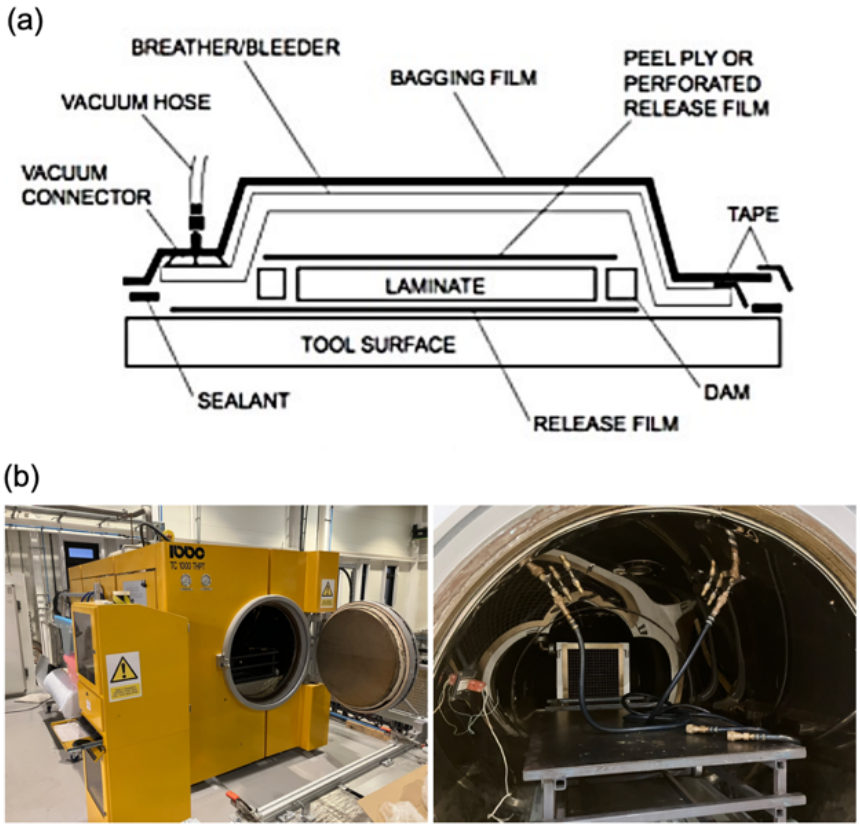

Figure 3-1. (a) Diagram of the curing process to produce laminates from the prepreg [85] and (b) the autoclave used to cure the prepreg and make panels.

Cross-ply and quasi-isotropic panels were used in the testing in this thesis, with both being manufactured in 'thin' and 'thick' variations to allow for various repair configuration. The specific lay-ups and thicknesses of the samples made up are given in Table 3-3 below.

Table 3-3. Material information for samples made from the unidirectional prepreg

	Thicker cross-ply	**Thinner cross-ply**	**Thicker QIT**	**Thinner QIT**
Lay-up	$[0_2/90_2]_{2s}$	$[0/90]_{2s}$	$[45_2/-45_2/0_2/90_2]_s$	$[45/-45/0/90]_s$
Plies	16	8	16	8
Thickness	4.58 mm	2.29 mm	4.58 mm	2.29 mm

The blocking lay-ups used for the thicker materials were chosen due to consistency with previous work within the research group and being commonly used in work by other researchers, allowing for comparisons to be made with other testing results. The 0° plies were aligned with the longer edge of the panels, which had a size of 100 mm x 150 mm, with a thickness, t, of 2.29 or 4.58 mm, as shown in Figure 3-2.

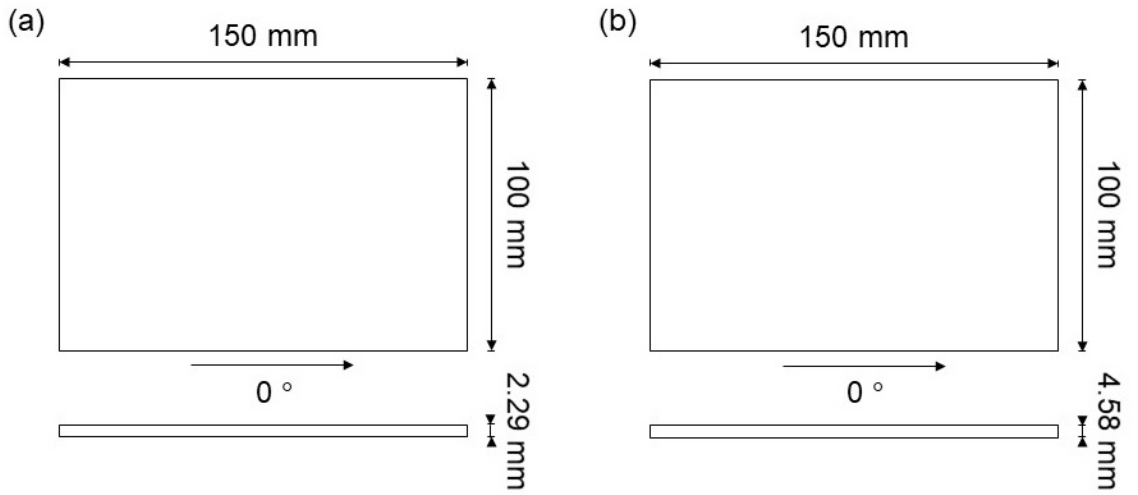

Figure 3-2. Plan- and side-views of (a) a thinner panel and (b) a thicker panel

3.3.2 Patch repaired sample preparation

The patch repair panels were produced by removing a disk from the centre of a pristine panel, which now became the parent CFRP composite, and a circular patch of CFRP material was then adhered over the hole using one layer of MTFA-500 toughened epoxy-film adhesive, supplied by SHD Composites Ltd, UK, which had a nominal thickness of 0.25 mm. The removal of this CFRP disc was performed by Polar Manufacturing Ltd, UK, and consisted of two stages: roughing and finishing. A 2 mm diameter carbide corn-cutter, at a spindle speed of 5000 rpm and feed rate of 300 mm/minute, and a 2 mm diameter carbide 3-flute end mill, at a spindle speed of 5000 rpm and feed rate of 400 mm/minute, were used for the roughing and finishing stages, respectively. Approximately 0.1 to 0.2 mm of CFRP material was left untrimmed after the roughing stage to ensure a high-quality finish. During machining, each pass only removed 1 mm of material in the Z-plane and started and finished away from the hole edge to minimise any damage initiation as far as possible. The machine was run without coolant and the panels were fixed to a sacrificial back-plate with double-sided tape and constrained with clamps. The surfaces of the parent, patch and plug (where relevant) were prepared prior to bonding using 50 grit sanding discs and then cleaned with acetone. The adhesive layer was cured under a constant pressure of 6 bar with a 90-minute dwell time at 130°C and a 3°C per minute temperature ramp, where the curing set up and autoclave used are shown in Figure 3-3. Additionally, when no plug was present in the repair, a sacrificial plug was used to ensure correct placement and a high quality repair.

(a)

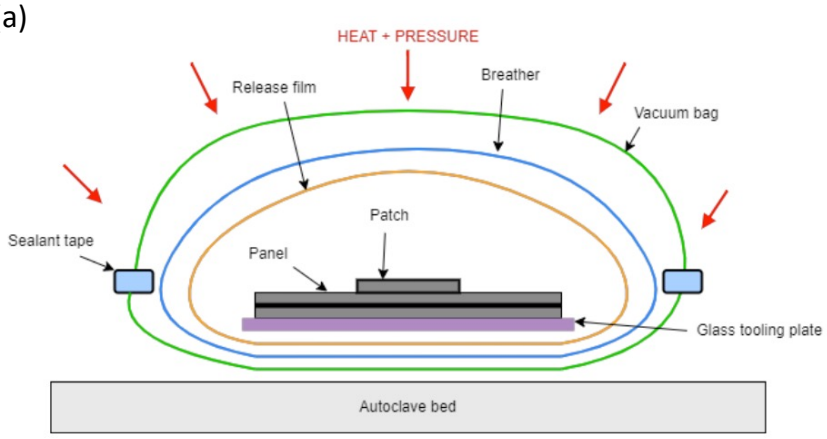

(b)

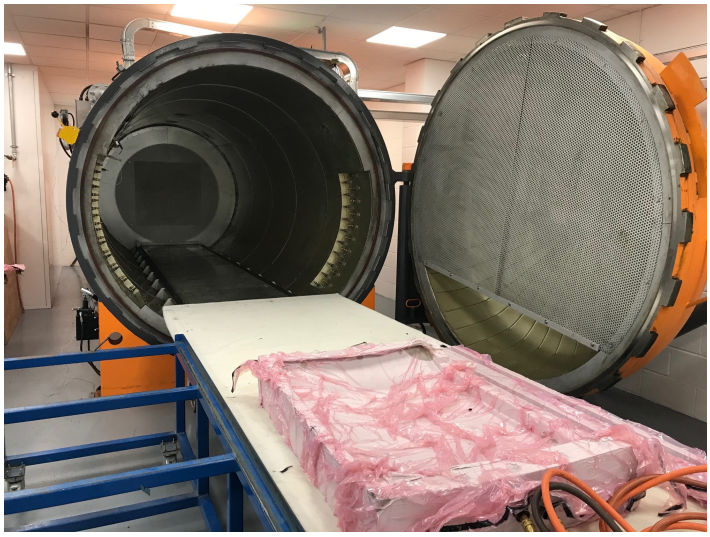

Figure 3-3. (a) Diagram of the curing process to produce repairs [85] and (b) the autoclave used to cure the adhesive for repairs.

The use of a glass tooling plate over a standard steel or aluminium plate allowed for a smoother release and quicker heating [85]. Two different thicknesses of the patch composite were employed, which gave a cured ply thickness, 0.5t, of 2.29 mm, and the thicker patch having the same lay-up and thickness, t, of 4.58 mm as that of the parent CFRP. Some repairs were made with a push-fit plug of the CFRP parent composite to fill the hole, whilst in other repair panels the hole was left unfilled. Where a plug was present, the orientation of the plies was identical to the parent panel and, since a disk of the film adhesive was used, both the parent panel and the plug were adhered to the patch. However, it was found from manufacturing and testing successive batches of patch repair panels, that a relatively easy push-fit of the composite plug was preferable to a very tight fit. Since the former enabled the adhesive to flow into the gap between the plug and the parent CFRP, and so prevented the patch from being dislodged on a few occasions during impact tests on the repaired panels. Such a failure mode resulted in the repaired panel having a relatively poor impact performance. Therefore, all the current tests

using plugs were conducted on patch repair panels where the composite plug was a relatively easy push-fit into the 40 mm diameter hole which had been cut out in the parent CFRP. Two different diameters of CFRP patches were used: 55 and 65 mm, as denoted by the dimension 'D' in Figure 3-4. The size of the removed material also varied depending on the testing and this was governed by the size of the damage area seen in a pristine panel, with the material removal size being chosen to contain all detected damage.

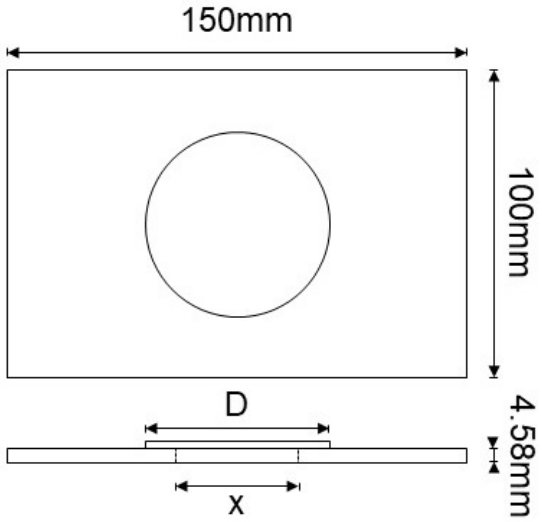

Figure 3-4. Plan- and side-views of a repaired panel

3.4 Overview of Experiments

3.4.1 Drop-weight testing

The pristine and patch-repair panels were tested under a low-velocity impact loading using an Instron 9340 drop-weight tower supplied by CEAST, Italy, shown in Figure 3-5, following the same test method as described elsewhere [86-88]. Basically, the panels were held in place with four rubber clamps, one at each corner, over a fixture with a 125 x 75 mm^2 cut out window. A 16 mm diameter, stainless steel impactor with an overall mass of 5.27 kg and either a rounded or flat end was used to impact the panels from varying heights. A catching system was used to prevent further impact events from occurring after the initial impact. No software filtering was applied to the load versus time data that was outputted and the accompanying software, provided by CEAST, produced both the impact load and resulting displacement of the panel as a function of time for the impact event.

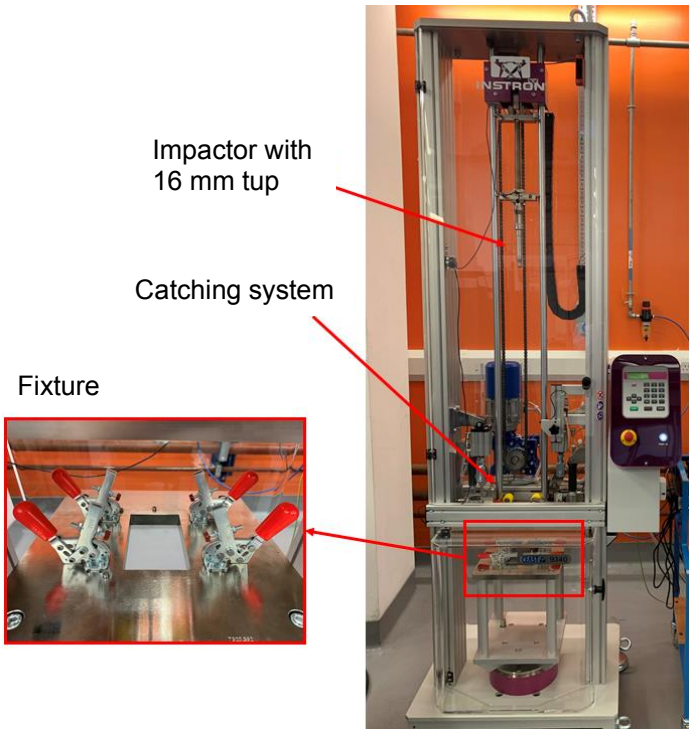

Figure 3-5. Drop-weight tower set-up.

3.4.2 Ultrasonic C-scanning

The impacted panels were inspected using a Prisma portable ultrasonic C-scanner supplied by Sonatest Ltd, UK (see Figure 3-6) to detect any interlaminar damage area. This technique has been discussed in detail elsewhere [88]. Essentially, a water spray was applied to the surface to act as a contact agent to ensure effective transmission of the ultrasonic waves from the transducer probe through the composite, using a scanning frequency of 5 MHz. These waves are reflected back to the transducer upon interacting with any delamination damage in the panel, and the position and size of the interlaminar damage can be determined from the total travel time and amplitude received by the transducer, respectively. The C-scanning equipment gave images with a scale from 0 to 4.58 mm (i.e., the thickness of the pristine and parent panel, and also of the thicker patch) or 0 to 2.29 mm (i.e., the thickness of the thinner patch). The total damage area was then calculated by counting the number of pixels that were not dark blue in colour, since dark blue corresponds to a region of the laminate free from interlaminar damage.

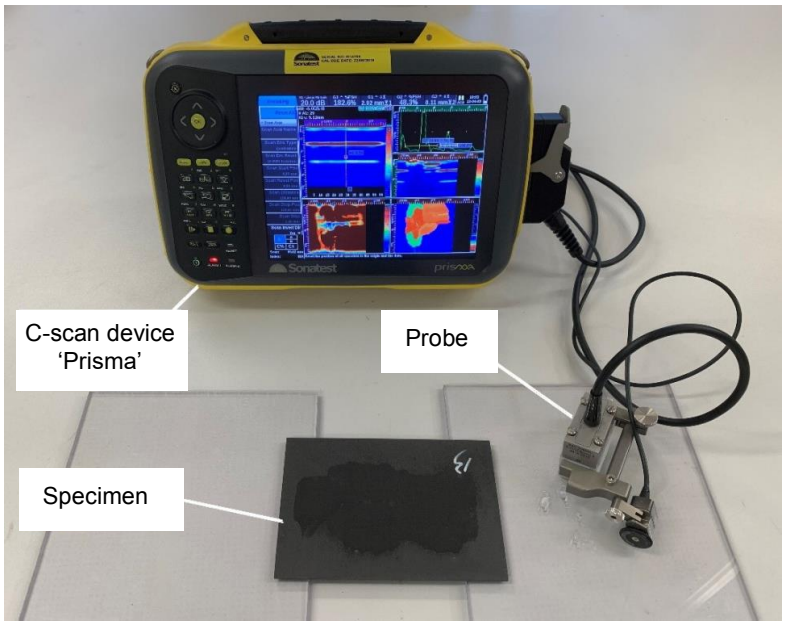

Figure 3-6. Ultrasonic C-scan equipment set-up.

3.4.3 Microscopic inspection

An optical microscope was used to inspect the damage in the samples after impact, to give further information from that gathered by using the c-scanning equipment.

The preparation process used before assessing the damage mechanisms with the microscope are described elsewhere [85]. Essentially, samples were prepared for inspection by cutting through the centre of the damage area with a diamond-blade circular saw, see Figure 3-7. The cutting blade speed was set to 3500 revolutions per minute and the panels were fed into the cutter at a rate of 0.3 mm per minute.

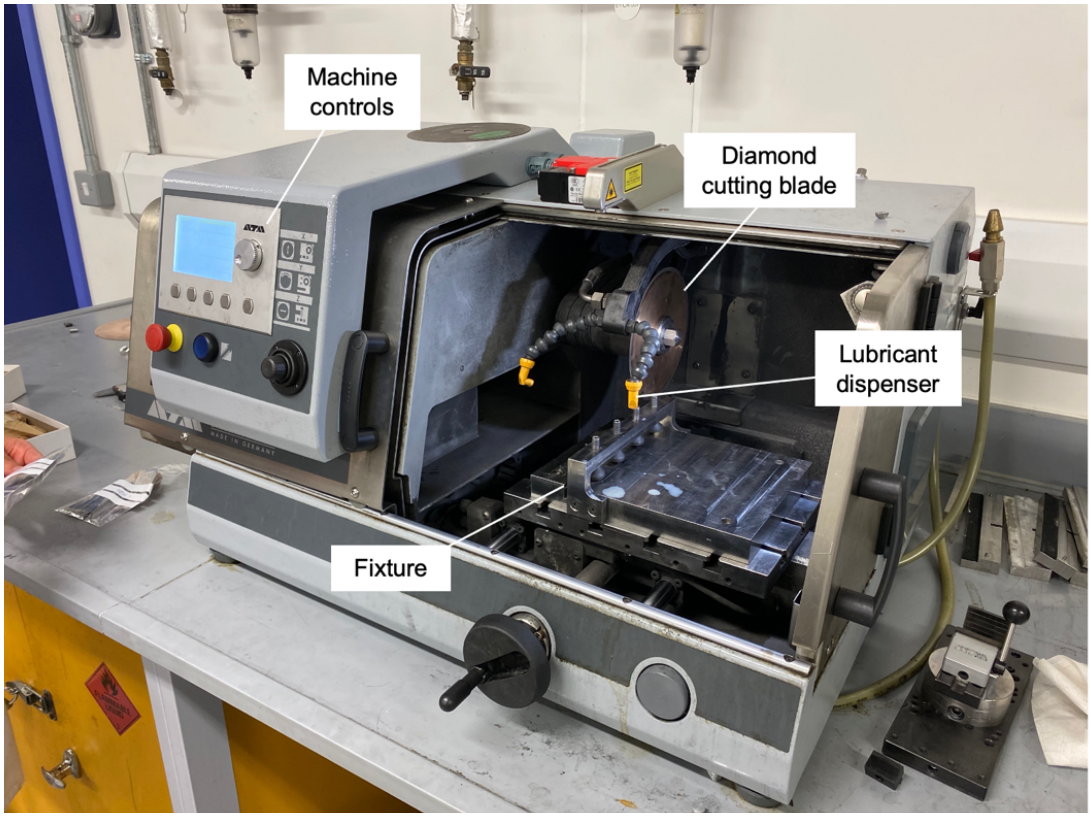

Figure 3-7. Diamond-bladed circular saw used to cut samples through the damage area in preparation for analysis via optical microscopy.

Once cut, the samples were ground, using silicon carbide grinding paper, gradually increasing in fineness by using: P180, P300, P600/P800, P1200, P2500 and, if available, P4000, and polished, using diamond suspension fluid on polishing cloths, gradually decreasing in size by using: 6, 3, 1 and 0.25 micron. Grinding and polishing the samples allows for better images to be taken when using the optical microscope to ensure the damage mechanisms are clearly visible. The equipment used for this process is shown in Figure 3-8.

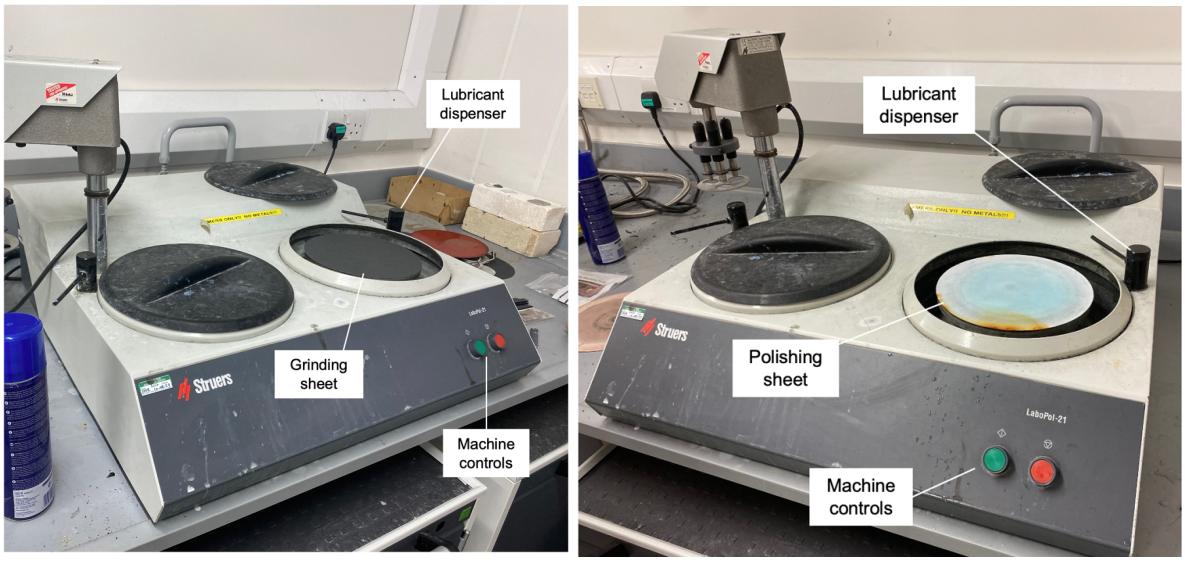

Figure 3-8.Grinding and polishing equipment with a sheet of silicon carbide grinding paper attached (left) and a polishing cloth sprayed with suspension fluid attached (right).

The samples were then viewed using the optical microscope (see Figure 3-9) and images were saved of what was seen. This internal viewing option was chosen over SEM due to less preparation being required as well as a lack of need for magnification above 100 times, which the optical microscope was more than suitable for [85].

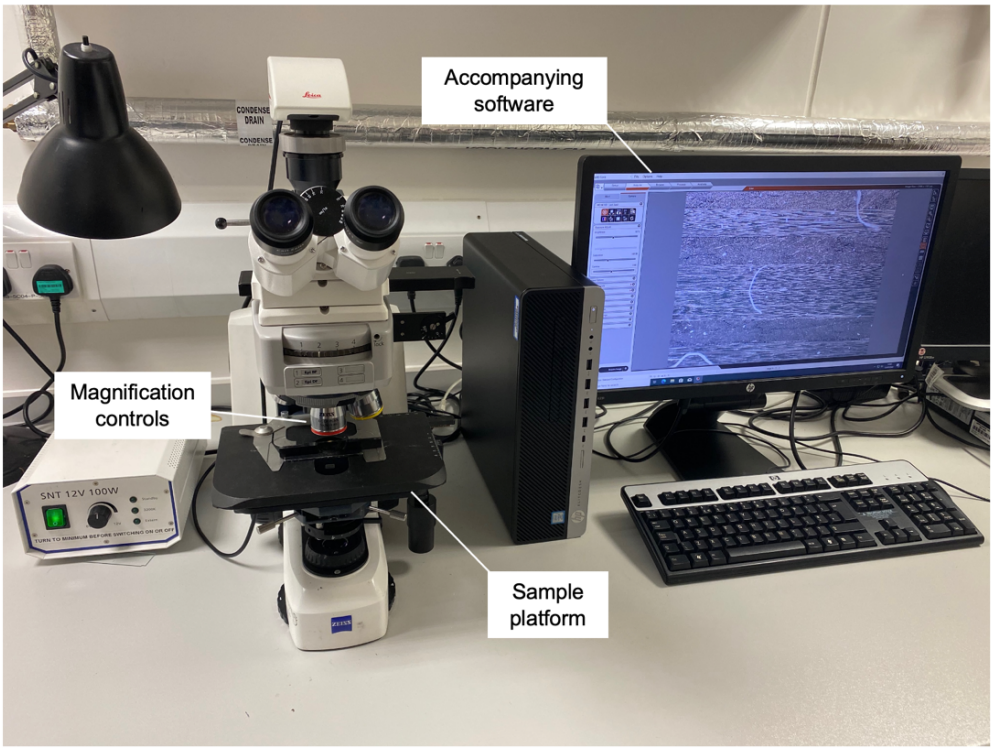

Figure 3-9. Optical microscope and accompanying software used to view damage mechanisms within composite panels after impact.

4 Experimental study on the effect of patch repair properties on quasi-isotropic CFRP panels under low-velocity impact loadings

This chapter comes from the following paper: 'The effectiveness of patch repairs to restore the impact properties of carbon-fibre reinforced-plastic composites' [83].

4.1 Introduction

Composite materials based upon carbon-fibre reinforced-plastics (CFRPs) have been widely used in aerostructures over the last three decades mainly due to (a) their excellent strength to weight, and stiffness to weight, ratios, (b) their very good cyclic fatigue resistance and (c) the ability to control their mechanical properties by suitably changing the fibre lay-up. However, an area of particular concern when considering the performance of composite materials, such as CFRPs, for aircraft structures is the impact performance of the composite. Therefore, firstly, the initial impact performance of the pristine CFRP is of interest because there are many impact scenarios. These include impact events which arise from dropped tools, bird strike, hail stones, runway debris, airport equipment striking the fuselage and hard landings. Secondly, these impact events may lead to damage in the CFRP which now needs to be repaired to recover the mechanical performance of the composite material. The two most common repair techniques for composite materials are patch and scarf repairs and, for secondary aircraft structures, these repair methodologies involve the use of adhesive bonding as the most common joining technology used for the repair. Thirdly, obviously of great interest is the impact behaviour of the repaired composite material.

Firstly, considering the impact of CFRP panels, and other more complex structures, then this has been the subject of much research [e.g., 86-97], since such composite materials are susceptible to impact damage, which may not be readily visible but which can lead to a significant loss of structural integrity. There are two major damage mechanisms observed when a CFRP composite is impacted at a relatively low velocity which cause a loss of mechanical performance. Firstly, there is intralaminar damage which typically involves plastic deformation of the matrix, matrix cracking, fibre debonding and localised fibre failure. Secondly, there is interlaminar damage which involves the initiation and growth of delaminations, i.e., interlaminar cracking

between the layers that form the composite laminate. These two main damage mechanisms are interactive during the impact event.

Secondly, when such intralaminar and interlaminar damage needs to be repaired there are two main types of repair techniques for composite materials [2,6,8,98], namely patch and scarf repairs, as shown schematically in Figure 4-1.

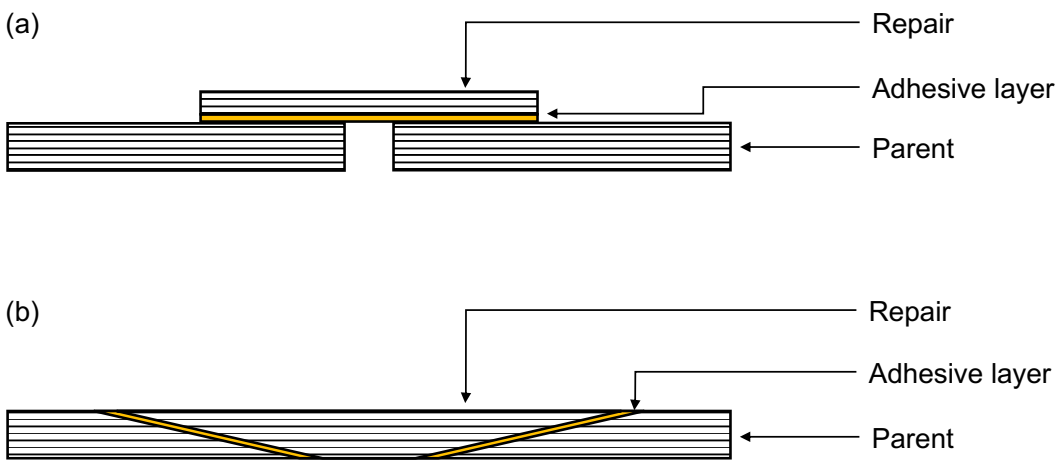

Figure 4-1. Schematic of the two main types of repair configurations: (a) patch repair and (b) scarf repair.

In the case of secondary, non-critical structures, the repair material is typically joined to the parent composite solely via the use of adhesive-bonding techniques. (If primary, critical structures are repaired then an alternative, or additional, joining method, e.g., titanium fasteners, must be used.) Scarf repairs, see Figure 4-1 (b), are often the preferred method to restore the load-bearing capacity of a composite structure, since they are associated with relatively lower stress-concentrations and are more aerodynamically efficient. However, they suffer from several disadvantages. For example, they are far more complex to manufacture and, if a relatively large patch is needed, then a great deal of undamaged composite material needs to be removed. Thus, patch repairs are also commonly used, and they cover, and overlap, the damaged area and are usually thinner than the parent material, as shown schematically in Figure 4-1 (a). The patch repair can be single- or double-sided, with the former type having a patch adhesively bonded to only one side of the parent panel, as in Figure 4-1 (a), and the latter type having a repair patch bonded onto both sides of the parent panel, which is not always possible of course in practice. When manufacturing a patch repair, the damage can either be removed, or the patch placed over the top of the damage area. If the damaged area is removed, a polymeric resin or a plug of the

parent composite material may often be used to fill the hole so generated. Single-sided patch repairs, which are adhesively bonded to the damaged parent composite material, are the focus of the present work since (a) they are widely used in repairing aerostructures, (b) they are relatively straightforward to manufacture and (c) their effectiveness can be readily assessed by impact testing of the repaired CFRP panel.

Thirdly, as mentioned above, obviously of great interest is the impact behaviour of the repaired composite material. The most common impact tests that have been undertaken on pristine and repaired composites have been conducted at a relatively low-velocity using hard impactors and some experimental and modelling research [44,46,49,99-102] has been reported. For example, Coelho et al. [46] tested single-sided, glass-fibre reinforced-plastic (GFRP) patch repairs which had been adhesively bonded to GFRP parent panels and subjected the repairs to impact tests, using impact energies from 2 to 6 J. They also studied the effect of repeated, multiple impacts. They concluded that the design of the patch adopted should have a stiffness as close as possible to that of the parent GFRP. However, such a design may well suffer from an undue weight penalty. Tie et al. [44] investigated the impact behaviour of single-sided, CFRP patch repairs which had been adhesively bonded to a CFRP parent panel at an impact velocity of 3.25 $m.s^{-1}$ and an impact energy of 13.2 J. They studied the shape of the patch and used patches which had the shapes of a circle, a square, a rhombus, a hexagon and an octagon, all with the same nominal area. They found that the use of the circular-shaped patch gave the best impact performance and thus circular patches will be used in the present work. Furthermore, Hou et al. [49] studied single-sided, CFRP patch repairs adhesively bonded to a CFRP parent panel using circular-shaped patches, again using an impact velocity of 3.25 $m.s^{-1}$ and an impact energy of 13.2 J. They investigated the effect of varying the impact location from 0 to 50 mm, as the distance from the centre of the repaired parent laminate, i.e., the centre of the circular patch, to the impact point. Their results showed that this distance had little significant effect on the maximum force, or maximum absorbed impact energy, that was recorded. In the present work, the impact point is the centre of the repaired parent laminate, i.e., the centre of the circular patch. Finally, Sun et al. [100] have studied single-sided CFRP patch repairs adhesively bonded to a CFRP parent panel, employing circular-shaped CFRP patches, using impact velocities of 2.82, 3.46 and 4.00 $m.s^{-1}$, with corresponding impact energies of 10, 15 and 20 J. They conducted three repeated multiple impacts per test in the centre of the patch and reported that the main damage mechanisms that were observed were intralaminar and interlaminar damage in the CFRP patch-repair. Further, by observing the damage profiles of the panels after repeated

impacts, it was found that the damage was mainly interlaminar matrix cracking at an impact energy of 10 J. However, significant fibre fracture occurred in the patch after repeated impacts at impact energies of 15 and 20 J. Further, at an impact energy of 20 J, the patch-repair was actually penetrated and damage to the parent panel was now also observed.

In the present work, single-sided CFRP patch repairs, which are adhesively bonded to the 'damaged' CFRP parent panel, are subjected to a low-velocity impact with the impact point being the centre of the repaired parent laminate, i.e., the centre of the circular patch. However, in the present work a relatively wide range of impact energies of 7.5, 10.5 and 30 J are employed. The effect of repeated, multiple impacts at these relatively high impact-energies are investigated on the pristine CFRP panel. These tests enable the typical impact-damaged area that results in such panels to be defined. For the repair panels, a hole is cut out in the centre of the parent panel, which represents removal of the impact damage. A single-sided, circular CFRP patch is then bonded over the hole so generated. The effects of the diameter and thickness of the patch are considered, as is the use of a plug of CFRP to fill the hole generated by removal of the 'damaged area' in the composite CFRP parent panel. Load versus time, and load versus displacement, traces are measured from the impact tests on the pristine CFRP panel and the patch-repair CFRP panels, and detailed maps of the interlaminar damage suffered by the various panels are also obtained. These experimental measurements are correlated to the various types of pristine and patch-repair CFRP panels studied.

4.2 Test specification and methods

4.2.1 Repairing samples

The panels used for this research were manufactured following the method described in Section 3.3. The quasi-isotropic lay-up used for the pristine panels was $[45_2/-45_2/0_2/90_2]_s$, where the 0° plies were aligned with the longer edge of the panels, which had a size of 100 mm x 150 mm, with a thickness, t, of 4.58 mm, as shown in Figure 4-2 (a).

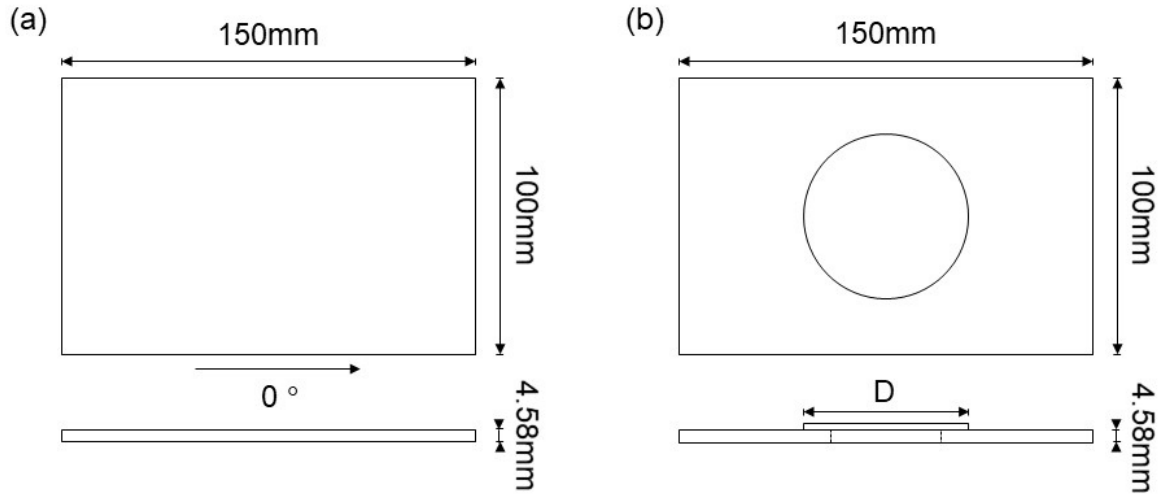

Figure 4-2. Plan- and side-views of (a) the pristine panel and (b) the patch-repair CFRP panel.

The patch-repair panels were produced by following the method detailed in Section 3.3.2, using quasi-isotropic lay-ups for the patches. Two different thicknesses of the patch composite were employed, with the thinner patch having a lay-up of $[45/-45/0/90]_s$ which gave a cured ply thickness of 2.29 mm, and the thicker patch having the same lay-up and thickness as that of the parent CFRP. Some repairs were made with a push-fit plug of the CFRP parent composite to fill the 40 mm hole, whilst in other repair panels the hole was left unfilled. Two different diameters of CFRP patches were used: 55 and 65 mm, as denoted by the dimension 'D' in Figure 4-2 (b).

4.2.2 Drop weight testing

The pristine and patch-repair panels were tested under a low-velocity impact loading using an Instron 9340 drop-weight tower supplied by CEAST, Italy, shown in Figure 3-5, following the same test method as described elsewhere [86-88] and in Section 3.4.1 of this thesis. A 16 mm diameter, stainless steel, round-nosed impactor with an overall mass of 5.265 kg was used to impact the panels from varying heights to give impact energies of 7.5, 10.5 or 30 J, with corresponding impact velocities of 1.69, 2.00 and 3.38 $m.s^{-1}$, respectively.

The impacted panels were inspected using a Prisma portable ultrasonic C-scanner supplied by Sonatest Ltd, UK to detect any interlaminar damage area. This technique has been discussed in detail elsewhere [88] and in Section 3.4.2 of this thesis.

4.3 Experimental results

4.3.1 Pristine samples

Repeat, i.e., multiple, impact tests were performed on the pristine CFRP panels, using impact energies of either 7.5, 10.5 or 30 J. Three successive impacts were performed for the highest and lowest impact energies and two were performed for the 10.5 J case. Figures 4-3, 4-4 and 4-5 show the load against time, and load against displacement, traces for each impact energy value.

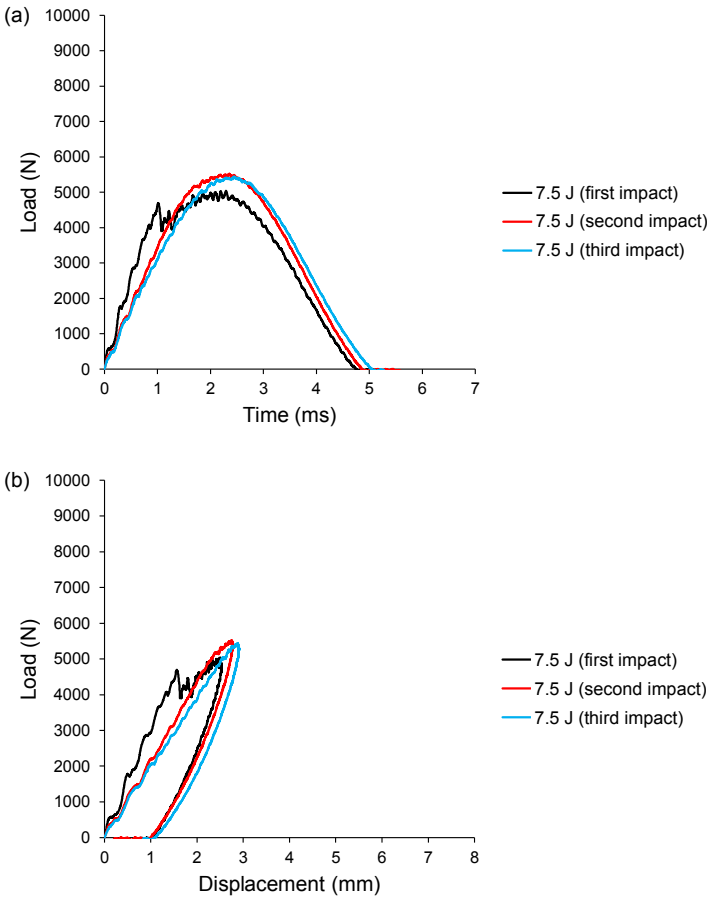

Figure 4-3. Load traces for repeated, i.e., multiple, impacts on a pristine QIT CFRP panel at 7.5 J: (a) load versus time traces and (b) load versus displacement traces.

From Figure 4-3, for an impact energy of 7.5 J, it can be seen that, when subjected to a first impact, there are relatively small amplitude, sinusoidal oscillations on the rising part of the load versus time, and load versus displacement, experimental curves up to a load of 4693 N. These oscillations have been observed previously by other researchers and are indicative of mass-spring oscillations, as first analysed in detail in [88, 102-106]. Once a local peak of approximately 4693 N is achieved, at a time of 1 ms, there is an appreciable decrease in the load,

and an increase in the associated subsequent oscillations. This significant load drop is indicative of the initiation of damage in the pristine CFRP panel. These oscillations that occur after the first point of this significant load drop, which is often called the initiation load, are typically associated with the first damage of the CFRP panel that occurs, e.g., matrix cracking, indentation including plasticity of matrix and subsequent damage propagation, but does not exclude the formation of delaminations, as has been described in detail by Liu et al. [88] and Bienias et al. [106]. However, both the load traces for the second and third impact events do not show this characteristic, implying that additional damage processes are not initiated but instead existing damage propagates due to the loading by the second or third impact. Furthermore, the peak (i.e., maximum) impact load is noticeably lower for the first impact compared to the second and third impacts. This observation arises because, in the first impact, the impact energy is dissipated through the damage that occurs at the load drops. For the subsequent second and third impacts, the CFRP panel has become softer and the effective damage threshold has increased due to the first impact. Thus, more energy can be stored through elastic deformation and a higher load and displacement of the panel are achieved.

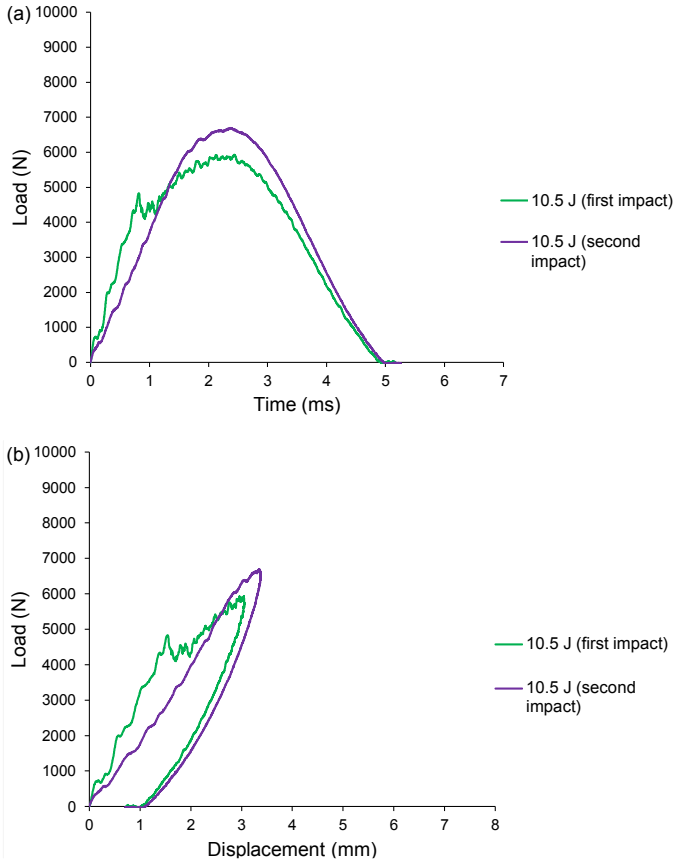

Figure 4-4. Load traces for repeated, i.e., multiple, impacts on a pristine QIT CFRP panel at 10.5 J: (a) load versus time traces and (b) load versus displacement traces.

Similarly, Figure 4-4, for an impact energy of 10.5 J, shows the same trends as for the 7.5 J impact energy tests, and the load traces again exhibit a change in gradient, or load drop, at 4800 N at a slightly reduced time of approximately 0.8 ms. Again, as for the 7.5 J impacts tests, damage is initiated during the first impact but not by the second impact. Both the tests conducted at 7.5 and 10.5 J use a relatively low impact-energy and so a 30 J impact test was next conducted.

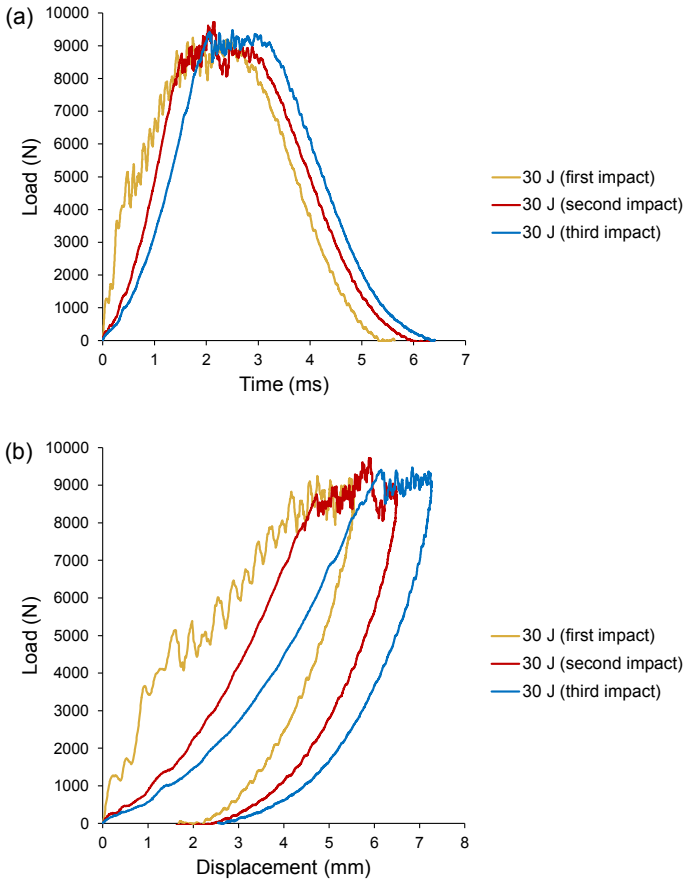

Figure 4-5. Load traces for repeated, i.e., multiple, impacts on a pristine QIT CFRP panel at 30 J: (a) load versus time traces and (b) load versus displacement traces.

From Figure 4-5, it can be seen that the load traces for the 30 J tests show that the first impact results in a very clear load drop at 5130 N, at an even shorter time of approximately 0.5 ms, followed by significant oscillations, indicative of damage initiation. At this higher impact energy of 30 J, the second and third impacts also exhibit a change in gradient and a load drop with accompanying oscillations, at a load of approximately 9000 N, indicative of further damage initiating. For this increased impact energy of 30 J then after the second and third impacts there also appears to be other damage processes that are initiated besides delaminations, e.g., transverse cracking along the fibres was observed on the rear face of the panels.

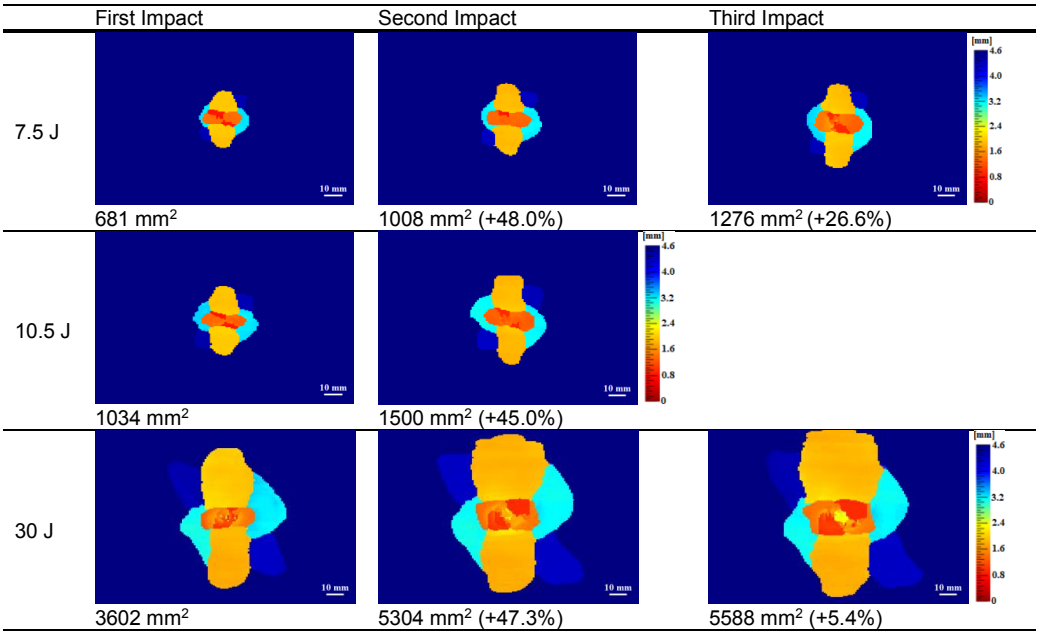

Figure 4-6. C-scan images taken from the top (impacted) surface for repeated, i.e., multiple, impacts on pristine QIT CFRP panels at various impact energies. (The scales show the depth of the different locations of the interlaminar damage. The percentage value, in brackets, is relative to the preceding impact).

The C-scan images shown in Figure 4-6 reveal the changes in the area of the interlaminar damage with each successive impact. The right-hand side scale in Figure 4-6, and similar figures later, indicates the location of the measured interlaminar delaminations as a function of the depth through the thickness of the panel, where the dark-red colour represents a reflection from the surface nearest the transducer probe and the dark-blue colour represents a reflection from the surface furthest away from the transducer probe, i.e., often the rear (non-impacted) surface. The delaminations form between plies of different fibre orientations and the colour code indicates their distance from the transducer probe. Each delamination tends to grow along the orientation of the ply beneath the delamination on the lower surface. The results show, for example, that the damage area footprint, which encompasses all delaminations, appears to grow by ca. 50% following the second impact for all the three energy levels studied. For the third impact at 7.5 J, the increase in the damage area is reduced to ca. 25%. Whilst, for the 30 J impact, the damage area has almost reached a maximum after the second impact and there is only a very slight further increase of ca. 5% for the third impact. From these impact tests on the pristine CFRP panel, it was decided to cut out a 40 mm diameter hole in the centre of the parent CFRP panel, since this is a good representation of the typical extent of impact damage in the CFRP corresponding to an impact energy of 7.5 J. Also, the presence of such a hole, i.e., 'damage area', gives a significant change in the measured impact response of the panel at 7.5 J but is not so large in size that edge-effects will be observed when the patch-repair CFRP panels are impacted.

4.3.2 Effect of varying the patch diameter, with a plug present

Four repair panels with CFRP plugs were manufactured in total: two for each patch diameter, i.e., 55 mm and 65 mm, with a patch thickness, 0.5t, of 2.29 mm. For these patch-repair panels with a plug present, the load versus time, and load versus displacement traces are compared to the performance of the pristine CFRP panel in Figure 4-7 for an impact energy of 7.5 J. From these traces, it can be seen that the overall stiffness of the panel and the initial damage load are increased, and the maximum displacement is reduced, when a repair is undertaken using a plug. This is mainly due to the increase in the overall thickness that the patch and plug together add to the patch repaired CFRP parent panel, compared to that of the pristine CFRP panel. However, there is a more sudden drop in the load after damage initiation in the repaired panel compared to the pristine panel, which could be due to the overall increased stiffness of the panel, but which could also arise from damage around the plug.

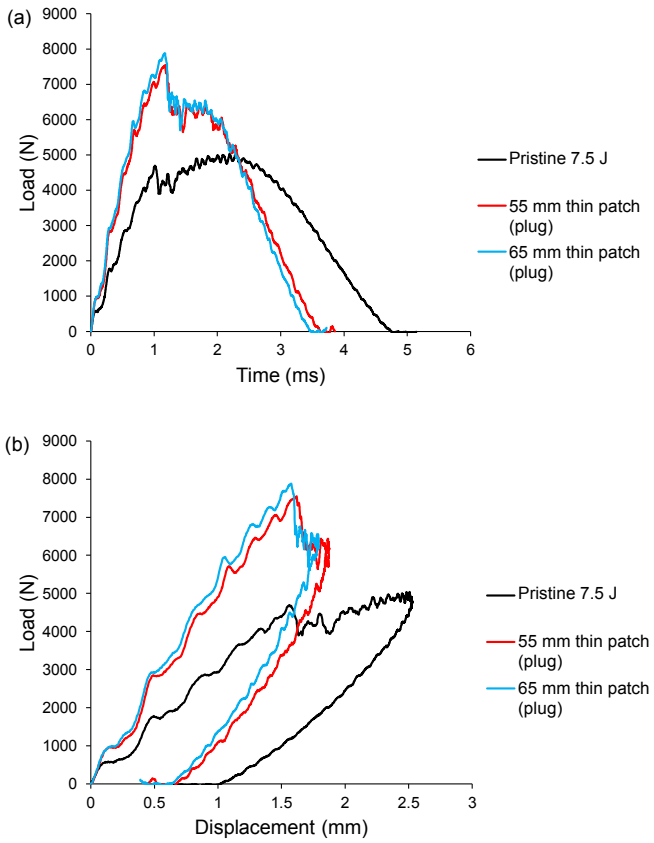

Figure 4-7. Load traces for a pristine QIT CFRP panel and 55 mm diameter and 65 mm patch-repair panels, with a QIT CFRP plug, impacted at 7.5 J. The thickness, t, of the parent and the plug QIT CFRP was 4.58 mm and the thickness, 0.5t, of the patch was 2.29 mm. Shown are the: (a) load versus time traces and (b) load versus displacement traces.

A notable point about Figure 4-7 is that the load versus time, and load versus displacement, traces for the patch-repair panels with a plug have a higher maximum load of just under 7880 N, at a time of approximately 1.2 ms, for the 65 mm diameter patch and 7550 N, at a time of approximately 1.2 ms, for the 55 mm diameter patch, compared to the pristine CFRP panel. In both cases, there is a significant load drop, indicative of damage initiation. Thus, an increase in patch diameter to 65 mm is somewhat beneficial in raising this initiation load from 7550 to 7880 N, as would be expected. Furthermore, these initiation loads are indeed much higher than for a pristine panel, i.e. 4693 N at 1 ms. For all these patch-repair panels with a plug, as for the pristine panel on first impact, there are slight oscillations in the load up to the maximum value due to mass-spring oscillations. Clearly, adding a patch of thickness, 0.5t, of 2.29 mm, together with a CFRP plug, of thickness, t, of 4.58 mm, is very beneficial in restoring the overall structural response of the parent CFRP composite, of thickness, t, of 4.58 mm, and this is evident by the increase in the initiation load and the stiffness for the patch-repair CFRP panels with a plug.

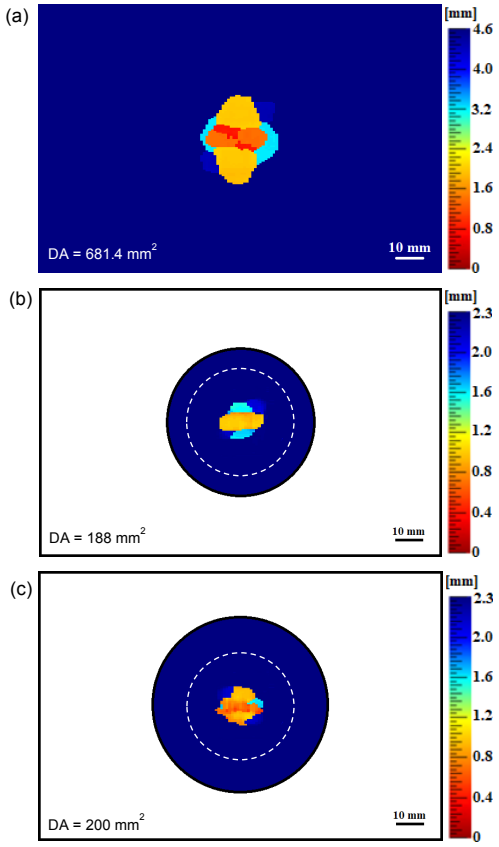

Figure 4-8. C-scan images taken from the top (impacted) face after a 7.5 J impact for: (a) the pristine QIT CFRP panel (of thickness, t, of 4.58 mm), (b) the 55 mm patch-repair QIT CFRP panel (of patch thickness, 0.5t, of 2.29 mm, with a plug) and (c) the 65 mm patch-repair QIT CFRP panel (of patch thickness, 0.5t, 2.29 mm, with a plug). The plug was 4.58 mm thick, i.e., the same thickness as the parent QIT CFRP. (The white-dashed line represents the 40 mm diameter hole that was initially cut out in the parent panel).

Figure 4-8 shows the C-scan images of the interlaminar damage area in the 55 and 65 mm diameter patch-repair CFRP panels containing a plug, compared to that of a pristine CFRP panel. All were impacted at the same impact energy of 7.5 J. It is clear that the damage area is greatly reduced when the repairs have been performed. If no repair had been performed after a 7.5 J impact and the panel was hit for a second time, the damage in the panel in Figure 4-8 (a) would have increased even further, by ca. 50% given the results discussed above. This again demonstrates the effectiveness of patch repairs when a plug is also employed at preventing further damage and restoring the impact properties even beyond that of the pristine CFRP panel. Additionally, a C-scan from the rear-face of the repair panels was performed to allow the damage in the plug to be observed and such scans also confirmed that there was no delamination damage in the parent material. Figure 4-9 shows these scans, with the damage area in the plug being larger than that in the patch, but still less than that in the pristine panel after just one impact. This further demonstrates the success of a patch repair with a plug in restoring the impact properties of a damaged panel.

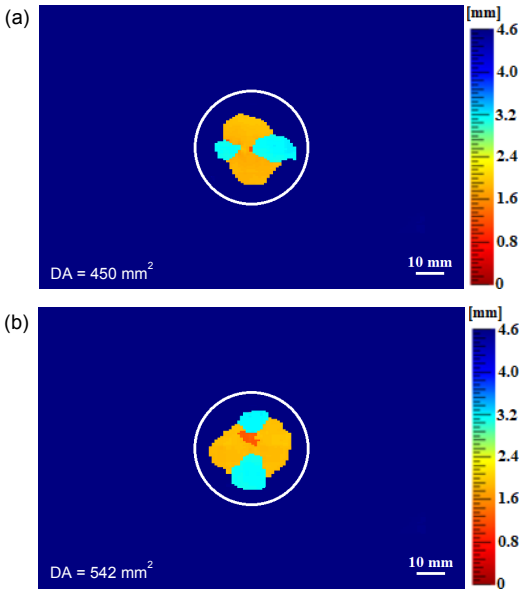

Figure 4-9. C-scan images of the plug and surrounding parent composite taken from the rear (non-impacted) face of the panel after a 7.5 J impact of: (a) the 55 mm patch-repair panel (of thickness, 0.5t, of 2.29 mm, with a plug) and (b) the 65 mm patch-repair panel (of thickness, 0.5t, of 2.29 mm with a plug). The plug was 4.58 mm thick, i.e., the same thickness as the parent QIT CFRP. (The solid-white line is 40 mm in diameter and represents the boundary between plug and the parent QIT CFRP panel).

4.3.3 Effect of varying the patch diameter, with no plug present

To consider the effect of having no plug in the repair, panels were manufactured with patch repairs but with no plug present and impacted at 7.5 J, and two different diameters of patch of 55 and 65 mm were used. As before,

the patch thickness, 0.5t, was 2.29 mm and the thickness, t, of the parent composite was 4.58 mm. Figure 4-10 shows the load versus time, and load versus displacement, traces for the two types of patch-repair panels, compared to a pristine panel. It can be seen that the loading response for both diameters of patch are similar but quite different to that of a pristine panel. For the smaller diameter patch (i.e., 55 mm diameter, with 0.5t of 2.29 mm), the initiation load is 1771 N at a time of approximately 0.6 ms. Whilst for the larger diameter patch (i.e., 65 mm diameter, with 0.5t of 2.29 mm), the initiation load is 1689 N at a time of approximately 0.6 ms. For comparison, the initiation load for a pristine sample is 4693 N at a time of approximately 1 ms.

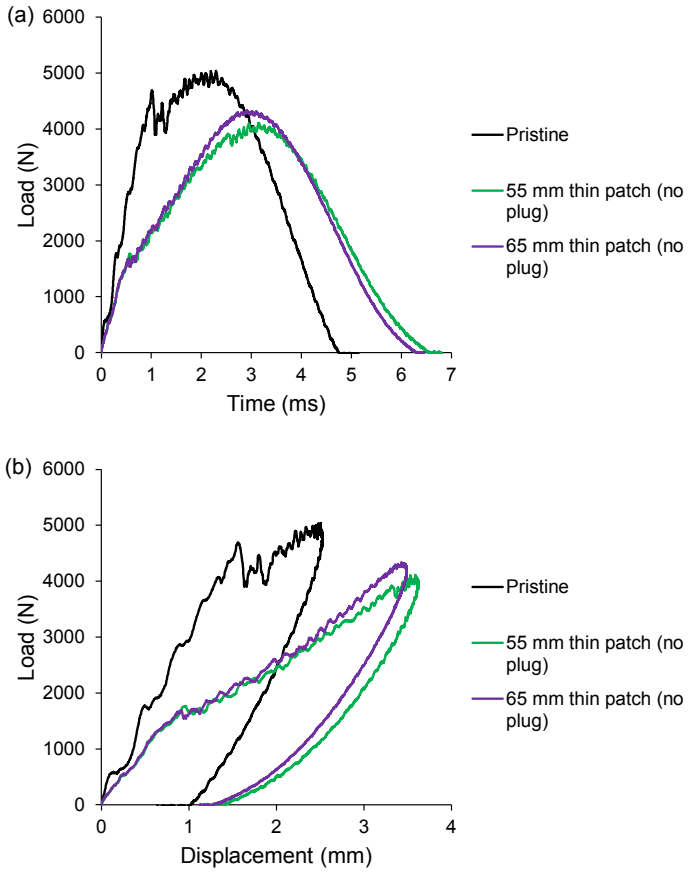

Figure 4-10. Load traces for a pristine QIT CFRP panel and 55 mm diameter and a 65 mm patch-repair panels, with no QIT CFRP plug, impacted at 7.5 J. The thickness of the parent was 4.58 mm and the thickness of the patch was 2.29 mm. Shown are the: (a) load versus time traces and (b) load versus displacement traces.

Therefore, for both patch diameters, the thinner patch, when it is not supported by a plug, deforms more easily around the drop-weight impact site where the impact stress is initially localised and concentrated. Thus, the accompanying localised strain gradients will initiate damage more readily at a lower initiation load. In both cases, as is evident in Figure 4-11, there is appreciably more interlaminar damage in the patch with no plug present, i.e., 1365 mm^2 for a patch diameter of 55 mm and 1252 mm^2 for a patch diameter of 65 mm, compared

to that in (a) the pristine panel, i.e., 681 mm^2, and (b) the patch-repairs containing a plug, see Figure 4-8. For the patch repairs containing no plug, then Figure 4-11 shows that the delaminations in the patch extend to, and overlap very slightly, the edge of the hole in the parent CFRP, as defined by the white-dashed line. The parent CFRP surrounding this white-dashed line supports the patch repair and inhibits further delaminations. C-scans were also taken from the rear face of the repair panels on the parent CFRP and, again, these tests revealed that there was no delamination damage in the parent CFRP composites.

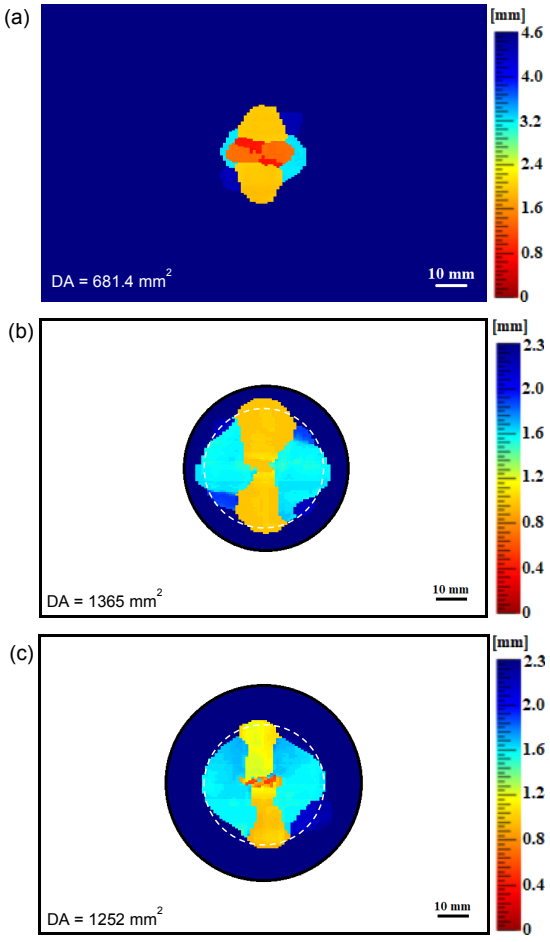

Figure 4-11. C-scan images taken from the top (impacted) face after a 7.5 J impact for: (a) the pristine QIT CFRP panel (of thickness, t, of 4.58 mm), (b) the 55 mm patch-repair panel (of patch thickness, 0.5t, of 2.29 mm, with no plug) and (c) the 65 mm patch-repair QIT CFRP panel (of patch thickness, 0.5t, 2.29 mm, with no plug). The thickness, t. of the parent QIT CFRP was 4.58 mm. (The white-dashed line represents the 40 mm diameter hole that was initially cut out in the parent panel).

4.3.4 Effect of varying the patch thickness, with no plug present

Another variable for the repair patch was the patch thickness. Two different thicknesses were studied with no plug present and the thicknesses, 0.5t, used were 2.29 and 4.58 mm, with the parent composite always having

a thickness, t, of 4.58 mm. The patch diameter chosen for this study was 65 mm and neither of the repaired panels had a plug inserted into the machined hole. The panels were impacted at an energy of 7.5 J.

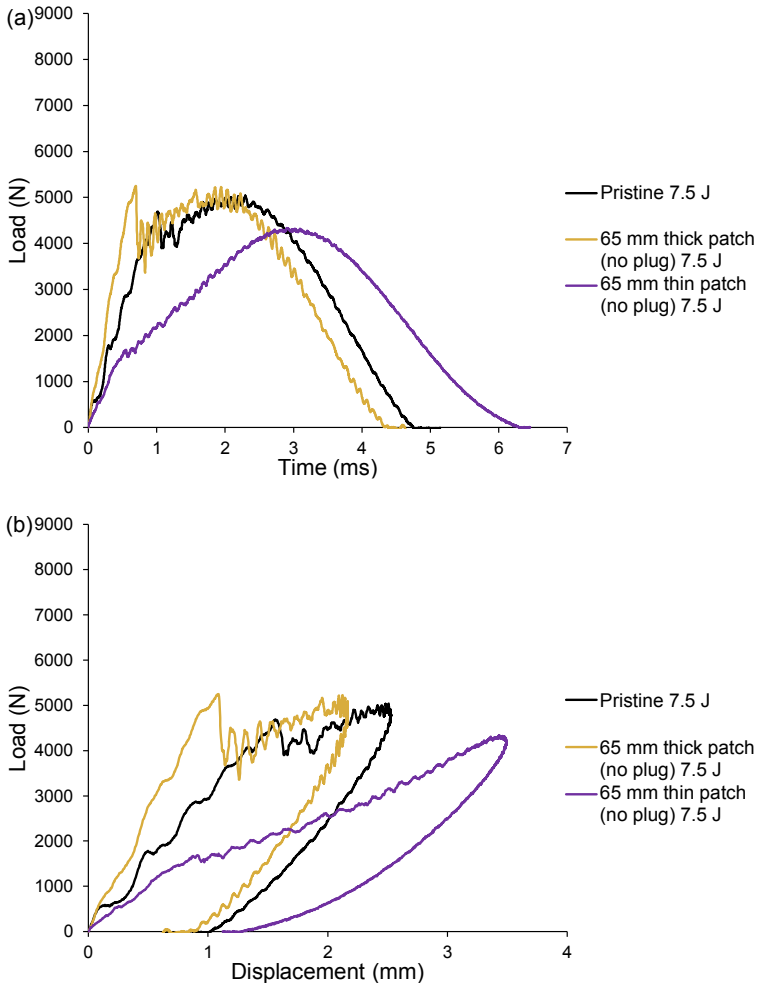

Figure 4-12. Load traces for a pristine panel, a 65 mm patch-repair QIT CFRP panel (of patch thickness, t, of 4.58 mm, with no plug) and a 65 mm patch-repair QIT CFRP panel (of patch thickness, 0.5t, of 2.29 mm, with no plug). Both patch-repair panels were impacted at 7.5 J. Shown are the: (a) load versus time traces and (b) load versus displacement traces.

Figure 4-12 shows the load versus time, and load versus displacement, traces for both the thicker patch (thickness, t, of 4.58 mm) and the thinner patch (thickness, 0.5t, of 2.29 mm) repair panels, all with a patch diameter of 65 mm and with no plug present, compared to a pristine panel. It can be seen that, with a thick patch and no plug, the loading response is very similar to that of the pristine CFRP panel. In contrast, the thinner patch results in a lower stiffness and a peak (i.e., maximum) load of around 1000 N less than both the pristine and thick patch-repair panels. For the thick patch, i.e., t = 4.58 mm, the initiation load is 5249 N at a time of approximately 0.7 ms and for a thin patch, i.e., 0.5t = 2.29 mm, the initiation load is 1689 N at a time of approximately 0.6 ms. For comparison, the initiation load for a pristine sample is 4693 N at a time of 1 ms. In

these patch-repair panels, the thin patch, when it is not supported by a plug, deforms more easily and the localised strain gradients will initiate damage more readily at a lower initiation load. The thick patch adds additional material to the parent panel and, in so doing, increases the stiffness and raises the corresponding initiation load. This is clearly very beneficial when no plug is present. The thick patch-repair panel suffers the largest drop in the load after damage initiation, which is possibly due to its relatively higher stiffness. On the other hand, the repair panel using the thinner patch does not exhibit any significant load drops, although there is a slight change in the gradient of the load versus time, and load versus displacement, traces which are indicative of damage initiation at 1689 N. This lower damage initiation load for the panel repaired using the thinner patch is most likely due to the reduction in stiffness from having a thinner patch and no plug present.

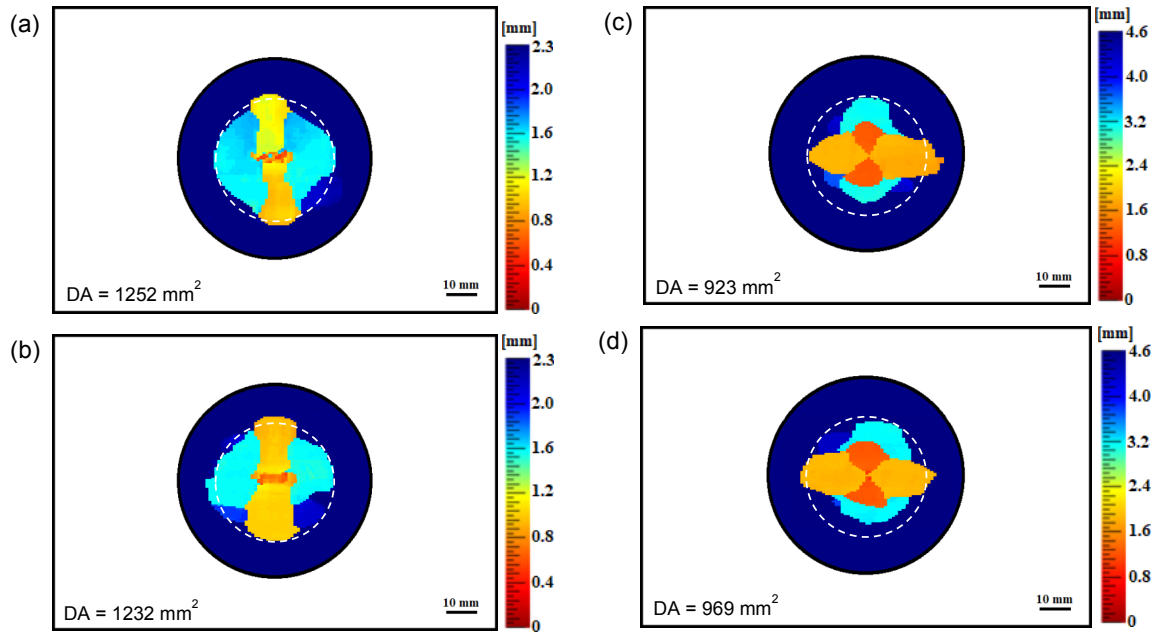

Figure 4-13. C-scan images of patch-repair QIT CFRP panels with no plugs taken from the top (impacted) face after a 7.5 J impact for: (a) the 65 mm thin (0.5t = 2.29 mm) patch repair – Test 1, (b) the 65 mm thin (0.5t = 2.29 mm) patch repair – Test 2, (c) the 65 mm thick (t = 4.58 mm) patch repair – Test 1, and (d) the 65 mm thick (t = 4.58 mm) patch repair – Test 2. (Tests 1 and 2 are duplicate tests. The white-dashed line represents the 40 mm diameter hole that was initially cut-out in the parent panel).

The C-scan images from these tests are shown in Figure 4-13, with the damage area in all four panels extending up to, and overlapping very slightly, the edge of the 40 mm diameter hole in the parent CFRP beneath the patch, which of course contains no plug in these panels. These images demonstrate that, although both the thin and thick patches have damage areas that exceed what was recorded in the pristine panels, the thicker patch gives an area of around 300 mm^2 smaller than the thinner patch. This implies that doubling the patch thickness improves the repair performance due to an increase in the stiffness of the repaired panel. C-scan

images were also taken for the entire thickness, i.e., for the patch and parent panel together, as well as from the rear face, to see if damage was present within the parent laminate or solely the patch. From these C-scan tests, yet again, no damage could be seen in the parent CFRP at all in the patch-repair panels, and so it was concluded that the damage was confined to the patch alone.

4.3.5 Comparing patch repairs with and without a plug present

The final study in this paper was to compare firstly the addition of a plug in the patch-repair panels versus the patch-repair panels without a plug, using the pristine panel as a baseline. All tests were conducted at an impact energy of 7.5 J. For this study, patches, with diameters of 55 and 65 mm, of half the thickness, 0.5t, of 2.29 mm of the parent material were used. The load versus time, and load versus displacement, traces are shown in Figure 4-14. These results reveal that the presence of a plug increases the stiffness and hence the load before damage initiation of the repaired panel occurs. On the other hand, thin patch-repairs of 0.5t = 2.29 mm, for both the 55 and 65 mm diameter patches, with no plug present, result in the lowest, and least well defined, load drops at the initiation of damage in the repaired panels, i.e., of 1771 N and 1689 N, respectively. In cases where the load drop was less significant, i.e. least well defined, the change in gradient of the load time curve was used to determine the point at which damage initiated. Further, a thin patch-repair (of thickness, 0.5t, = 2.29 mm) panel, for both 55 and 65 mm diameter patches, with a plug present, results in the highest values of the peak loads of 7550 N (for the 55 mm patch) and 7880 N (for the 65 mm patch), and these designs of repair clearly provide very impact-resistant repaired panels. Secondly, a 65 mm diameter patch of thickness, t = 4.58 mm, with no plug present, results in a load drop which is well defined at 5249 N. The behaviour here is similar to that of the pristine panel with a load drop at 4693 N.

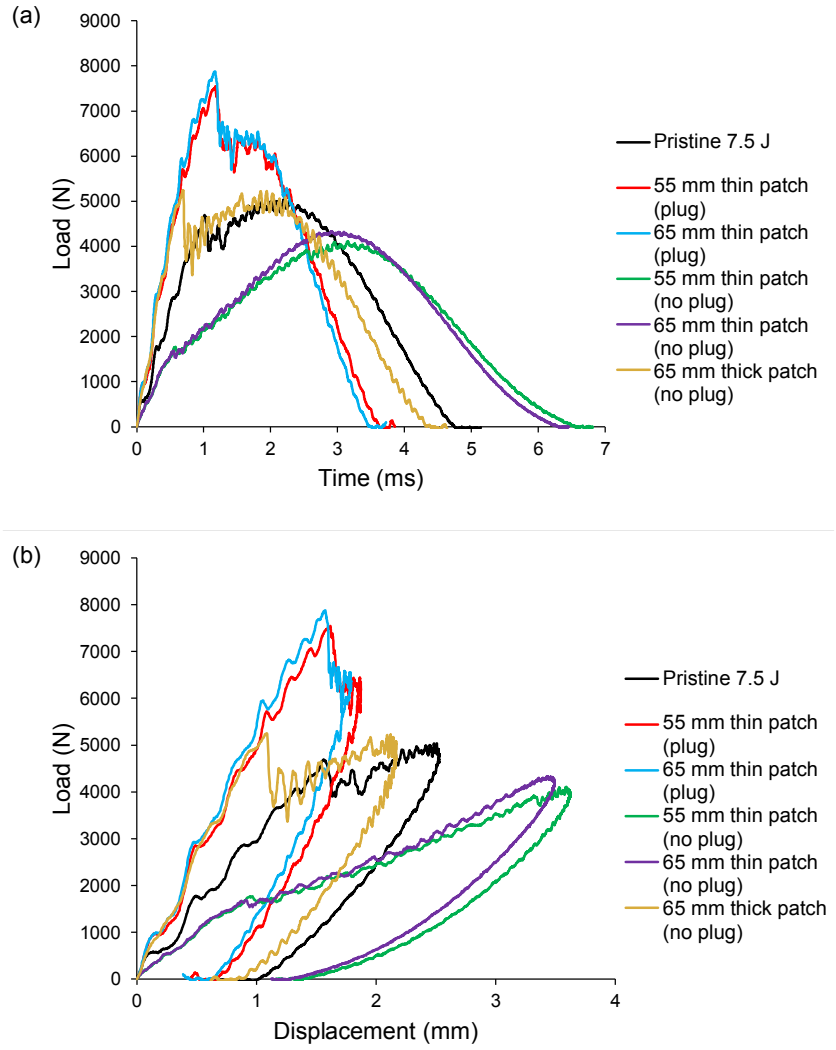

Figure 4-14. Load traces for the pristine panel, the 55 mm diameter thin (0.5t = 2.29 mm) patch-repair panel with a plug, the 65 mm diameter thin (0.5t = 2.29 mm) patch-repair panel with a plug, the 55 mm thin (t = 2.29 mm) patch-repair panel with no plug, the 65 mm thin (0.5t = 2.29 mm) patch-repair panel with no plug and the 65 mm thick (t = 4.58 mm) patch-repair panel with no plug. All impacted at 7.5 J: (a) load versus time traces and (b) load versus displacement traces.

Figure 4-15 shows the C-scan images taken of the four panels, as viewed from the top face of the panels. For both the 55 mm and 65 mm diameter patches, with no plug present, the damage area increases over six-fold compared to similar patch repairs but with a plug present. This again demonstrates that the presence of the plug is very beneficial to the impact performance of the repaired panel for both diameters of patch.

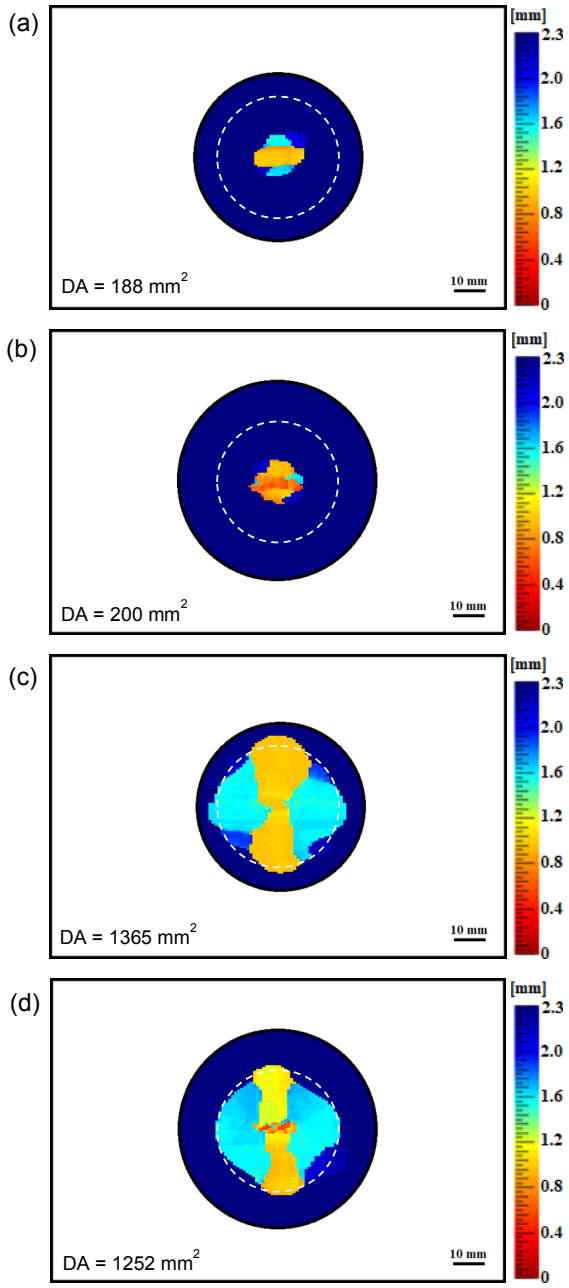

Figure 4-15. C-scan images of patch-repair QIT CFRP panels taken from the top (impacted) face after 7.5 J impact for: (a) the 55 mm diameter thin (0.5t = 2.29 mm) patch-repair CFRP panel with a plug present, (b) the 65 mm diameter thin (0.5t = 2.29 mm) patch-repair QIT CFRP panel with a plug present, (c) the 55 mm diameter thin (0.5t = 2.29 mm) patch-repair QIT CFRP panel with no plug present and (d) the 65 mm diameter thin (0.5t = 2.29 mm) patch-repair QIT CFRP panel with no plug present. (The white-dashed line represents the 40 mm diameter hole that was initially cut out in the parent panel).

4.3.6 Discussion

The repair results are summarised in Table 4-1, which gives the initiation load and time, peak (i.e., maximum) load, maximum displacement and damage area for all the pristine and patch-repair CFRP panels tested under a single impact at an energy of 7.5 J.

Table 4-1. Measured impact behaviour of the pristine and patch-repair QIT CFRP panels, with all panels impacted at 7.5 J.

Panel and test number		Drop-weight traces				Damage area (mm^2)		Variation in damage area
		Damage initiation load (N)	Damage initiation time (ms)	Peak load (N)	Max. displacement (mm)	Patch	Plug	
Pristine (first impact)		4693	1.0	5040	2.4	681		-
Diameter 55 mm Patch (with plug) Thin (2.29 mm)		7550	1.2	7550	1.8	188	450	-
Diameter 65 mm Patch (with plug) Thin (2.29 mm)		7880	1.2	7880	1.7	200	542	-
Diameter 55 mm Patch (no plug) Thin (2.29 mm)	1	1771	0.6	4106	3.4	1365	-	±6.8%
	2	1785	0.6	4078	3.4	1191	-	
Diameter 65 mm Patch (no plug) Thin (2.29 mm)	1	1689	0.6	4335	3.3	1252	-	±0.8%
	2	1717	0.6	4200	3.4	1232	-	
Diameter 65 mm Patch (no plug) Thick (4.58 mm)	1	5249	0.7	5249	2.1	923	-	±2.4%
	2	5362	0.7	5362	2.1	969	-	

Patch-repair panels without a plug were manufactured and tested using duplicate specimens, employing an impact energy of 7.5 J, and the results from these duplicate patch-repair panels are shown in Table 4-1. Firstly, all the measured impact properties are seen to be in good agreement from the two tests, i.e., for Test 1 versus Test 2, for each type of repair with no plug present. To further illustrate this point, the variation in the damage area was calculated between each pair of panels. The percentage variation in the values of the measured damage area is found to be ±6.8%, ±0.8% and ±2.4% for the 55 mm thin patch, 65 mm thin patch and 65 mm thick patch-repair panels respectively, see Table 4-1. The very good agreement in the measured impact load traces, and the low degree of variation in the comparative values of the damage area, reveals a very good repeatability for the manufacture and testing of these patch-repair panels. Secondly, it can be seen that the panels with either plugs, or a thick patch, have relatively high values of the peak load and a lower maximum displacement than the pristine panel. However, the patch-repair panels manufactured using a plug are the only ones that produce a damage area that is significantly smaller than that of the pristine panel. Thirdly, the patch diameter does not seem to significantly affect the impact performance of repaired composites, at least for 55 mm patches compared to 65 mm patches. Fourthly, on the other hand, the patch thickness has a significant effect on the impact performance of the patch-repair composites. Both the thick patch-repair panel, with no plug, and the pristine panel had peak (i.e., maximum) load values of around 5000 N, compared with the thinner patch, with no plug, that had a peak load value of approximately 1000 N lower. This indicates that the thick

patch results, in terms of impact properties, are very similar to that of a pristine panel. Furthermore, the average damage area between two panels with the thinner patch was 296 mm^2 larger than the average of the two thicker patch-repair panels, demonstrating the superior impact properties of a repair with the thicker patch. Since only half-thickness and full-thickness patches were considered in this research, it is unclear whether the optimum patch thickness is the same thickness as the original parent CFRP, or whether it would fall somewhere between these two values. Finally, the inclusion of a CFRP plug, to fill the hole created by the removal of the damaged material in the parent CFRP, (a) resulted in a reduction in the damage area of over 1000 mm^2 in the patch, (b) increased the maximum load by around 3500 N and (c) almost halved the maximum displacement. These results therefore show that both the patch thickness and the addition of a plug are repair design features that significantly influence the impact performance of the repaired panel, with the latter feature having the largest effect of all three design variables that were considered.

Thus, when considering the peak load, the maximum displacement and the damage area, the panels repaired with the presence of a plug exhibited an impact performance significantly better than that of the pristine panel, implying that using a thin patch and a plug is the most effective patch repair technique investigated in this paper. An alternative would be to use a thicker patch without a plug, as this gives load traces similar to that of the pristine panel and results in peak load and maximum displacement values greater than those of the pristine panel. A further benefit to this alternative technique is that the initial damage does not have to be cut out before the repair is undertaken, thereby reducing the repair time and the risk of inducing further damage during machining. However, when superior impact properties are required, such as for a critical component, the removal of the initial damage and the inclusion of a plug would be beneficial since this design of repair was seen to restore the impact performance to that of a pristine panel. Additionally, it should be noted the use of a relatively thicker patch would likely result in inferior aerodynamic performance, thus making a thin patch with the inclusion of a plug a potentially more suitable repair technique.

5 Experimental study on the effect of impact location on repaired cross-ply CFRP panels under low-velocity impact loadings

5.1 Introduction

As explained throughout this thesis, the impact resistance of materials for aerostructures is critical due to the numerous impact events an aircraft is subjected to in its life. The residual strength of carbon fibre reinforced polymer composite materials is greatly reduced after an impact event and the risk of failure due to fatigue is increased [1]. When a panel has been previously damaged, the chance that the centre of the repair will be where a second impact occurs is extremely unlikely. For this reason, impacts offset from the repair must also be considered.

From previous research [48,49], it has been shown that the weakest part of the repair is not the centre but instead a point offset from it. Liu et al. considered scarf repairs and found the weakest part of the repair was the adhesive join between the parent panel and the repair [48]. Whereas Hou et al. impacted patch repairs and found that the part of the repair most susceptible to damage and that gave the largest damage area was 20 mm from the centre of the patch, which was on the parent panel rather than the patch [49]. There is limited research in this area, but these sources demonstrate that it is critical to consider offset impacts when testing a repair configuration for its suitability.

In this section, pristine and patch repaired cross-ply CFRP panels are impacted to consider the effect of impact location on the response of the panels. There are five repair cases considered: a pristine panel with a central patch; a central patch repair with a plug; a central patch repair without a plug; an offset patch repair without a plug with the impact site being on the patch and at the edge of the cut-out; and an offset patch repair without a plug with the impact site being 15 mm from the edge of the hole. All impacts were in the centre of the panel, with the offset cases having the cut-out to one side, and an impact energy of 7.5 J was used. Load versus time and load versus displacement traces are measured from the impact tests and detailed maps of the resultant interlaminar damage of the various panels are also obtained, allowing the effect of impact location to be considered and the weakest part of the repair to be identified.

5.2 Test specification and methods

5.2.1 Repairing samples

The panels used for the testing in this section were manufactured according to the method in Section 3.3. The cross-ply lay-up used for a pristine panel was $[0_2/90_2]_{2s}$, with the 0° plies being aligned with the long edge of the panel. The dimensions of a pristine panel are shown in Figure 5-1 (a).

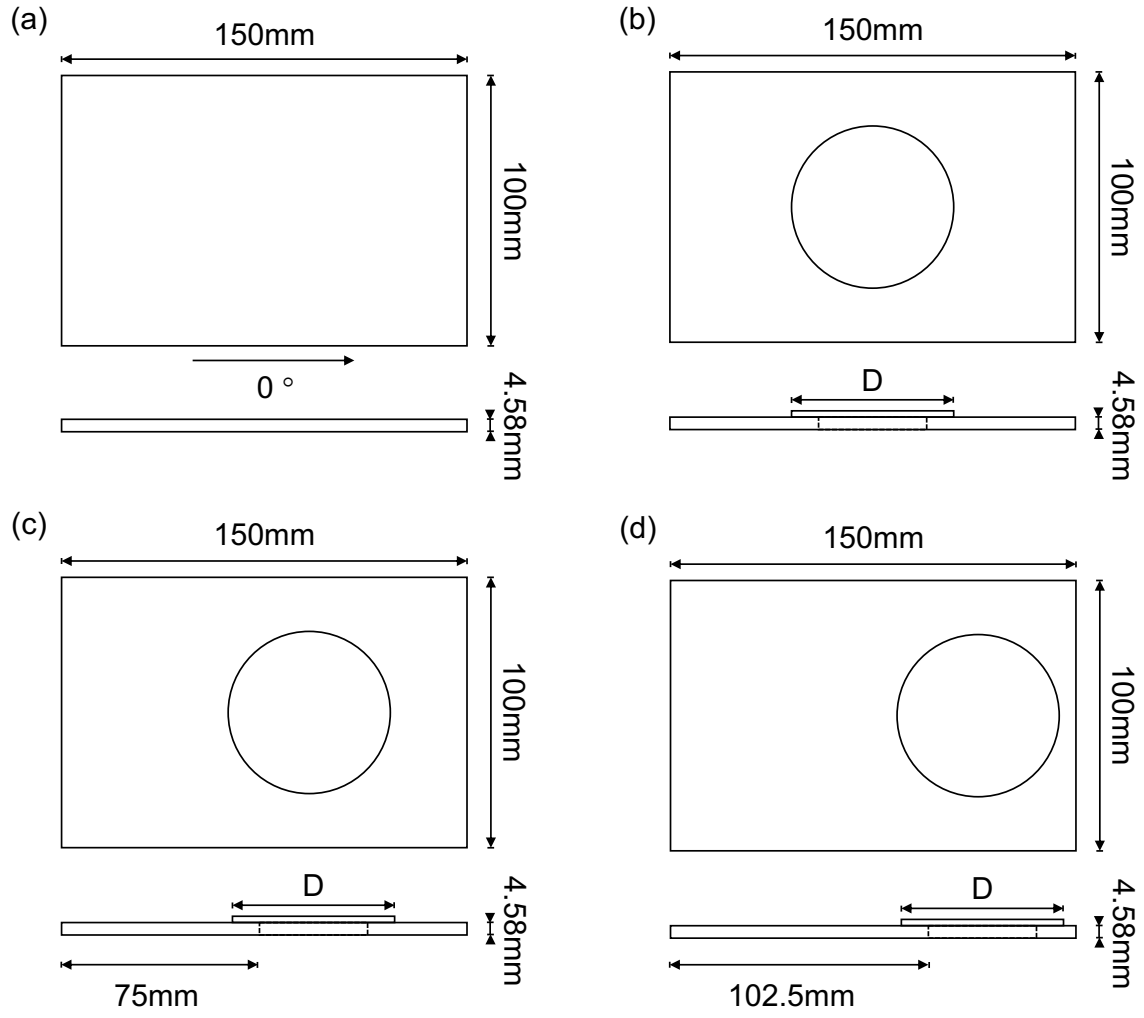

Figure 5-1. Plan- and side-views of (a) the pristine panel, (b) the central patch-repair panel, (c) the edge of hole patch-repair panel and (d) the 15 mm offset patch-repair panel.

The panels were repaired by removing a 30 mm diameter disk of material and adhering a 55 mm diameter patch over the subsequent hole. The patches were cut from half thickness, cross-ply material that had a lay-up of $[0/90]_{2s}$. In one case, no material removal was performed as the repair case was a patched pristine panel. Additionally, another repair case included a plug of parent material being implemented to fill the 30 mm

diameter hole left from the material removal. In the offset repair cases, the centre of the hole was offset by 15 and 42.5 mm for the edge of hole impact and the 15 mm offset impact cases, respectively. A diagram of the central repair case is shown in Figure 5-1 (b) and the offset repair cases are shown in Figure 5-1 (c) and (d).

5.2.2 Drop weight testing

The pristine and repaired panels were tested under low-velocity impact conditions using the Instron 9340 drop-weight tower shown in Figure 3-5 in Section 3.4.1, where the test method is described in detail. For these impacts, a 16 mm diameter, stainless steel, round-nosed impactor with an overall mass of 5.265 kg was implemented and impacts were performed at an energy of 7.5 J, with a corresponding impact velocity of 1.69 $m.s^{-1}$.

After impact, the panels were inspected using the Prisma portable ultrasonic C-scanner shown in Figure 3-6 in Section 3.4.2 to determine the size of the damage area.

5.3 Experimental results

5.3.1 Pristine samples

Repeat, i.e. multiple, impacts were performed on pristine panels, with two successive impacts at three different impact energies: 7.5, 15 and 30 J. This testing demonstrates what might happen if damage is left unrepaired and a second impact event occurs. Figures 5-2, 5-3 and 5-4 show the load versus time and load versus displacement traces for each of these impact energies.

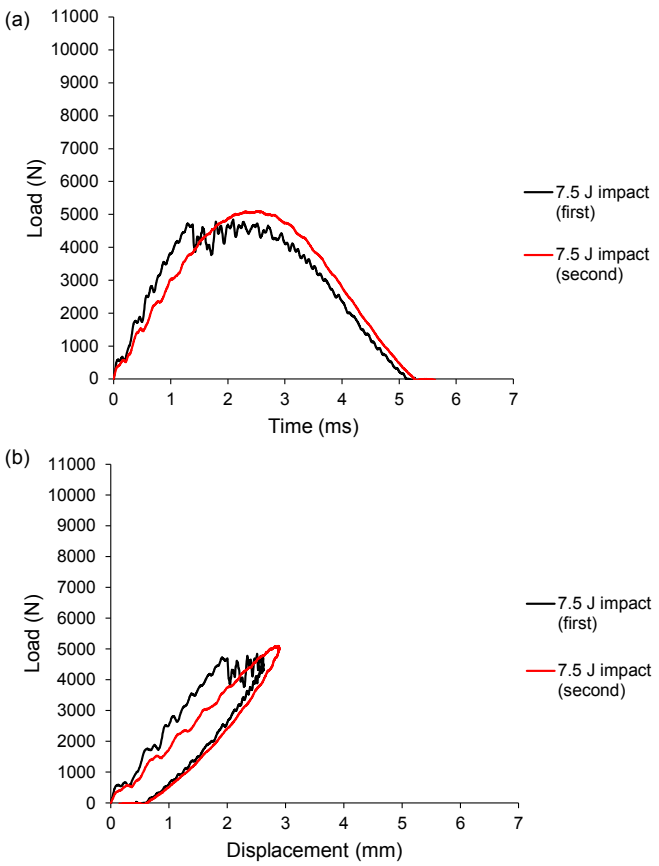

Figure 5-2. Load traces for repeated, i.e., multiple, impacts on a pristine cross-ply CFRP panel at 7.5 J: (a) load versus time traces and (b) load versus displacement traces.

Figure 5-2 shows the load versus time and load versus displacement traces for a pristine cross-ply CFRP panel impacted twice at 7.5 J, with the black and red lines showing the first and second impacts, respectively. During the first impact event, damage initiation occurs at 4727 N, which is demonstrated by the drop in load and change in gradient at this point. Contrastingly, there is not an obvious load drop or change in gradient for the second impact. This suggests that no new damage modes are introduced and any difference in the damage area comes from a propagation of the damage caused by the first impact rather than damage initiating. Additionally, the peak load value is higher for the second impact, which occurs due to the damage initiated during the first impact allowing it to absorb more energy due to an increased flexibility. This is also shown by the increase in displacement from the first impact event to the second.

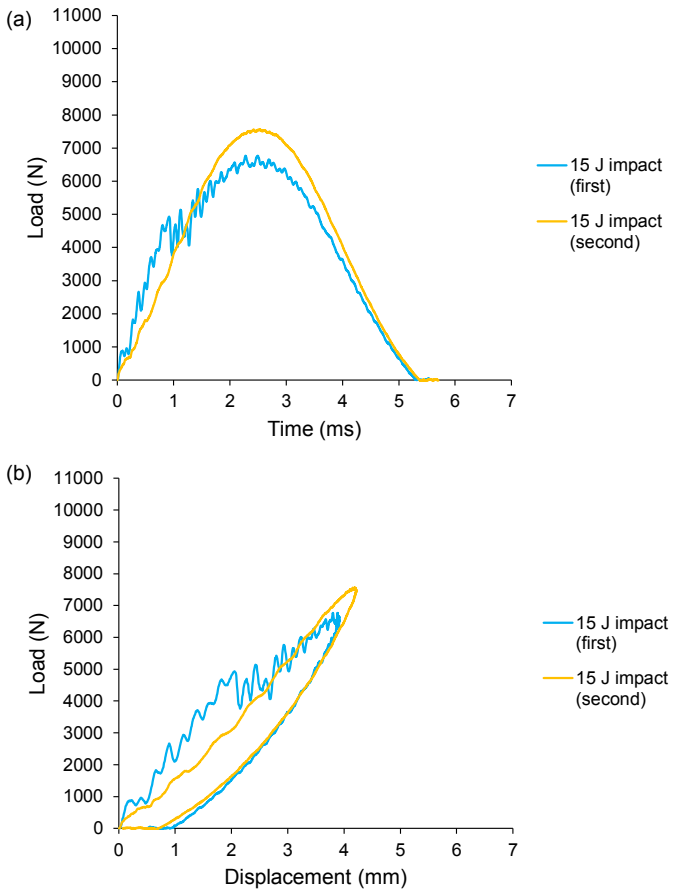

Figure 5-3. Load traces for repeated, i.e., multiple, impacts on a pristine cross-ply CFRP panel at 15 J: (a) load versus time traces and (b) load versus displacement traces.

Similarly, Figure 5-3 shows the load versus time and load versus displacement traces for repeat impacts at 15 J and the same trend as at 7.5 J is observed in this case. During the first impact event, damage initiation again occurs at ca. 5000 N, which suggests that this load value is the limit for no damage to occur in this panel. In this case, the damage initiation time is just under 1 ms, while it was just over 1 ms for the 7.5 J impact, implying that an increase in impact energy causes the damage initiation to occur sooner. As was seen previously, the second impact demonstrates no clear damage initiation, but instead implies propagation of the existing damage through the panel. Although significantly larger than 7.5 J, 15 J is still a relatively low impact energy and so to continue this investigation some repeat impacts were performed at 30 J.

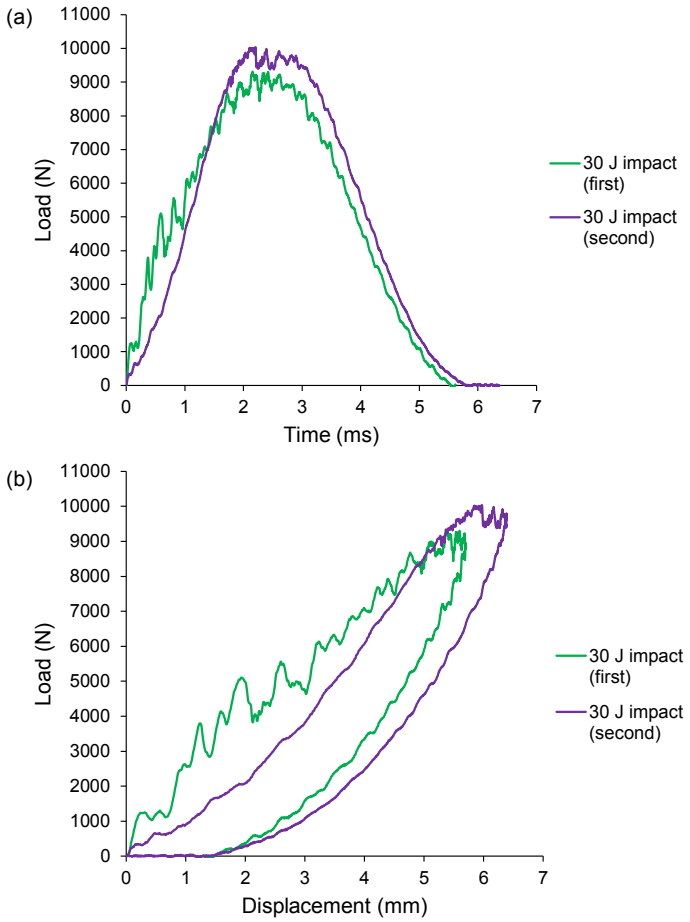

Figure 5-4. Load traces for repeated, i.e., multiple, impacts on a pristine cross-ply CFRP panel at 30 J: (a) load versus time traces and (b) load versus displacement traces.

At 30 J, the force time and force displacement traces are slightly different than for the lower impact energies, which can be seen in Figure 5-4. In this case a clear load drop followed by oscillations, indicative of damage initiation, occurs at around 5000 N for the first impact, which follows the same trend observed at the lower energies, but in this case it happens at a time of roughly 0.5 ms. However, the main difference between the 30 J impacts and the 7.5 and 15 J impacts is that, during the second impact event, damage initiation occurs at around 10000 N, demonstrated by a clear load drop. This suggests that the second impact doesn't just propagate the existing damage but instead causes new damage mechanisms to be introduced in the panel.

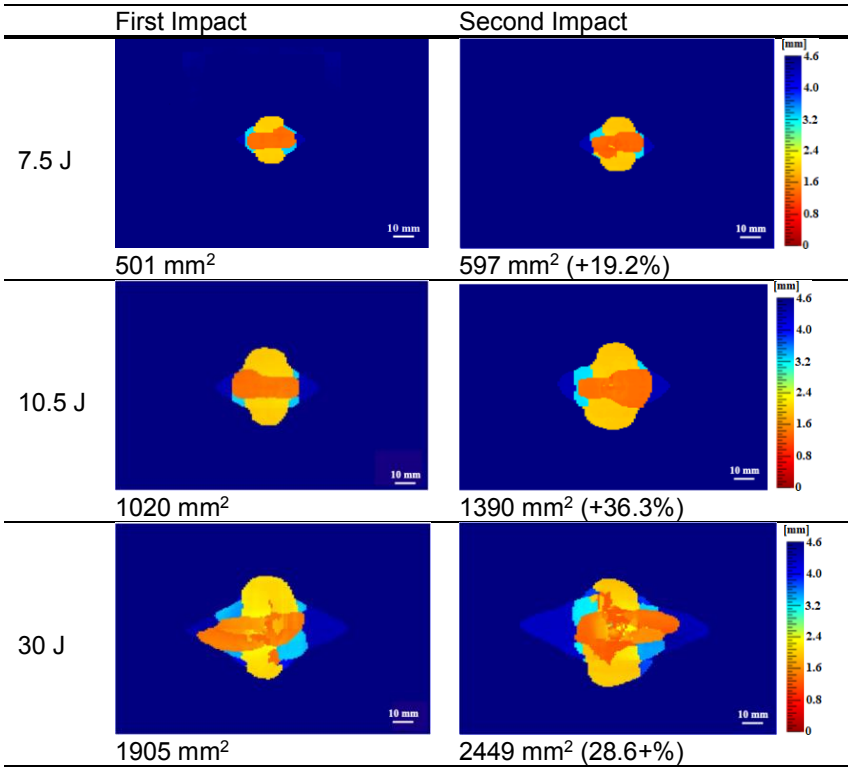

Figure 5-5. C-scan images taken from the top (impacted) surface for repeated, i.e., multiple, impacts on pristine cross-ply CFRP panels at various impact energies. (The scales show the depth of the different locations of the interlaminar damage. The percentage value, in brackets, is relative to the preceding impact).

The C-scans after each of the impacts are shown in Figure 5-5 above and, as explained in Section 4.3.1, the scale bar to the right demonstrates the depth within the panel that the interlaminar damage occurs, with dark blue being nearest the rear surface through to red which is the top surface. The scans demonstrate a significant increase in the damage area after the second impact in each case, with an average increase of 28%. From this testing, it was decided that a 30 mm diameter hole would be cut from pristine parent panels as this would encompass the entirety of the damage from a 7.5 J impact and therefore act as a representation of damage or damage removal when assessing the effectiveness of repair techniques. Additionally, using a slightly smaller hole than used in the previous section allows for a larger offset distance without introducing edge effects.

5.3.2 Pristine patched versus patch repair with plug

The first repair configurations that were considered were a pristine panel with a patch adhered on the top surface and a central repair with a plug of the same parent cross-ply CFRP. The force time and force displacement traces are shown in Figure 5-6 below, as well as that of a pristine panel to allow for comparison.

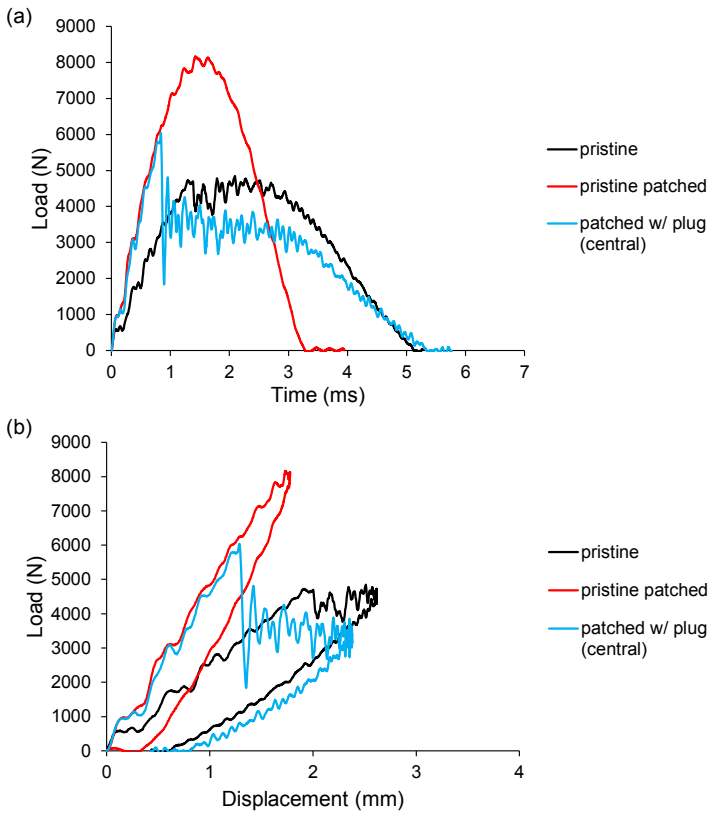

Figure 5-6. Load traces for a pristine cross-ply CFRP panel and pristine patched and central plugged repair panels, impacted at 7.5 J. The thickness, t, of the parent and the plug cross-ply CFRP was 4.58 mm and the thickness, 0.5t, of the patch was 2.29 mm. Shown are the: (a) load versus time traces and (b) load versus displacement traces.

Both the repair configurations have a steeper gradient compared to the pristine panel in the traces above, which shows that the stiffness is increased and this is likely due to the effective thickness being greater at the impact site, in both cases being 1.5t instead of 1t for the pristine panel. In the pristine patched case, shown by the red line in Figure 5-6, a maximum load of 8165 N was reached with no clear load drop or change in gradient, which suggests that no damage initiated within the panel from the impact. In contrast, the plugged repair case, shown by the blue line, had a maximum load value of 6041 N, which is closer to the pristine panel maximum load of 4846 N. This, as well as the significant drop in load at this point, implies that dislodgement of the plug occurred at this point, leading to a significant reduction in impact strength. Four samples with a central plugged repair were tested in total, all of which resulted in dislodgement of the plug. This outcome reduces the significance of any trends observed beyond the point of dislodgement, meaning the only clear conclusion to be drawn from these results is that both the pristine patched and central plugged repair cases are much stiffer than the pristine panel. To investigate the damage in each case, specifically the dislodgement for the plugged repair, the optical microscope was utilised and the images from this are shown in Figures 5-8 and 5-9 below.

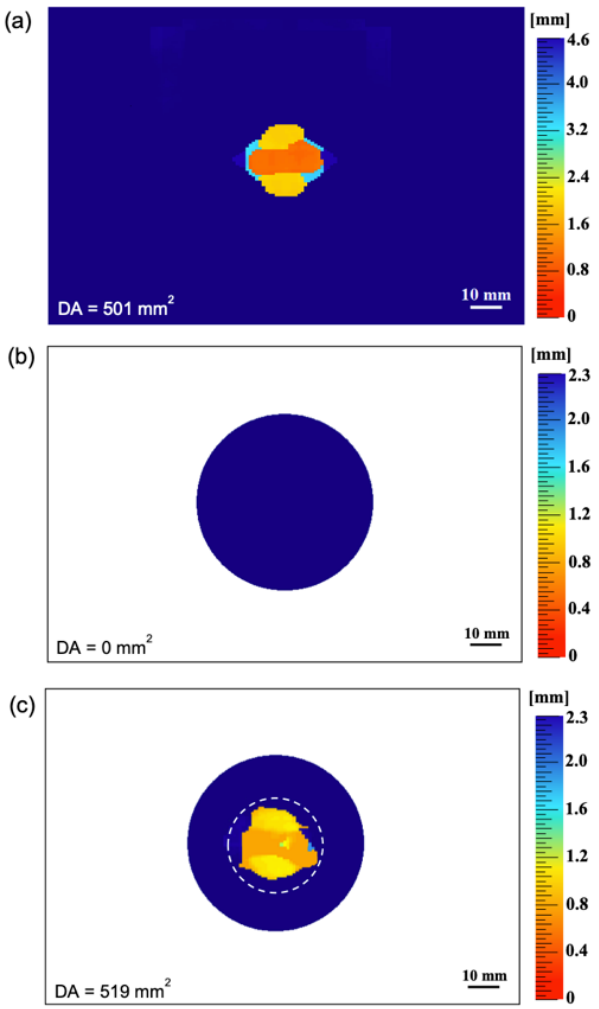

Figure 5-7. C-scan images taken from the top (impacted) face after a 7.5 J impact for: (a) the pristine cross-ply CFRP panel (of thickness, t, of 4.58 mm), (b) the pristine patched cross-ply CFRP panel (of patch thickness, 0.5t, of 2.29 mm) and (c) the central patch-repair cross-ply CFRP panel (of patch thickness, 0.5t, 2.29 mm, with a plug). The plug was 4.58 mm thick, i.e., the same thickness as the parent cross-ply CFRP. (The white-dashed line represents the 30 mm diameter hole that was initially cut out in the parent panel).

Figure 5-7 shows the damage areas in the pristine panel as well as in the patches of the pristine patched and central plugged repair panels, with the parent panel for the two repairs not being shown as there was no damage for the pristine patched case and the dislodgement in the central plugged repair case meant scanning of the rear surface was not possible. It can be seen from these scans that there was more damage in the central plugged repair than in the pristine panel, which might suggest that this repair is not entirely effective at restoring the impact properties of a damaged panel. However, this is most likely in part due to the dislodgement of the plug weakening the repair and causing the effective thickness at the impact site to reduce from 1.5t to only 0.5t during the impact event. Contrastingly, the pristine patched case has a damage area of 0 mm^2, which demonstrates that increasing the thickness by 50% at the site of the impact strengthens the material enough to withstand a 7.5 J impact and sustain no damage.

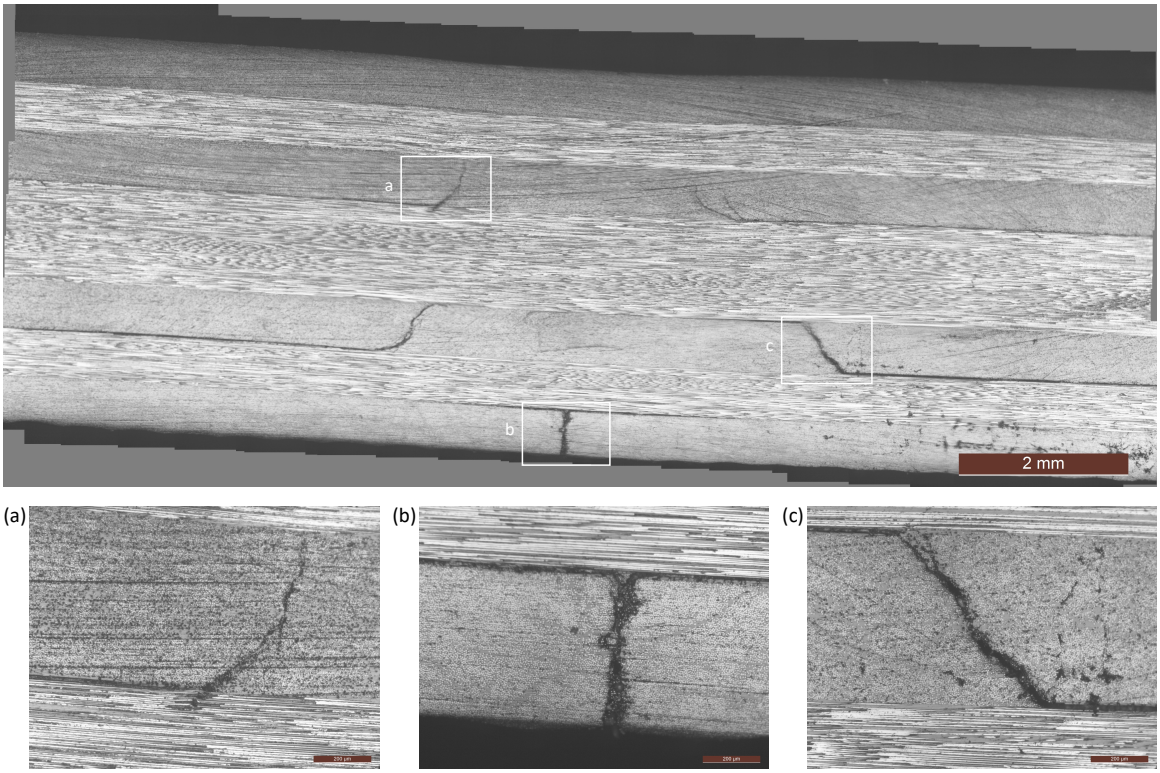

Figure 5-8. Optical microscopy images of a pristine cross-ply CFRP panel after a 7.5 J impact, with key features highlighted by white boxes shown in images (a), (b) and (c).

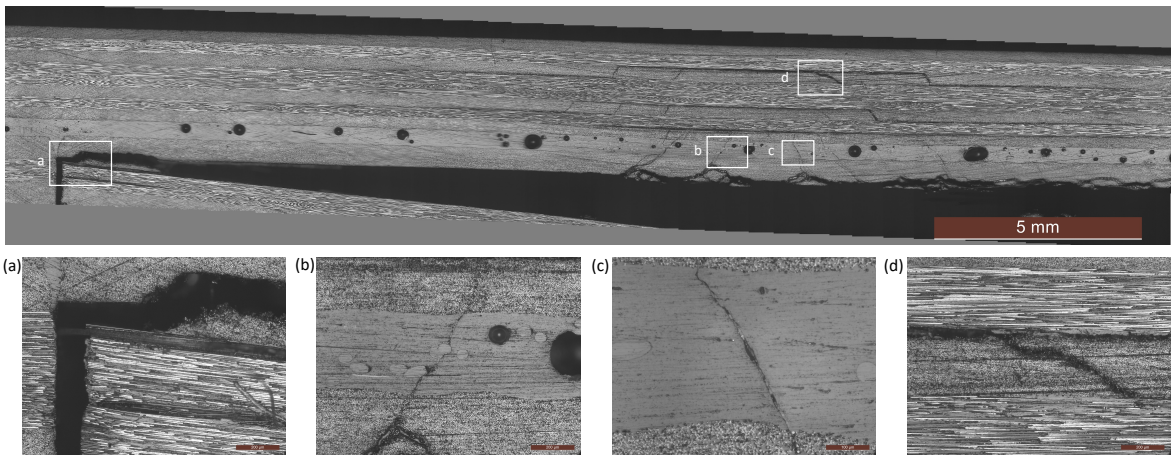

Figure 5-9. Optical microscopy images of a central patch-repair cross-ply CFRP panel with a plug after a 7.5 J impact, with key features highlighted by white boxes shown in images (a), (b), (c) and (d).

Figures 5-8 and 5-9 show the microscopy images that were taken of the impact site cross-section for a pristine panel and central patch repair panel with a plug. In Figure 5-8 (a), a kink band can be seen at the ply interface where the intralaminar damage is propagating into a delamination. Furthermore, Figure 5-8 (b) depicts the propagation of intralaminar damage through the rear ply that suggests rear face cracking has occurred during this impact event. From Figure 5-9, it can be seen that damage propagates through the plies of the repair

patch, through the adhesive and into the first ply of the repair plug, where they cause a delamination across the entirety of the plug. This demonstrates that what was thought to be dislodgement of the plug is actually extreme interlaminar damage between the first and second ply of the plug. Both figures show the expected damage evolution for this type of test, with intralaminar damage transitioning into interlaminar damage when it reaches a ply interface.

5.3.3 Effect of varying impact offset distance

To consider the effect of the impact location on the repair panel response, three configurations were tested: a central repair, a repair offset to give an impact location on the edge of the 30 mm cut out under the patch (edge of hole), and a repair offset to give location 15 mm from the edge of the patch (15 mm offset), diagrams of which can be seen in Section 5.2.1. The force time and force displacement traces of these three samples, as well as the pristine case, are presented in Figure 5-10.

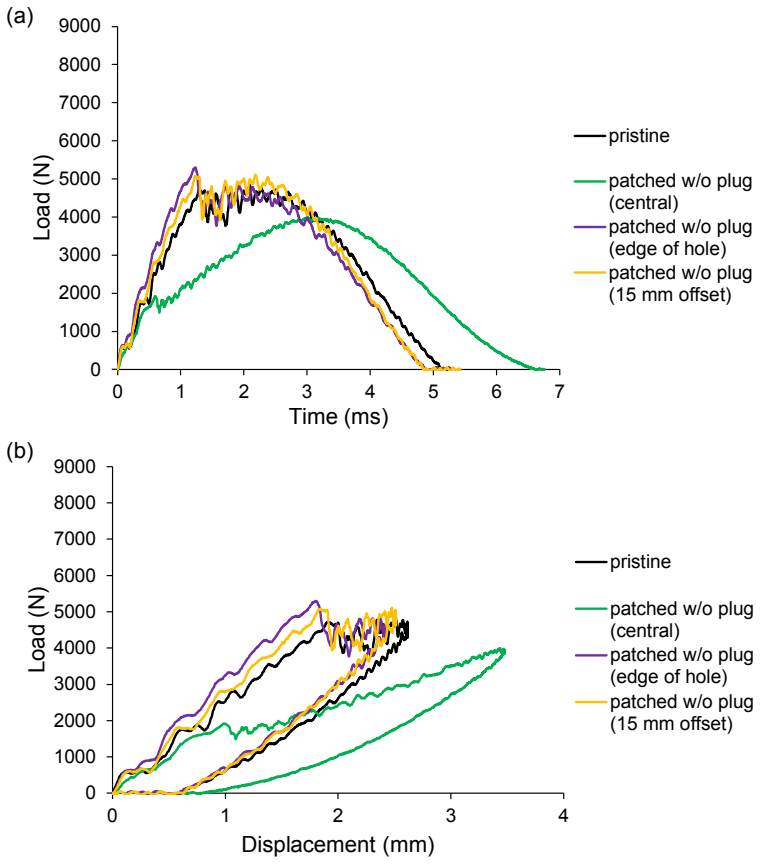

Figure 5-10. Load traces for a pristine cross-ply CFRP panel and central, edge of hole and 15 mm offset patch-repair panels, without plugs, impacted at 7.5 J. The thickness, t, of the parent cross-ply CFRP was 4.58 mm and the thickness, 0.5t, of the patch was 2.29 mm. Shown are the: (a) load versus time traces and (b) load versus displacement traces.

From the traces in Figure 5-10, it can be seen that both the offset repair cases perform similarly to the pristine sample, whereas the central repair is much less stiff and experiences a more extreme displacement upon impact, with a displacement of roughly 1 mm more than the other three panels. This is further demonstrated by the damage initiation loads and times for each of the four samples, with the central repair case having values of 1915 N and 0.6 ms compared to 4727 N and 1.3 ms, 5300 N and 1.2 ms, and 5083 N and 1.2 ms for the pristine, edge of hole offset repair and 15 mm offset repair panels, respectively. It is likely that the offset repair panels perform similarly to the pristine panel because of the effective thickness at the impact site being the same as the thickness of a pristine panel. However, although the values are very similar, the damage initiation load and stiffness slightly increase for the edge of hole offset impact and then lower again for the 15 mm offset impact, which can be seen from the steepest gradient being that of the purple line and then the gold and black lines have slightly decreasing gradients. This is likely because the edge of hole offset case has an impact site where to one side of the impactor the thickness is only that of the patch, 0.5t, and to the other side the thickness is 1.5t, resulting in similar performance to a pristine panel of thickness t but with a slight increase in stiffness. In continuation, the 15 mm offset case has the same thickness as the pristine panel, t, at the impact site but, due to the repair, that section away from the impact site is stiffer than the rest of the panel, causing a slight increase compared to the pristine panel. Lastly, the central repair case has an effective thickness of only 0.5t at the impact site, hence this repair having the shallowest gradient.

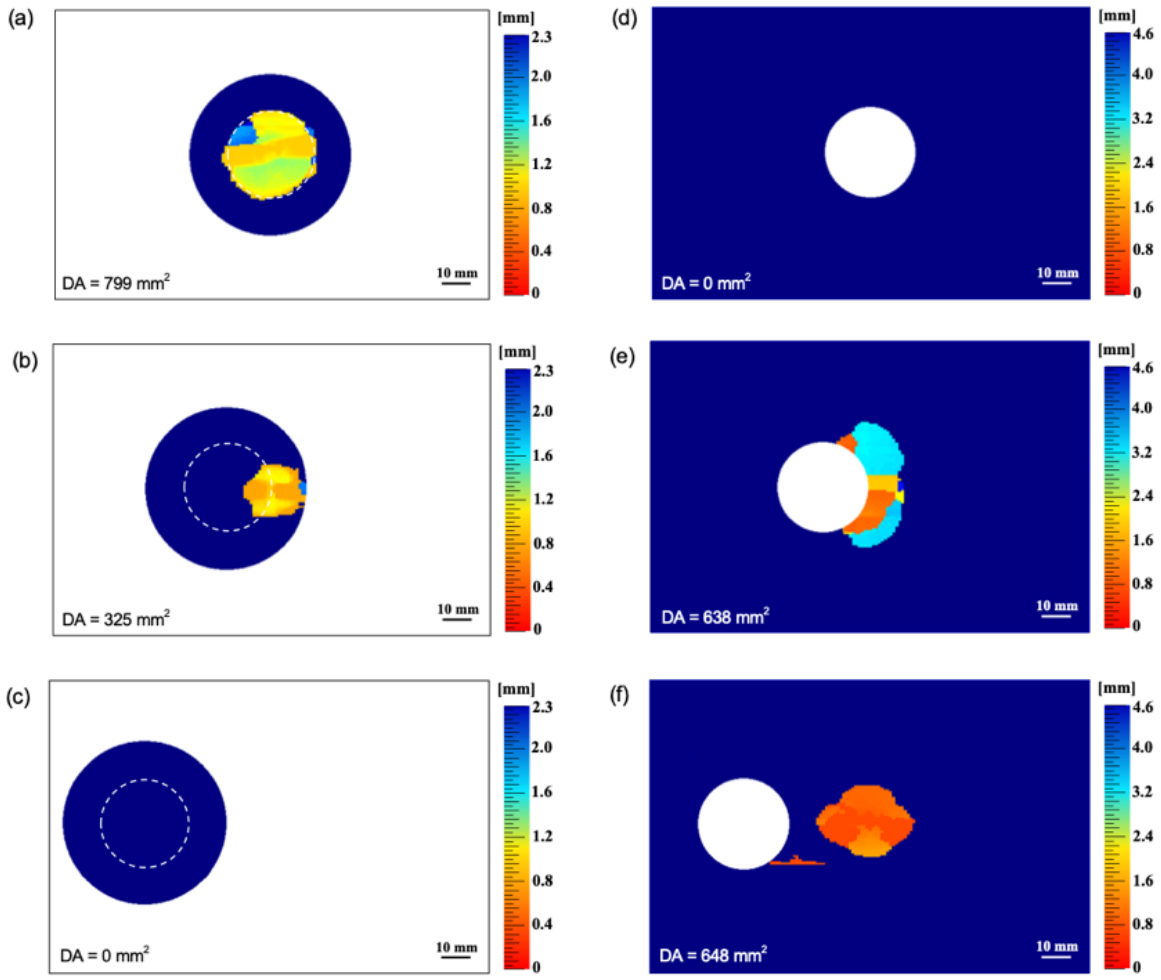

Figure 5-11. C-scan images taken from the top (impacted) face after a 7.5 J impact for: (a) the central patch-repair cross-ply CFRP panel (of patch thickness, 0.5t, 2.29 mm), (b) the edge of hole offset patch-repair cross-ply CFRP panel (of patch thickness, 0.5t, 2.29 mm) and (c) the 15 mm offset patch-repair cross-ply CFRP panel (of patch thickness, 0.5t, 2.29 mm), all without plugs. And c-scan images taken from the bottom face for the same three panels are shown in (d), (e) and (f), respectively. (The white-dashed line represents the 30 mm diameter hole that was initially cut out in the parent panel).

Figure 5-11 shows the c-scan images of the damage in both the patches and parent panels of the unplugged repair panels, demonstrating how offsetting the impact site affects the damage initiation and propagation when no plug is present. In both of the offset cases, the damage area in the parent panel is ca. 150 mm^2 less than the damage in the patch of the central repair case. However, the total damage area in both the patch and parent panel is largest for the edge of hole offset repair case, at 963 mm^2, which implies that this is the part of the repair that is the most susceptible to damage and should therefore be considered when testing other repair configurations. Additionally, although the individual damage area values are less for the offset repair cases, the damage is primarily or entirely in the parent panel, which would make further repairs challenging. However, in the central case, the patch can be removed and replaced to restore the impact properties as no damage occurred in the parent panel.

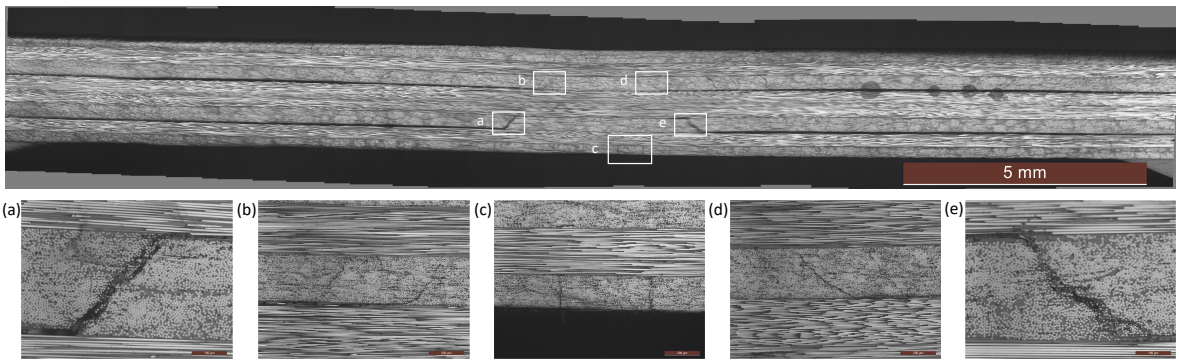

Figure 5-12. Optical microscopy images of a central patch-repair cross-ply CFRP panel without a plug after a 7.5 J impact, with key features highlighted by white boxes shown in images (a), (b), (c), (d) and (e).

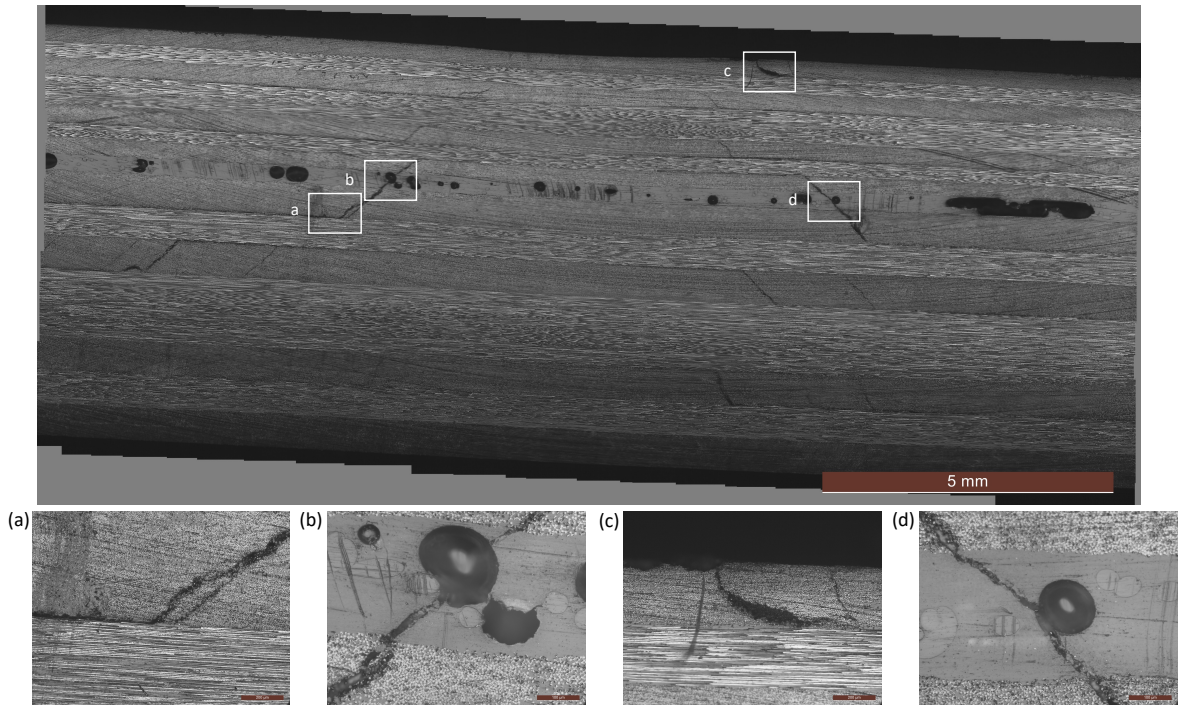

Figure 5-13. Optical microscopy images of an edge of hole offset patch-repair cross-ply CFRP panel without a plug after a 7.5 J impact, with key features highlighted by white boxes shown in images (a), (b), (c) and (d).

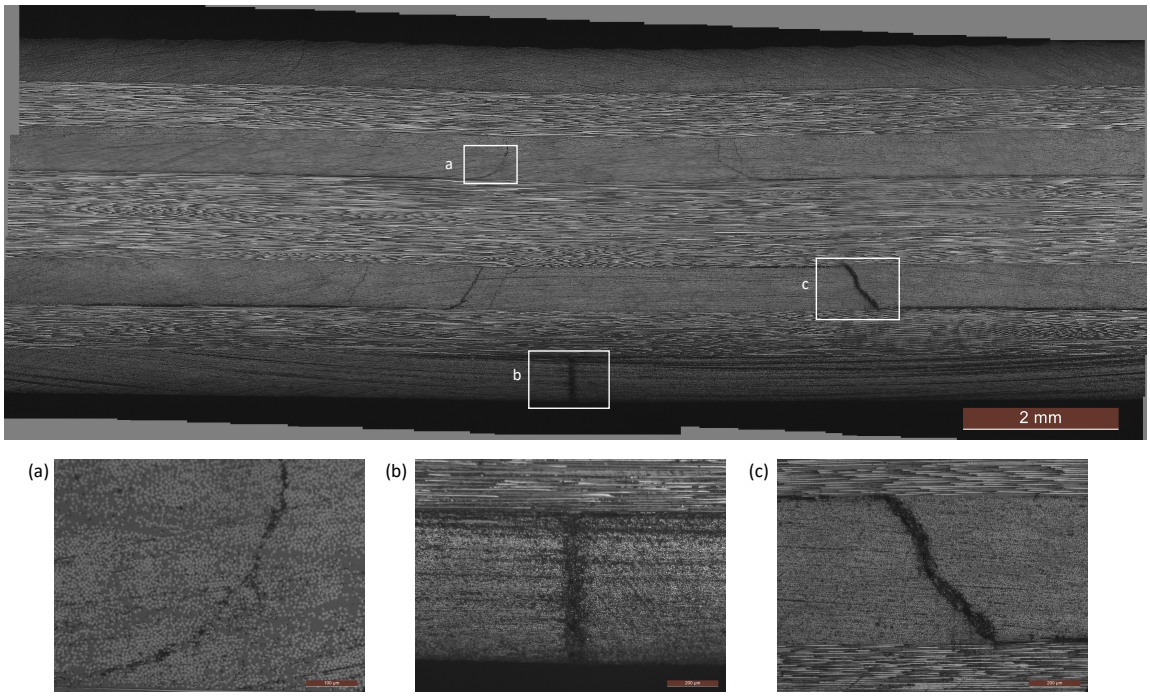

Figure 5-14. Optical microscopy images of a 15 mm offset patch-repair cross-ply CFRP panel without a plug after a 7.5 J impact, with key features highlighted by white boxes shown in images (a), (b) and (c).

Figures 5-12, 5-13 and 5-14 show the microscopy images that were taken of the impact site cross-section for a central patch repair, edge of hole offset repair and 15 mm offset repair panel without a plug. Figure 5-12 shows that the damage initiation and propagation in the patch repair panel without a plug is similar to that of a pristine panel, but the intralaminar damage in the rear ply that could lead to rear face cracking is much less prominent. This is likely due to the patch having the panel as reinforcement outside the 30 mm diameter cut out. In continuation, Figure 5-14 has essentially identical damage features to that of a pristine panel. Contrastingly, in Figure 5-13 there is no visible intralaminar damage that could lead to rear face cracking in the final two plies, demonstrating that the increased thickness at the impact site stiffens the panel to protect against this failure mechanism. However, the most significant intralaminar cracks are through the adhesive and into the first ply of the panel below, with both cracks forming around or through small voids in the adhesive. This suggests that these are areas of weakness in the repair where damage mechanisms will likely initiate.

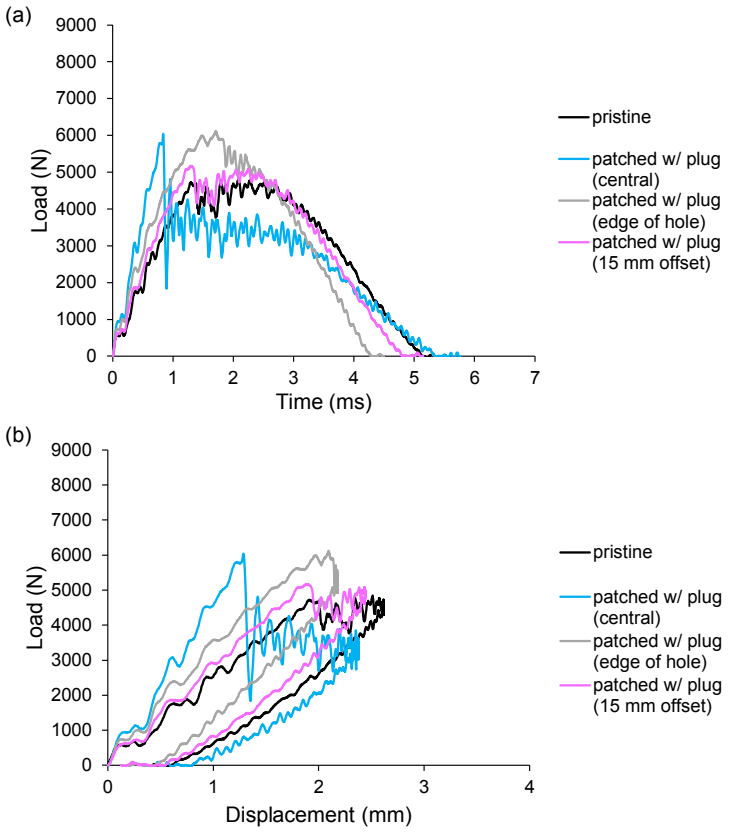

Figure 5-15. Load traces for a pristine cross-ply CFRP panel and central, edge of hole and 15 mm offset patch-repair panels, with cross-ply CFRP plugs, impacted at 7.5 J. The thickness, t, of the parent and the plug cross-ply CFRP was 4.58 mm and the thickness, 0.5t, of the patch was 2.29 mm. Shown are the: (a) load versus time traces and (b) load versus displacement traces.

The same repair configurations were tested but this time with plugs under the patches, with Figure 5-15 showing the force time and force displacement traces for these cases. Similarly to those without plugs, the edge of hole offset repair case was slightly stiffer than both the 15 mm offset repair case and pristine panel, but the damage initiation load value was significantly larger, with values of 6123, 5176 and 4727 N for the edge of hole offset repair, 15 mm offset repair and pristine panel, respectively. This is likely due to the effective thickness for the edge of hole offset repair case now being 1.5t on both sides of the impactor. However, the join between the plug and parent panel causes the impact response to be slightly less stiff than the central repair case, which is demonstrated by the blue line having a steeper gradient than the grey line in Figure 5-15. As was mentioned in Section 5.3.2, the central repair case with a plug resulted in plug dislodgement and therefore only the trends prior to damage initiation can reasonably be compared with the other repair cases, meaning the initial gradient is all that can be assessed.

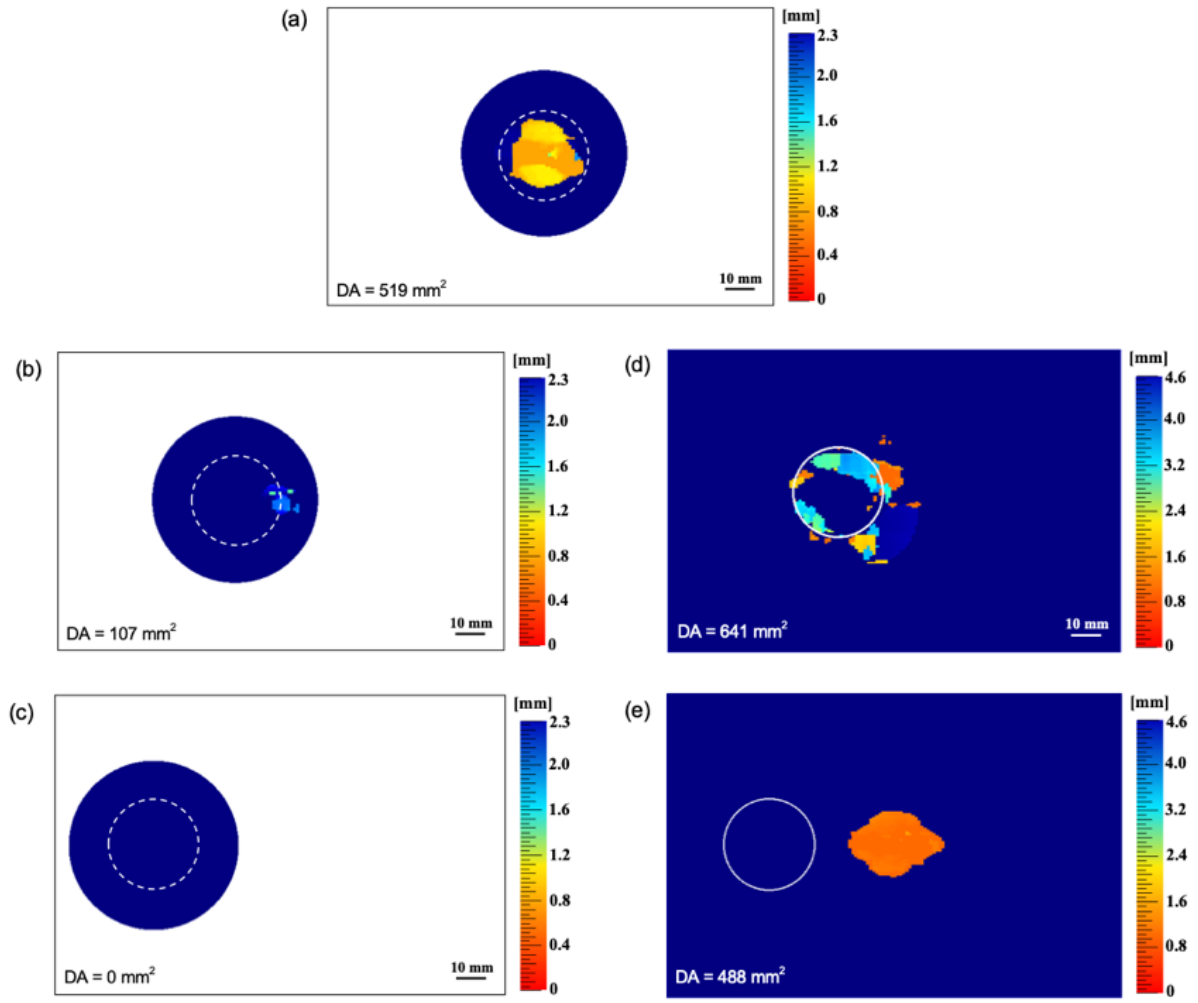

Figure 5-16. C-scan images taken from the top (impacted) face after a 7.5 J impact for: (a) the central patch-repair cross-ply CFRP panel (of patch thickness, 0.5t, 2.29 mm), (b) the edge of hole offset patch-repair cross-ply CFRP panel (of patch thickness, 0.5t, 2.29 mm) and (c) the 15 mm offset patch-repair cross-ply CFRP panel (of patch thickness, 0.5t, 2.29 mm), all with plugs. And c-scan images taken from the bottom face for the latter two panels are shown in (d) and (e), respectively. (The white-dashed line represents the 30 mm diameter hole that was initially cut out in the parent panel and the solid white line depicts the positioning of the plug).

Figure 5-16 shows the c-scan images of the damage in the patches of all the repair panel configurations with plugs as well as in the parent panel and plug for both offset cases. The rear face could not be scanned for the central repair case due to dislodgement of the plug, causing the surface to not be flat enough for the equipment. Comparing the damage in the patch, as for the case without a plug, the damage was greatest in the central impact case and the 15 mm offset case had less damage in the parent panel than in the patch of the central impact case. However, where the plugged cases differ from those without plugs is in the damage area in the parent panel and plug of the edge of hole impact case, as the damage area is significantly larger than in the patch of the central impact case. Having said this, a large amount of this damage is contained in the plug and the damage to the parent panel is closer to 400 mm^2, which suggests a similar trend to that of the unplugged

cases. Additionally, the combined damage in the edge of hole impact case is the largest, with a value of 748 mm^2, again suggesting that this is the area of the repair that is the most susceptible to damage.

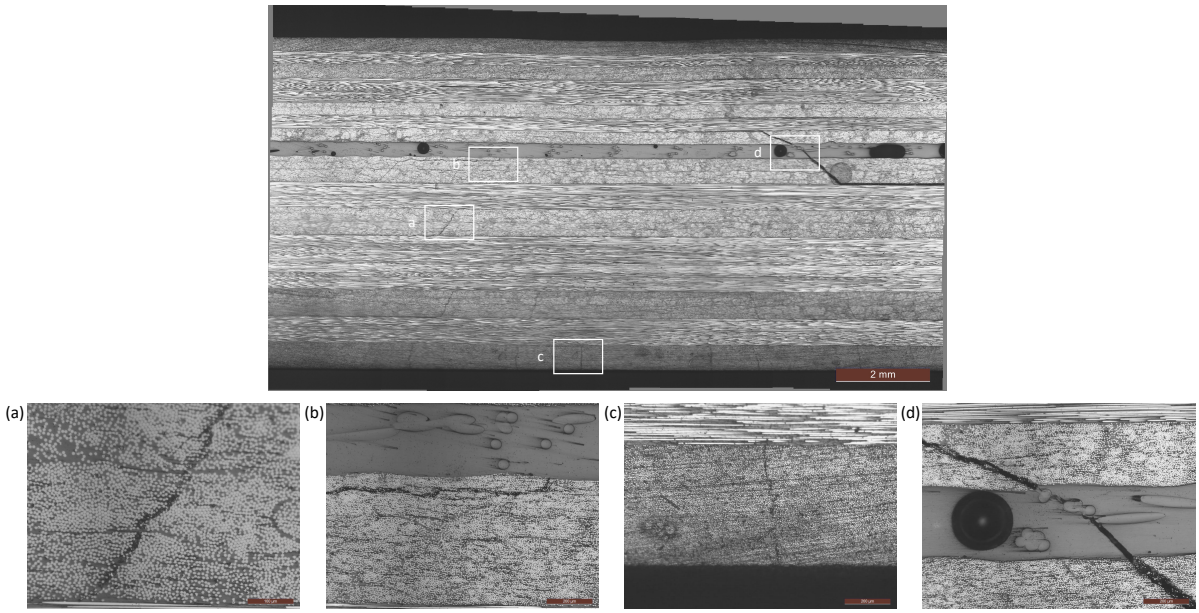

Figure 5-17. Optical microscopy images of an edge of hole offset patch-repair cross-ply CFRP panel with a plug after a 7.5 J impact, with key features highlighted by white boxes shown in images (a), (b), (c) and (d).

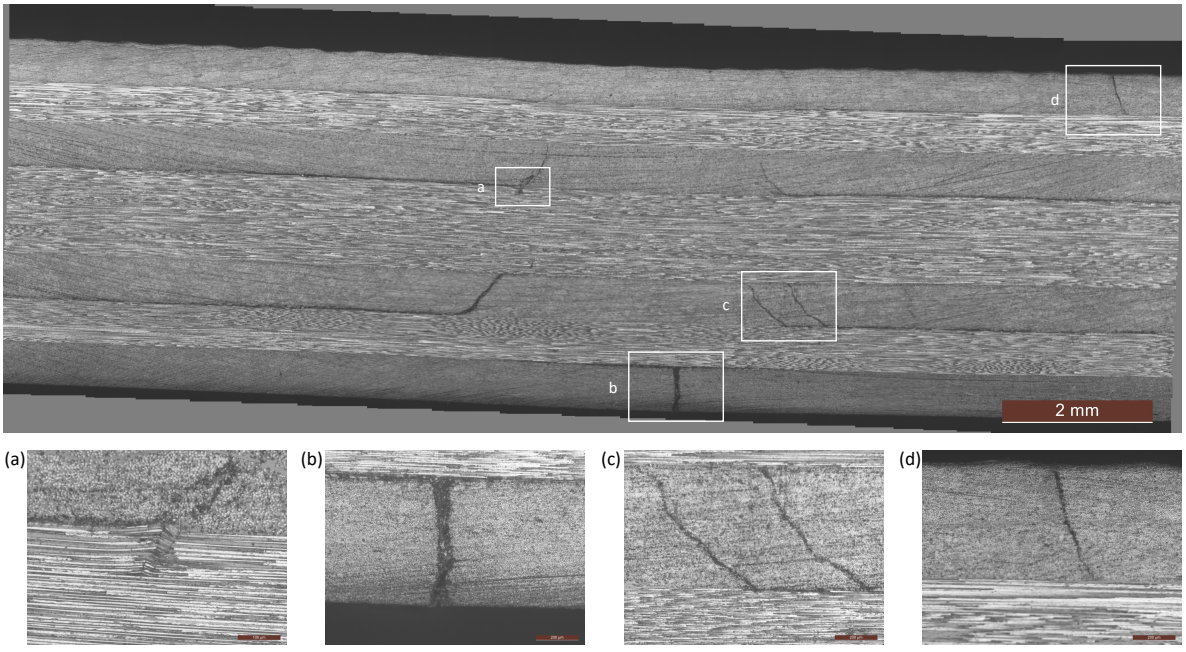

Figure 5-18. Optical microscopy images of a 15 mm offset patch-repair cross-ply CFRP panel with a plug after a 7.5 J impact, with key features highlighted by white boxes shown in images (a), (b), (c) and (d).

Figures 5-9, 5-17 and 5-18 show the microscopy images that were taken of the impact site cross-section for a central patch repair, edge of hole offset repair and 15 mm offset repair panel with a plug. As with the

repairs without a plug, Figure 5-18 demonstrates that the 15 mm offset repair case has damage mechanisms almost identical to that of a pristine panel, including a kink band forming where the intralaminar damage meets the ply interface as a delamination propagates. This implies that, if the impact site is not on the patch, the damage evolution occurs similarly to that of a pristine panel as the repair panel at the point of impact is essentially the same. In Figure 5-9, there are a lot of small cracks throughout the patch and a separation of plies in the plug, showing that the central repair case is very susceptible to intralaminar damage. Lastly, Figure 5-17 depicts a similar damage propagation to that of the edge of hole offset repair case without a plug, with the most prominent intralaminar damage occurring in and around the adhesive layer. There is significant intralaminar cracking in this case, but much less extreme than in the 15 mm offset case, with the damage in the rear ply being much less likely to lead to rear face cracking. This again suggests that the increased thickness at the impact site aids in stiffening the sample and thus reduces bending, causing rear ply damage to be minimised in comparison.

5.3.4 Effect of plug when varying impact offset distance

The final variable to be considered in this testing was the effect of the inclusion of a plug on the response of the repaired panels impacted at different locations. For this, the repairs discussed separately in Section 5.3.3 were now compared with each other. The force time and force displacement traces of all six repair configurations as well as the pristine panel are shown in Figure 5-19.

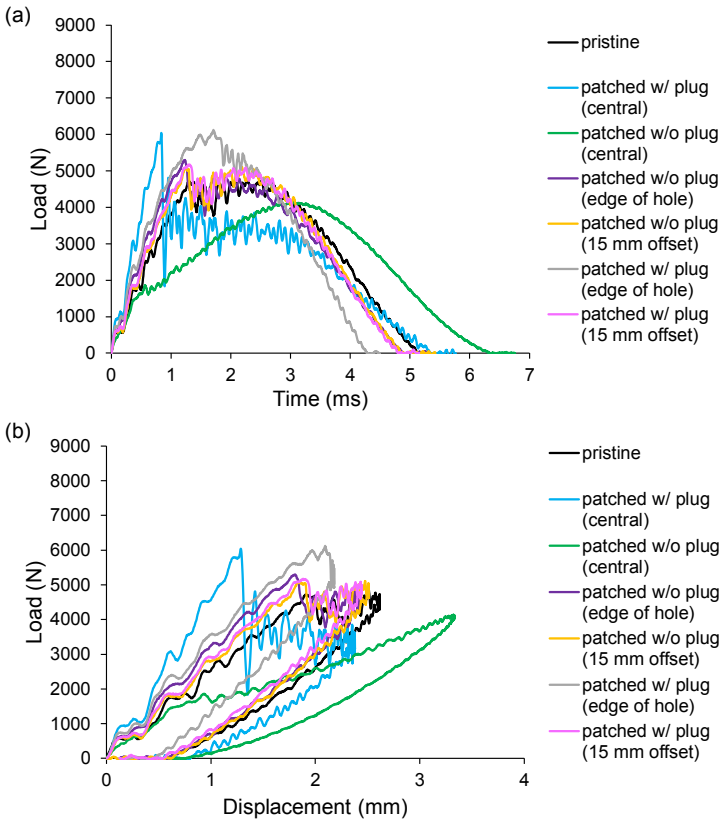

Figure 5-19. Load traces for a pristine cross-ply CFRP panel and central, edge of hole and 15 mm offset patch-repair panels, with and without cross-ply CFRP plugs, impacted at 7.5 J. The thickness, t, of the parent and the plug cross-ply CFRP was 4.58 mm and the thickness, 0.5t, of the patch was 2.29 mm. Shown are the: (a) load versus time traces and (b) load versus displacement traces.

From Figure 5-19 above, it can be seen that, as the offset distance increases, the effect of including a plug reduces. When the impact is central with respect to the repair, the panel with no plug, shown by the green line, has a very shallow gradient and a displacement of 3.5 mm. This is in comparison to the panel with a plug, shown by the blue line, which has the steepest gradient of all the panels in this testing and also a displacement of 2.4 mm. This demonstrates that the inclusion of a plug greatly increases the stiffness and also appears to strengthen the repair at this impact location. However, due to plug dislodgement, the amount of strengthening cannot be quantified. When the impact is on the patch and in line with the edge of the 30 mm cut out below, the panel with no plug, shown by the purple line, has a damage initiation load of 5300 N and a maximum displacement of 2.4 mm where the sample with a plug, shown by the grey line, has a steeper gradient as well as values of 6123 N and 2.2 mm, respectively. This implies that the inclusion of a plug slightly increases the stiffness and strength of the repair at this impact location. Lastly, when the impact is 15 mm away from the edge of the patch, the panel with no plug and the panel with a plug have very similar values for both damage initiation load and maximum displacement, with values of 5083 N and 2.5 mm and 5176 N and 2.5 mm, respectively, which suggests

the effect of a plug at this impact location is much less significant. This is further demonstrated by the similarity in the gradients for both of these cases, shown by the gold and pink lines, respectively.

Comparing the c-scan images in Figures 5-11 and 5-16, the reduction in damage in the patches demonstrates that the addition of a plug strengthens and stiffens the repair, giving the patch itself more support. This is also reflected in the 15 mm offset case as the damage area is 160 mm^2 less when a plug is included, suggesting that, even with the impact site being away from the repair, the increased stiffness by having both a patch and plug cause the panel to be less susceptible to damage. In continuation, the plugged 15 mm offset case is the only offset repair configuration with less damage in the parent panel than in a pristine panel at the same impact energy, with the central impact cases having no damage in the parent panel but more damage in the patches.

In both the central and edge of hole offset repairs, the microscopy images show more damage in the case without a plug. This can be seen by comparing Figures 5-9 and 5-12, with the latter, i.e. the case without a plug, having a more obvious divide between plies where delaminations are extending through the panel and this interlaminar damage propagating further than when a plug is present. Figures 5-13 and 5-17 depict the edge of hole offset repairs without and with a plug, respectively, and it can be seen that, in the case of the former, there is not only more cracking throughout the panel in general but also a significant crack through the adhesive and ply below on both sides of the impact site. Contrastingly, in Figure 5-17, the inclusion of a plug results in a crack through the adhesive on only the right hand side of the microscopy image as well as a reduction in intralaminar damage overall. In both of these cases, the addition of a plug stiffens the panel and this reinforcement leads to a reduction in damage initiation and propagation. In the case of the 15 mm offset repair panels, shown in Figures 5-14 and 5-18, the damage evolution is essentially the same with or without a plug and matches that observed in a pristine panel in Figure 5-8. This suggests that when the impact site is not on the repair itself the panel behaves in a way that is similar to that of a pristine panel, with the addition of a plug making no apparent difference to the damage observed.

5.3.5 Discussion

The repair results for all panels impacted at 7.5 J are presented in Table 5-1 below, including all the repeat data. The damage initiation load and time, peak load, maximum displacement and damage areas are given and, in the case of repeats, the variation in total damage area is also included.

Table 5-1. Measured impact behaviour of the pristine and repaired cross-ply CFRP panels, with all panels impacted at 7.5 J.

Panel and test number		Drop-weight traces				Damage area (mm^2)		Variation in total damage area
		Damage initiation load (N)	Damage initiation time (ms)	Peak load (N)	Max. displacement (mm)	Patch	Parent/ Plug	
Pristine (first impact)	1	4727	1.3	4846	2.6	-	501	±2.5%
	2	4837	1.4	4961	2.6	-	477	
Pristine patched		-	-	8165	1.8	0	0	-
Central repair (with plug)	1	6041	0.8	6041	2.4	519	-	±10.4%
	2	4380	0.7	4380	2.6	558	-	
	3	4510	0.7	4510	2.4	450	-	
	4	4124	0.6	4124	2.8	549	-	
Central repair (without plug)	1	1915	0.6	3997	3.5	799	-	±2.8%
	2	1862	0.5	4140	3.3	779	-	
	3	1788	0.5	3940	3.4	755	-	
	4	1819	0.6	3994	3.5	769	-	
Edge of hole repair (with plug)		6123	1.7	6123	2.2	107	641	-
Edge of hole repair (without plug)	1	5300	1.2	5300	2.4	325	638	±19.2%
	2	4699	1.2	5243	2.4	126	521	
	3	5029	1.2	5029	2.4	248	611	
15 mm offset repair (with plug)		5176	1.3	5176	2.4	0	488	-
15 mm offset repair (without plug)	1	5083	1.2	5111	2.5	0	648	±11.7%
	2	4970	1.2	5105	2.5	0	512	

Up to four panels were tested for each repair configuration with the only exceptions being the pristine patched case and the two offset plugged repair cases. This was due to no damage in the pristine patched case and no plug dislodgement in the offset plugged repair cases, especially since the variation between repeats in other cases was generally very minimal. Overall, the similarity in the drop weight trace values across repeats was extremely good, with only the central plugged repair and edge of hole repair without a plug having significant differences. The former is likely due to the plug dislodgement and this occurring at different points in the impact event on each sample. The latter is in reference to the second edge of hole repair case without a plug having dissimilar values to the first and third cases, which cannot easily be explained but is most likely an outlier due to some inconsistencies in the repair. However, otherwise, these results suggest very good repeatability and give confidence in the conclusions drawn. In continuation, the variations in total damage area in the relevant cases were ±2.5%, ±10.4%, ±2.8%, ±19.2% and ±11.7%, which further show the repeatability of both the

manufacturing and testing of these panels, especially since this includes the central plugged repair case as well as the potential outlier in the edge of hole repair without a plug case.

In comparison to the pristine panel, only the pristine patched and offset repair cases had a higher peak load, with the former also having a lower total damage area and the latter having less damage in the patch than was in the pristine panel. The central plugged repair case was affected by dislodgement but the central repair without a plug did not perform as well as a pristine panel likely due to the effective thickness at the impact site being 0.5t rather than the thickness, t, of the pristine panel. The pristine patched case performed the best, with the edge of hole plugged repair case performing the second best, which could be a result of the increased thickness at the impact site. These observations demonstrate that the thickness at the impact site greatly affects the performance of the panel, with a thicker panel being able to withstand more force before damage initiation, which suggests that the inclusion of a plug strengthens the repair.

A further observation is that, although the patch damage area was less than in the pristine panel and the largest individual damage area was in the central repair without a plug, the total damage area is greatest for the edge of hole repair without a plug case. This highlights the adhesive join as a potential point of weakness in the repair and suggests this impact sight is the most susceptible to damage of those tested in this work, thus demonstrating the importance of testing repair panels not only at the central point of the repair.

Lastly, the microscopy images show that the 15 mm offset cases, with and without a plug, perform similarly to a pristine panel, with the same damage features and propagation. This implies that moving away from the repair itself leads to a reduction in the effect the repair has on the performance of the panel and suggests that increasing the distance further would continue to minimise this until eventually a point is found where the repair behaves like a pristine one.

6 Experimental study on the effect of impactor shape and hardness on pristine quasi-isotropic CFRP panels under low-velocity impact loadings

6.1 Introduction

In the last few decades, the use of composites in aerostructures has become more prominent, with modern commercial aircraft increasing the percentage of composite components and reducing the content of metals, such as aluminium and steel. This adjustment in materials can be seen when comparing the Boeing 777 and 787, with the former comprising of 50% aluminium and 12% composite materials but the more modern Dreamliner flipping these values to give 50% composites and only 12% aluminium [107]. Although metals are advantageous due to being widely available and easy to machine, composites allow for more customisation of their properties according to purpose and have excellent weight to strength ratios. To allow composite materials to be used in aerostructures, rigorous testing is required, including under impact loading conditions. Aircraft are subjected to a variety of impact scenarios during use from tool drop to bird strikes, with the former being an example of a hard, low velocity impact and the latter being an example of a soft, high velocity impact. The impact events also vary in the sharpness of the impactor, with some cases having a blunter surface that comes into contact with the aircraft while others are sharper and thus direct the impact energy on one point rather than over a larger area. It is therefore, firstly, important to be able to characterise if an impact is hard or soft or somewhere between the two and, if it is the latter, how to classify it appropriately. Secondly, what the difference in damage initiation and response within the CFRP panel is for both soft and hard impacts. And, thirdly, it is of interest to also consider the shape of the impactor and analyse how the panel is damaged when impacted with a sharper impactor in comparison to a blunter one.

Firstly, considering how to characterise if an impact is hard or soft, Yankelevsky defined a hard impact as one where the impactor deforms significantly less than the object it hits and generally remains undamaged [108]. However, Koechlin et al. disagreed with this classification as it suggests that the hardness of an impact depends only on the material of the impactor rather than the velocity it travels at and instead label this type of

impact as an elastic impact. At a low velocity, an impact can be said to be soft if the projectile is damaged and the target is not, with a hard impact being one where penetration occurs [11]. Since the impact energies and materials used in the experimentation in this chapter don't result in penetration, hard impacts are defined as impacts where the impactor itself does not deform and soft impacts are defined as when the impactor does deform, with examples of the former being tool drop and runway debris and examples of the latter being hailstones and bird strikes.

Secondly, the most common impact conditions implemented when testing pristine CFRP panels are those that would be characterised as hard, low-velocity impacts and some results [1,96,109-114] have been reported. Caprino et al. found that the energy at which penetration occurred when impacting CFRP panels with a hard projectile at a low velocity could be as low as 1 J depending, primarily, on the total fibre thickness and the impactor diameter, among other factors [113]. Contrastingly, Dau et al. found that panels had a critical threshold energy of between 272 and 307 J when impacting with a soft projectile at a low velocity, above which perforation was observed [51]. Comparisons between hard and soft impacts at high velocities have been considered [55,56]. Liu et al. impacted CFRP panels with both hard and soft projectiles at high velocities and found that a velocity of 100 $m.s^{-1}$ was required for any damage to initiate in the panels impacted with a soft projectile. Contrastingly, damage was detected in the panels impacted with a hard projectile at a velocity of 30 $m.s^{-1}$ and penetration occurred above 70 $m.s^{-1}$, showing that more energy is required in the case of the soft projectile to cause the same damage as seen when using the hard projectile [55]. This research also highlights the large difference in energy required for damage between the two classifications on impact, suggesting that using a projectile made of a combination of both gelatine and aluminium or a less soft material than gelatine might give an intermediate value. At the time of writing this thesis, there is little to no research on transitioning from a hard to a soft impact and comparing hard and soft impacts at a low velocity. These findings demonstrate the drastic difference between hard and soft impacts and the need for more research on the transition between the two.

Thirdly, the effect of the impactor shape on the performance of the CFRP panels has been investigated previously and some results [57-59] have been reported. Mitrevski et al. found that the sharpest impactor resulted in the most energy being absorbed and the deepest indentation, whilst the bluntest impactor gave the highest peak force value and the shortest contact time between impactor and panel [57,58]. Kazemianfar et al.

found that a sharper impactor resulted in more damage and also that damage initiated at a lower load value [59]. These findings show that the impactor shape has a significant effect on the response of the panel, however both were at one impact energy or two very similar energies and so further investigation into the effects at different impact energies is of interest, especially since aircraft are subjected to a variety of impacts and a variety of energy levels during their use.

In this section, quasi-isotropic CFRP panels are subjected to impacts with flat and round-nosed hard impactors as well as with flat impactors with rubber adhered to the end to simulate a softer impact and the transition between hard and soft impacts. Impacts are performed at 7.5, 15 and 30 J, with the softer impactors being implemented at 30 J only due to the results from the flat-ended impactor at the lower impact energies. The effect of the thickness of the rubber layer on the softer impactors on the performance of the panels is investigated by employing three thicknesses: 1, 1.5 and 2 mm. Load versus time and load versus displacement traces are measured from the impact tests and detailed maps of the resultant interlaminar damage of the various panels are also obtained, allowing the effect of impactor shape and hardness to be investigated by comparing these findings for each case.

6.2 Test specification and methods

6.2.1 Hard low-velocity impacts

Two different shaped impactors were used in conjunction with the drop weight tower for the hard low-velocity impacts, to allow the effect of the impactor shape on the impact performance of the panels to be considered. Quasi-isotropic samples were tested under a low-velocity impact loading using an Instron 9340 drop-weight tower supplied by CEAST, Italy, shown in Figure 3-5, following the same test method as described elsewhere [86-88] and in Section 3.4.1 of this thesis. The first of these was a flat-ended impactor and the second was a round-nosed impactor, with both having diameters of 16 mm, an overall mass of 5.266 and 5.265 kg, respectively, and being made from stainless steel. For each impactor, a variety of energy levels were used: 7.5, 15 and 30 J, giving impact velocities of: 1.69, 2.39, and 3.38 $m.s^{-1}$, respectively.

The impacted panels were inspected using a Prisma portable ultrasonic C-scanner supplied by Sonatest Ltd, UK to detect any interlaminar damage area. This technique has been discussed in detail elsewhere [88] and in Section 3.4.2 of this thesis.

6.2.2 Soft low-velocity impacts

For the soft low-velocity impacts, a flat-ended impactor was used, and different thicknesses of rubber were adhered to the end. The rubber used was neoprene, with the mechanical properties of which being given in Table 6-1 below, with thicknesses of 1, 1.5 and 2 mm being implemented. To adhere the rubber, the surface of the flat-ended impactor was cleaned with acetone, to ensure a good join, and two-part Araldite ultra-strong adhesive was used. As per the adhesive instructions, the two adhesive components were combined for 30 seconds, applied to both surfaces, the two surfaces were pressed together, and the impactors were left for at least 14 hours to allow the join to harden and strengthen before being used for testing. With the rubber adhered, the mass of the impactor was 5.267 kg and impacts were performed at an impact energy of 30 J, which gave an impact velocity of 3.38 $m.s^{-1}$. Only the highest impact energy was used for this testing as the flat-ended impactor gave no damage at the lower impact energies. The samples were tested and inspected with the drop weight tower and ultrasonic C-scanner in the same way as described for the hard low-velocity impacts.

Table 6-1. Mechanical properties of neoprene rubber supplied by PVC Tube Online Ltd [115]

Property	Value	Units	Test Method
Indentation hardness	60 shore A -4 +5	Degrees	ASTM D2240 00
Specific gravity	1.5 +/- 0.05	g/cm^3	ASTM D792
Tensile strength (minimum)	3	MPa	ASTM D412
Elongation at break (minimum)	250	%	-
Minimum continuous working temperature	-20	°C	-
Maximum continuous working temperature	65	°C	-
Maximum intermittent working temperature	70	°C	-
Compression set 70°C 22 hours	35% max	%	ASTM D395 Method B

6.3 Experimental results

6.3.1 Hard impacts

Pristine samples were impacted at 7.5, 15 and 30 J with two different impactors: a round-nosed (sharper) impactor and a flat-ended (blunter) impactor. Figures 6-1, 6-2 and 6-3 show the load versus time and load versus displacement traces using both impactors at each of these energies.

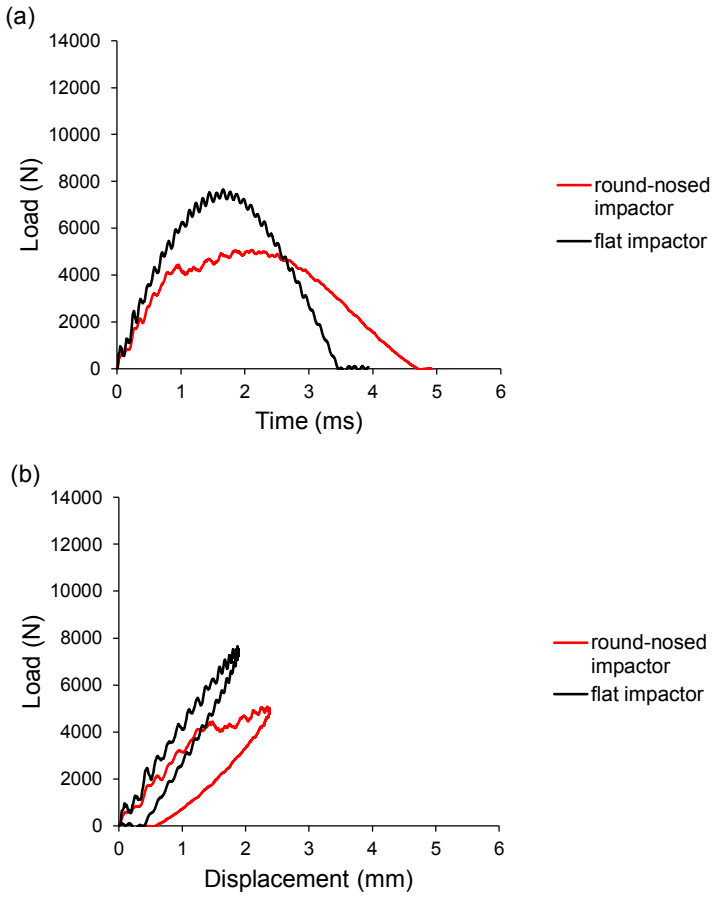

Figure 6-1. Load traces for the pristine panels impacted with a round-nosed impactor (red line) and a flat-ended impactor (black line). Both impacted at 7.5 J: (a) load versus time traces and (b) load versus displacement traces.

The load response of pristine CFRP panels when impacted with a sharp and blunt impactor at 7.5 J is shown in Figure 6-1. For the panel impacted with the sharper impactor, shown by the red line, there was a slight load drop at ca. 1 ms, which suggests damage initiated within the panel. Contrastingly, no load drop is clear in the traces from the panel impacted with the blunter impactor, which implies that damage did not occur within this panel. Additionally, the peak load for the sample impacted with the flat-ended impactor was 7649 N, which is significantly greater than the damage initiation load value of 4445 N recorded for the sample impacted with

the round-nosed impactor. This suggests that the damage initiation load is larger when impacting with a blunter impactor, which is likely due to the round-nosed impactor concentrating the impact energy on one point where the flat impactor spreads this energy out over a larger area. However, the round-nosed impactor allowed the panel to deform and bend more around it, resulting in the panel behaving in a less stiff manner. This is demonstrated by the higher displacement value for the round-nosed impactor, with values of 2.4 and 1.9 mm for the round-nosed and flat-ended impactors, respectively.

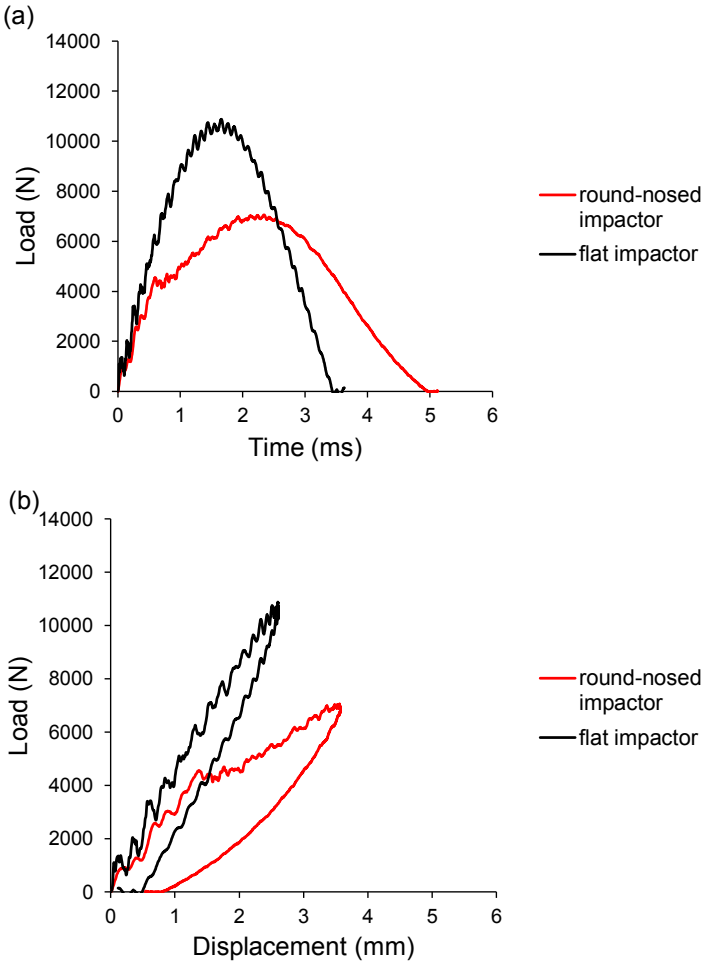

Figure 6-2. Load traces for the pristine panels impacted with a round-nosed impactor (red line) and a flat-ended impactor (black line). Both impacted at 15 J: (a) load versus time traces and (b) load versus displacement traces.

Figure 6-2 demonstrates the load response of panels impacted with round-nosed and flat-ended impactors at 15 J. Both graphs show a very similar trend to that observed in Figure 6-1, with a load drop occurring for the panel impacted with the sharper impactor, suggesting damage initiated within the panel, but no such event occurring for the panel impacted with the blunt impactor. Furthermore, the damage initiation load for the panel impacted with the round-nosed impactor was found to be 4558 N, which is very similar to the value of

4445 N that was observed for the impact at 7.5 J. This implies that ca. 4000 N is the load value at which damage will initiate within the CFRP panel when impacting with the round-nosed impactor. Since there is no load drop in the traces for the panel impacted with the flat impactor, it can be assumed that the damage initiation load has not yet been reached, showing that the value is significantly higher than for the sharper impactor.

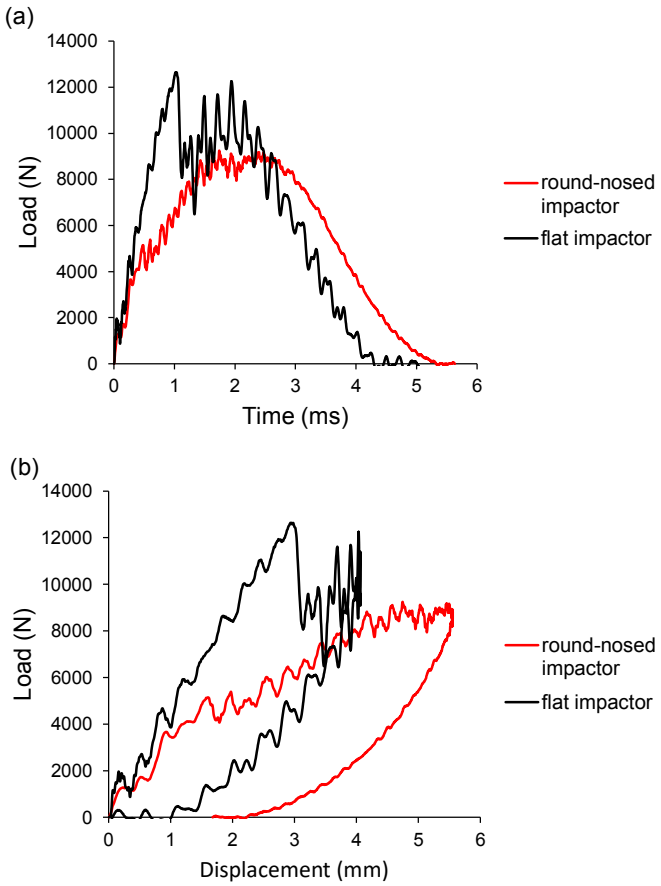

Figure 6-3. Load traces for the pristine panels impacted with a round-nosed impactor (red line) and a flat-ended impactor (black line). Both impacted at 30 J: (a) load versus time traces and (b) load versus displacement traces.

At an impact energy of 30 J, the damage initiation load when impacting with a flat-ended impactor was reached, as can be seen by the clear load drop in the black line in Figure 6-3. The load drop for the panel impacted with the round-nosed impactor is ca. 4000 N again, in contrast to 12641 N for the panel impacted with the flat-ended impactor. This large difference is likely due to the fact that the blunt impactor spreads the impact energy over a larger area rather than concentrating it all to one point, like the sharper impactor, and this demonstrates that the shape of the impactor has a significant effect on the response of the CFRP panel.

The C-scan images of these panels can be seen in Figure 6-4 below. As expected from the load versus time and load versus displacement traces, there was no damage in the panels impacted with the flat-ended

impactor at 7.5 and 15 J. At these values, however, there was damage observed in the panels impacted with the round-nosed impactor, with damage areas of 681 and 1986 mm^2, respectively. The damage area at 15 J is approximately three times as large as that at 7.5 J, showing that the damage area increases dramatically as the impact energy is doubled. Comparing this to the damage area at 30 J, which is 3602 mm^2 and so just under double the damage area at 15 J, there is not a clear relationship between the impact energy and the damage area, beyond the damage area increasing as the impact energy is raised. Lastly, at 30 J, it can be seen that damage has initiated and propagated in the panel impacted with the flat-ended impactor, with a damage area of 4440 mm^2 being observed. This value is roughly 1000 mm^2 larger than that for the panel impacted with the round-nosed impactor, which suggests that the panel was able to deform more around the sharper impactor and thus absorb more of the energy to result in a smaller damage area. Lastly, it is also interesting to compare the damage maps for the round-nosed and flat-ended impacts since the centre of the panel impacted with the flat-ended impactor is undamaged. This shows that the damage pattern is affected by the shape of the impactor.

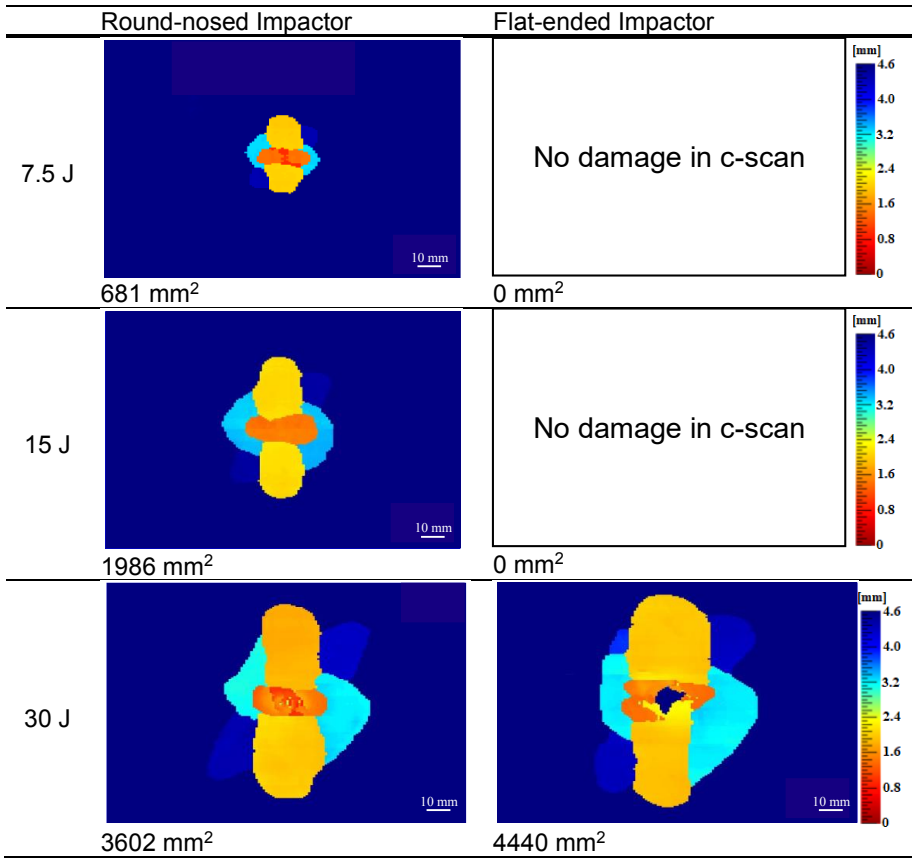

Figure 6-4. C-scan images taken from the top (impacted) surface of pristine CFRP panels impacted with a round-nosed impactor and a flat-ended impactor at various impact energies. The damage area values are given below each image. (The scales show the depth of the different locations of the interlaminar damage).

6.3.2 Soft impacts

Since damage initiated in the panel impacted with the flat-ended impactor at an impact energy value of 30 J, the investigation into the effect of softening the impactor was carried out at this impact energy. The aim of this investigation was to learn more about how the impact event is affected as the impact transitions from a hard impact to a softer impact. Adhering rubber to the impactor in this case would not give a purely soft impact as, once the rubber is compressed, the load from the stainless-steel impactor results in a hard impact. However, the rubber does soften and dampen the impact and performing this experimentation could allow the transition from hard to soft impacts to be defined and categorized more clearly. Figure 6-5 shows the load versus time and load versus displacement traces for the panels impacted with a flat-ended impactor without rubber and with 1, 1.5 and 2 mm of rubber adhered to it.

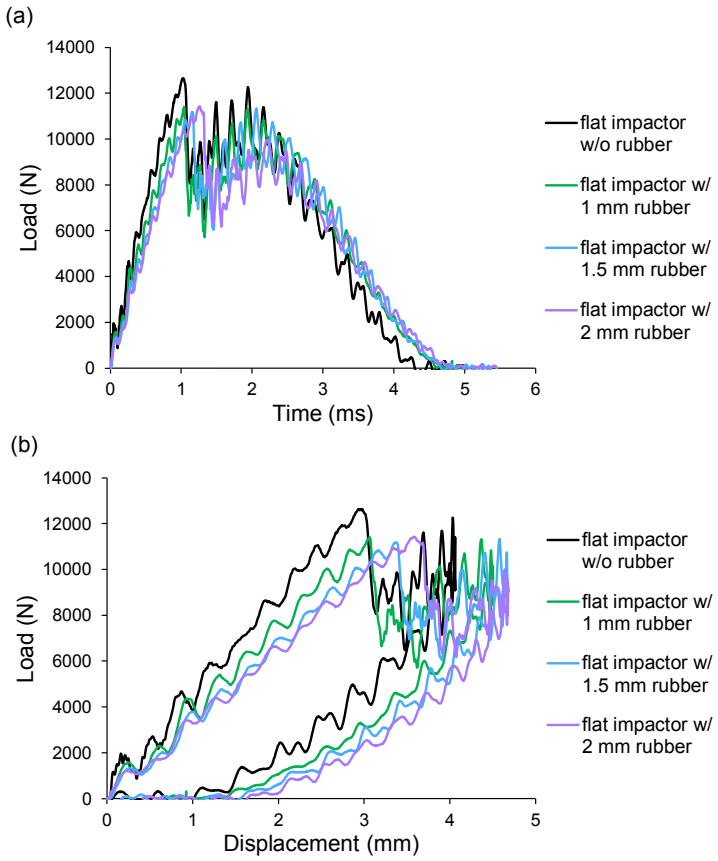

Figure 6-5. Load traces for the pristine panels impacted with a flat-ended impactor without rubber and with rubber disks of 1, 1.5 and 2 mm in thickness adhered to the end. All impacted at 30 J: (a) load versus time traces and (b) load versus displacement traces.

From the graphs in Figure 6-5, it can be seen that the addition of rubber to the end of the impactor results in a drop in the damage initiation load from 12641 N, for the sample impacted with the flat-ended

impactor without rubber, to 11406, 11183 and 11431 N, for the samples impacted with the flat-ended impactors with 1, 1.5 and 2 mm of rubber adhered to them, respectively. It also suggests that the peak load value drops when rubber is added but does not change as the thickness of rubber increases. However, what does change as the thickness of rubber increases is the maximum displacement and the time that damage initiates, with values of 4.5, 4.7 and 4.7 mm and 1.0, 1.2 and 1.3 ms for 1, 1.5 and 2 mm of rubber, respectively. This is likely to be because the flexibility of the rubber allows the panel to deform more around the impactor as more of it is present.

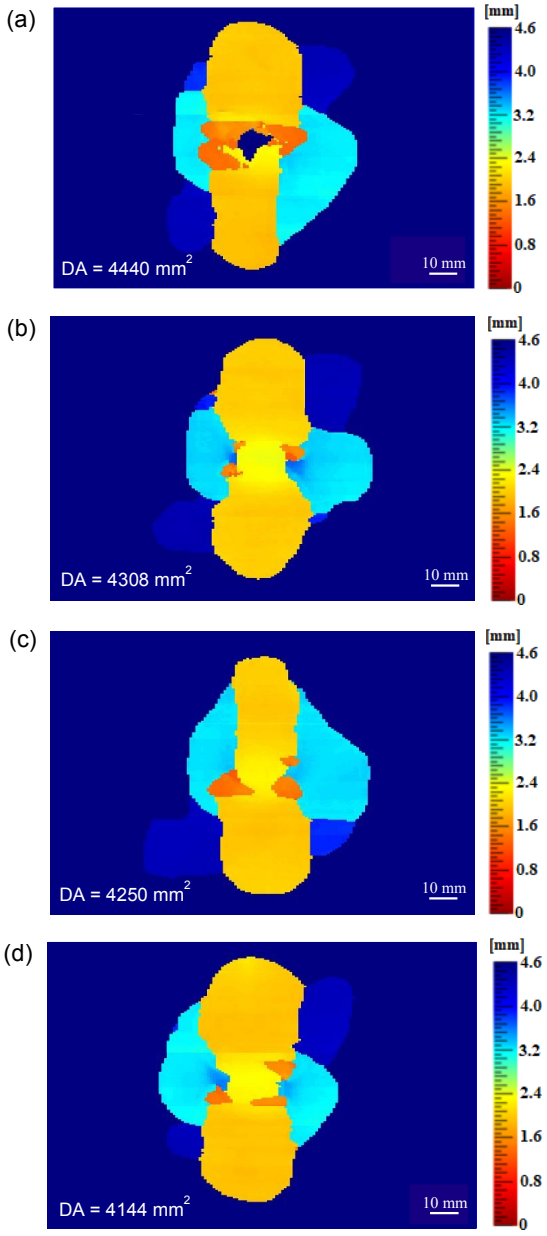

Figure 6-6. C-scan images of pristine CFRP panels taken from the top (impacted) face after 30 J impact for: (a) the panel impacted with a flat-ended impactor, (b) the panel impacted with a flat-ended impactor with a 1 mm thick rubber disk

adhered to the end, (c) the panel impacted with a flat-ended impactor with a 1.5 mm thick rubber disk adhered to the end and (d) the panel impacted with a flat-ended impactor with a 2 mm thick rubber disk adhered to the end.

Figure 6-6 shows the C-scan images for these panels. Comparing the damage area in each panel, the values suggest that the damage area decreases as the thickness of rubber increases. Additionally, the three cases where there was rubber adhered to the impactor have significantly less damage at the shallowest depth, shown in orange, compared to the case with no rubber. This implies that, even if the damage area is only reduced by around 200 mm^2, the top plies are much more protected.

6.3.3 Discussion

The impact data from the investigation into the effect of impactor shape and hardness on the performance of CFRP panels is summarised in Table 6-2 below. The damage initiation load and time, peak load, maximum displacement, and damage area are given for all the pristine panels impacted with the four different impactor types at all three energies.

Table 6-2. Measured impact behaviour of the pristine CFRP panels impacted with different impactors at varying energy levels.

Impactor		Impact Energy (J)	Drop-weight traces				Damage area (mm^2)	Variation in damage area
			Damage initiation load (N)	Damage initiation time (ms)	Peak load (N)	Max. displacement (mm)		
Round-nosed		7.5	4445	1.0	5071	2.4	681	-
Flat-ended		7.5	-	-	7649	1.9	-	-
Round-nosed		15	4558	0.6	7054	3.6	1986	-
Flat-ended		15	-	-	10879	2.6	-	-
Round-nosed		30	4115	0.4	9248	5.6	3602	-
Flat-ended		30	12641	1.0	12641	4.0	4440	-
Flat-ended w/ 1 mm rubber	1	30	11406	1.0	11406	4.5	4308	±2.1%
	2	30	11530	1.0	11530	4.4	4490	
Flat-ended w/ 1.5 mm rubber	1	30	11183	1.2	11330	4.6	4250	±5.1%
	2	30	10822	1.1	10822	4.6	4711	
Flat-ended w/ 2 mm rubber		30	11431	1.3	11431	4.6	4144	-

Repeat test were performed for the flat-ended impactor cases with 1 and 1.5 mm thick rubber adhered to the end due to issues with the c-scans in the first batch, which are shown in Appendix C in Section 11.3 of this thesis. The similarity between the drop-weight traces and the low values for the variation in damage area

demonstrates the repeatability of this testing. There are a number of findings from this testing. Firstly, the damage initiation load for the CFRP panels when impacting with a round-nosed impactor can be seen to be ca. 4000 N, which is much lower than the load required for damage to initiate when impacting with a flat-ended impactor that was found to be ca. 12000 N. Having said this, once damage initiated in the panels impacted with a flat-ended impactor, the damage area was larger than that for a panel impacted with a round-nosed impactor. This shows that the CFRP panels are more susceptible to damage from a sharper impactor at lower impact energies however, once higher energies are achieved, a blunter impactor results in more detrimental damage. It is likely that damage initiates sooner for a sharper impact because the energy is concentrated on one point rather than over an area, but the damage area is smaller because the panel can bend more around the rounded impactor and thus absorb more of the energy than for the case with a blunt impactor. Secondly, the addition of rubber on the end of the flat-ended impactor can be seen to reduce the damage area and increase the damage initiation time and maximum displacement. This shows that the rubber acts as a dampener in the impact event by absorbing some of the energy and, whilst deforming, it allows for the panel to bend more around the impactor to give more displacement. These results imply that, even a thin layer of rubber, has an effect on the damage initiation and propagation within a panel and that softening impacts where possible will result in less damage in the composite. Thirdly, the panels impacted with a flat-ended impactor with rubber had lower damage initiation load values, which might suggest that a lower impact energy is required to initiate damage in softer impacts but, for the damage to propagate, more energy is required than in harder impacts.

Not all impacts can be controlled, such as debris and hail stones, but ground equipment can be and, from this research, it is implied that a blunter impact will result in a higher threshold for impact energy thus making a blunt surface more appropriate for components that interact with the fuselage of the aircraft than a sharper edge. However, once damage does initiate, this type of impact will give a larger damage area and so it would be beneficial to have blunter impacts that are softened with a rubber layer. Therefore, when designing the connection between the aircraft and ground equipment, rubber layers should be adhered to blunt surfaces to ensure the composite panels maintain their strength properties over time.

7 Numerical modelling on the impact performance of CFRP panels

7.1 Introduction

The ability to numerically model an impact event and obtain accurate results allows for a reduction in testing and thus saves both time and money. This is due to the fact that modelling can be performed with minimal experimental testing, only what is required to validate the model, and a number of test conditions can be run to decide which tests are worthwhile performing experimentally and which ones will provide no useful insight. Additionally, scenarios that are complicated, expensive or even impossible to test in a laboratory can be considered. Therefore, developing an accurate model is invaluable. To produce such a model requires consideration of a number of elements, with various methods available, some of which will give more accurate results than others. Firstly, how the damage initiates and propagates through the material must be considered and there are numerous criteria that can be chosen for this. Secondly, how to model the rubber layer of the impactor for the soft impacts, since Abaqus/Explicit 2018 has built-in options, and it is critical to choose the correct one. Thirdly, the FEA model details, such as the element type and material properties, must be defined.

Firstly, the damage initiation and propagation can be modelled using the 2D Hashin criterion, which considers both the fibre and matrix failure modes [116]. Other criteria that can be used include 3D Hashin and Chang-Chang, both of which require VUMAT subroutines, where the 2D Hashin criterion is included in Abaqus/Explicit 2018. Although including the effect on the damage within the matrix from the normal stress that acts through the thickness of the composite, as done in 3D damage models, does give results that align more closely with those obtained experimentally, the 2D Hashin criterion does predict the same trends as seen in experiments [117]. The 2D Hashin criterion has been implemented in a number of different scenarios and has given good agreement, thus demonstrating its suitability for this application [52, 54, 79, 83, 117, 118].

Secondly, there are a number of ways to model the rubber on the impactor for the soft impacts, with three potentially suitable options being Mooney-Rivlin, Neo-Hookean and Ogden [119]. The former has been shown to be an accurate model for a rubber layer applied to the end of a round-nosed impactor, with conditions being set to give the Neo-Hookean simplification, and good agreement between the experimental and numerical results was found [120]. Additionally, when considering an alternate application that is based on puncturing

rubber gloves rather than compressing rubber disks upon impact, it was seen that the first two methods were much more effective at predicting the experimental results than the latter [119]. Overall, using the Mooney-Rivlin or Neo-Hookean techniques for modelling rubber in numerical analysis give reasonable agreement for a number of different applications [119,120].

Paired with the 2D Hashin damage model and the rubber modelling techniques, the fundamentals of the simulation are in the Finite Element Analysis (FEA) model that provides the panel and impactor dimensions and any properties not defined elsewhere. A mesh is applied to the panel, with the element type and characteristic length chosen to give the best prediction based on a compromise between precision and computational time, examples of values implemented in other research include: 0.5 mm [52, 79], 1 mm [82, 117], 1.5 mm [118], and 2.5 mm [54]. To allow the interply contact properties to be applied, the panel is often modelled as multiple plies stacked together rather than one solid block [52, 79, 82].

In this thesis chapter, a model has been produced in Abaqus/Explicit 2018 using built-in damage initiation and propagation criteria to predict the performance of pristine CFRP panels under a variety of impact loading conditions. This includes assessing the performance of a pristine panel under impacts of increasing impact energy and comparing the damage between impacts with round and blunt impactors. A rubber disk is included in some of the simulations to allow the effect of the thickness of the rubber, and thus the increasing softness of the impact event, to be considered as well. These results will then be compared with the experimental results collected in Chapter 6 of this thesis to assess the effectiveness of the model for this application.

7.2 Numerical modelling methods

For the FEA model, Abaqus/Explicit 2018 was used to simulate pristine panels under different impact loading conditions. The built-in composite material failure function was utilised, with details of its implementation as well as how each ply and impactor was modelled discussed in the following section. The model was given a maximum run time of 4, 4.5 and 5 ms for the round nosed, flat ended and flat ended with rubber impactors, respectively, with approximately 100 time-steps using 4 CPUs, giving a run time of 2-3 hours. These time periods were chosen as they are approximately the length of the impact event according to the experimental data recorded.

7.2.1 Composite Panel

The carbon fibre reinforced epoxy panel was simulated in the FEA model as a three-dimensional deformable solid and meshed using an 8-node quadrilateral in-plane general-purpose continuum shell with reduced integration element (SC8R). Each element had dimensions of 1 mm x 1 mm, giving a total of 105,000 elements in the composite panel.

The composite to be modelled was a pristine QIT CFRP panel with a layup of $[45_2/-45_2/0_2/90_2]_s$, meaning that there are blocked plies. For this reason, when modelling the panel, to save on computation time and simplify the model, 7 plies were simulated instead of the 16 present, with the 45, -45 and 0 fibre orientation plies modelled as double thickness and the 90 fibre orientation ply modelled as four times thickness due to symmetry. Doing so reduces the risk of over complication introducing errors in the simulation and ensures damage will only form between plies of differing orientation, as seen in experimental work.

For the interaction between each ply, to be consistent with previous work, a coefficient of friction of 0.25 was applied and the normal behaviour was defined as a hard contact with separation after contact being allowed. Additionally, to ensure the panel itself would not move upon impact and to simulate the fixture from the drop weight tower, the edges of the back face of the rear ply were pinned in place.

7.2.2 Impactor

Both the round-nosed and flat-ended steel impactors were modelled as analytical rigid bodies, meaning they wouldn't deform and to avoid unnecessarily meshing the part. The primary difference between the two impactors was the mass applied, with the former having a value of 5.265 kg and the latter 5.266 kg. They were constrained to only move in the direction normal to the top face of the composite panel, starting at the point just before impact with a velocity of 1.69, 2.39, and 3.38 $m.s^{-1}$ for impact energies of 7.5, 15 and 30 J, respectively.

For the case of the soft impacts, the rubber disk adhered to the impactors experimentally was modelled as a three-dimensional deformable solid and was meshed using 8-node linear brick elements with reduced integration (C3D8R). The elements were approximately 1 mm x 1 mm, with one layer for the thinnest rubber

disk and two layers for the other two, meaning there were a total of 272, 544 and 544 elements in the 1, 1.5 and 2 mm rubber disks, respectively.

The global friction constant, and therefore the value applied to the interaction between the impactor/rubber disk and the panel, was set as 0.2 and the normal behaviour was defined as a hard contact with separation after contact being allowed, to be consistent with previous work.

The final meshed assemblies for the round-nosed impactor and the flat-ended impactor with a 1 mm disk of rubber cases are shown in Figure 7-1 below. The impactor, composite panel and rubber disk are highlighted in blue, green and red, respectively.

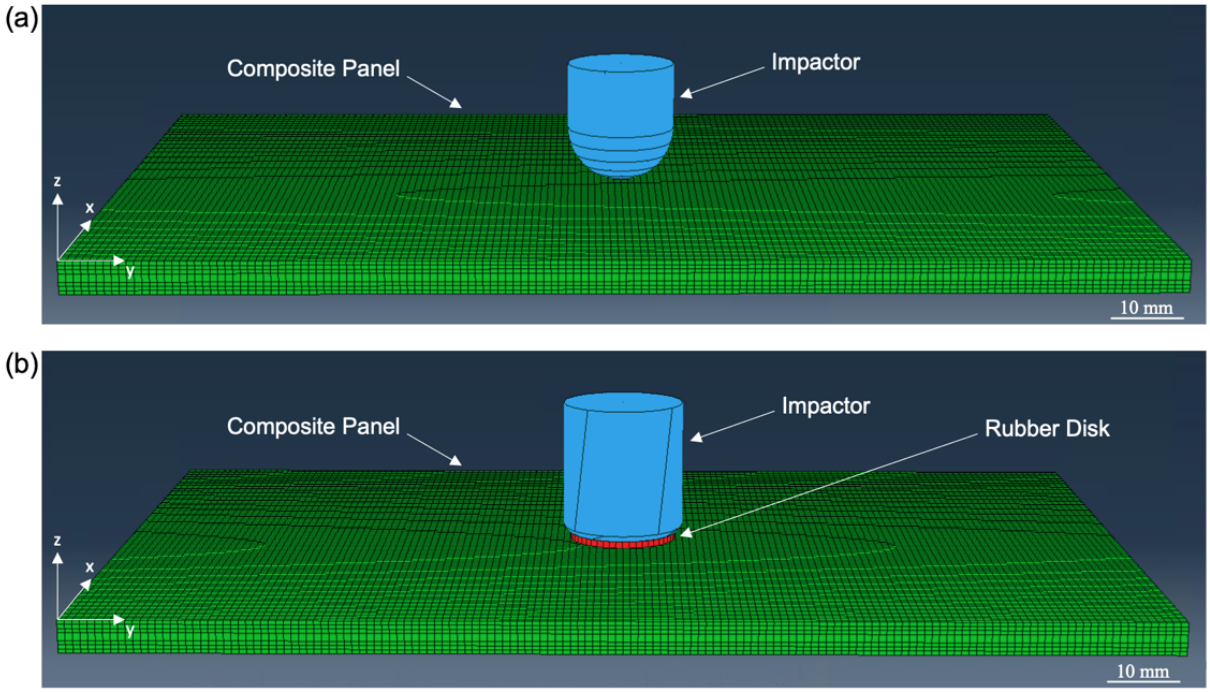

Figure 7-1. Meshed assembly with (a) round-nosed impactor and (b) flat-ended impactor with 1 mm of rubber (the impactor, rubber disk and composite panel are shown in blue, red and green, respectively).

7.2.3 Damage Model

The properties applied to the FE model, described above, are given in Table 7-1 below, including those applied to the rubber disk simulated for the soft impacts.

Table 7-1. Properties of the unidirectional composite from [52,87,88,101,121] and of the rubber disk from [115,120,122]

Property	Simulation value	Units
	COMPOSITE PLY	
Density	1600	kg/m^2
Moduli	$E_{11} = 115, E_{22} = 8.2,$ $G_{23} = 3.6, G_{12} = G_{13} = 3.6$	GPa
Poisson's ratio	$\upsilon_{12} = 0.34$	-
Strength values	$S_{1t} = 2282, S_{2t} = 54,$ $S_{1c} = 1067, S_{2c} = 200,$ $S_{12} = S_{13} = 99$	MPa
Intralaminar ply fracture energies	$G_{Ic\|ft} = 133, G_{Ic\|fc} = 40,$ $G_{Ic\|mt} = 0.4, G_{Ic\|mc} = 1.3, G_{IIc\|ms} = 1.3$	kJ/m^2
Interlaminar ply fracture energies	$G_{Ic} = 0.4, G_{IIc} = 1.3$	kJ/m^2
Benzeggagh-Kenane (B-K) exponent	$\eta = 1.45$	-
Cohesive strengths	$t_{33}^0 = 43.0, t_{31}^0 = t_{32}^0 = 50.0$	MPa
Initial cohesive law stiffness	$k = 1 \times 10^5$	MPa/mm
	RUBBER DISK	
Density	1500	kg/m^2
Neo Hookean constants	$c_{10} = 0.9, d_1 = 0.001$	-

7.2.3.1 Intralaminar Damage

To model the intralaminar damage initiation and propagation, the 2D Hashin Criterion property function [116] within Abaqus/Explicit 2018 was implemented. This theory predicts four types of damage: tensile fibre failure, compressive fibre failure, tensile matrix failure and compressive matrix failure, where the longitudinal and transverse fibre directions are denoted as the 11- and 22-directions, respectively. Therefore, the following equations are used to predict the initiation and propagation of these modes [52,54,79,82,116-118,123]:

Tensile fibre failure ($\hat{\sigma}_{11} \geq 0$): $$F_f^t = \left(\frac{\hat{\sigma}_{11}}{S_{1t}}\right)^2 \quad (1)$$

Compressive fibre failure ($\hat{\sigma}_{11} \leq 0$): $$F_f^c = \left(\frac{\hat{\sigma}_{11}}{S_{1c}}\right)^2 \quad (2)$$

Tensile matrix failure ($\hat{\sigma}_{22} \geq 0$): $$F_m^t = \left(\frac{\hat{\sigma}_{22}}{S_{2t}}\right)^2 \quad (3)$$

Compressive matrix failure ($\hat{\sigma}_{22} \leq 0$): $$F_m^c = \left(\frac{\hat{\sigma}_{22}}{2S_{13}}\right)^2 + \left[\left(\frac{S_{2c}}{2S_{13}}\right)^2 - 1\right]\frac{\hat{\sigma}_{22}}{2S_{13}} + \left(\frac{\hat{\tau}_{12}}{S_{12}}\right)^2 \quad (4)$$

where F_f^t, F_f^c, F_m^t and F_m^c are the damage criteria for the four damage mechanisms, respectively, and a value of $F \geq 1$ is when damage is predicted to initiate. S_{1t} and S_{1c} represent the tensile and compressive strengths in the 11-direction, respectively, and S_{2t} and S_{2c} represent the same in the 22-direction, respectively. S_{12} and $S_{13} = S_{2c}/2$ represent the shear strength in the 11- and 22-directions, respectively. Lastly, $\hat{\sigma}_{11}$, $\hat{\sigma}_{22}$ and $\hat{\tau}_{12}$ are taken from the effective stress tensor, $\hat{\sigma}$, and are used to evaluate the above equations. As discussed elsewhere [52], Equation 4 is derived from the von Mises yield criterion.

Four damage parameters are calculated, one for each failure mechanisms: d_f^t, d_f^c, d_m^t and d_m^c. The equation for these values is given by the following equation from the Abaqus documentation [124]:

$$d = \frac{\varepsilon^f(\varepsilon - \varepsilon^0)}{\varepsilon(\varepsilon^f - \varepsilon^0)} \quad (5)$$

where setting $d = d_f^t$, $d = d_f^c$, $d = d_m^t$ and $d = d_m^c$, represents fibre tension, fibre compression, matrix tension and matrix compression failures, respectively, and ε is the equivalent strain of the composite ply. The terms ε^0 and ε^f represent the equivalent strain at the initiation of and final point of failure. When considering failure in the fibres, the strain values are set to those in the 11-direction, when considering the failure in the matrix, the strain values are set to those in the 22-direction, with the ε^0 terms being calculated using Equations 1 to 4 and the ε^f terms being calculated using intra- and interlaminar ply fracture energies.

From the four failure variables, three damage variables are determined, d_f, d_m and d_s, as defined in Equations 6 to 8 below [52,82]:

Fibre damage: $$d_f = \begin{cases} d_{f,}^t & \hat{\sigma}_{11} \geq 0 \\ d_f^c, & \hat{\sigma}_{11} < 0 \end{cases} \quad (6)$$

Matrix damage: $d_m = \begin{cases} d_{m,}^t & \hat{\sigma}_{22} \geq 0 \\ d_m^c, & \hat{\sigma}_{22} < 0 \end{cases}$ (7)

Shear damage: $d_s = 1 - \left(1 - d_f^t\right)\left(1 - d_f^c\right)(1 - d_m^t)(1 - d_m^c)$ (8)

Additionally, for intralaminar damage, a maximum degradation value of 0.99 was specified to be consistent with previous work, rather than the default value of 1, so that damage evolution stops and elements are deleted when the damage variable reaches d_i $(i = f, m, s) \geq 0.99$.

7.2.3.2 Interlaminar Damage

The quadratic stress criterion was used to determine the initiation of interlaminar damage, which was implemented using the follow equation [52,82,124-128]:

$$\left(\frac{\langle t_{33} \rangle}{t_{33}^0}\right)^2 + \left(\frac{t_{31}}{t_{31}^0}\right)^2 + \left(\frac{t_{32}}{t_{32}^0}\right)^2 \geq 1 \quad (9)$$

where t_i $(i = 33, 31, 32)$ and t_i^0 $(i = 33, 31, 32)$ are the current and normal shear stresses and the current and normal cohesive law strengths, respectively, with the 33-, 31- and 32-directions being purely normal to the interface, the first shear and the second shear, respectively. When the above inequality is met, damage is assumed to initiate, allowing the displacement at this point to be calculated.

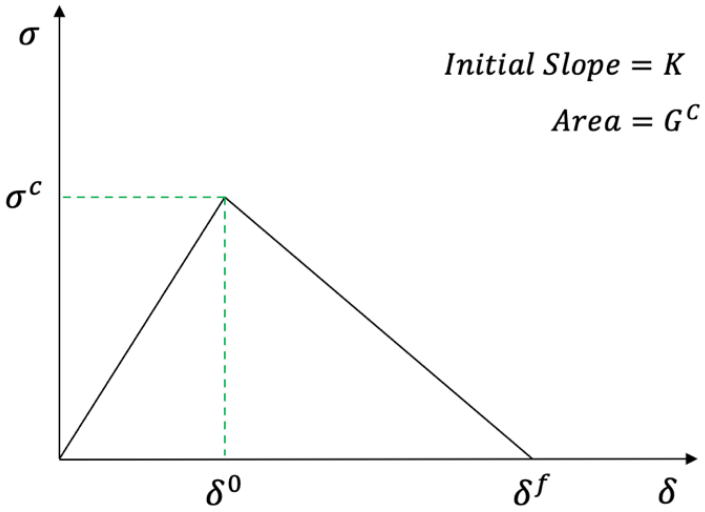

Figure 7-2. Diagram of the bilinear surface cohesive law, where the area under the curve is G_c.

How the interlaminar damage propagates during the impact event is simulated using a linear-softening material model embedded into a bilinear surface cohesive law [124], demonstrated in Figure 7-2. To simulate

this, a value for the interlaminar fracture energy, G_c, must be calculated, which is done using the Benzeggagh-Kenane (B-K) criterion demonstrated in Equation 10 [52,82,124,128-130]:

$$G_c = G_{Ic} + (G_{IIc} - G_{Ic}) \left[\frac{G_{II}}{G_I + G_{II}}\right]^{\eta} \quad (10)$$

where G_{Ic} and G_{IIc} are the Mode I and Mode II interlaminar fracture energies, respectively, and η is the B-K Mixed-mode interaction exponent. These three variables can be calculated experimentally [127,129,130], with the values used, given in Table 7-1, coming from the material supplier or literature. Lastly, G_I and G_{II} are the Mode I and Mode II energy-release rates, respectively, and are determined by the model. Delamination is said to occur when the value of displacement for an interface element is equal to or greater than the 0.9 times displacement of that element at failure, i.e. $\delta/\delta_f \geq 0.9$, with the results in the following section showing a red area of delamination for the elements that meet this criterion. This value was chosen to be more stringent in predicting the damage area.

To demonstrate how these equations are implemented within the model, the flowchart in Figure 7-3 can be referred to. This is taken from Liu et al. [52] and is very similar to the one implemented elsewhere, including [88].

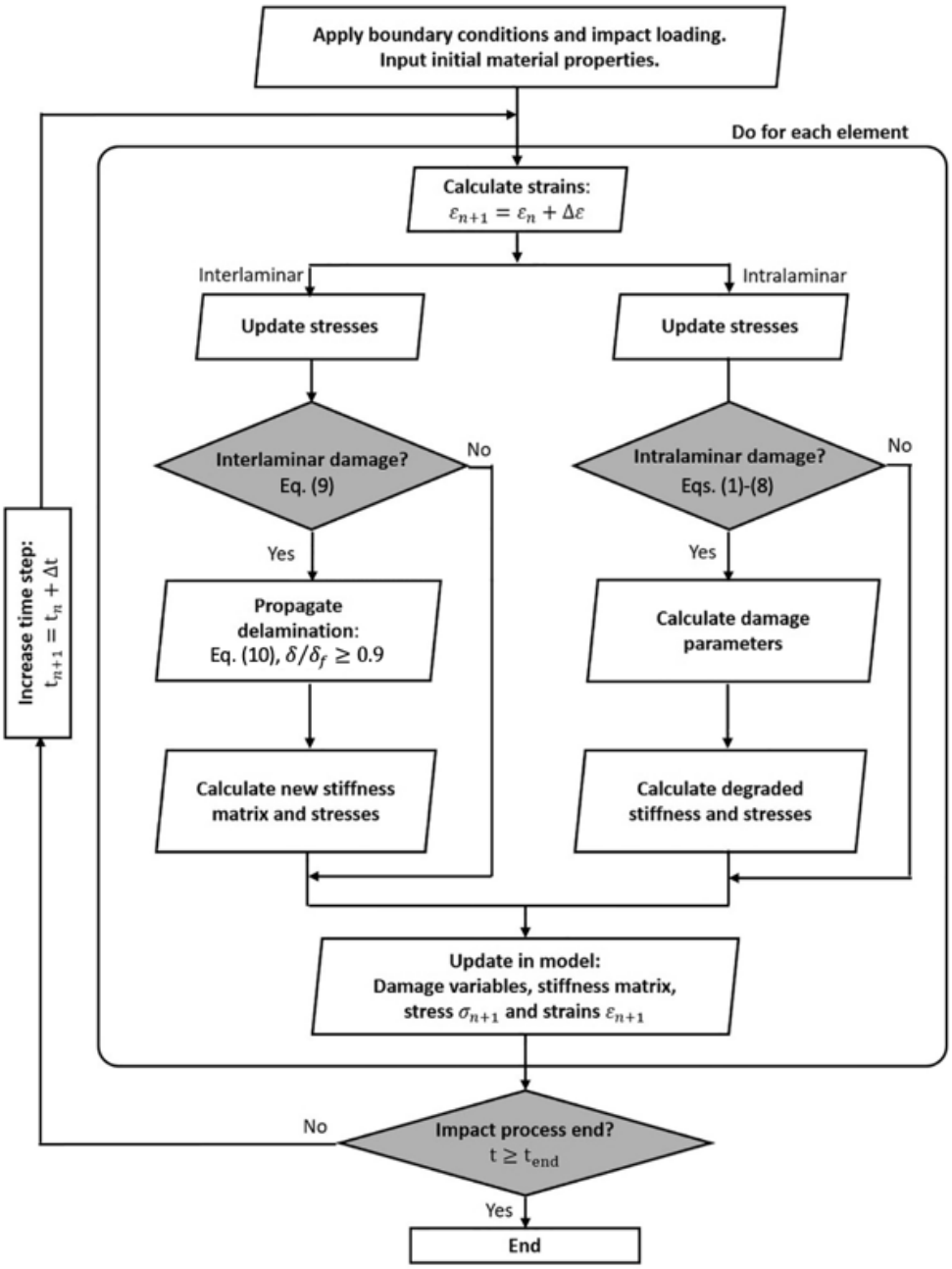

Figure 7-3. Flow chart demonstrating the implementation of Eqs. (1)-(10) to predict the impact response of CFRP panels using 2D Hashin Criteria [52].

7.2.3.3 Rubber Disk

From the literature [119,120], it was deemed that implementing the Neo-Hookean hyperelastic model would be an effective method to simulate the rubber disks on the impactor in the soft impact testing cases. The following equation for the strain energy potential is executed by the software, given in Abaqus documentation [124]:

$$U = c_{10}(\bar{I}_1 - 3) + \frac{1}{d_1}(J^{el} - 1)^2 \quad (11)$$

where U is the strain energy potential per unit volume, c_{10} and d_1 are material parameters and J^{el} is the elastic volume ratio. $\bar{I}_1$ is the first deviatoric strain invariant and is given by [124]:

$$\bar{I}_1 = \bar{\lambda}_1^2 + \bar{\lambda}_2^2 + \bar{\lambda}_3^2 \tag{12}$$

where $\bar{\lambda}_i = J^{-\frac{1}{3}}\lambda_i$ $(i = 1,2,3)$ are the deviatoric stretches and then J is the total volume ratio and λ_i $(i = 1,2,3)$ are the principal stretches.

7.3 Numerical modelling results

7.3.1 Pristine panels

The first scenarios to be considered when modelling were the round-nosed impacts, with three impact energies being simulated: 7.5, 15 and 30 J. The velocity of the impactor was the only variable adjusted between simulations to model the three impact energies. Once each simulation had finished, the damage maps were produced by colour-coding each point according to the value of the damage variables for each element. To give an estimate for the damage area, elements with a damage variable value above 0.9 were highlighted in red and the resulting damage maps are shown alongside the respective experimental c-scan images in Figure 7-4. Additionally, a plot of the damage variable value in every element for all of the cases presented in this chapter is given in Appendix E.

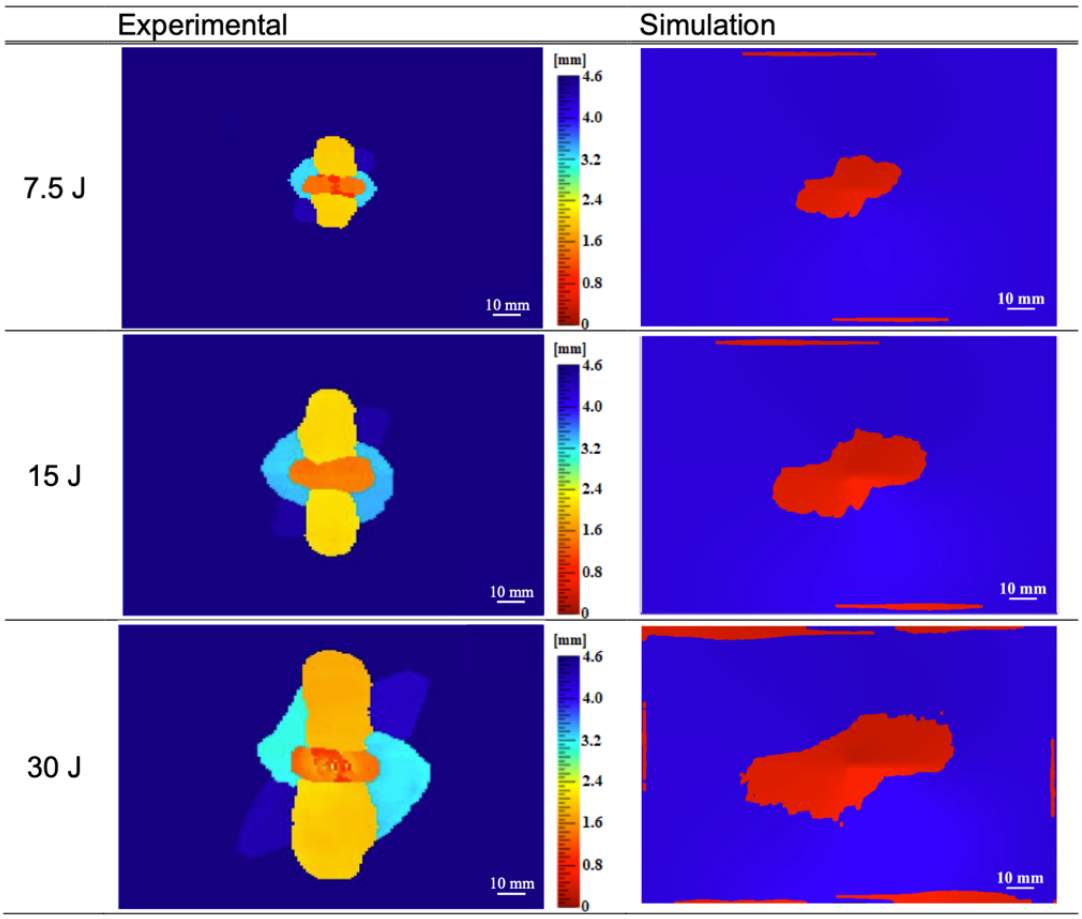

Figure 7-4. Damage maps from experimental testing and numerical simulation for impacts at 7.5, 15 and 30 J (with a damage variable of 0.9 for the numerical modelling).

As can be seen from Figure 7-4 above, the increase in impact energy causes the damage area to increase significantly. This matches the trends observed in the experimental work in Section 6.3.1, demonstrating the suitability of this model to predict how the CFRPs will perform under impact. Table 7-2 below compares the damage areas found experimentally and numerically.

Table 7-2. Damage area values for the experimental testing and numerical simulation results of round-nosed impacts at impact energies of 7.5, 15 and 30 J.

Impact Energy	Damage Area (mm^2)		Variation in Damage Areas
	Experimental	Numerical	
7.5 J	681	662	±1.4%
15 J	1986	1282	±21.5%
30 J	3602	2401	±20.0%

As can be seen by the values in Table 7-2, the model is accurate at predicting the damage area at the lowest impact energy, but above this the values differ significantly.

7.3.2 Effect of impactor shape

The effect of the impactor shape on the performance of the CFRP panels under impact was then considered with the model, by simulating both round-nosed and flat-ended impacts at 30 J. The flat-ended impactor was modelled with a fillet, as is present in the impactor used experimentally, to ensure as accurate a model as possible. As for the different impact energies simulated above, damage maps were produced by colour-coding each point according to the value of the damage variables for each element and compared to the respective experimental results.

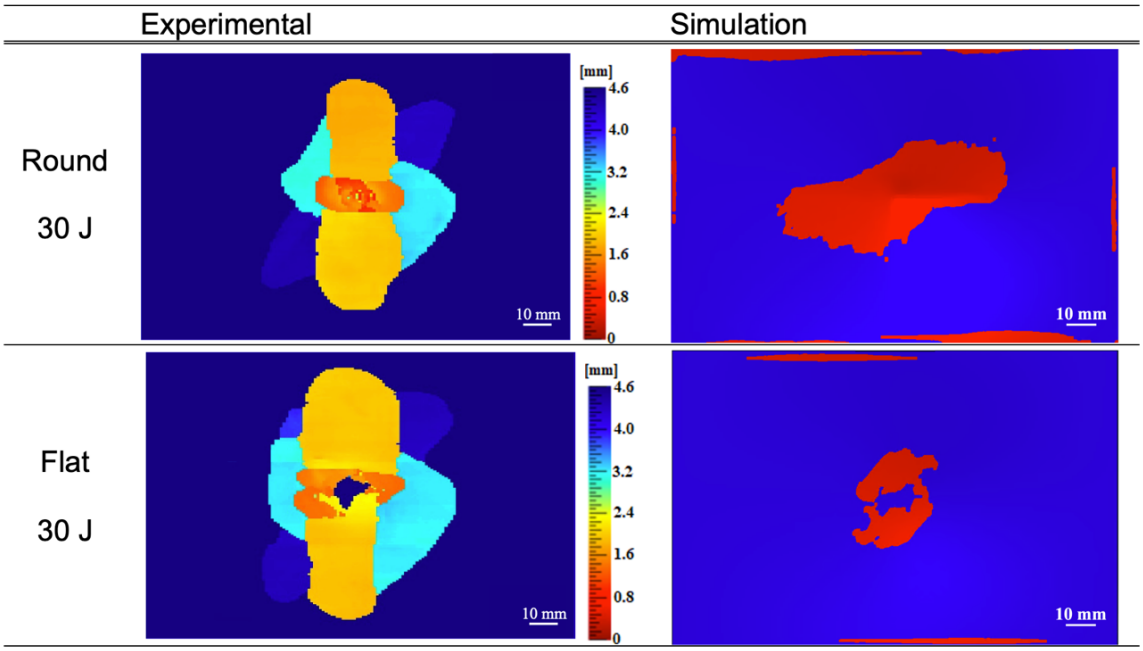

Figure 7-5. Damage maps from experimental testing and numerical simulation for impacts with a round-nosed impactor and a flat-ended impactor at 30 J (with a damage variable of 0.9 for the numerical modelling).

Figure 7-5 demonstrates an opposing trend to that observed in the experimental testing presented in Section 6.3.1, as the flat-ended impactor resulted in significantly less damage than the round-nosed impactor at the 30 J impact energy. This suggests that the model needs some refinement before it is used to predict the damage from these two impactor types at high impact energies, specifically with the simulation of the flat-ended impactor requiring some adjusting. However, the model does accurately predict the central area of no damage that is also seen experimentally. The experimental and numerical damage areas are given in Table 7-3.

Table 7-3. Damage area values for the experimental testing and numerical simulation results of round-nosed and flat-ended impacts at an impact energy of 30 J.

Impact Energy	Damage Area (mm^2)		Variation in Damage Areas
	Experimental	Numerical	
Round-nosed	3602	2401	20.0%
Flat-ended	4440	1069	61.2%

The variation in the damage areas recorded experimentally and predicted by the model given in Table 7-3, especially for the flat-ended impactor case, highlight the limitations of the model. The shape of the damage areas in Figure 7-5 demonstrates the potential in this model but these values show that some improvements are required before it can be utilised in the place of experimental work to determine how a CFRP panel will perform under impact.

7.3.3 Hard/soft impacts

The final case to be considered using the model was investigating the effect of implementing different thicknesses of rubber disks on the flat-ended impactor to compare hard and soft impact conditions. For this investigation, the flat-ended impactor modelled previously was again implemented and this time a rubber disk was also included. The only variable adjusted between each simulation was the thickness of the rubber disk, with 1, 1.5 and 2 mm all being simulated and all three being considered at an impact energy of 30 J. Again, damage maps were produced by colour-coding each point according to the value of the damage variables for each element and then compared with the experimental results. Figure 7-6 shows these diagrams to allow a comparison to be made between the three thicknesses of rubber.

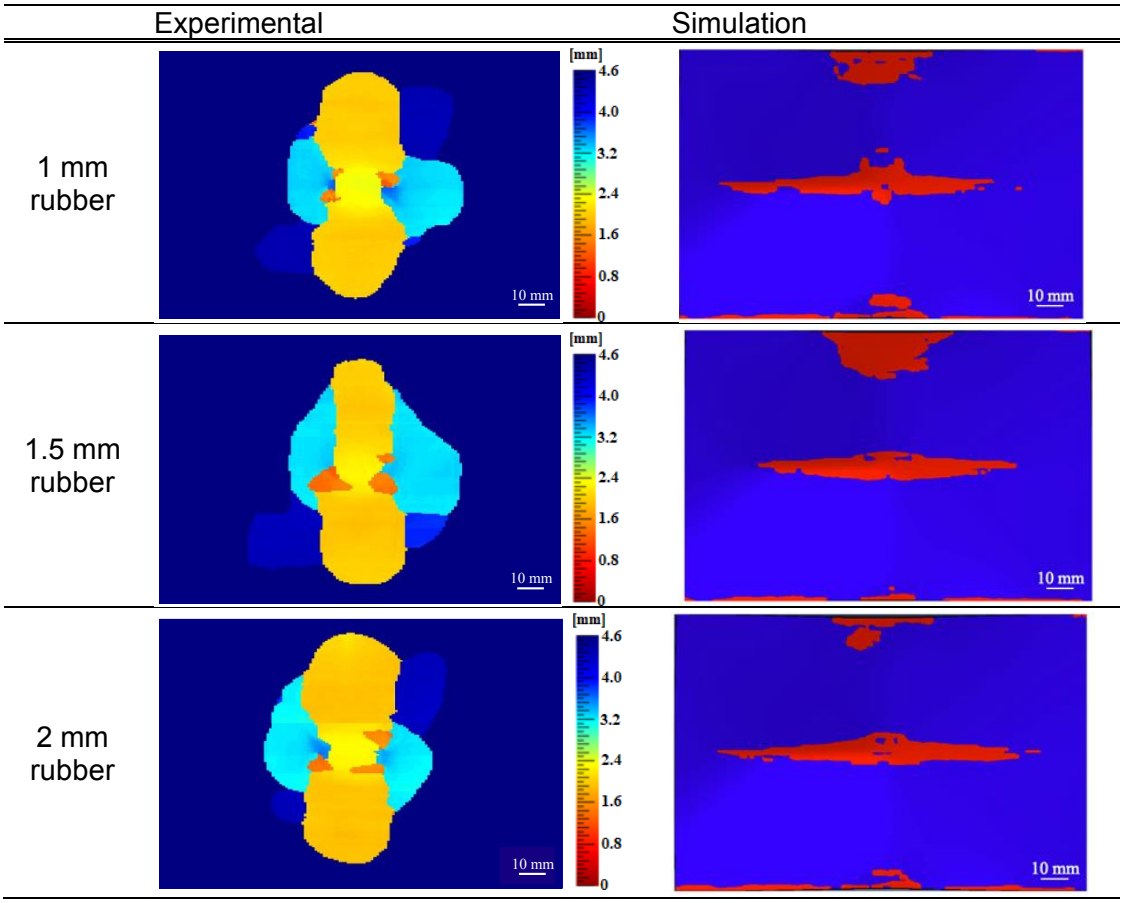

Figure 7-6. Damage maps from experimental testing and numerical simulation for impacts with a flat-ended impactor with 1, 1.5 and 2 mm of rubber at 30 J (with a damage variable of 0.9 for the numerical modelling).

Figure 7-6 generally shows the same trend as observed experimentally, with an increase in rubber thickness resulting in a reduction in the central damage. However, the model also results in significant delaminations on the top and bottom edge of the panel, which affect the damage areas presented in Table 7-4 below.

Table 7-4. Damage area values for the experimental testing and numerical simulation results of flat-ended impacts with 1, 1.5 and 2 mm rubber disks at an impact energy of 30 J.

Impactor	Damage Area (mm^2)		Variation in Damage Areas
	Experimental	Numerical	
1 mm rubber	4308	1465	±49.2%
1.5 mm rubber	4250	1582	±45.7%
2 mm rubber	4144	1299	±52.2%

From the results in Table 11, it can be seen that the predictions of damage area are largely different from those observed experimentally and also that the numerical analysis of the case with 1.5 mm of rubber is an outlier with regards to the trend observed. The models of the 1 and 2 mm rubber disks give a difference in damage area of 166 mm^2, which has good agreement with the difference of 164 mm^2 measured experimentally. This suggests that this model is an effective method of predicting the performance of CFRP panels under impact loading conditions, but just that some refinement and adjustments are required to improve the accuracy in certain areas.

7.3.4 Discussion

Although the modelling results presented in the chapter do not have good agreement with the size of damage areas observed experimentally, the general trends and damage footprints found show the potential effectiveness of this simulation for predicting experimental results if further development is carried out. The model can be seen to be very effective at an impact energy of 7.5 J, with only a variation in damage area of ±1.4%, and also at predicting the general trends when comparing impact energies and the effect of increasing the softness of the impact. Additionally, the difference in damage areas between the impact cases with 1 and 2 mm of rubber adhered to the flat-ended impactor only varied by 2 mm^2 between the experimental and numerical results. These results show that the 2D Hashin criterion and other formulae used to determine damage initiation and evolution are a viable option for simulating the testing performed in other sections in this thesis, but that further iterations and optimisation is required for more accurate results in the areas that are currently significantly dissimilar to the experimental results, namely the damage area values.

8 Conclusions

8.1 Introduction

From the research in this thesis, a number of conclusions can be drawn about the performance of CFRP panels under a variety of impact conditions. These conclusions are laid out in this section and a short summary of what the main points are that can be taken from this work is given for each chapter.

8.2 Effects of the patch properties on the impact performance of repaired quasi-isotropic CFRPs

These conclusions come from the following paper: 'The effectiveness of patch repairs to restore the impact properties of carbon-fibre reinforced-plastic composites' [83].

In conclusion, impact testing on pristine CFRP and CFRP patch-repair panels has been performed to investigate the suitability of a single-sided, adhesively bonded CFRP patch to restore the impact properties of damaged CFRP panels. The primary findings were:

- Interlaminar damage observed from the ultrasonic C-scans is clearly linked to a marked initiation load drop in the load versus time and load versus displacement traces. The delaminations form between plies of different fibre orientations and tend to grow along the orientation of the ply beneath the delamination.
- Repeat impacts on pristine panels at 7.5, 10.5 and 30 J demonstrated that the damage area increases by almost 50% when impacted for a second time. Impacting for a third time at 30 J implied an upper-damage threshold that the panel can sustain, with only a small (i.e., 5.4%) incremental increase in the damage area in comparison to the third impact at 7.5 J.
- Using a patch-repair of half the thickness of the parent panel, with no plug, produced delamination damage greater in extent than the pristine panel incurred, but it was all contained within the patch and did not spread into the parent panel. These observations arise since the thin patch, when it is not supported by a plug, deforms relatively easily and the localised strain gradients that result initiate damage more readily at a lower initiation load.

- Using a thicker patch of the same thickness as the parent material, but with no plug, resulted in a lower extent of delamination damage, at 7.5 J, but this was still more than that observed for the pristine panel for the same impact energy. Again, the delamination damage was contained within the patch and thus protected the surrounding parent material.
- Using a patch of half the thickness of the parent panel, together with a plug of identical thickness and lay-up to the parent panel, resulted in impact properties superior to that of the pristine CFRP panel, suggesting that this is a very good patch-repair configuration. Indeed, the delamination area in the patch was found to be less than that seen in the pristine panel for the same impact energy.
- For a given design, there were found to be no clear, major overall benefits to be gained by increasing the patch diameter from 55 mm to 65 mm.
- To summarise, patch-repair panels with either a plug, or having a relatively thick patch, give higher values of peak load and a lower maximum displacement than that recorded for the pristine panel upon testing at a given impact energy. However, the patch-repair panels manufactured using a plug are the only designs that produce a resulting interlaminar damage area that is smaller than that seen in the pristine panels, tested at the same impact energy. Thus, adding a CFRP plug when undertaking a patch-repair clearly increases the structural performance of the repaired CFRP panel.

8.3 Effects of impact location on repaired cross-ply CFRPs under low-velocity impact loading

In conclusion, pristine and patch repaired CFRP panels have been tested under impact loading conditions to assess the effect of impact location on the performance of the repair in restoring the impact properties after damage. The primary findings were:

- At the two lower impact energy values a pristine panel was repeat impacted at, the second impact only led to propagation of the damage initiated by the first impact rather than introducing new damage mechanisms. Contrastingly, at 30 J, new damage mechanisms were introduced on the second impact, as is demonstrated by the load drop and change in gradient on the load versus time trace, which is indicative of damage initiation.

- The further from the centre of the repair that the impact location is, the more similarly the repair performs to a pristine panel impacted at the same energy. This is likely due to the effective thickness at the impact site and, at the impact site furthest from the centre of the repair, this being the same as a pristine panel.
- The nearer to the centre of the repair that the impact location is, the more effect the inclusion of a plug has on the performance of the repair. This is again likely to do with the effective thickness at the impact site as, with a central repair, the thickness increases from 0.5t to 1.5t with the addition of a plug. At the edge of the hole, the thickness also increases from 0.5t to 1.5t but only on one side of the impact site, with the other side having a thickness of 1.5t with and without a plug. And, at an impact site off the patch, the thickness is a constant with or without a plug.
- The largest total damage area was found to be in the edge of hole offset repair case without a plug as damage occurred in both the patch and the parent panel. Contrastingly, in both other repair cases, the damage was limited to either the patch or the parent panel. This highlights that the adhesive join of the repair and an impact site that results in damage in both the patch and the parent panel is the point in the repair that is the most susceptible to damage.
- What was thought to be dislodgement of the plug for the central repair case was seen to be a delamination that extended across the diameter of the plug between the first and second ply, causing a split and for the remaining plies to be pushed out from underneath the patch. This shows that damage was introduced in the plug in this case and to prevent this failure in the future the diameter of the plug or the thickness of the patch would potentially need to be increased.

8.4 Effects of impactor shape and hardness on the failure modes in CFRPs

In conclusion, impact testing has been performed on pristine CFRP panels using five different impactors to investigate the effect of the impactor shape and hardness on the performance of CFRPs under impact. The primary findings were:

- Both the hardness and the shape of the impactor affect the performance of the panels under low velocity impact conditions.

- The round-nosed impactor was found to have a much lower damage initiation energy than the flat-ended impactor, which is most likely due to the blunt impactor distributing the energy more evenly over the surface rather than concentrating it at one point.

- At the impact energy where damage did occur from the flat-ended impactor, the round-nosed impactor gave a smaller damage area and displaced the panel further. This suggests that, although damage initiated at a lower energy, the panel was able to deform more around the impactor and thus absorb more of the energy.

- The addition of rubber caused the peak load, and therefore the damage initiation load, to decrease and the displacement to increase whilst also potentially reducing the damage area. This implies that the rubber absorbed some of the energy by acting as a dampener.

8.5 Numerical modelling of hard and soft impacts

In conclusion, a FEA model in conjunction with damage criteria has been implemented to produce a numerical simulation to investigate the effect of the impactor shape and hardness on the performance of CFRPs under impact. The primary findings were:

- At low impact energies, specifically 7.5 J, the model predicts a damage area very similar to that of the experimental testing, with a variation of ±1.4%. This demonstrates the effectiveness of the model to simulate the experiments presented in Chapter 6.
- The general trends observed experimentally when considering increasing the impact energy and softness of the impactor are reflected in the numerical analysis results. This suggests that the model, as it stands, could be used to predict the trends that will be seen in experimentation, even if the damage areas outputted are not in good agreement.
- When simulating the effect of softening the impact, the variation in damage area between an impact with a 1 mm rubber disk and a 2 mm one was seen to be 166 mm^2 and, in the case of the experimental testing, this value was measured to be 164 mm^2. This gives a difference between the numerical and experimental results for this value of only 2 mm^2, highlighting further the promising results of the modelling performed in this chapter.

- The damage areas are significantly different for the higher impact energies and not all trends observed experimentally were reflected numerically, implying that further development and optimisation of this model is required for it to be implemented as a method of predicting experimental results and determining what experiments should be performed.

8.6 Summary

In summary, the work in this thesis demonstrates the potential of patch repairs to restore the impact properties of CFRP panels, the effect of different impactor properties on the performance of the panels and also the strengths and weaknesses of the FEA model developed as part of this research.

9 Future Work

9.1 Introduction

The work in this thesis lends itself to further work continuing the research to allow more of an understanding about the response of CFRP panels under different types of impacts. Only a small number of variables have been considered and evaluated and building on this would be invaluable. Two potential areas for further research are outlined in this section.

9.2 Performance of repaired CFRP panels under high-velocity impact loading

This thesis focused on the performance of pristine and patch repaired CFRP panels under low-velocity impacts, but it would be of interest to consider the performance of repaired panels under high-velocity impact as the research in this area is currently very limited. Looking at patch repaired panels subjected to high velocity impacts might show some very interesting results with regards to how the adhesive joint performs and whether it remains intact enough to ensure the patch does not detach from the panel.

9.3 Quasi-static testing of repaired CFRP panels

Another area that would be interesting to consider would be quasi-static testing of pristine and repaired CFRP panels and then comparing this to the testing in this thesis. Loading the panels at a slower rate might give some interesting results and the opportunity to observe how the damage progresses over time.

9.4 Patch repair of biodegradable composites

Composite materials as a concept are not extremely environmentally friendly since two different materials are combined and cannot then be separated at the end of their use. This means that, often, the composite components are buried as a means of disposal with the hope that future generations might be able to find a solution to the problem. However, the fact they are often more lightweight than alternative materials results in a reduction in emissions, which is extremely beneficial both economically and environmentally. For this reason, developing a composite material that retains the lightweight quality and strength characteristics of the current options but is produced from biodegradable materials is an area of interest. Current research includes

biodegradable polymers, such as PLA, reinforced with natural fibres, such as hemp. These studies have found that there is potential in these bio-composites to meet the requirements, however their performance is still lacking in comparison to conventional composites, such as CFRPs. In the development of bio-composites, it would be beneficial and crucial to consider the repair process and perform similar testing to that in this thesis. This would allow for further advantages environmentally but might also show the durability of bio-composites and adhesive joints between them or highlight weaknesses that need further consideration.

9.5 Model development

The model produced and utilised in Chapter 7 showed a lot of potential for predicting the damage areas for different levels of hardness of impactor and impact energy. However, the variation between experimental and numerical results highlights the limitations of this model and the importance of continuing development to reduce the difference in results before implementation. The aim is to produce a model that can be used to predict experimental results before testing begins to inform the decisions on what testing cases are considered. To reach this point, a 3D Hashin model could be utilised instead of the current 2D Hashin model. This would allow for more variables that can be adjusted to give the most accurate simulation results since, in the 2D case, all the relevant variables have already been considered. Using the 3D Hashin criteria has already been implemented with excellent results in other testing cases, but not yet for this work as these initial results were critical to obtain and will be extremely useful to dictate the properties used in the 3D case.

10 References

[1] Clark, G. & Van Blaricum, T. J. (1987). Load spectrum modification effects on fatigue of impact-damaged carbon fibre composite coupons. *Composites*. 18 (3), 243-251. https://doi.org/10.1016/0010-4361(87)90414-9.

[2] Rider, A. N., Wang, C. H. & Chang, P. (2010). Bonded repairs for carbon/BMI composite at high operating temperatures*. Composites Part A.* 41, 902-912. https://doi.org/10.1016/j.compositesa.2010.03.006.

[3] Wang, C. H. & Gunnion, A. (2006). *Design Methodology for Scarf Repairs to Composite Structures.* Australian Government Dept. of Defence, Defence Science and Technology Organisation. Report number: DSTO-RR-0317.

[4] Archer, E. & McIlhagger, A. (2015). Repair of damaged aerospace composite structures. *Polymer Composites in the Aerospace Industry.* 393-412. https://doi.org/10.1016/B978-0-85709-523-7.00014-1.

[5] Pinto, A. M., Campilho, R. D., de Moura, M. F. & Mendes, I. R. (2010). Numerical evaluation of three-dimensional scarf repairs in carbon-epoxy structures. *International Journal of Adhesion and Adhesives.* 30 (5), 329-337. https://doi.org/10.1016/j.ijadhadh.2009.11.001.

[6] Katnam, K. B., Da Silva, L. F. & Young, T. M. (2013). Bonded repair of composite aircraft structures: A review of scientific challenges and opportunities. *Progress in Aerospace Sciences.* 61, 26-42. https://doi.org/10.1016/j.paerosci.2013.03.003.

[7] Baker, A., Bitton, D. & Wang, J. (2012). Development of a proof test for through-life monitoring of bond integrity in adhesively bonded repairs to aircraft structures. *International Journal of Adhesion and Adhesives.* 36, 65-76. https://doi.org/10.1016/j.ijadhadh.2012.03.004.

[8] Baker, A., Rose, F. & Jones, R. (eds.) (2003). *Advances in the Bonded Composite Repair of Metallic Aircraft Structure.* Amsterdam, Elsevier Science.

[9] Preau, M. & Hubert, P. (2016). Processing of co-bonded scarf repairs: Void reduction strategies and influence on strength recovery. *Composites Part A.* 84, 236-245. https://doi.org/10.1016/j.compositesa.2016.01.016.

[10] Abrate, S. (2016). Soft impacts on aerospace structures. *Progress in Aerospace Sciences.* 81, 1-17. https://doi.org/10.1016/j.paerosci.2015.11.005.

[11] Koechlin, P. & Potapov, S. (2009). Classification of soft and hard impacts – Applications to aircraft crash. *Nuclear Engineering and Design.* 239 (4), 613-8. https://doi.org/10.1016/j.nucengdes.2008.10.016.

[12] Kashtalyan, M. & Soutis C. (2005). Analysis of composite laminates with intra- and interlaminar damage. *Progress in Aerospace Sciences*. 41 (2), 152-73. https://doi.org/10.1016/j.paerosci.2005.03.004.

[13] Shuart, M.J. (1989). Failure of compression-loaded multidirectional composite laminates. *AIAA Journal*. 27 (9), 1274-9. https://doi.org/10.2514/3.10255.

[14] Zhao, L., Qin, T., Zhang, J. & Chen, Y. (2015). 3D gradual material degradation model for progressive damage analyses of unidirectional composite materials. *Mathematical Problems in Engineering*. 5, 1-11. https://doi.org/10.1155/2015/145629.

[15] Ogin, S.L., Brondsted, P. & Zangenberg, J. (2016). Composite materials: constituents, architecture, and generic damage. In: Talreja R. & Varna, J. (eds). *Modelling Damage, Fatigue and Failure of Composite Materials*. Woodhead Publishing Series in Composites Science and Engineering (65). Sawston, Cambridgeshire, UK, Woodhead Publishing. 3-23. https://doi.org/10.1016/B978-1-78242-286-0.00001-7.

[16] Yang, L., Yan, Y., Liu, Y. & Ran, Z. (2012). Microscopic failure mechanisms of fiber-reinforced polymer composites under transverse tension and compression. *Composites Science and Technology*. 72 (15), 1818-25. https://doi.org/10.1016/j.compscitech.2012.08.001.

[17] Berbinau, P., Soutis, C. & Guz, I.A. (1999). Compressive failure of 0° unidirectional carbon-fibre-reinforced plastic (CFRP) laminates by fibre microbuckling. *Composites Science and Technology*. 59 (9), 1451-5. https://doi.org/10.1016/S0266-3538(98)00181-X.

[18] Soutis, C. (1991). Measurement of the static compressive strength of carbon-fibre/epoxy laminates. *Composites Science and Technology*. 42 (4), 373-92. https://doi.org/10.1016/0266-3538(91)90064-V.

[19] Schultheisz, C. & Waas, A. (1996). Compressive failure of composites, part I: testing and micromechanical theories. *Progress in Aerospace*. 32 (1), 1-42. https://doi.org/10.1016/0376-0421(94)00002-3.

[20] Guynn, E.G., Bradley, W.L. & Ochoa, O.O. (1992). A parametric study of variables that affect fiber microbuckling initiation in composites laminates: part 2 – experiments. *Journal of Composite Materials*. 26 (11), 1594-627. https://doi.org/10.1177/002199839202601104.

[21] Soutis, C. (1997). Compressive strength of unidirectional composites: measurement and predictions. In: Hooper, S.J. (ed). *Composite Materials: Testing and Design*. (13th ed). Pennsylvania, USA, ASTM STP. 168-76.

[22] Soutis, C. & Turkmen, D. (1997). Moisture and temperature effected of the compressive failure of CFRP unidirectional laminates. *Journal of Composite Materials*. 31 (8), 832-48. https://doi.org/10.1177/002199839703100805.

[23] Fleck, N.A., Budiansky, B. (1991). Compressive Failure of Fibre Composites Due to Microbuckling. In: Dvorak, G.J. (eds) *Inelastic Deformation of Composite Materials*. International Union of Theoretical and Applied Mechanics. Springer, New York, NY. 235-73. https://doi.org/10.1007/978-1-4613-9109-8_12.

[24] Evans, A.G. & Adler, W.F. (1978). Kinking as a mode of structural degradation in carbon fiber composites. *Acta Metallurgica.* 26 (5), 725-38. https://doi.org/10.1016/0001-6160(78)90023-8.

[25] Hahn, H.T. & Williams, J.G. (1986). Compression failure mechanisms in unidirectional composites. In: Whitney, J.M. (ed). *Composite Materials: Testing and Design*. (7th ed). Pennsylvania, USA, ASTM STP. 115-39.

[26] Weaver, C.W. & Williams, J.G. (1975). Deformation of carbon-epoxy composite under hydrostatic pressure. *Journal of Materials Science*. 10, 1323-33. https://doi.org/10.1007/BF00540822.

[27] Moran, P.M., Liu, X.H. & Shih, C.F. (1995). Kink band formation and band broadening in fiber composites under compressive loading. *Acta Metallurgica et Materialia*. 43 (8), 2943-58. https://doi.org/10.1016/0956-7151(95)00001-C.

[28] Brunbauer, J. & Pinter, G. (2015). Effects of mean stress and fibre volume content on the fatigue-induced damage mechanisms in CFRP. *International Journal of Fatigue*. 75, 28-38. https://doi.org/10.1016/j.ijfatigue.2015.01.014.

[29] Dassios, K.G. (2007). A review of the pull-out mechanism in the fracture of brittle-matrix fibre-reinforced composites. *Advanced Composites Letters*. 16 (1), 17-24. https://doi.org/10.1177/096369350701600102.

[30] Short, G.J., Guild F.J. & Pavier, M.J. (2001). The effect of delamination on the compressive failure of composite laminates. *Composites Science and Technology*. 61 (14), 2075-86. https://doi.org/10.1016/S0266-3538(01)00134-8.

[31] Pavier, M.J. & Clarke, M.P. (1995). Experimental techniques for the investigation of the effects of impact damage on carbon fibre composites. *Composites Science and Technology*. 55 (2), 157-69. https://doi.org/10.1016/0266-3538(95)00097-6.

[32] Sekine, H., Flu, N. & Kouchakzadeh, M.A. (2000). Buckling analysis of elliptically delaminated composite laminates with consideration of partial closure of delamination. *Journal of Composite Materials*. 34 (7), 551-74. https://doi.org/10.1177/002199830003400702.

[33] Peck, S.O. & Springer, G.S. (1991). The behaviour of delaminations in composite plates – analytical and experimental results. *Journal of Composite Materials*. 25 (7), 907-29. https://doi.org/10.1177/002199839102500708.

[34] Bolotin, V.V. (1996). Delaminations in composite structures: its origin, buckling, growth and stability. *Composites Part B: Engineering*. 27 (2), 129-45. https://doi.org/10.1016/1359-8368(95)00035-6.

[35] Kardomateas, G.A. & Schmueser, D.W. (1988). Buckling and postbuckling of delaminated composites under compressive loads including transverse shear effects. *AIAA Journal*. 26 (3), 373-43. https://doi.org/10.2514/3.9894.

[36] Hashemi, S., Kinlock, A.J. & Williams, J.G. (1990). The analysis of interlaminar fracture in uniaxial fibre-polymer composites. *Proceedings of The Royal Society A: Mathematical, Physical and Engineering Sciences*. 472 (1872), 173-99. https://doi.org/10.1098/rspa.1990.0007.

[37] Choi, N.S., Kinloch, A.J. & Williams, J.G. (1999). Delamination fracture of multidirectional carbon-fiber/epoxy composites under mode I, mode II and mixed-mode I/II loading. *Journal of Composite Materials.* 33 (1), 73-100. https://doi.org/10.1177/002199839903300105.

[38] Rountree C.L., Kalia, R.K., Lidorikis, E., Nakano, A., Van Brutzel, L. & Vashishta, P. (2002). Atomistic aspects of crack propagation in brittle materials: multimillion atom molecular dynamics simulations. *Annual Review of Materials Research.* 12 (32), 377-400. https://doi.org/10.1146/annurev.matsci.32.111201.142017.

[39] Liu, B., Xu, F., Qin, J. & Lu, Z. (2017). Study on impact damage mechanisms and TAI capacity for the composite scarf repair of the primary load-bearing level. *Composite Structures.* 181, 183-193. https://doi.org/10.1016/j.compstruct.2017.08.087.

[40] Liu, B., Han, Q., Zhong, X. & Lu, Z. (2019). The impact damage and residual load capacity of composite stepped bonding repairs and joints*. Composites Part B*. 158, 339-351. https://doi.org/10.1016/j.compositesb.2018.09.096.

[41] Atas, C., Akgun, Y., Dagdelen, O., Icten, B.M. & Sarikanat, M. (2011). An experimental investigation on low velocity impact response of composite plates repaired by VARIM and hand lay-up process*. Composite Structures*. 93 (3), 1178-1186. https://doi.org/10.1016/j.compstruct.2010.10.002.

[42] Li, H.C.H., Mitrevski, T. & Herszberg, I. (2006). Impact on bonded repairs to CFRP laminates under load. In: *2006 25th International Congress of the Aeronautical Sciences, Hamburg, Germany.*

[43] Herszberg, I., Feih, S., Gunnion, A. J. & Li, H.C.H. (2007). Impact damage tolerance of tension loaded bonded scarf repairs to CFRP laminates. In: *16th International Conference on Composite Materials, Kyoto, Japan.*

[44] Tie, Y., Hou, Y., Li, C., Zhou, X., Sapanathan, T. & Rachik, M. (2018). An insight into the low-velocity impact behaviour of patch repaired CFRP laminates using numerical and experimental approaches*. Composite Structures*. 190, 179-188. https://doi.org/10.1016/j.compstruct.2018.01.075.

[45] Andrew, J.J., Srinivasan, S.M. & Arockiarajan, A. (2019). Influence of patch lay-up configuration and hybridisation on low velocity impact and post-impact tensile response of repaired glass fibre reinforced plastic composites. *Journal of Composite Materials.* 53 (1), 3-17. https://doi.org/10.1177/0021998318779430.

[46] Coelho, S.R.M., Reis, P.N.B., Ferreira, J.A.M. & Pereira, A.M. (2017). Effects of external patch configuration on repaired composite laminates subjected to multi-impacts. *Composite Structures.* 168, 259-265. https://doi.org/10.1016/j.compstruct.2017.02.069.

[47] Harman, A.B. & Rider, A.N. (2011). Impact damage tolerance of composite repairs to highly-loaded, high temperature composite structures. *Composites Part A.* 42 (10), 1321-1334. https://doi.org/10.1016/j.compositesa.2011.05.015.

[48] Liu, S.F., Cheng, X.Q., Xu, Y.Y., Bao, J.W. & Guo, X. (2015). Study on impact performances of scarf-repaired carbon fibre reinforced polymer laminates. *Journal of Reinforced Plastics and Composites.* 34 (1), 60-71. https://doi.org/10.1177/0731684414562465.

[49] Hou, Y., Tie, Y., Li, C., Sapanathan, T. & Rachik, M. (2019). Low-velocity impact behaviours of repaired CFRP laminates: Effect of impact location and external patch configurations*. Composites Part B*. 163, 669-680. https://doi.org/10.1016/j.compositesb.2018.12.153.

[50] Balaganesan, G. & Khan, V.C. (2016). Energy absorption of repaired composite laminates subjected to impact loading*. Composites Part B*. 98, 39-48. https://doi.org/10.1016/j.compositesb.2016.04.083.

[51] Dau, F., Dano, M.-L. & Duplessis-Kergomard, Y. (2016). Experimental investigations and variability considerations on 3D interlock textile composites used in low velocity soft impact loading. *Composite Structures.* 153, 369-79. https://doi.org/10.1016/j.compstruct.2016.06.034.

[52] Liu, H., Liu, J., Kaboglu, C., Zhou, J., Kong, X., Blackman, B.R.K., Kinloch, A.J. & Dear, J.P. (2020). The behaviour of fibre-reinforced composites subjected to a soft impact-loading: An experimental and numerical study. *Engineering Failure Analysis*. 111, 104448. https://doi.org/10.1016/j.engfailanal.2020.104448.

[53] Liu, J., Kaboglu, C., Liu, H., Blackman, B.R.K., Kinloch, A.J. & Dear, J.P. (2018). High speed digital image correlation for impact performance of thermoplastic and thermoset composites. In: *18th European Conference on Composite Materials, Athens, Greece.*

[54] Heimbs, S. & Bergmann, T. (2012). High-velocity impact behaviour of prestressed composite plates under bird strike loading. *International Journal of Aerospace Engineering.* 2012, 372167. https://doi.org/10.1155/2012/372167.

[55] Liu, J., Liu, H., Kaboglu, C., Kong, X., Ding, Y., Chai, H., Blackman, B.R.K., Kinloch, A.J. & Dear J.P. (2019). The impact performance of woven-fabric thermoplastic and thermoset composites subjected to high-velocity soft- and hard-impact loading. *Applied Composite Materials.* 26, 1389-410. https://doi.org/10.1007/s10443-019-09786-2.

[56] Liu, H., Liu, J., Kaboglu, C., Chai, H., Kong, X., Blackman, B.R.K., Kinloch, A.J. & Dear, J.P. (2020). Experimental investigations on the effects of projectile hardness on the impact response of fibre-reinforced composite laminates. *International Journal of Lightweight Materials and Manufacture.* 3 (2), 77-87. https://doi.org/10.1016/j.ijlmm.2019.10.001.

[57] Mitrevski, T., Marshall, I.H., Thomsom, R., Jones, R. & Whittingham, B. (2005). The effect of impactor shape on the impact response of composite laminates. *Composite Structures.* 67 (2), 139-48. https://doi.org/10.1016/j.compstruct.2004.09.007.

[58] Mitrevski, T., Marshall, I.H., Thomsom, R. & Jones, R. (2006). Low-velocity impacts on preloaded GFRP specimens with various impactor shapes. *Composites Structures.* 76 (3), 209-17

[59] Kazemianfar, B., Esmaeeli, M. & Nami, M.R. (2020). Response of 3D woven composites under low velocity impact with different impactor geometries. *Aerospace Science and Technology.* 102, 105849. https://doi.org/10.1016/j.ast.2020.105849.

[60] Diamanti, K. & Soutis, C. (2010). Structural health monitoring techniques for aircraft composite structures*. Progress in Aerospace Sciences.* 46 (8), 342-352. https://doi.org/10.1016/j.paerosci.2010.05.001.

[61] Komorowski, J. P., Simpson, D. L. & Gould, R. W. (1990). A technique for rapid impact damage detection with implication for composite aircraft structures. *Composites.* 21 (2), 169-173. https://doi.org/10.1016/0010-4361(90)90009-L.

[62] Marty, P. N., Desai, N. & Andersson, J. (2004). NDT of kissing bond in aeronautical structures. In: *2004 16th World Conference on NDT, Montreal, Canada.*

[63] Wood, M., Charlton, P. & Yan, D. (2014). Ultrasonic evaluation of artificial kissing bonds in CFRP composites. *The e-Journal of Nondestructive Testing.* 19 (12).

[64] Yan, D., Drinkwater, B. W. & Neild, S. A. (2009). Measurement of the ultrasonic nonlinearity of kissing bonds in adhesive joints. *NDT & E International.* 42 (5), 459-466. https://doi.org/10.1016/j.ndteint.2009.02.002.

[65] Deane, S., Avdelidis, N. P., Ibarra-Castanedo, C., Zhang, H., Nezhad, H. Y., Williamson, A. A., Mackley, T., Davis, M. J., Maldague, X. & Tsourdos, A. (2019). Application of NDT thermographic imaging of aerospace structures. *Infrared Physics and Technology.* 97, 456-466. https://doi.org/10.1016/j.infrared.2019.02.002.

[66] Grammatikos, S. A., Kordatos, E. Z., Matikas, T. E. & Paipetis, A. S. (2013). Real-time debonding monitoring of composite repaired materials via electrical, acoustic and thermographic methods. *Journal of Materials Engineering and Performance.* 23, 169-180. https://doi.org/10.1007/s11665-013-0672-2.

[67] Cantwell, W.J. & Morton, J. (1992). The significance of damage and defects and their detection in composite materials: A review. *The Journal of Strain Analysis for Engineering Design*. 27 (1), 29-42. https://doi.org/10.1243/03093247V271029.

[68] Hanhan, I, Agyei, R., Xiao, X. & Sangid, M.D. (2019). Comparing non-destructive 3D X-ray computed tomography with destructive optical microscopy for microstructural characterization of fiber reinforced composites. *Composites Science and Technology*. 184, 107843. https://doi.org/10.1016/j.compscitech.2019.107843.

[69] Hayes, B.S. & Gammon, L.M. (2012). *Optical microscopy of fiber-reinforced composites*. Ohio, USA, ASM International.

[70] ATA Scientific Instruments. (2018). *Under the microscope: key differences between SEM and optical microscopy*. https://www.atascientific.com.au/microscope-key-differences-sem-optical-microscopy/ [Accessed 20th June 2022].

[71] Purslow, D. (1988). Fractography of fibre-reinforced thermoplastics, Part 3. Tensile, compressive and flexural failures. *Composites*. 19 (5), 358-66. https://doi.org/10.1016/0010-4361(88)90123-1.

[72] Morris, G.E. (1978). Determining fracture directions and fracture origins on failed graphite/epoxy surfaces. In: Pipes, R.B. (ed). *Nondestructive evaluation and jaw criticality for composite materials*. Pennsylvania, USA, ASTM STP. 274-97.

[73] Mukhopadhyay, A. (2015). *Measure of magnetic hysteresis loops in continuous and patterned ferromagnetic nanostructures by static magneto-optical kerr effect magnetometer*. Satyendra Nath Bose National Centre for Basic Sciences.

[74] Xin, S.H. & Wen, H.M. (2015). A progressive damage model for fibre reinforced plastic composites subjected to impact loading. *International Journal of Impact Engineering.* 75, 40-52. https://doi.org/10.1016/j.ijimpeng.2014.07.014.

[75] Ansari, M.M. & Chakrabarti, A. (2016). Impact behaviour of FRP composite plate under low to hyper velocity impact. *Composite Part B.* 95, 462-474. https://doi.org/10.1016/j.compositesb.2016.04.021.

[76] Pham, D.C., Lua, J., Sun, H. & Zhang, D. (2020). A three-dimensional progressive damage model for drop-weight impact and compression after impact. *Journal of Composite Materials.* 54 (4), 449-462. https://doi.org/10.1177/0021998319859050.

[77] Cheng, X., Du, X., Zhang, J., Zhang, J., Guo, X. & Bao, J. (2018). Effects of stacking sequence and rotation angle of patch on low velocity impact performance of scarf repaired laminates. *Composite Part B.* 133, 78-85. https://doi.org/10.1016/j.compositesb.2017.09.020.

[78] Cheng, X., Zhang, J., Bao, J., Zeng, B., Cheng, Y. & Hu, R. (2018). Low-velocity impact performance and effect factor analysis of scarf-repaired composite laminates. *International Journal of Impact Engineering.* 111, 85-93. https://doi.org/10.1016/j.ijimpeng.2017.09.004.

[79] Liu, H., Liu, J., Kaboglu, C., Chai, H., Kong, X., Blackman, B.R.K., Kinloch, A.J. & Dear, J.P. (2019) Experimental and numerical studies on the behaviour of fibre-reinforced composites subjected to

soft impact loading. In: *The 3rd International Conference on Structural Integrity, Madeira, Portugal.* Elsevier. 992-1001.

[80] Johnson, A.F. & Holzapfel, M. (2006). Numerical prediction of damage in composite structures from soft body impacts. *Journal of Materials Science.* 41, 6622-30. https://doi.org/10.1007/s10853-006-0201-x.

[81] Johnson, A.F. & Holzapfel, M. (2003). Modelling soft body impact on composite structures. *Composite Structures.* 61 (1-2), 103-13. https://doi.org/10.1016/S0263-8223(03)00033-3.

[82] Liu, H., Liu, J., Ding, Y., Zheng, J., Luo, L., Kong, X., Zhou, J., Blackman, B.R.K., Kinloch, A.J. & Dear, J.P. (2020). Modelling the effect of projectile hardness on the impact response of a woven carbon-fibre reinforced thermoplastic-matrix composite. *International Journal of Lightweight Materials and Manufacture.* 3 (4), 403-15. https://doi.org/10.1016/j.ijlmm.2020.05.005.

[83] Hall, Z.E.C., Liu, J., Brooks, R.A., Liu, H., Crocker, J.W.M., Joesbury, A.M., Harper, L.T., Blackman, B.R.K., Kinloch, A.J. & Dear, J.P. (2022). The effectiveness of patch repairs to restore the impact properties of carbon-fibre reinforced-plastic composites. *Engineering Fracture Mechanics*. 270, 108570. https://doi.org/10.1016/j.engfracmech.2022.108570.

[84] American Society for Testing and Materials. (2005). ASTM D7136/D7136M. *Standard Test Method for Measuring the Damage Resistance of a Fiber-Reinforced Polymer Matrix Composite to a Drop-Weight Impact Event.* Pennsylvania, ASTM. https://doi.org/10.1520/D7136_D7136M-20.

[85] De Silva, K. (2022). *Final Year Project Report: The impact performance of repaired composites*. Imperial College London.

[86] Liu, H., Liu, J., Ding, Y., Zheng, J., Kong, X., Zhou, J., Harper, L., Blackman, B.R.K., Kinloch, A.J. & Dear, J.P. (2020). The behaviour of thermoplastic and thermoset carbon-fibre composites subjected to low-velocity and high-velocity impact. *Journal of Material Science*. 55, 15751-68. https://doi.org/10.1007/s10853-020-05133-0.

[87] Liu, H., Liu, J., Ding, Y., Zhou, J., Kong, X., Blackman, B.R.K., Kinloch, A.J., Falzon, B.G. & Dear, J.P. (2020). Effects of impactor geometry on the low velocity impact behaviour of fibre-reinforced composites: an experimental and theoretical investigation. *Applied Composite Materials.* 27, 533-53. https://doi.org/10.1007/s10443-020-09812-8.

[88] Liu, H., Liu, J., Ding, Y., Hall, Z.E., Kong, X., Zhou, J., Blackman, B.R.K., Kinloch, A.J. & Dear, J.P. (2020). A three-dimensional elastic-plastic damage model for predicting the impact behaviour of fibre-reinforced polymer-matrix composites. *Composites Part B*. 201, 108389. https://doi.org/10.1016/j.compositesb.2020.108389.

[89] Cantwell, W.J. & Morton, J. (1985). Detection of impact damage in CFRP laminates. *Composite Structures*. 3, 241-57. https://doi.org/10.1016/0263-8223(85)90056-X.

[90] Dorey, G., Bishop, S.M. & Curtis, P.T. (1985). On the impact performance of carbon fibre laminates with epoxy and PEEK matrices. *Composites Science and Technology*. 23, 221-37. https://doi.org/10.1016/0266-3538(85)90019-3.

[91] Cantwell, W.J. & Morton, J. (1989). Comparison of the low and high velocity impact response of CFRP. *Composites*. 20, 545-51. https://doi.org/10.1016/0010-4361(89)90913-0.

[92] Cantwell, W.J & Morton, J. (1989). The influence of varying projectile mass on the impact response of CFRP. *Composite Structures*. 13, 101-14. https://doi.org/10.1016/0263-8223(89)90048-2.

[93] Ghaseminejhad, M.N. & Parvizi-Majidi, A. (1990). Impact behaviour and damage tolerance of woven carbon fibre-reinforced thermoplastic composites. *Construction and Building Materials*. 4, 194–207. https://doi.org/10.1016/0010-4361(90)90008-K.

[94] Cantwell, W.J. & Morton, J. (1991). The impact resistance of composite materials - a review. *Composites*. 22, 347-62. https://doi.org/10.1016/0010-4361(91)90549-V.

[95] Morita, H., Adachi, T., Tatesiha, Y. & Matsumoto, H. (1997). Characterization of impact damage resistance of CF/PEEK and CF/Toughened epoxy laminates under low and high velocity tests.

Journal of Reinforced Plastics and Composites. 16, 131-43. https://doi.org/10.1177/073168449701600203.

[96] Batra, R.C., Gopinath, G. & Zheng, J.Q. (2012). Damage and failure in low energy impact of fiber-reinforced polymeric composite laminates. *Composite Structures*. 94: 540-47. https://doi.org/10.1016/j.compstruct.2011.08.015.

[97] Liu, H., Falzon, B.G. & Tan, W. (2018). Experimental and numerical studies on the impact response of damage-tolerant hybrid unidirectional/woven carbon-fibre reinforced composite laminates. *Composites Part B*. 136, 101-18. https://doi.org/10.1016/j.compositesb.2017.10.016.

[98] Wang, C.H. & Duong, C.N. (2016). *Bonded Joints and Repairs to Composite Airframe Structures*. London, Academic Press. https://doi.org/10.1016/C2013-0-00565-8.

[99] Kashfuddoja, M. & Ramji, M. (2014). Design of optimum patch shape and size for bonded repair on damaged carbon fibre reinforced polymer panels. *Materials and Design*. 54, 174-83. https://doi.org/10.1016/j.matdes.2013.08.043.

[100] Sun, Z., Li, C. & Tie, Y. (2021). Experimental and numerical investigations on damage accumulation and energy dissipation of patch-repaired CFRP laminates under repeated impacts. *Materials and Design*. 202, 109540. https://doi.org/10.1016/j.matdes.2021.109540.

[101] Liu, H., Brooks, R.A., Hall, Z.E.C., Liu, J., Crocker, J.W.M., Joesbury, A.M., Harper, L.T., Blackman, B.R.K., Kinloch, A.J. & Dear, J.P. (2022). Experimental and numerical investigations on the impact behaviour of pristine and patch-repaired composite laminates. *Philosophical Transactions of the Royal Society A*. 380, 20210340. https://doi.org/10.1098/rsta.2021.0340.

[102] Dear, J.P. & MacGillivray, J.H. (1991). Strain gauging for accurate determination of K and G in impact tests. *Journal of Materials Science*. 26, 2124-32. https://doi.org/10.1007/BF00549178.

[103] Crouch, B.A. & Williams, J.G. (1988). Modelling of dynamic crack propagation behaviour in the three-point bend impact specimen. *Journal of the Mechanics and Physics of Solids*. 36, 1-13. https://doi.org/10.1016/0022-5096(88)90017-8.

[104] Williams, J.G. & Adams, G.C. (1987). The analysis of instrumented impact tests using a mass-spring model. *International Journal of Fracture*. 33, 209-22. https://doi.org/10.1007/BF00013171.

[105] Dear, J.P. (1990). High speed photography of impact effects in three-point bend testing of polymers. *Journal of Applied Physics*. 67, 4304-12. https://doi.org/10.1063/1.344946.

[106] Bieniaś, J., Jakubczak, P. & Surowska, B. (2013). Comparison of polymer composites behavior to low-velocity impact and quasi-static indentation. *Composites Theory and Practice*. 13, 155-9.

[107] Griffiths, B. (2005) *Boeing sets pace for composites usage in large civil aircraft.* https://www.compositesworld.com/articles/boeing-sets-pace-for-composite-usage-in-large-civil-aircraft [Accessed 18th January 2022].

[108] Yankelevsky, D. (1997). Local response of concrete slabs to low velocity missile impact. *International Journal of Impact Engineering*. 19 (4), 331-43. https://doi.org/10.1016/S0734-743X(96)00041-3.

[109] Sjogren, A., Krasnikovs, A. & Varna, J. (2001) Experimental determination of elastic properties of impact damage in carbon fibre/epoxy laminates. *Composites Part A*. 32, 1237-1242. https://doi.org/10.1016/S1359-835X(01)00058-6.

[110] Heimbs, S., Heller, S., Middendorf, P., Hahnel, F. & Weisse, J. (2009). Low velocity impact on CFRP plates with compressive preload: Test and modelling. *International Journal of Impact Engineering*. 36 (10-11), 1182-93. https://doi.org/10.1016/j.ijimpeng.2009.04.006.

[111] Hongkarnjanakul, N., Bouvet, C. & Rivallant, S. (2013). Validation of low velocity impact modelling on different stacking sequences of CFRP laminates and influence of fibre failure. *Composite Structures*. 106, 549-59. https://doi.org/10.1016/j.compstruct.2013.07.008.

[112] Zhou, J., Liao, B., Shi, Y., Zuo, Y., Tuo, H. & Jia, L. (2019). Low-velocity impact behaviour and residual tensile strength of CFRP laminates. *Composites Part B*. 161, 300-13. https://doi.org/10.1016/j.compositesb.2018.10.090.

[113] Caprino, G. & Lopresto, V. (2001). On the penetration energy for fibre-reinforced plastics under low-velocity impact conditions. *Composites Science and Technology*. 61 (1), 65-73. https://doi.org/10.1016/S0266-3538(00)00152-4.

[114] Cantwell, W.J. & Morton, J. (1990). Impact perforation of carbon fibre reinforced plastic. *Composites Science and Technology*. 38 (2), 119-41. https://doi.org/10.1016/0266-3538(90)90002-M.

[115] PVC Tube Online Ltd. *Neoprene Rubber Sheet*. http://www.pvctubeonline.co.uk/neoprene_rubber_sheet.htm [Accessed: 16th November 2021].

[116] Hashin, Z. & Rotem, A. (1973). A fatigue failure criterion for fibre reinforced materials. *Journal of Composite Materials*. 7, 448. https://doi.org/10.1177/002199837300700404.

[117] Shao, J.R., Liu, N. & Zheng, Z.J. (2021). Numerical comparison between Hashin and Chang-Chang failure criteria in terms of inter-laminar damage behaviour of laminated composites. *Materials Research Express*. 8, 085602. https://doi.org/10.1088/2053-1591/ac1d40.

[118] Bogert, P.B., Satyanarayana, A. & Chunchu, P.B. (2006). Comparison of damage path predictions for composite laminates by explicit and standard finite element analysis tools. In: AIAA. *47th Structures, Structural Dynamics, and Materials Conference: 1-4 May 2006, Newport, Rhode Island*. Rhode Island, USA.

[119] Gzaiel, M., Triki, E. & Barkaoui, A. (2019). Finite element modelling of the puncture-cutting response of soft material by a pointed blade. *Mechanics of Materials*. 136, 103082. https://doi.org/10.1016/j.mechmat.2019.103082.

[120] Heimbs, S., Van Den Broucke, B., Kergomard, Y.D., Dau, F. & Malherbe, B. (2012). Rubber impact of 3D Textile Composites. *Appl Compos Mater*. 19, 275-95. https://doi.org/10.1007/s10443-011-9205-z.

[121] Abir, M.R., Tay, T.E., Ridha, M. & Lee, H.P. (2017). On the relationship between failure mechanism and compression after impact (CAI) strength in composites. *Composite Structures*. 182, 242–50. https://doi.org/10.1016/j.compstruct.2017.09.038.

[122] WELSIM – Engineering Simulation Software. (2020). *Mooney-Rivlin hyperelastic model for nonlinear finite element analysis*. https://getwelsim.medium.com/mooney-rivlin-hyperelastic-model-for-nonlinear-finite-element-analysis-b0a9a0459e98 [Accessed 26th October 2022].

[123] Xu, J. & El Mansori, M. (2015). Cutting modelling using cohesive zone concept of titanium/CFRP composite stacks. *International Journal of Precision Engineering and Manufacturing*. 16 (10), 2091-100. https://doi.org10.1007/s12541-015-0271-2.

[124] Abaqus 2018 documentation, Dassault Systèmes, Provid. Rhode Island, USA, 2018.

[125] Turon, A., Davila, C.G., Camanho, P.P. & Costa, J. (2007). An engineering solution for mesh size effects in the simulation of delamination using cohesive zone models. *Engineering Fracture Mechanics*. 74, 1665-82. https://doi.org/10.1016/j.engfracmech.2006.08.025.

[126] Liu, H., Liu, J., Kaboglu, C., Zhou, J., Kong, X., Blackman, B.R.K., Kinloch, A.J. & Dear, J.P. (2020). The behaviour of fibre-reinforced composites subjected to a soft impact loading: an experimental and numerical study. *Engineering Failure Analysis*. 111, 101448. https://doi.org/10.1016/j.engfailanal.2020.104448.

[127] Brewer, J.C. & Lagace, P.A. (1988). Quadratic stress criterion for initiation of delamination. *Journal of Composite Materials*. 22, 1141-55. https://doi.org/10.1177/002199838802201205.

[128] Camanho, P.P., Davila, C.G. & de Moura, M.F. (2003). Numerical simulation of mixed- mode progressive delamination in composite materials. *Journal of Composite Materials*. 37, 1415-38. https://doi.org/10.1177/0021998303034505.

[129] Benzeggagh, M.L. & Kenane, M. (1996). Measurement of mixed-mode delamination fracture toughness of unidirectional glass/epoxy composites with mixed- mode bending apparatus. *Composites Science and Technology*. 56, 439-49. https://doi.org/10.1016/0266-3538(96)00005-X.

[130] Sarrado, C., Turon, A., Renart, J. & Urresti, I. (2012). Assessment of energy dissipation during mixed-mode delamination growth using cohesive models. *Composites Part A*. 43, 2128-36. https://doi.org/10.1016/j.compositesa.2012.07.009.

[131] Hashemi, S., A.J. Kinloch, A.J. & J.G. Williams. (1990). The analysis of interlaminar fracture in uniaxial fibre polymer composites. *Proceedings of The Royal Society A: Mathematical, Physical and Engineering Sciences*. 427, 173-90. https://doi.org/10.1098/rspa.1990.0007.

11 Appendices

11.1 Appendix A – Repeat data for Chapter 4

Figure 11-1 below shows the repeat cases for the testing summarised in Section 4. Figure 11-1 (b) and (c) were both presented in Section 4.3.4 when comparing the effect of patch thickness but are included here for completeness.

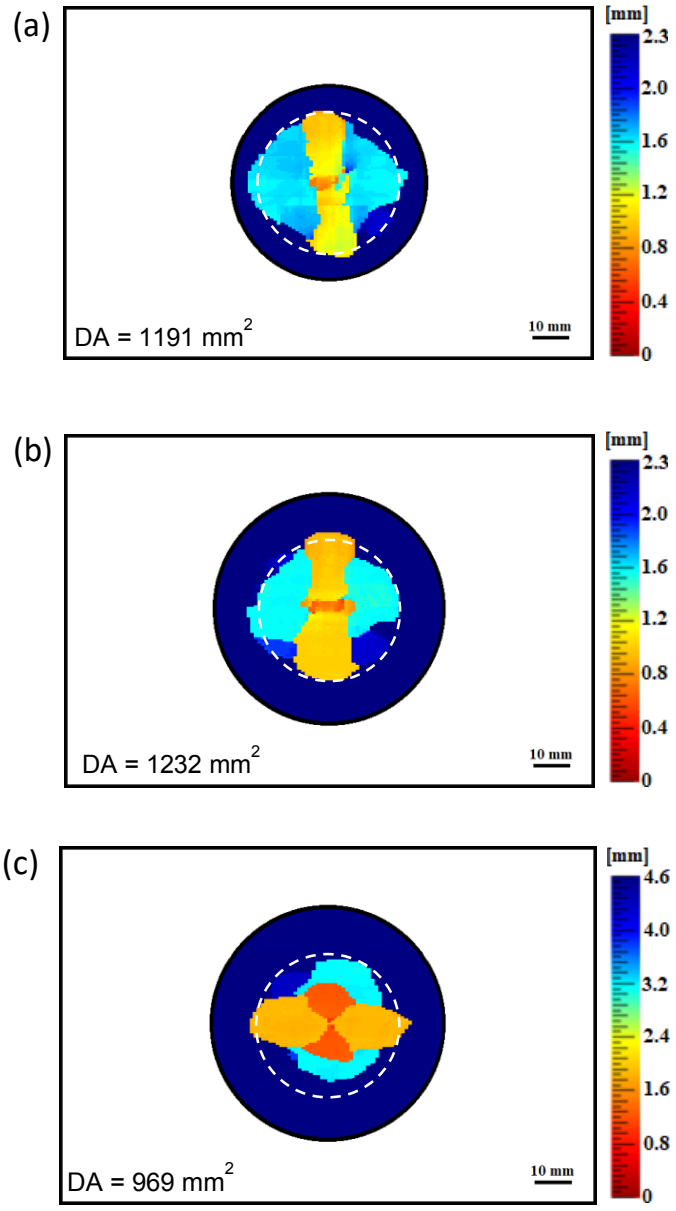

Figure 11-1. C-scan images of patch-repair QIT CFRP panels with no plugs taken from the top (impacted) face after a 7.5 J impact for: (a) the 55 mm thin (0.5t = 2.29 mm) patch repair – Test 2, (b) the 65 mm thin (0.5t = 2.29 mm) patch repair – Test 2, and (c) the 65 mm thick (t = 4.58 mm) patch repair – Test 2. (The white-dashed line represents the 40 mm diameter hole that was initially cut-out in the parent panel).

11.2 Appendix B – Repeat data for Chapter 5

Due to issues when repairing the panels for the offset impact testing presented in Section 5, a large number of repeat cases were tested. The issues came from the curing cycle used, with the maximum temperature exceeding the glass transition temperature of the panels and causing a slight depression on the patch surface that was an imprint of the cut out hole beneath. This affected the c-scan images, meaning some filtering was required in the first batch of tests, hence why repeats were used to verify the damage areas were correct. Figure 11-2 shows an example of the filtering by showing the initial and edited c-scans.

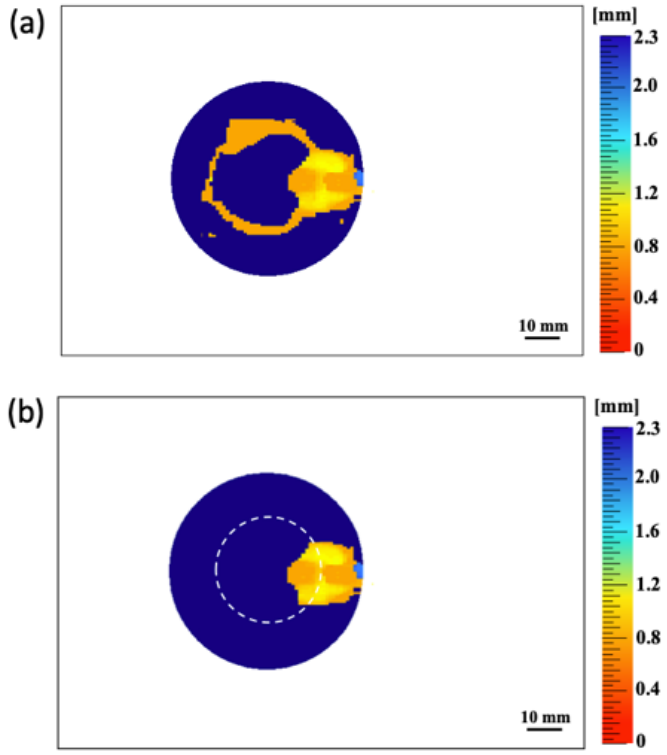

Figure 11-2. C-scan images of an edge of hole offset repaired cross-ply CFRP panel impacted at 7.5 J (a) before and (b) after editing to remove noise from surface impurities. (The white-dashed line represents the 30 mm diameter hole that was initially cut-out in the parent panel).

For the pristine impact, a duplicate case of the first impact at 7.5 J was performed, with the drop weight data and c-scan shown in Figures 11-3 and 11-4, respectively. The load versus time and load versus displacement traces can be seen to be very similar between the two tests, with almost negligible difference. The damage area recorded was very similar to that of the sample presented in Section 5.3.

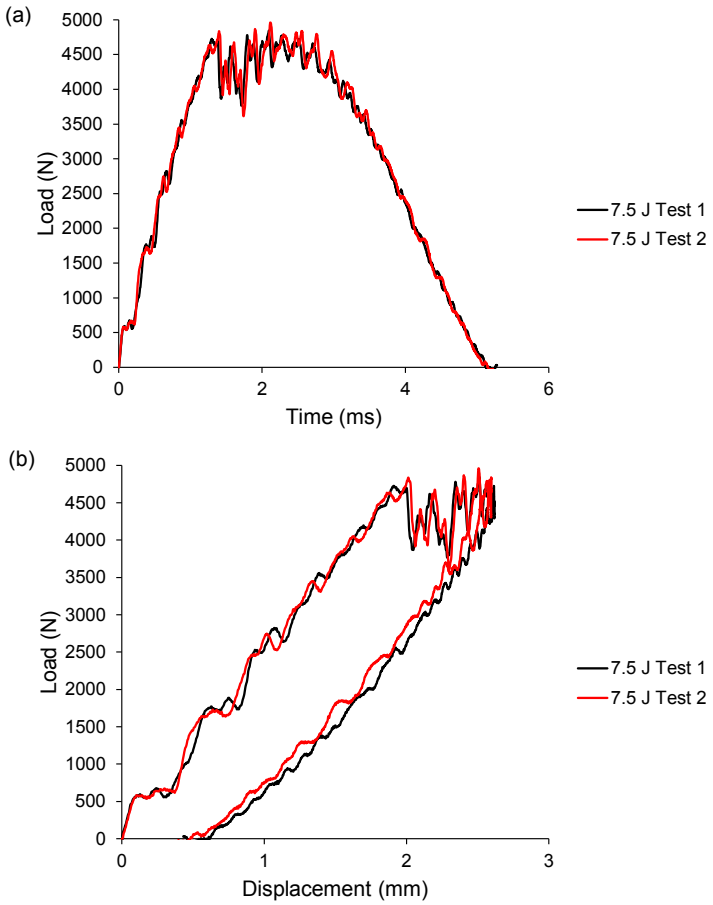

Figure 11-3. Load traces for both pristine cross-ply CFRP panel impacts at 7.5 J, with Test 1 represented by the black line and Test 2, the duplicate case, represented by the red line.

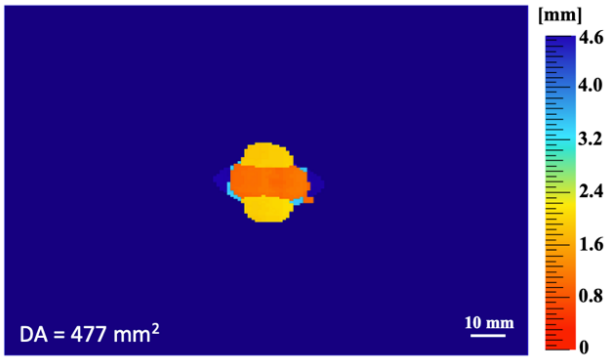

Figure 11-4. C-scan of pristine cross-ply CFRP panel impacted at 7.5 J, Test 2.

Figures 11-5 and 11-6 show the load traces and c-scan images for the duplicate cases of the central repair with a plug, respectively. This case was tested four separate times due to the plug dislodgement causing a sudden and significant drop in the load and affecting the performance of the panel. This occurred in all cases, potentially due to the plug diameter, adhesive thickness or some other factors causing the plug to be the weakest part of the repair, with the damage initiation load varying for each case.

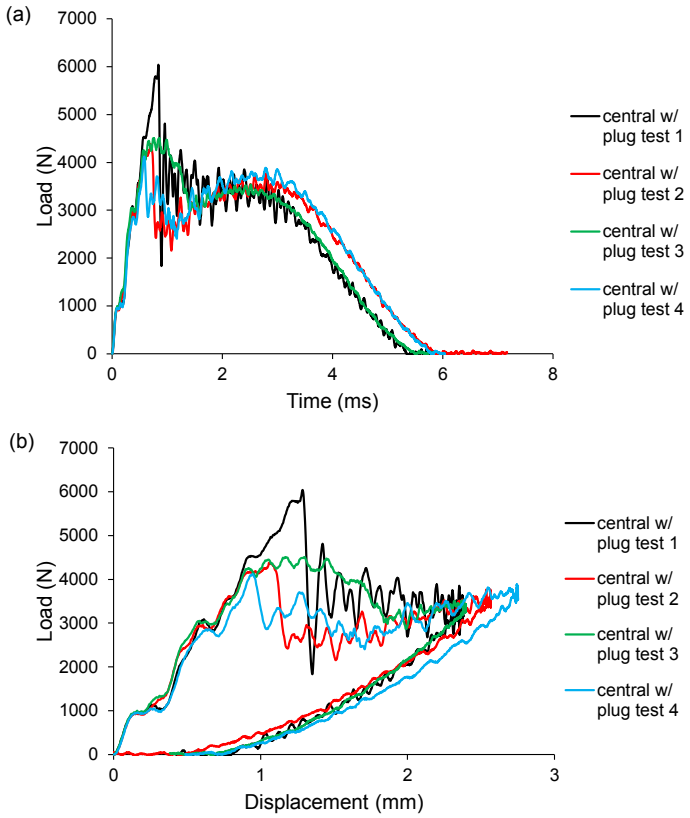

Figure 11-5. Load traces for all four central cross-ply CFRP patch repaired panels with a plug, with Test 1 represented by the black line and Tests 2, 3 and 4, the duplicate cases, represented by the red, green and blue lines, respectively.

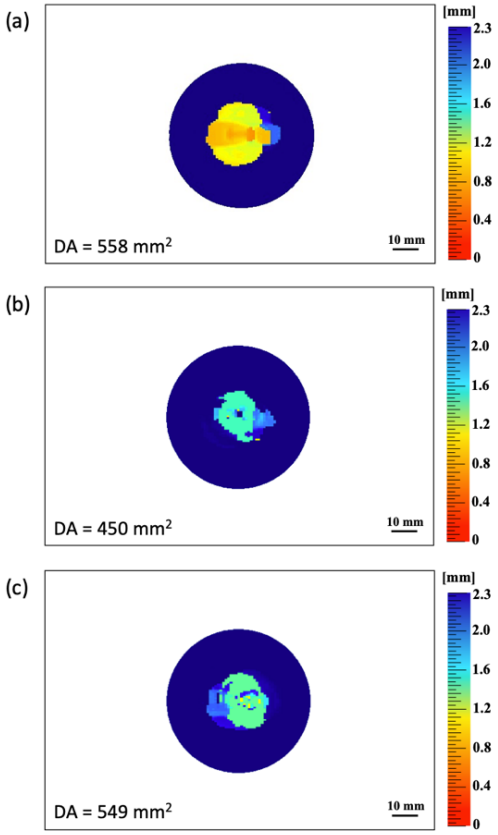

Figure 11-6. C-scans of central cross-ply CFRP patch repaired panels with a plug, (a) Test 2, (b) Test 3, and (c) Test 4.

Three repeats of the central repair without a plug were tested, giving four sets of data for this repair configuration. The load traces and c-scans are shown in Figures 11-7 and 11-8, respectively. There is very good agreement between all four data sets.

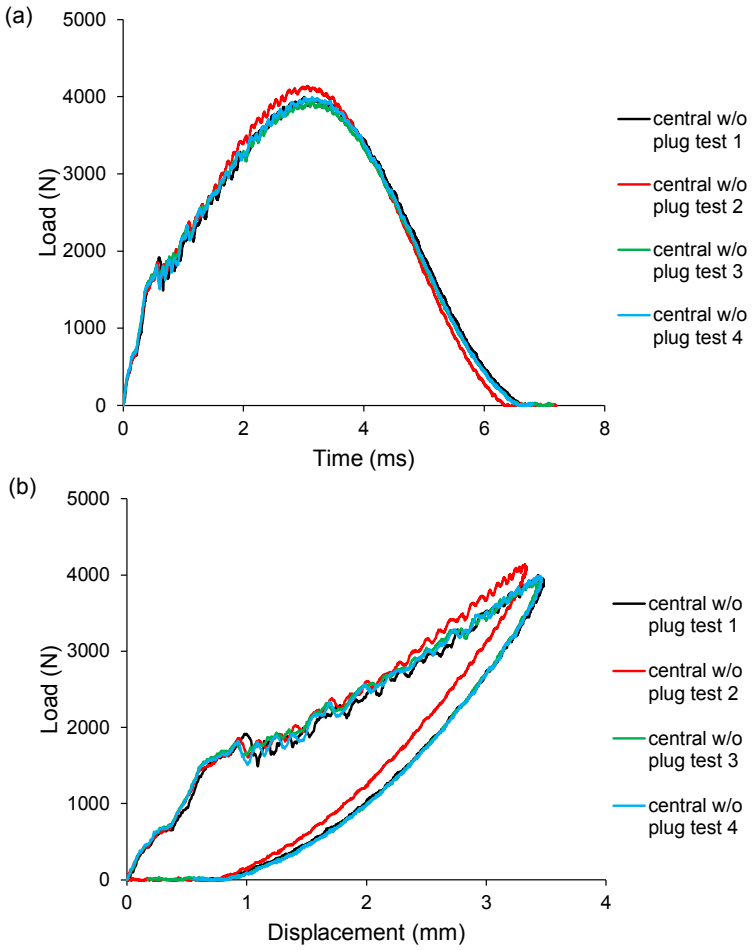

Figure 11-7. Load traces for all four central cross-ply CFRP patch repaired panels without a plug, with Test 1 represented by the black line and Tests 2, 3 and 4, the duplicate cases, represented by the red, green and blue lines, respectively.

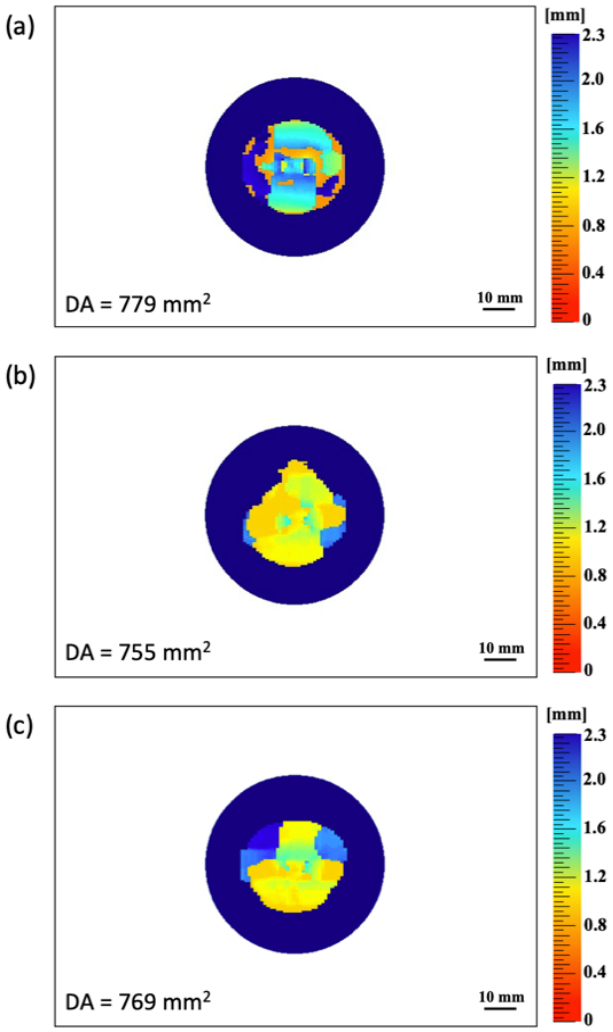

Figure 11-8. C-scans of central cross-ply CFRP patch repaired panels without a plug, (a) Test 2, (b) Test 3, and (c) Test 4.

Three samples repaired with an edge of hole offset patch without a plug were tested, with the repeat load, time and displacement data and c-scans shown in Figures 11-9 and 11-10. Comparing the load traces and c-scans of the two repeat cases with the data presented in the main body of this thesis, it can be seen that Tests 1 and 3 compare well and demonstrate repeatability and validity in the conclusions drawn. However, Test 2 is slightly different from both of the other samples, suggesting this may be an outlier.

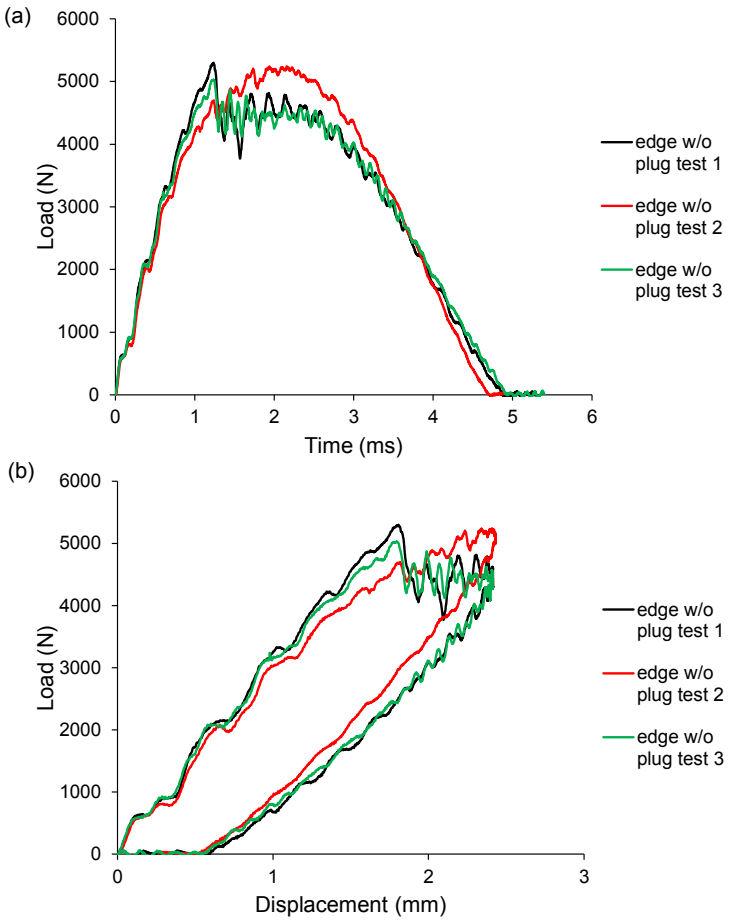

Figure 11-9. Load traces for all three edge of hole offset cross-ply CFRP patch repaired panels without a plug, with Test 1 represented by the black line and Tests 2 and 3, the duplicate cases, represented by the red and green lines, respectively.

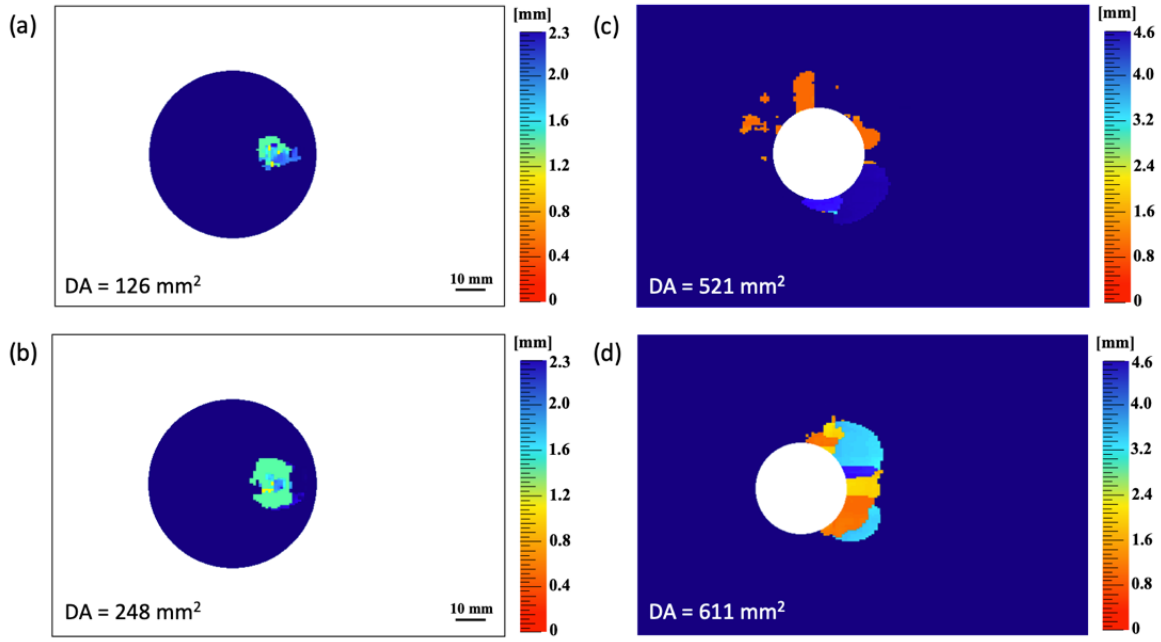

Figure 11-10. C-scans of the edge of hole offset cross-ply CFRP patch repaired panels without a plug, (a) Test 2 patch, (b) Test 3 patch, (c) Test 2 parent panel, and (d) Test 3 parent panel.

Figures 11-11 and 11-12 show the load traces and c-scan for the duplicate case of the 15 mm offset repair case, respectively. Good agreement is demonstrated. Note that the c-scan of the patch was not shown as there was no damage detected.

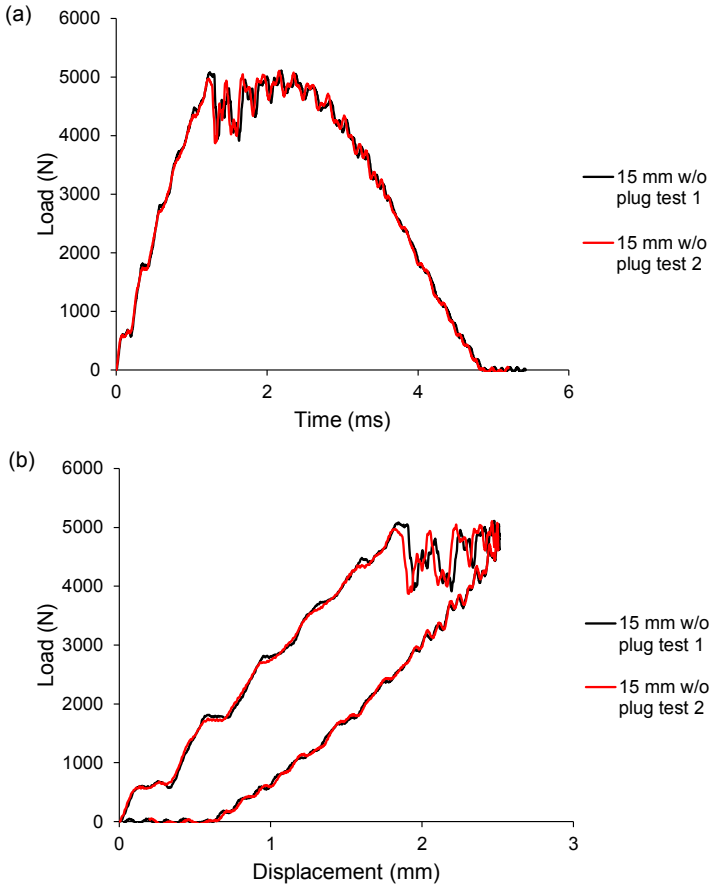

Figure 11-11. Load traces for both 15 mm offset cross-ply CFRP patch repaired panels without a plug, with Test 1 represented by the black line and Test 2 represented by the red line.

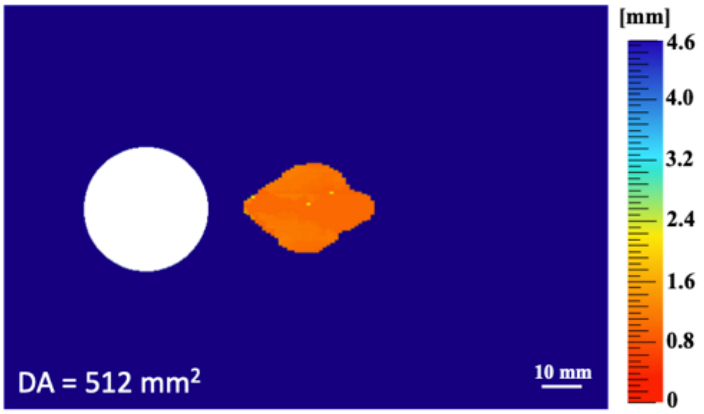

Figure 11-12. C-scan of a 15 mm offset cross-ply CFRP patch repaired panel without a plug, Test 2.

11.3 Appendix C – Repeat data for Chapter 6

The first sample impacted with 1 and 1.5 mm thick disks of rubber adhered to the end of the flat ended impactor had damage that extended to the edge of the panel. Due to the size of the damage areas in this testing, this phenomenon was a probable outcome as once damage is close to the edge it can very easily propagate quickly to give damage maps such as those in Figures 11-13 and 11-14 below. For this reason, another sample was tested in each of these cases and these were the ones presented in Section 6.3.2 as they did not have the same issue.

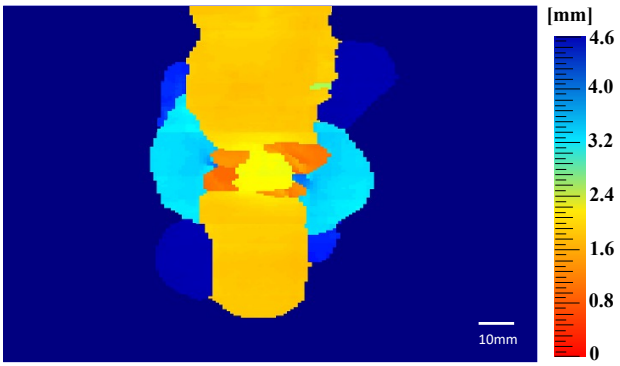

Figure 11-13. C-scan of a panel impacted with a flat-ended impactor with a 1 mm thick rubber disk adhered to the end, Test 1.

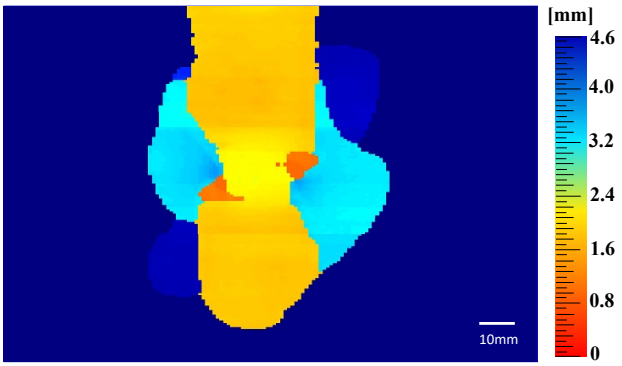

Figure 11-14. C-scan of a panel impacted with a flat-ended impactor with a 1.5 mm thick rubber disk adhered to the end, Test 1.

Additionally, Figures 11-15 and 11-16 show the load traces for both of the samples tested with 1 and 1.5 mm thick rubber. These results demonstrate the repeatability of these experiments due to the good agreement in both cases.

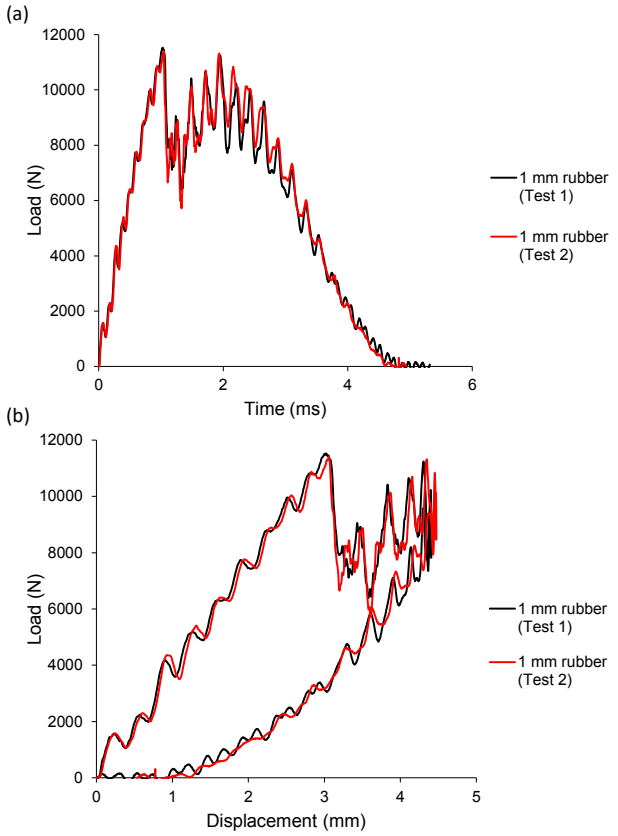

Figure 11-15. Load traces of a panel impacted with a flat-ended impactor with a 1 mm thick rubber disk adhered to the end, Test 1.

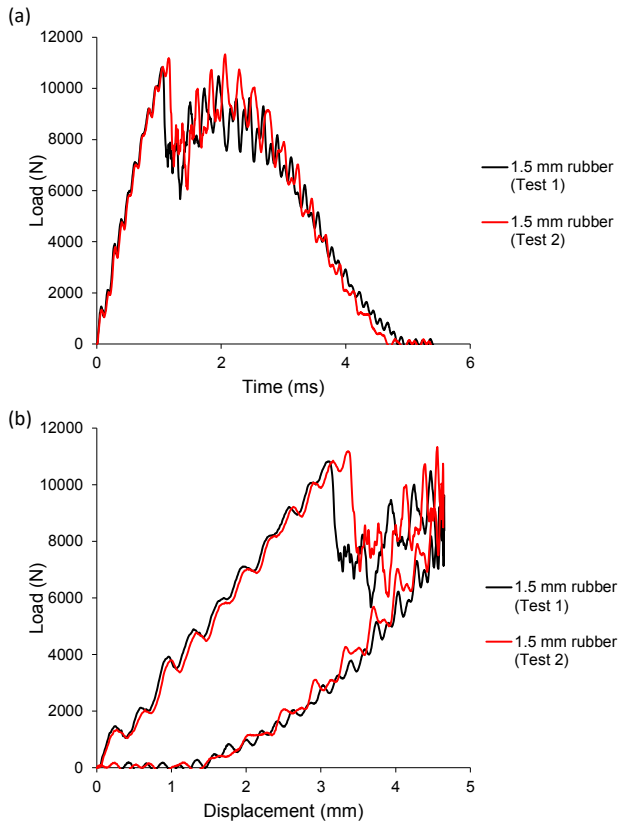

Figure 11-16. Load traces of a panel impacted with a flat-ended impactor with a 1.5 mm thick rubber disk adhered to the end, Test 1.

11.4 Appendix D – Abaqus Tutorial

When learning to model the composite panels in Abaqus and creating my model presented in Section 7, I produced a document detailing how to produce my model step by step. Additionally, I made a video tutorial that will be used by my research group for future modelling. The information contained in the document is as follows:

Making an Abaqus model of a composite drop weight impact test

1. Create a New Model Database with Standard/Explicit Model

IN PART MODULE

2. Create a new part – 3D, deformable, solid, extrusion, approx. size 200 – and name it composite *ply orientation*, e.g. composite 45
3. Use the rectangle tool to draw the composite ply and add dimensions in mm e.g. 150 x 100
4. Enter thickness in mm, using the thickness of two plies if panel has blocked plies e.g. 0.572
5. Create a new part – 3D, analytical rigid, revolution – and name it impactor
6. Draw a centre line down the middle and then use the line (and circle if doing a round impactor) tool to draw half the outline of the impactor to the right of the centre line
7. Revolve around 360 degrees

IN PROPERTY MODULE, IMPACTOR

8. Tools > reference point > select the centre point of the impacting face of the impactor
9. Special > inertia > create > name it mass > select the reference point as the region and set the mass value in tonnes e.g. 0.005266

IN PROPERTY MODULE, COMPOSITE PLY

10. Create material > name it composite > add Hashin Damage (MPa), with Damage Evolution (kJ/m^2), Density ($tonnes/mm^3$) and Elastic, lamina (MPa) > input values e.g. in Table 11-1 below

Table 11-1. Modelling properties for CFRP.

HASHIN DAMAGE		
Longitudinal tensile strength	2282	MPa
Longitudinal compressive strength	1067	MPa
Transverse tensile strength	54	MPa
Transverse compressive strength	200	MPa
Longitudinal shear strength	99	MPa
Transverse shear strength	99	MPa
DAMAGE EVOLUTION		
Longitudinal tensile fracture energy	100	kJ/m^2
Longitudinal compressive fracture energy	50	kJ/m^2
Transverse tensile fracture energy	1	kJ/m^2
Transverse compressive fracture energy	2	kJ/m^2
DENSITY		
Density	1.6 e-9	$tonnes/mm^3$
ELASTIC (lamina)		
E1	115	GPa
E2	8.2	GPa
Nu12	0.34	-
G12	3.6	GPa
G13	3.6	GPa
G23	3.6	GPa

11. Create composite layup > continuum shell > 1 ply count > select panel as region, material as composite, relative thickness same as ply thickness e.g. 0.572, rotation angle as ply orientation e.g. 45
12. Copy composite ply to give one for each ply orientation e.g. composite 45, composite -45, composite 0 and composite 90
13. For central ply, change thickness to be double all the other plies due to symmetry causing blocking in the centre e.g. 1.144
14. In each ply, edit composite layup > change rotation angle to correct value e.g. -45, 0, 90, and change relative thickness in central ply to double e.g. 1.144 for composite 90
15. In each ply, create two surfaces, one top and one bottom and name as such

IN ASSEMBLY MODULE

16. Create instance ply by ply, naming them accordingly e.g. ply 1 (45), ply 2 (-45) etc.
17. Translate the first ply to have the front, bottom left corner at the origin
18. Translate each added ply to be behind the previous one until your full panel is simulated

19. Create instance inserting impactor > rotate instance by 90 degrees around line on top face > translate instance to the origin and then to the centre of the panel by inputting half the height and width e.g. (75,50,0)

IN STEP MODULE

20. Create step > set time period e.g. 0.002
21. Create field output > CFAILURE, CSDMG, CSTRESS, DAMAGEC, DAMAGEFC, DAMAGEFT, DAMAGEMC, DAMAGEMT, DAMAGESHR, DAMAGET, DMICRT, E, EVF, RF, S, SDEG, STATUS, U > interval 100

IN INTERACTION MODULE

22. Create interaction property > name impact > contact > tangential behaviour (penalty) friction coefficient value e.g. 0.25, normal behaviour
23. Create interaction property > name interply > contact > tangential behaviour (penalty) friction coefficient value e.g. 0.2, normal behaviour, cohesive behaviour (any slave nodes, specify stiffness coefficients e.g. 10000, 10000, 10000), damage (specify damage evolution) initiation e.g. 40, 60, 60, and evolution e.g. energy, linear, specify mixed mode behaviour, benzeggagh-kenane, specify BK exponent e.g. 2, fracture energy e.g. 1, 2, 2
24. Create constraint > rigid body > select impactor as region for region type analytical surface > select reference point as point
25. Find contact pairs > find contact pairs
26. Interaction manager > delete all
27. Create interaction > general contact > set global assignment to impact > individual assignments select bottom of ply and top of next ply and set as interply, do for all touching ply faces

IN LOAD MODULE

28. Create boundary condition > symmetry/antisymmetry/encastre > step-1 > region select rear ply rear edges > pinned
29. Create boundary condition > displacement/rotation > step-1 > region select reference point > tick all except U3

30. Create predefined field > initial > velocity > region select reference point > input impactor velocity in V3, in mm/s e.g. -3350

IN MESH MODULE, COMPOSITE PLY

31. Seed part > set approximate size e.g. 1 > apply
32. Assign mesh controls > hex > structured
33. Assign element type > explicit, continuum shell, stiffness, yes, specify, 0.99
34. Mesh part
35. Repeat for all composite ply parts

IN JOB MODULE

36. Job manager > create > submit

11.5 Appendix E – Preliminary Modelling Results

As mentioned in Section 7.2.3, the model was run with a variety of different parameters to optimise the simulation. A number of these iterations are presented below.

The first version of the model run had the property values given in Table 11-2 and delamination was defined as occurring when $\delta/\delta_f \geq 0.85$.

Table 11-2. Preliminary properties of the unidirectional composite from [66,87,88,101,131-133] and of the rubber disk from [115,120,134]

Property	Simulation value	Units
	COMPOSITE PLY	
Density	1600	kg/m^2
Moduli	$E_{11} = 115, E_{22} = 8.2,$ $G_{23} = 3.6, G_{12} = G_{13} = 3.6$	GPa
Poisson's ratio	$v_{12} = 0.34$	-
Strength values	$S_{1t} = 2282, S_{2t} = 54,$ $S_{1c} = 1067, S_{2c} = 200,$ $S_{12} = S_{13} = 99$	MPa
Intralaminar ply fracture energies	$G_{Ic\|ft} = 100, G_{Ic\|fc} = 50,$ $G_{Ic\|mt} = 1, G_{Ic\|mc} = 2, G_{IIc\|ms} = 2$	kJ/m^2
Interlaminar ply fracture energies	$G_{Ic} = 1, G_{IIc} = 2$	kJ/m^2
Benzeggagh-Kenane (B-K) exponent	$\eta = 2$	-
Cohesive strengths	$t_{33}^0 = 40, t_{31}^0 = t_{32}^0 = 60$	MPa
Initial cohesive law stiffness	$k = 1 \times 10^5$	MPa/mm
	RUBBER DISK	
Density	1500	kg/m^2
Neo Hookean constants	$c_{10} = 0.9, d_1 = 0.001$	-

This model was used to simulate a 30 J impact with all five impactors. The resulting damage areas are presented in Figures 11-17 and 11-18 below.

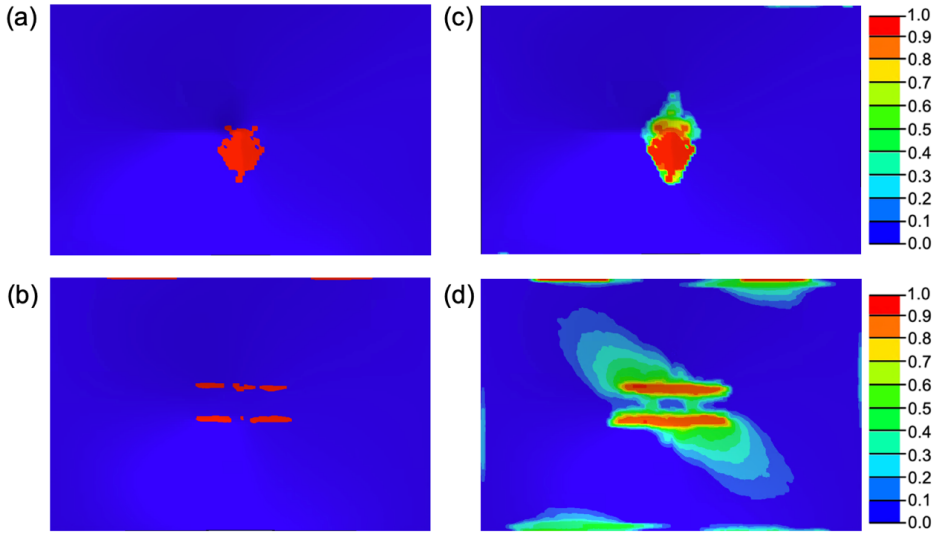

Figure 11-17. Damage maps from 30 J impacts using the preliminary model with damage variables above 0.85 shown in red for (a) round-nosed and (b) flat-ended impactors, and with damage variables according to the scale bar on the right for (c) round-nosed and (d) flat-ended impactors.

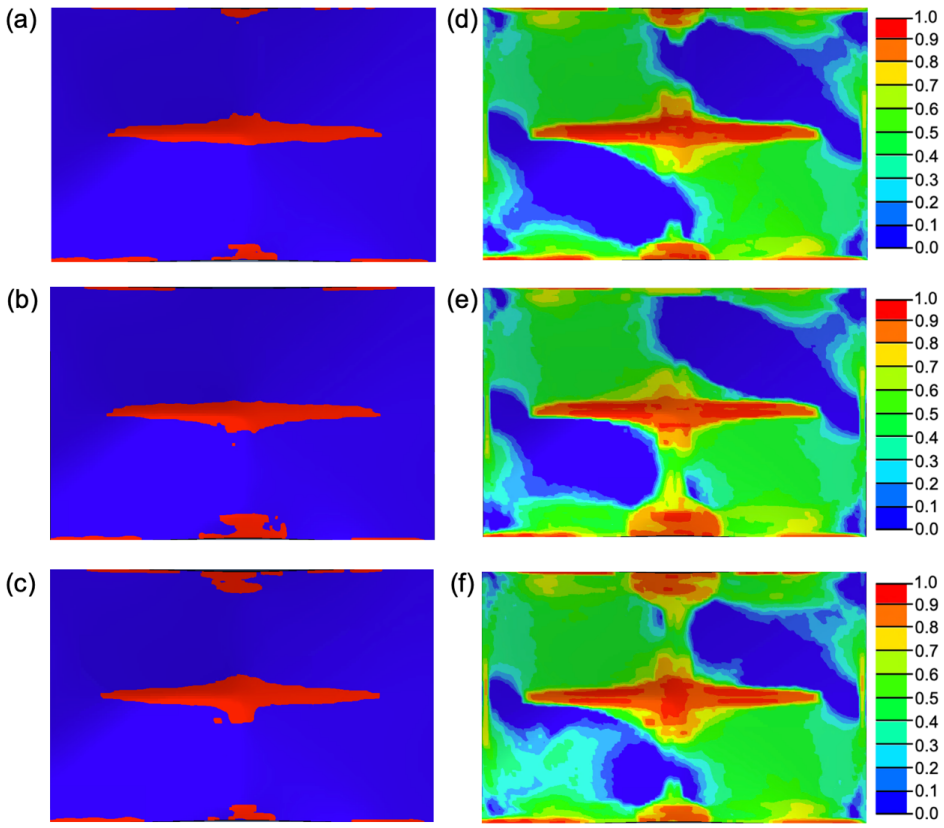

Figure 11-18. Damage maps from 30 J impacts using the preliminary model, and c_{10} = 0.9, d_1 = 0.001 and c_1 = 0, with damage variables above 0.85 shown in red for a flat-ended impactor with (a) 1 mm, (b) 1.5 mm, and (c) 2 mm of rubber and with damage variables according to the scale bar on the right for a flat-ended impactor with (d) 1 mm, (e) 1.5 mm, and (f) 2 mm of rubber.

Using this preliminary model, the properties used to simulate the rubber disk in the soft impacts were adjusted to determine their effect on the modelling results and allow the optimal values to be chosen. Initially the rubber disk was modelled as Neo-Hookean, meaning that the variable c_1 is equal to zero and only the variables c_{10} and d_1 are given values. Numerous values for both of the latter variables were simulated before then considering the Mooney-Rivlin model, where c_1 is non-zero. For all the combinations of variables considered, the simulation was only run for the 1 mm rubber disk flat-ended impactor case, with the damage area in each case given in Table 11-3.

Table 11-3. Damage area values calculated by implementing the preliminary model and varying the rubber model variables for a flat-ended impactor with 1 mm of rubber adhered to the end.

Impactor	c_{10}	d_1	c_1	Damage Area (mm^2)
1 mm rubber	0.1	0.001	0	44
1 mm rubber	0.5	0.001	0	164
1 mm rubber	0.9	0.001	0	1293
1 mm rubber	0.9	0.005	0	96
1 mm rubber	0.9	0.01	0	142
1 mm rubber	0.9	0.001	0.1	156
1 mm rubber	0.9	0.001	0.5	517
1 mm rubber	0.9	0.001	1	1137

From the above, it was chosen to use $c_{10} = 0.9$, $d_1 = 0.001$ and $c_1 = 0$ as the main issue with the model was a damage area that is less than that observed experimentally and every other variation of values gave a smaller damage area. The model was then adjusted to use the properties given in Section 7.2.3 and, with delamination occurring when $\delta/\delta_f \geq 0.85$, the damage maps presented in Figures 11-19, 11-20 and 11-21 were produced.

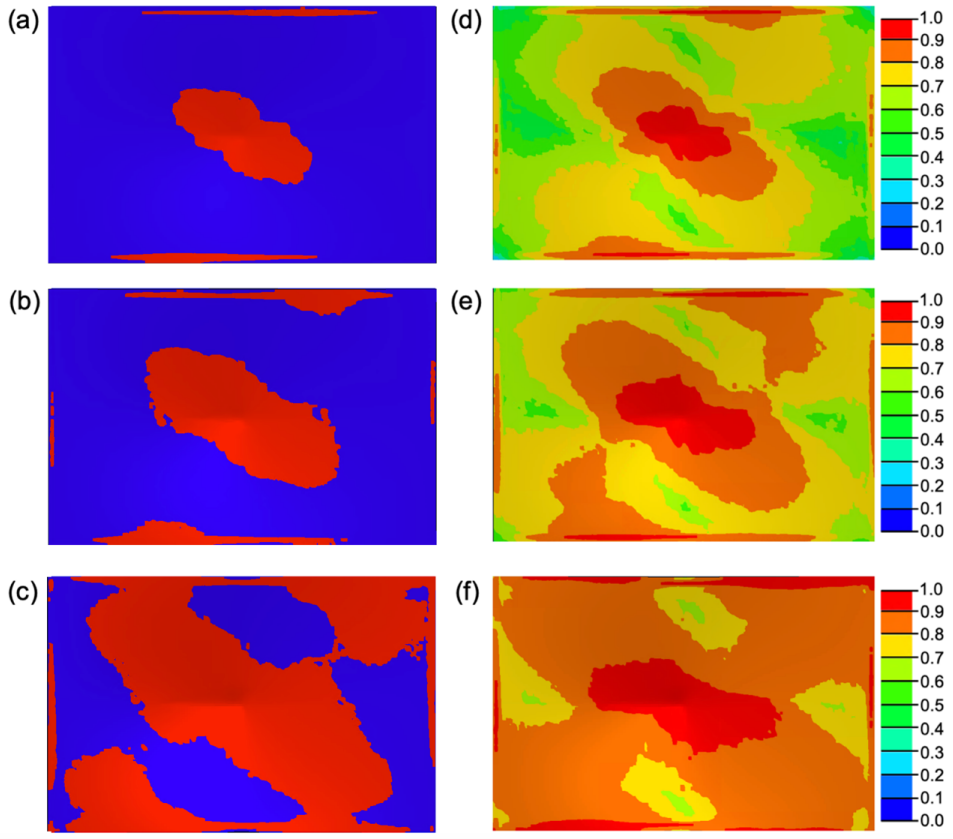

Figure 11-19. Damage maps using the final model with damage variables above 0.85 shown in red for (a) 7.5 J, (b) 15 J, and (c) 30 J and with damage variables according to the scale bar on the right for (d) 7.5 J, (e) 15 J, and (f) 30 J.

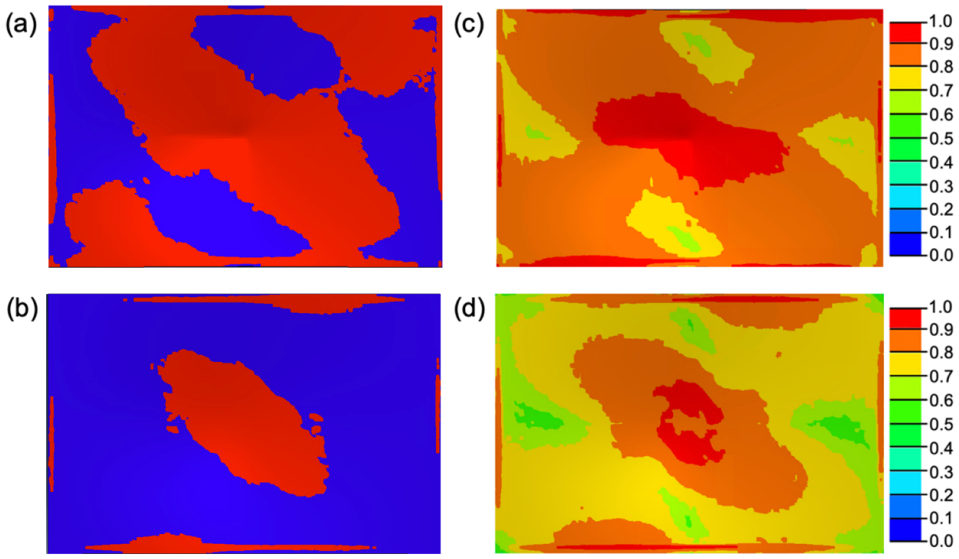

Figure 11-20. Damage maps from 30 J impacts using the final model with damage variables above 0.85 shown in red for (a) round-nosed and (b) flat-ended impactors, and with damage variables according to the scale bar on the right for (c) round-nosed and (d) flat-ended impactors.

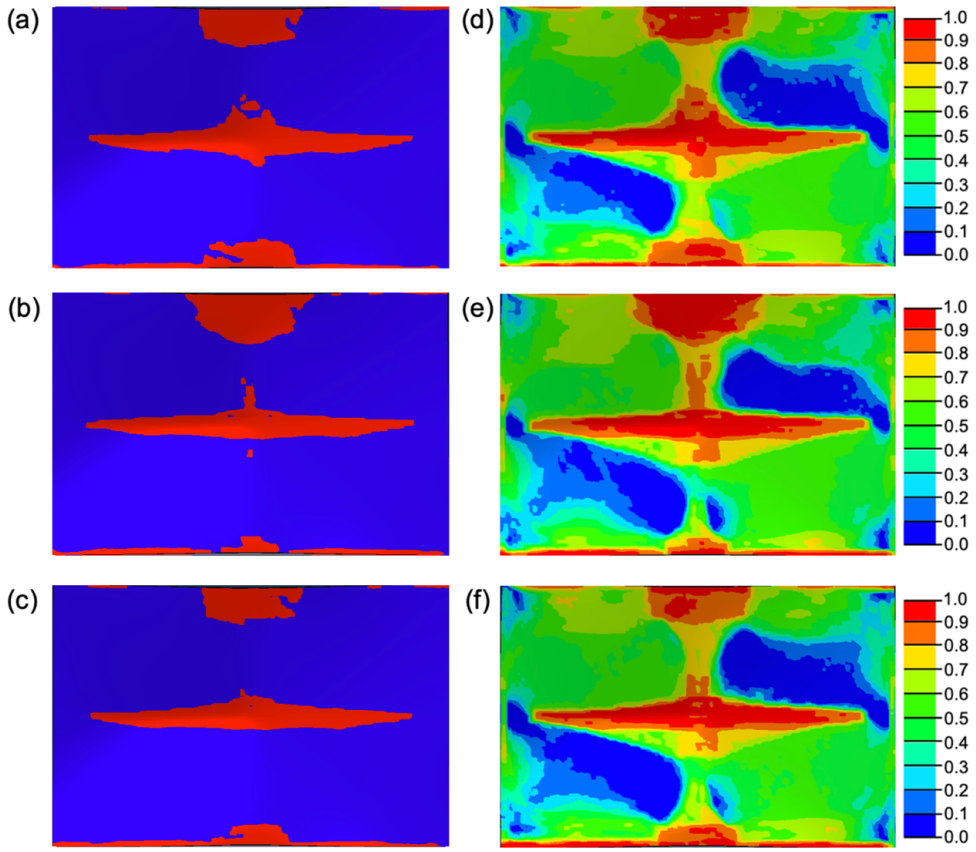

Figure 11-21. Damage maps from 30 J impacts using the final model, and c_{10} = 0.9, d_1 = 0.001 and c_1 = 0, with damage variables above 0.85 shown in red for a flat-ended impactor with (a) 1 mm, (b) 1.5 mm, and (c) 2 mm of rubber and with damage variables according to the scale bar on the right for a flat-ended impactor with (d) 1 mm, (e) 1.5 mm, and (f) 2 mm of rubber.

The damage areas of the preliminary model versus the final model are given in Table 11-4 below. Considering this data, the second variation of the model was chosen and the delamination damage ratio was adjusted to 0.9 instead of 0.85, causing a reduction in damage area values for the damage maps presented from Table 11-4 to those in Chapter 7.

Table 11-4. Damage area values calculated by implementing the preliminary model and final model for all cases simulated.

Impactor	Impact Energy (J)	Damage Area (mm^2)
Preliminary Model		
Round	30	265
Flat	30	239
Preliminary Model ($c_{10} = 0.9, d_1 = 0.001$)		
1 mm rubber	30	1293

1.5 mm rubber	30	1101
2 mm rubber	30	1011
Final Model		
Round	7.5	1605
Round	15	3375
Round	30	8788
Flat	30	3060
Final Model ($c_{10} = 0.9, d_1 = 0.001$)		
1 mm rubber	30	2048
1.5 mm rubber	30	1947
2 mm rubber	30	1766